

**EFFECT OF CRYO-FSP ON MICROSTRUCTURAL
EVOLUTION AND MECHANICAL PROPERTIES OF STIR CAST
Al7075-SiC_p NANOCOMPOSITES**

Ph.D. THESIS

by

ATUL KUMAR



**DEPARTMENT OF METALLURGICAL AND MATERIALS ENGINEERING
INDIAN INSTITUTE OF TECHNOLOGY ROORKEE
ROORKEE - 247667 (INDIA)
MAY, 2019**

**EFFECT OF CRYO-FSP ON MICROSTRUCTURAL
EVOLUTION AND MECHANICAL PROPERTIES OF STIR CAST
Al7075-SiC_p NANOCOMPOSITES**

A THESIS

*Submitted in partial fulfilment of the
requirements for the award of the degree*

of

DOCTOR OF PHILOSOPHY

in

METALLURGICAL AND MATERIALS ENGINEERING

By

ATUL KUMAR



**DEPARTMENT OF METALLURGICAL AND MATERIALS ENGINEERING
INDIAN INSTITUTE OF TECHNOLOGY ROORKEE
ROORKEE - 247667 (INDIA)
MAY, 2019**

**©INDIAN INSTITUTE OF TECHNOLOGY ROORKEE, ROORKEE- 2019
All RIGHTS RESERVED**



INDIAN INSTITUTE OF TECHNOLOGY ROORKEE ROORKEE

CANDIDATE'S DECLARATION

I hereby certify that the work which is being presented in the thesis entitled “**EFFECT OF CRYO-FSP ON MICROSTRUCTURAL EVOLUTION AND MECHANICAL PROPERTIES OF STIR CAST Al7075-SiC_p NANOCOMPOSITES**” in partial fulfilment of the requirements for the award of the degree of Doctor of Philosophy and submitted in the Department of Metallurgical and Materials Engineering of the Indian Institute of Technology Roorkee, Roorkee is an authentic record of my own work carried out during the period from July, 2014 to May, 2019 under the supervision of Dr. Suhrit Mula, Associate Professor, Department of Metallurgical and Materials Engineering and Dr. Kaushik Pal, Associate Professor, Department of Mechanical and Industrial Engineering, Indian Institute of Technology Roorkee, Roorkee.

The matter presented in this thesis has not been submitted by me for the award of any other degree of this or any other Institution.

(ATUL KUMAR)

This is to certify that the above statement made by the candidate is correct to the best of our knowledge.

(Suhrit Mula)
Supervisor

(Kaushik Pal)
Supervisor

The Ph.D. Viva-Voce Examination of **Mr. Atul Kumar**, Research Scholar, has been held on

Chairperson, SRC

Signature of External Examiner

This is certify that the student has made all the corrections in the thesis.

(Suhrit Mula)
Supervisor

(Kaushik Pal)
Supervisor

Head of the Department

Dated.....

Acknowledgements

First and foremost, I would like to express my gratitude from the core of my heart to God for giving courage, strength and patience to carry out my research work.

I take this opportunity to express my sincere gratitude, deepest respect and heartiest thanks to my supervisors, Dr. Suhrit Mula, Associate Professor, Department of Metallurgical and Materials Engineering and Dr. Kaushik Pal, Associate Professor, Department of Mechanical and Industrial Engineering, Indian Institute of Technology Roorkee for their valuable and intellectual guidance, unwavering support and encouragement throughout the tenure of my research work. This thesis could not have attained its present form both in content and presentation, without their active interest, timely help, painstaking efforts, direction and valuable guidance. The words prove to be insufficient to express my deep feelings and heartfelt thanks to my supervisors for their high benevolence guidance throughout my doctoral work. The experience of working with them, I strongly believe, will have far-reaching influence in my future life.

I express my immense gratitude and indebtedness to Professor G.P. Chaudhari, Head of Metallurgical and Materials Engineering Department, Professor S. K. Nath (Chairman SRC), Dr. G.P. Chaudhari (Internal member), Metallurgical and Materials Engineering Department and Dr. P. K. Jha (External member), Department of Mechanical and Industrial Engineering, Indian Institute of Technology Roorkee for their continuous help and valuable suggestions encouragements to pursue this work.

I am deeply indebted to Dr. Vivek Pancholi, Associate Professor, Department of Metallurgical and Materials Engineering, Indian Institute of Technology Roorkee, for his help and providing the access of Friction Stir Processing machine.

I am grateful to all the staff members of Heat treatment, Fabrication, Materials Testing and Metallography Laboratory, who have assisted me despite the difficulties they faced during the closure of the laboratory. I am also grateful to all the technical and administrative staff from the Department and Institute Instrumentation Centre, IIT Roorkee.

Special thanks to my friends Mr. Himanshu Kala, Mr. Anirudh Malakar, Mr. Surendra chaurasiya, Mr. Mrinmoy Sinha, Mr. Abhishek Gupta, Mr. Sumit Kumar, Mr. Pankaj Rawat, Dr. Ram Kishore and Dr. Nitin Gavankar, who helped me any time when I needed. I also thankful to Dr. Dasharath Mabrukar, Dr. Sumit Ghosh, Dr. V. M. Suntharavelu Muthaiah and Mr. G. Ashwin Kumar, co-research scholars for their help and cooperation during my research.

Finally, I would like to share this moment of happiness with my father, Mr. Babu Ram Sharma, mother Mrs. Savitri Devi and my siblings. I express my profound regards to my parents and sisters for their blessings and constant encouragement and inspiration to succeed in my endeavors. You are waited for many years to see this moment. Thank you for all sacrifices that you are made. I would like to express my reverence and great admiration to my wife, Mrs. Sandhya Sharma for her sacrifice, help and providing me constant encouragement. I would like to thank my loving son Atharv Sharma for beginning each day with a great smile.

I would like to express my deep gratitude to all who contributed in successful conclusion of this work and submission of this dissertation.

IIT Roorkee

Date:

(ATUL KUMAR)

Abstract

Over the years, aluminum matrix composites (AMCs) have become the subject of extensive research because of possibility to achieve outstanding properties such as high strength to weight ratio, high stiffness, superior wear resistance and high thermal stability. The driving force for AMCs manufacturing is to tailor the desirable properties of the material by combining the light weight, tough and ductile aluminum (Al) alloy with a suitable ceramic reinforcement which have high wear resistance, high specific stiffness and superior high temperature mechanical properties. Therefore, AMCs could be highly useful as potential structural materials to substitute conventional monolithic Al alloys in automotive and aerospace industries. Because the AMCs not only possess excellent combination of mechanical properties, but also they are economically and environmentally sustainable. Presently, they are being used in some applications in aerospace and automobile sectors, such as cylinder blocks, drive shaft, rotor vanes etc. However, AMCs in as-cast states often show inferior mechanical properties due to its poor particle/matrix interface characteristics, dendritic structure of matrix phase, non-uniformity of reinforcement, lack of matrix continuity and presence of associated porosities, which limit their widespread adoption for the engineering applications to a large extent. To overcome this, present work investigates an effective two-steps method (stir casting followed by friction stir processing (FSP)) for development of cast Al7075-SiC nanocomposites and improvement of mechanical properties by FSP. To achieve the objectives, an attempt has been made to synthesize nanosize SiC particles (<100 nm) reinforced Al7075 composites through stir casting followed by modification of cast microstructures by FSP at two different cooling conditions, i.e. with cryocooling effect and normal air cooling (NAC) state. Aim of the FSP is to modify the cast microstructure thereby enhancing its mechanical strength, ductility, wear resistance and corrosion resistance simultaneously for its practical applicability.

As the concept of the FSP is relatively new, first the Al 7075 alloy has been exploited to optimize the process parameters in details to obtain defect-free fine recrystallized microstructure after FSP. The alloy plates were friction stir processed (FSPed) using different combination of traverse speeds (25, 45, 65, 85, 100 and 150 mm/min) and rotational speeds (508 and 720 rpm) in order to investigate their influences on the microstructure, mechanical properties and corrosion resistance. The optimized result in terms of defect-free processed zone with refined microstructure was obtained only at a rotational speed of 720 rpm for a traverse speed of 25, 45,

65 and 85 mm/min. The grain size of the nugget zone was found to decrease with increase in the traverse speed from 25 to 85 mm/min at a constant rpm of 720. As a result, the yield strength (YS) and hardness of the FSPed samples increased gradually with an increase in the traverse speed, which effectively decrease the heat input during the FSP operation.

Further, critical analysis was carried out thoroughly on the FSP parameters for the as-cast Al7075-2wt.% SiC micro- and nanocomposites. After the FSP, the nanoparticles reinforced composite showed better mechanical properties than that of the microparticles reinforced composite. Tensile strength (>3 times) and wear resistance were found to increase significantly with simultaneous enhancement of the ductility (10 times). The improvement is ascribed to the grain size reduction, distribution of SiC nanoparticles uniformly within the matrix, increase particle-matrix interface characteristics and elimination of casting defects such as porosity after the FSP. The corrosion potentials of the as-cast composites were found to shift towards noble direction after the FSP. Enhancement of corrosion resistance after the FSP is attributed to the decrease in the heterogeneity on the surface and uniform dispersion of the reinforced particles, which reduced the effective active surface area exposed to the corrosive solution.

In the next set of experiments, FSP using in-process cryocooling (IPC) approach has been designed in the safe workable regions in order to control the precipitate kinetics besides the grain size refinement during FSP of Al7075 alloy. This study is aimed to understand external cryocooling effects during FSP on microstructural evolution, especially precipitate kinetics and mechanical properties. An indigenous cooling setup is designed to effectively draw out the generated heat from stir zone during FSP. The IPC during the FSP led to about 2 times more grain size refinement in the nugget zone (2.4 μm) with nanosize precipitates of η' phase (20-30 nm) as compared to 4.7 μm average grain size after FSP at NAC state. This is due to the effective way of heat rejection from the nugget zone by circulating a chilled mixture (at $-30\text{ }^\circ\text{C}$) of liquid nitrogen and methanol in the IPC condition. This controls the thermal boundaries of the material during FSP. The best combination of strength and ductility is achieved (UTS=535 MPa El.%= 22) for the IPC FSPed sample. The results have been analyzed in terms of working temperature, strain rate, Zener–Holloman parameter Z, precipitate interface characteristics & its strengthening effect, Hall–Petch strengthening due to grain size reduction and trade-off between them.

Finally, similar kind of in-process cryocooling FSP schedule has been conducted for the stir cast Al7075-SiC nanocomposites with varying weight percentage of nanosize SiC particles (2%, 3% and 5%). It was found that the FSP with IPC approach offered a great potential in the development of fine grained Al7075-SiC nanocomposites with much improved mechanical properties through microstructural modification. The FSP at IPC state has resulted uniform distribution of the reinforced SiC nanoparticles, refined the matrix grain size, control the precipitation kinetics, enhanced the particle/matrix interface characteristics and eliminated the casting defects from the as-cast composites. Microstructural analysis through TEM and EBSD confirmed the formation of extremely fine matrix grains in which nanosize SiC particles and precipitates of η' phase are dispersed uniformly in the nanocomposite samples after the FSP. These microstructural changes significantly improved the mechanical properties both strength (YS, hardness) and ductility. Overall, cryo-FSPed Al7075-3wt.% SiC nanocomposite sample showed superior mechanical properties (UTS=552 MPa, %El.=17) and excellent wear resistance. Moreover, the corrosion resistance of these samples (in aerated 3.5% NaCl solution) was also found to be highly significant as the corrosion potentials of the nanocomposites were found to shift towards noble direction after the FSP.

Keywords: Age-hardenable Al7075 alloy; Nanocomposites; Stir casting; Friction stir processing; In-process cryocooling; Precipitation hardening; Grain boundary strengthening; Dynamic recrystallization; EBSD; Electron microscopy.

Contents

	Page No
Candidate's Declaration	i
Acknowledgements	iii
Abstract	v
Contents	ix
List of Figures	xiii
List of Tables	xvii
List of Symbols	xix
Abbreviations	xxi

Chapter 1:

Introduction

1.0	Introduction	1
-----	--------------	---

Chapter 2:

Literature review

2.1	Introduction	9
2.2	Aluminium and its alloys	9
2.3	Strengthening mechanisms in Al alloys	10
	2.3.1 Grain boundary strengthening	11
	2.3.2 Solid solution strengthening	12
	2.3.3 Work hardening/ Strain hardening	13
	2.3.4 Precipitation strengthening	13
2.4	Composite materials	15
	2.4.1 Metal matrix composites	16
	2.4.1.1 Aluminium matrix composites	16
2.5	Synthesis of metal matrix composites	17
2.6	Secondary processing of AMCs through FSP	20
	2.6.1 Effect of process parameters	24
	2.6.1.1 Tool geometry	25
	2.6.1.2 Machine variables	26
	2.6.1.3 Effect of cryocooling	28

2.6.2	Recrystallization mechanisms during FSP	29
2.7	National and international status	31
2.8	Research gaps and formulation of problem	37
2.8.1	Research gaps	37
2.8.2	Formulation of the problem	37
2.9	Objectives of the present research work	38
2.10	Plan of the present study	40

Chapter 3: Materials, experimental and characterization details

3.1	Material selection	41
3.1.1	Preparation of reinforcement	42
3.2.2	Synthesis of AMCs	43
3.2	Experimental techniques	45
3.2.1	Friction stir processing setup	45
3.2.1.1	Selection of FSP parameters	47
3.2.1.2	Temperature measurement	48
3.3	Microstructural investigation	49
3.3.1	Optical microscopy	50
3.3.2	Scanning electron microscope (SEM) and Electron backscatter diffraction (EBSD)	51
3.3.3	Transmission electron microscopy (TEM)	53
3.4	Mechanical testing	55
3.4.1	Vickers hardness measurement	55
3.4.2	Tensile testing	56
3.4.3	Wear testing	57
3.5	Corrosion testing	60

Chapter 4: Results and discussion

4.1	FSP on Al7075 alloy and its analysis	63
4.1.1	Microstructural characterization	63
4.1.2	Mechanical properties	68

	4.1.3	Wear characteristics	72
	4.1.4	Corrosion behavior	77
	4.1.5	Summary	80
4.2		FSP on Al7075-2wt.% SiC composites developed by stir casting	81
	4.2.1	Optimization of the FSP parameters for cast AMCs	81
	4.2.2	FSP on stir-cast Al7075-2wt.% SiC micro- and nanocomposites	84
	4.2.2.1	Microstructural characterization	84
	4.2.2.2	Mechanical properties	92
	4.2.2.3	Wear characteristics	97
	4.2.2.4	Corrosion behavior	100
	4.2.2.5	Summary	102
4.3		Cryo-FSP on Al7075 alloy and its analysis	103
	4.3.1	Microstructural characterization	104
	4.3.2	Mechanical properties	110
	4.3.3	Summary	115
4.4		Cryo-FSP on Al7075-SiC nanocomposites and their analysis	116
	4.4.1	Microstructural characterization	117
	4.4.2	Mechanical properties	122
	4.3.3	Summary	126
4.5		Comparison of properties of Al7075 and its composites FSPed in NAC and IPC conditions	127

Chapter 5: Conclusions and future scope of study

5.1	Conclusions	133
5.2	Future scope of study	135
	References	137
	List of Publications	157

List of Figures

Figure No.	Description	Page No.
Figure 2.1	Schematic representation of the grain boundary strengthening: Dislocations approaching a grain boundary and grain boundary acts as a barrier to dislocation motion.	11
Figure 2.2	Schematic representation of (a) Substitutional and (b) Interstitial solid solution strengthening.	13
Figure 2.3	Bowing and bypassing between precipitates and dislocation through Orowan mechanism, (b) shearing of precipitates by moving dislocations through Friedel mechanism.	14
Figure 2.4	Schematic diagram of stir casting technique.	19
Figure 2.5	The schematic illustration of FSP.	21
Figure 2.6	(a) Macrostructure of FSPed sample at 720 rpm-85 mm/min, microstructure of (b) TMAZ and (c) base metal (Al7075 T651).	22
Figure 2.7	Effect of processing parameters on shapes of NZ in FSP of cast A356 aluminium (a) 300 rpm, 51 mm/min; (b) 900 rpm, 203 mm/min.	23
Figure 2.8	List of attributes and the potentiality of the FSP as a diversified process.	24
Figure 2.9	Classification of FSP process variables.	25
Figure 2.10	Basic tool geometry along with different types of pin profile and shoulder end surface features.	26
Figure 2.11	Schematic of various stages of dynamic recrystallization mechanisms (a) DDRX, (b) CDRX and (c) GDRX.	30
Figure 2.12	Contribution of each chapter to overall objectives.	39
Figure 2.13	Flow diagram of detailed plan of the present study.	40
Figure 3.1	Planetary ball mill.	42
Figure 3.2	(a) SEM image of as received SiC particles (b) TEM image of 25 h ball milled SiC particles.	43
Figure 3.3	Schematic image of bottom pouring stir casting machine.	44
Figure 3.4	(a) As cast Al7075 alloy (b) Al7075-2wt.% SiC nanocomposite, (c) Al7075-3wt.% SiC nanocomposite and (d) Al7075-5wt.% SiC nanocomposite.	44
Figure 3.5	Photograph of friction stir processing machine used in this work.	45
Figure 3.6	Experimental setup used in this study along with surface appearance of the samples after FSP: (a) normal air cooling (b) in-process cryocooling.	46
Figure 3.7	Photograph of the hollow fixture along with schematic drawing.	47
Figure 3.8	Schematic drawing of tool used for this study.	48
Figure 3.9	Schematic representation of the temperature measurement system, (b) Photograph of the K-type thermocouples fitted into the FSP sample and (c) Photograph of the data logger connected with computer and thermocouples for temperature measurement.	49

Figure 3.10	Photograph of high speed diamond cutter IsoMet 4000.	50
Figure 3.11	Leica DMI 5000 M inverted optical microscope.	51
Figure 3.12	Photograph of the SEM (ZEISS 51-ADD0048).	52
Figure 3.13	Schematic representation of the EBSD setup.	53
Figure 3.14	Photograph of the TEM sample preparation unit (a) Gatan punching tool (Model: 656 punch), (b) Dimple grinder (Model: Fischione 200) (c) Twin jet electropolisher.	54
Figure 3.15	Photograph of the FEI Technai 20 G2S-Twin TEM.	55
Figure 3.16	Photograph of the FEI-VM50 Vickers hardness tester.	56
Figure 3.17	Schematic drawing and photograph of a tensile specimen.	57
Figure 3.18	The picture of the S-Series, H25K-S tensile testing machine.	57
Figure 3.19	Photograph of the pin-on-disc tribometer (TR-201E-M2, DUCOM, India).	58
Figure 3.20	Photograph of the SJ 400, Mitutoyo, profilometer.	59
Figure 3.21	Weighing machine with density kit setup (ML204/A01, Mettler Toledo, Switzerland).	60
Figure 3.22	Grammy potentiodynamic polarization setup.	61
Figure 4.1	Macrostructure of (a) FSPed sample at 720 rpm-85 mm/min, microstructure of (b) TMAZ and (c) BM.	64
Figure 4.2	Microstructures of the center of the NZ at (a) 720 rpm-25 mm/min, (b) 720 rpm-45 mm/min, (c) 720 rpm-65 mm/min and (d) 720 rpm-85 mm/min.	65
Figure 4.3	Effect of traverse speed on grain size.	66
Figure 4.4	TEM micrographs of (a) BM, and (b) and (c) NZ of the FSPed sample at 720 rpm-85 mm/min.	67
Figure 4.5	(a) Variation in hardness of NZs with traverse speed and (b) Variation in hardness of NZs with inverse of the square root of grain size.	68
Figure 4.6	Engineering stress-strain curves for BM and FSPed samples at different conditions.	71
Figure 4.7	SEM fractographs of (a) BM, (b) FSPed at 720 rpm-25mm/min and (c) FSPed at 720 rpm-85mm/min.	72
Figure 4.8	Variation of friction coefficient with sliding time for (a) BM, (b) FSPed sample at 720 rpm-25 mm/min, (c) FSPed sample at 720 rpm-45 mm/min, (d) FSPed sample at 720 rpm-65 mm/min and (e) FSPed sample at 720 rpm-85 mm/min.	73
Figure 4.9	Surface profiles of wear scars for (a) BM and (b) FSPed sample at 720 rpm-25 mm/min (c) FSPed sample at 720 rpm-45 mm/min, (d) FSPed sample at 720 rpm-65 mm/min and (e) FSPed sample at 720 rpm-85 mm/min.	74
Figure 4.10	Effect of traverse speed on wear volume of FSPed samples.	76
Figure 4.11	SEM micrographs of worn surfaces of (a) BM, (b) FSPed sample at 720 rpm-25 mm/min, (c) FSPed sample at 720 rpm-85 mm/min and (d) EDS analyses of the sample FSPed at 720 rpm-85 mm/min.	77

Figure 4.12	Potentiodynamic polarization scans for BM and FSPed samples at different conditions.	79
Figure 4.13	SEM micrographs of corroded surfaces of (a) BM and (b) FSPed sample at 720 rpm-85 mm/min.	80
Figure 4.14	Macrostructure of the samples at different FSP parameters.	82
Figure 4.15	(a) Stitched optical micrograph of Al7075-2wt.% SiC microcomposite, FSPed at 1025 rpm-25 mm/min, (b) magnified view of NZ, (c) as-cast Al7075-2wt.% SiC microcomposite and (d) TMAZ	83
Figure 4.16	(a) SEM image of as received SiC particles (b) TEM image of 25 h ball milled SiC particles; SEM (SE) images of the as-cast (c) MC2 and (d) NC2; magnified SEM (BSE) images of the as-cast (e) MC2 and (f) NC2.	85
Figure 4.17	SEM image with EDS mapping of as-cast Al7075-2wt.% SiC nanocomposite: (a) Micrograph, (b) EDS mapping of C, (c) EDS mapping of Al and (d) EDS mapping of Si.	86
Figure 4.18	SEM image with EDS mapping of as-cast Al7075-2wt.% SiC microcomposite: (a) Micrograph, (b) EDS mapping of C, (c) EDS mapping of Al and (d) EDS mapping of Si.	87
Figure 4.19	Optical images of friction stir processed (a) Al7075-2wt.% SiC microcomposite and (b) Al7075-2wt.% SiC nanocomposite.	88
Figure 4.20	SEM image with EDS mapping of FSPed Al7075-2wt.% SiC microcomposite: (a) Micrograph, (b) EDS mapping of C, (c) EDS mapping of Al and (d) EDS mapping of Si.	89
Figure 4.21	SEM image with EDS mapping of FSPed Al7075-2wt.% SiC nanocomposite: (a) Micrograph, (b) EDS mapping of C, (c) EDS mapping of Al and (d) EDS mapping of Si.	90
Figure 4.22	Bright field TEM image of (a) FSPed Al7075-2wt.% SiC nanocomposite and (b) SAED pattern corresponding to the TEM image.	91
Figure 4.23	Variation in hardness of composites in the as-cast state and after the FSP.	93
Figure 4.24	(a) Representative stress-strain curves for the FSPed NC2 to indicate the variation of tensile strength of the composite samples; stress-strain curve of (b) the as-cast Al7075-2wt.% SiC micro- and nanocomposites and (c) FSPed Al7075-2wt.% SiC micro- and nanocomposites.	95
Figure 4.25	SEM micrographs of the tensile fracture surface of (a) as-cast Al7075-2wt.% SiC microcomposite, (b) as-cast Al7075-2wt.% SiC nanocomposite, (c) FSPed Al7075-2wt.% SiC microcomposite and (d) FSPed Al7075-2wt.% SiC nanocomposite.	97
Figure 4.26	Variation in weight loss of composites in the as-cast state and after the FSP.	98
Figure 4.27	SEM micrographs of the worn surface of (a) as-cast Al7075-2wt.% SiC microcomposite, (b) as-cast Al7075-2wt.% SiC nanocomposite, (c) FSPed Al7075-2wt.% SiC microcomposite and (d) FSPed Al7075-2wt.% SiC nanocomposite.	99

Figure 4.28	Potentiodynamic polarization curves for the as-cast and friction stir processed Al7075-2wt.% SiC micro- and nanocomposites.	100
Figure 4.29	Experimental setup used in this study along with surface appearance of the samples after FSP: (a) normal air cooled (b) in-process cryocooled.	104
Figure 4.30	Optical micrographs of the (a) ST base metal, (b) FSPed sample with NAC and (c) FSPed sample with IPC.	105
Figure 4.31	Typical EBSD maps and distribution of grain size as a function of area fraction for (a) FSP with NAC and (b) FSP with IPC condition.	106
Figure 4.32	Temperature profile recorded during FSP with IPC and NAC condition.	108
Figure 4.33	TEM micrographs of FSPed sample processed with (a and b) NAC and (c and d) IPC condition.	110
Figure 4.34	Variation of hardness for different process conditions.	111
Figure 4.35	Tensile curves of alloy processed at different cooling conditions.	114
Figure 4.36	SEM fractographs of (a) ST base metal, (b) FSPed sample with NAC and (c) FSPed sample with IPC.	115
Figure 4.37	Optical microstructures in as-cast condition of (a) Al7075 alloy, (b) Al7075-2wt.% SiC nanocomposite, (c) Al7075-3wt.% SiC nanocomposite and (d) Al7075-5wt.% SiC nanocomposite.	118
Figure 4.38	Image quality map of the cryo-FSPed samples (a) Al7075 alloy, (b) Al7075-2wt.% SiC nanocomposite, (c) Al7075-3wt.% SiC nanocomposite and (d) Al7075-5wt.% SiC nanocomposite.	119
Figure 4.39	Grain size distribution as a function of number fraction for (a) Al7075 alloy, (b) Al7075-2wt.% SiC nanocomposite, (c) Al7075-3wt.% SiC nanocomposite and (d) Al7075-5wt.% SiC nanocomposite.	120
Figure 4.40	(a,b,c) EBSD maps (IQ+IPF) and misorientation angle as a function of number fraction for Al7075-3wt.% SiC nanocomposite (d) STEM image of Al7075-3wt.% SiC nanocomposite.	122
Figure 4.41	Variation in hardness of the different samples before and after cryo-FSP.	124
Figure 4.42	Tensile curves of samples FSPed at in-process cryocooling condition.	125
Figure 4.43	Tensile curves of Al7075 alloy FSPed at different cooling conditions (Repeated from Fig. 4.35).	127
Figure 4.44	Variation of engineering stress-strain curves of the FSPed Al7075 alloy and its nanocomposite samples as a function of different processing environments.	128
Figure 4.45	Variation in hardness of the different samples after FSP with NAC and IPC condition.	129
Figure 4.46	Variation in weight loss of composites in the as-cast state and after the FSP	130
Figure 4.47	Variation of potentiodynamic polarization curves of FSPed Al7075 alloy and its composites as a function of different processing environments.	131

List of Tables

Table No.	Description	Page No.
Table 2.1	Comparison of stir casting method with other techniques commonly used for MMCs production.	18
Table 3.1	Chemical composition (wt.%) of the alloy obtained by optical emission spectroscopy analysis.	42
Table 4.1	Tensile properties and Vickers hardness values of the Al7075-2wt.% SiC micro- and nanocomposites before and after the FSP. Improvement of the mechanical properties has been compared with that of the previous studies.	94
Table 4.2	Electrochemical parameters obtained from Tafel plots of both the as-cast and FSPed composites.	102
Table 4.3	Measured values of temperature, calculated values of the strain rate ($\dot{\epsilon}$) and Z parameter for the samples FSPed with IPC and NAC conditions.	109
Table 4.4	Vickers hardness value of different investigated samples.	122

List of Symbols

$^{\circ}\text{C}$	Degree Celsius
h	Hour
min	Minute
nm	Nanometer
μm	Micrometer
mm	Millimeter
cm^3	Cubic centimeter
GPa	Giga Pascal
MPa	Mega Pascal
N	Newton
$N\cdot m$	Newton-meter
kg	Kilogram
λ	Inter-particle spacing
V	Volt
mV	Milli Volt
T_{max}	Maximum nugget zone temperature
T_m	Melting temperature
kJ	Kilojoule
k	Hall-Petch constant
d	Grain size
K	Kelvin
b	Burgers vector
Z	Zener-Hollomon parameter
Q	Activation energy
G	Shear modulus
R	Universal gas constant
r	Radius of the precipitates
b	Burgers vector
ρ	Dislocation density

α	Dislocation strengthening constant
τ	Shear stress
σ_0	Friction stress
σ_Y	Yield strength
$\Delta\sigma_{ss}$	Solid solution strengthening
σ_{ppt}	Precipitation strengthening
$\Delta\sigma_D$	Strain hardening
ν	Poisson ratio
C	Solute concentration
HV	Vickers hardness
BHN	Brinell hardness number
$\dot{\epsilon}$	Strain rate
L_e	Effective depth of the nugget zone
r_e	Effective radius of the nugget zone
ω	Rotational speed of the tool in rpm
v	Traverse speed
i_{corr}	Corrosion current density
E_{corr}	Corrosion potential
E_{pit}	Pitting potential

Abbreviations

AMCs	Aluminium matrix composites
BM	Base metal
BSE	Back scattered electron
CARB	Cross accumulative roll bonding
CCD	Charge couple device
CDRX	Continuous dynamic recrystallization
CMCS	Ceramic matrix composites
DDRX	Discontinuous dynamic recrystallization
DRX	Dynamic recrystallization
EBSD	Electron back scattered diffraction
ECAP	Equal channel angular pressing
EDM	Electric discharge machining
EDS	Energy dispersive spectroscopy
Fig	Figure
FSP	Friction stir processing
FSPed	Friction stir processed
FSW	Friction stir welding
GB	Grain boundary
GDRX	Geometric dynamic recrystallization
GP	Guinier Preston
HAZ	Heat affected zone
IPC	In-process cryocooling
IPF	Inverse pole figure
MMCs	Metal matrix composites
MC	Microcomposite
NAC	Normal air cooling
NC	Nanocomposite
NZ	Nugget zone

OIM	Orientation imaging microscopy
PMCs	Polymer matrix composites
SAED	Selected area electron diffraction
SE	Secondary electron
SEM	Scanning electron microscope
SFE	Stacking fault energy
SPD	Severe plastic deformation
SZ	Stir zone
TEM	Transmission electron microscopy
TMAZ	Thermo mechanically affected zone
TS	Tensile strength
UFG	Ultrafine grains
UTS	Ultimate tensile strength
YS	Yield strength

Aluminium (Al) is the world's most abundant metal on the earth, comprising 8% of the earth's crust. It is the second most widely used metal after steel. Over the last 15 years, the worldwide production of Al has approximately doubled from 30 million tons/year in 2005, to 63 million tons/year in 2017. The density of Al (2.7 g/cm^3) is approximately one-third of steel (7.83 g/cm^3) along with well-balanced mechanical properties, makes it best suitable metal for efficiency enhancement in automobile and aerospace sector (Callister et al., 2007). Unfortunately, pure Al has a low elastic modulus (E) and tensile strength (TS) ($E = 70 \text{ GPa}$ and $TS = 90 \text{ MPa}$ (Callister et al., 2007)). Alloying and age hardening effects discovered at the beginning of the last century were used as the main approaches to enhance the mechanical strength of Al. Depending upon the alloying elements added in Al, the mechanical properties of the alloys can be improved by responding to solid solution strengthening, precipitation hardening and also by work hardening. The major problems existing in Al-based alloys are: they possess very low wear resistance and a moderate level of mechanical strength (Mohseni et al., 2014). Moreover, the performance and efficiency of these alloys are required to enhance continually to fulfill the socioeconomic requirements and challenges throughout the world (Barnwal et al., 2018). Reinforcing the Al alloy with ceramic particulates could be an effective way to further enhance the various mechanical properties of these alloys (Boostani et al., 2015; Harichandran et al., 2016; Moslehshirazi et al., 2016; Suryanarayana et al., 2013). Aluminium matrix composites (AMCs) could offer distinguished solution to the classic problems of wear resistance, strength to weight ratio and high temperature thermal stability (Kalaiselvan et al., 2014; Li et al., 2016; Mula et al., 2012). The driving force for AMCs manufacturing is to tailor the desirable properties of the materials by combining the light weight, tough and ductile Al alloy with a suitable type of ceramic particles, which have high wear resistance, high specific stiffness and superior high temperature mechanical properties. The ductile matrix phase reduces the stress concentration by blunting the cracks through plastic deformation and resulting in improved fracture toughness of the material. Therefore, AMCs could be highly useful as potential structural materials to substitute conventional monolithic Al alloys. The AMCs have received much attention by automotive and aerospace industries because they not only possess excellent combination of mechanical properties, but also they are economically and environmentally sustainable. They are being used

in numerous applications in aerospace and automobile sectors, such as cylinder blocks, drive shaft, rotor vanes etc. Particularly, the SiC reinforced AMCs are investigated extensively for automotive applications such as brake drum, cylinder liners, connecting rods, pistons and piston rings (Suryanarayana et al., 2013; Lee et al., 2001). By proper selection of matrix, reinforcements and manufacturing techniques, the AMCs could offer practical solutions for different sectors, including automobile, aerospace, military and medical applications.

Though several processing methods (e.g. stir casting, compo-casting, ultrasonic casting etc.) have been developed to prepare the particles reinforced Al-based composites, the widespread adoption of the same for the engineering applications has not been successful. This is due to the fact that the conventional size particulate reinforced composites encounter various practical problems such as: (i) ductility/toughness decreases abruptly to much lower range (Jia, 2000; Zabihi et al., 2013), (ii) fracturing of particles as well as composites during deformation for further processing (Ozben et al., 2008; Zabihi et al., 2013), (iii) poor bonding between the particles/matrix interface and (iv) settling of the particles during solidification (Hashim et al., 1999). Moreover, comparatively large amount of particulates are needed to reinforce to achieve the desired mechanical strength (Kok, 2005; Singla et al., 2009). To overcome these difficulties, concept of reinforcing a small amount of nanosize particles in the bulk matrix has been evolved and various researchers (Kang et al., 2004; Li et al., 2008; Li et al., 2004; Mula et al., 2009; Srivastava et al., 2016; Yang et al., 2004; Zhang et al., 2015) have tried to develop nanoparticle reinforced Al-alloy matrix nanocomposites using different techniques. For the same percent of reinforcement, nanoparticles reinforced composites will have more strength. Because, a moving dislocation will encounter more number of obstacles (particles) in nanoparticle reinforced composites and shear strength, τ ($\tau=Gb/l$) required to move a dislocation is enhanced due to the decrease in the inter-particles distance (l) (Dieter, 1986). For example, the ultimate tensile strength (180 MPa) of a 1vol.% Si₃N₄ (10 nm) reinforced Al composite is comparable to that of a 15vol.% SiC (3.5 μ m) reinforced Al composite (Ma et al., 1996). It is also reported that with only 1wt.% of SiC nanoparticles (30 nm) reinforcement in A356 alloy enhanced the ultimate tensile strength (UTS) and yield strength (YS) by 100% while the ductility remained almost unchanged (Li et al., 2008). Mula et al. (Mula et al., 2009) also reported to produce Al-2wt.% Al₂O₃ (av. size 10 nm) nanocomposite by a non-contact ultrasonic casting method. The nanosize dispersoids caused a significant increase in the mechanical strength, i.e., nearly 57% increase in the YS and 92% increase in the hardness as compared to that of the commercially pure Al. Reinforcement of SiC

nanoparticles in Al-alloy matrix is expected to improve mechanical strength and hardness of the matrix, while maintaining good ductility (Zhang et al., 2015). However, uniform dispersion of nanoparticles in the matrix (by most of the production methods) is not an easy task due to the large surface-to-volume ratio of the nanoparticles, attractive van der Waals interactions and poor wettability of the nanoparticles with molten Al (Boostani et al., 2015; Zhou et al., 2015). To overcome these constraints, it is necessary to use some secondary processing methods, which can effectively improve the distribution of particles in the matrix, reduce the level of porosities and hence improve the mechanical properties of the composites. Several approaches such as rolling (Lokesh et al., 2014), forging, friction stir processing (FSP) (Hoziefa et al., 2016), equal channel angular pressing (Ramu et al., 2009), hot extrusion (Mousavian et al., 2016) were applied to improve dispersion of reinforcement and to remove various casting defects. Some researchers found that the above-mentioned secondary processes were useful to modify the microstructural constituents and thereby enhance the mechanical properties of the composites. Amongst the several aforementioned metal working processes, the FSP has been established as a standard technique for microstructural modification and material processing (Bauri et al., 2011; Gibson et al., 2014; Mishra et al., 2005; Rajan et al., 2016).

The FSP technique was originally proposed by Mishra et al. (Mishra et al., 1999, 2001) using the same fundamentals as friction stir welding. It uses extreme plastic deformation and frictional force to mix the metal and refine the microstructure thereby removing inherent casting defects (porosity, micro void, inhomogeneity, and clustering & agglomeration of particles in case of composites). Thus, microstructural modification by FSP significantly enhances the mechanical properties (ductility, tensile strength and hardness) and wear resistance (Cavaliere, 2005; Rahsepar et al., 2016; Rajan et al., 2016). Bauri et al. (2011) investigated the influence of FSP on microstructural characteristics and thereby improved various mechanical properties, such as tensile strength/yield strength and ductility of Al-5wt.% TiC composite. They found that the FSP could effectively homogenize the particles distribution in the composites. Besides the distribution of particles uniformly, the FSP led to refine the grain structure. Thus, the mechanical properties of the cast composites could be enhanced significantly. Kurtyka et al. (2015) used the FSP to enhance the mechanical properties of A339-10wt.% SiC cast composite. They reported a substantial improvement in the distribution of SiC particles and enhancement of mechanical properties in comparison to the starting cast sample. Recently, the effect of the FSP on modification of microstructure and mechanical characteristics of AA7075-TiB₂ in-situ composite

has been reported in (Rajan et al., 2016). Initially, TiB_2 particles were found to cluster and segregate along the grain boundaries. After the FSP, distribution and morphology of the TiB_2 particles were changed significantly and thereby enhanced the tribological and mechanical properties of the composite. Hoziefa et al. (2016) demonstrated that the casting followed by FSP was a promising route to develop Al-based nanocomposite. An Al₂₀₂₄ alloy based composite containing 1wt.% of Al_2O_3 nanoparticles (50 nm) was fabricated by compocasting method followed by FSP. They found that the FSP of the cast composite enhanced its yield strength and ultimate tensile strength, respectively, by 30 and 71% in comparison to that of the as-cast composite. This is attributed to the distribution of Al_2O_3 nanoparticles uniformly and matrix grain size refinement. These results indicate that the FSP is an effective method to modify the microstructure and thus improve mechanical properties of the cast AMCs.

However, secondary processing (e.g. FSP) of the composite in which matrix phase is precipitation hardenable alloy, the FSP at room temperature has shown limited success in improvement of mechanical properties due to the coarsening or dissolution of the strengthening precipitates (results in loss of strength) during processing. After the FSP, a competition is observed between strengthening due to grain size refinement, uniform distribution of reinforced nanoparticles within the matrix, elimination of casting defects and softening due to change in precipitate characteristics (Feng et al., 2013; Kumar et al., 2017). In addition, Xu et al. (2014) have found that fine grains evolved during FSP grow very quickly due to slow cooling rate during/after FSP at room temperature. Aforementioned issues associated with the FSP hinder the real purpose of FSP of enhancing the mechanical properties. To overcome these constraints, cryo-FSP (FSP with in-process cryocooling) is identified as a potential low temperature severe plastic deformation route for refining the microstructure, controlling the precipitation kinetics and homogenizing the distribution of particles in cast metal matrix composites. The FSP with in-process cryocooling setup could effectively suppress precipitate coarsening/overaging and arrest the grain growth by reducing the peak temperature, increasing cooling rate and limiting holding time. This tactic can combine the precipitation strengthening (due to refine precipitate size and distribution) and grain size strengthening along with other strengthening mechanisms in age hardenable Al alloys and its composites. Some researchers have investigated the effect of processing environment on microstructural evolution and mechanical behavior of various alloy systems (Chang et al., 2007; Imam et al., 2016; Kumar et al., 2018; Xu et al., 2012) and Al-based composites (Ashjari et al., 2015; Khodabakhshi et al., 2014) processed by FSP. The FSP with

active/in-process cooling showed exciting improvement of mechanical properties. Inspired from the results of the cooling effects, the present research aims to develop high strength Al7075/SiCp nanocomposite (through precipitation hardening, dispersion strengthening by SiC nanoparticles and grain boundary hardening by formation of ultra-fine matrix grains) by integration of stir casting and FSP.

From the above discussion, it can be concluded that several techniques have been employed to produce bulk size Al/Al-alloy matrix nanocomposites. But till today, the composites have not been used commercially for practical applications because of following reasons: (i) the mixing of ceramic nanoparticles uniformly in the bulk alloy matrix is still challenging, (ii) limited improvement of mechanical properties, (iii) difficulty in further processing, i.e., limited workability and (iv) high cost of production. To overcome these constraints, it is necessary to develop methods which can effectively improve the distribution of nanoparticles in Al matrix, reduce the level of porosities and hence improve the ductility/toughness of the nanocomposites. Moreover, load bearing capacity of any engineering components completely depends on its deformation characteristics, and rarely, any study has been carried out on the deformation mechanisms of the composites. Therefore, an attempt has been made to synthesize nanosize SiC particles (<100 nm) reinforced Al7075 composites through stir casting followed by modification of cast microstructures by FSP with in-process cryocooling (IPC) and normal air cooling (NAC) effects. Aim of the FSP is to modify the cast microstructure thereby enhancing its mechanical strength, ductility, wear resistance and corrosion resistance simultaneously for its practical applicability. The idea is to develop high strength Al7075-SiCp nanocomposites through mechanisms of precipitation hardening, dispersion strengthening by SiC nanoparticles and grain boundary hardening by formation of ultra-fine matrix grains. As the concept of the FSP is relatively new to modify the composite structure, first the Al 7075-T651 alloy has been exploited to optimize the process parameters in details to obtain defect-free fine recrystallized microstructure. Then, modification of the Al7075-SiCp microstructures has been performed using the FSP. Detailed analysis of mechanical properties (such as tensile strength and hardness), corrosion resistance and microstructural features (grain size and precipitate characteristics) was carried out to establish the effectiveness of the in-process cryocooling and mechanisms of microstructural evolution during FSP of Al7075 alloy and its composites.

1.1 Structure of the dissertation

Detailed plan of the present study is summarized in the literature review chapter (Fig. 2.13) for better convenience. In order to make reading in effective manner, the thesis is organized as follows:

1.1.1 Chapter 1: Introduction

This chapter provides a brief introduction to the present research including the significance of the material and its critical review, need and motivation for this research and finally objectives of the work.

1.1.2 Chapter 2: Literature review

This chapter provides the detailed literature review on the significance of aluminium and its alloys, various approaches to enhance their properties, development of aluminium based composites and nanocomposites. In addition, FSP of Al-alloys and its composites, fundamentals of recrystallization mechanisms and grain growth during processing, effect of different strengthening mechanisms are discussed in the light of improvement of their mechanical properties through microstructural modification. At the end, major objectives of the research are defined based on the important findings and research gap found from the literature review.

1.1.3 Chapter 3: Experimental techniques

In this chapter, experimental setup and methodology used for present investigation are explained in details according to sequence of the work performed. First, details about material synthesis are provided. This is followed by optimization of the FSP parameters including the detailed design of the experimental setup made to conduct the FSP with in-process cryocooling and normal air cooling. In the last section, metallurgical and mechanical characterization techniques and procedures are described in details.

1.1.4 Chapter 4: Results and discussion

1.1.4.1 FSP on Al7075 alloy and its analysis

This chapter elaborates the effect of FSP parameters in details to obtain defect-free fine recrystallized microstructure. It is followed by discussion related to microstructural evolution

and their analysis which includes degree of grain size refinement, precipitate characteristics and structure-property relationship. Finally, these process parameters are optimized to maximize the tensile strength, hardness and wear resistance of processed samples.

1.1.4.2 FSP on Al7075-2wt.% SiC composites developed by stir casting

In this chapter, FSP parameters were optimized separately for the as-cast composites as the FSP parameters have different influences to produce defect free samples of the composites and base metal. After choosing the processing parameters in safe workable regions, effect of FSP on the stir cast Al7075-2wt.% SiC micro- and nanocomposites were investigated. Initially, Al7075-2wt.% SiC micro- and nanocomposites were produced in a bottom pouring stir casting machine. This was followed by the mechanical and metallurgical characterization of the as-cast composites. In order to modify the cast microstructure to enhance its mechanical strength, ductility, wear resistance and corrosion resistance, the FSP was carried out on the cast composite samples. The final results were analyzed in terms of distribution of reinforcement, matrix grain size refinement, particle-matrix interface characteristics and elimination of casting defects such as porosity after the FSP.

1.1.4.3 Cryo-FSP on Al7075 alloy and its analysis

This work investigates an effective way of heat extraction from the friction stir processed (FSPed) zone to control the precipitate evolution besides the grain size refinement during the FSP of Al7075 alloy. Detailed analysis of mechanical properties (such as tensile strength and hardness) and microstructural features (grain size and precipitate characteristics) was carried out to establish the effectiveness of the in-process cryocooling and mechanisms of microstructural evolution during the FSP of Al7075 alloy.

1.1.4.4 Cryo-FSP on Al7075-SiC nanocomposites and their analysis

In this chapter, the microstructural evolution and mechanical properties have been studied for the Al7075-SiC nanocomposites developed by integration of stir casting and cryo-FSP. To understand the fundamentals of the deformation characteristics and microstructural evolution, different strengthening mechanisms and fracture morphology have been investigated in details.

1.1.4.5 Comparison of properties of Al7075 and its composites FSPed in NAC and IPC conditions

In this section, different mechanical properties (such as hardness, tensile strength & ductility), wear resistance and corrosion behavior of the Al7075 alloy and Al7075-SiC nanocomposites FSPed under NAC and IPC conditions have been discussed.

1.1.5 Chapter 5: Conclusions

The major outcomes of the work presented in various chapters were summarized in this chapter and suggest some future work that can be done in this area.

2.1 Introduction

First part of this chapter presents the significance of aluminium and its alloys, and critical review on development of aluminium based metal matrix composites/nanocomposites. This includes various aspects of metal matrix composites, especially aluminium matrix composites, such as properties, applications and problems in production of these materials. The second half of this chapter is focused briefly about secondary processing of these materials and development of ultrafine grained materials by several techniques. An overview of friction stir processing and factors affecting the process such as tool rotational speed, traverse speed, in-process cooling etc. are also discussed. At the end, based on the literature survey and research gaps identified, the objectives of the project have been formulated.

2.2 Aluminium and its alloys

Aluminium (Al) is one of the most attractive metallic material used by modern industries owing to their versatile properties. It has unique properties like low density, high ductility, high thermal conductivity and electrical conductivity. Furthermore, it is highly resistance to corrosion in most environments including sea water, ambient atmosphere and great variety of chemical agents. However, pure Al has very inferior mechanical strength properties (Callister et al., 2007). The mechanical properties of Al can be enhanced by adding various alloying elements like copper (Cu), manganese (Mn), silicon (Si), magnesium (Mg), zinc (Zn) etc. so as to produce an alloy with properties tailored for a desired application (Brammer et al., 2010; Ray et al., 2010; Stoichev et al., 2010). Depending on the alloying elements, mechanical properties of the Al alloys can be increased by responding to precipitation hardening (age hardening), work hardening and solid solution hardening. Al alloys are mostly used in structural, aerospace, military and automobile sectors due to their excellent specific strength, high stiffness and good corrosion resistant (Starke et al., 1996). Among them, 7xxx series (Al-Zn-Cu-Mg) alloys are one of the high strength Al alloy group developed to optimize the mechanical properties and corrosion resistance (Jata et al., 2000a; Panigrahi et al., 2011a). It is the mainly combination of Zn and Mg which makes the 7xxx series alloys heat treatable and gives rise to their very high strength. In this alloy, the strengthening effect is mainly depends upon the precipitation of the strengthening phases $MgZn_2$

or $(Al_2Zn_3Mg_3)$. Usually Zn:Mg ratio of about 3 is mostly preferred to avoid the formation of T ($Mg_3Zn_3Al_2$) and S (Al_2CuMg) phases (Mishra et al., 2016). Cu refines the grains and enhances the hardness, giving benefits on the mechanical properties (Miao et al., 2000). Zn alters the precipitation sequence and endorses the precipitation of the coarse T phases with the increasing Zn content in Al-Zn-Cu-Mg alloys (Chen et al., 2013). Generally, the precipitate evolution in case of the age hardenable Al7075 alloy is take place in the following sequence (Panigrahi et al., 2011b):

Supersaturated solution \rightarrow Guinier Preston zones \rightarrow η' precipitates \rightarrow Stable η precipitates.

Guinier Preston (GP) zones are basically solute rich spherical regions (less than 10 nm in size) that are coherent to the matrix. The interfacial energy between matrix and coherent GP zones is low, so that zones of a very minor size can form (Chen et al., 2013; Zhao et al., 2004). Generally, GP zones are precursors to the metastable η' phase (Mandal et al., 2017). The η' precipitate of the order of 10-50 nm is demarcated as the intermediate phase which is semi-coherent to the matrix and has a hexagonal crystal structure with plate like morphology; whereas, incoherent stable η precipitate >100 nm size has both plate like and lath type morphology. The semi-coherent η' precipitate provide the most significant contribution to the strengthening of the material, and the presence of a 3 dimensional coherency strain field around the η' precipitate would be the most effective obstacles against dislocation movement, which consequently increases the strength.

2.3 Strengthening mechanisms in Al alloys

In order to improve the uses of Al alloys in engineering applications, the performance and efficiency of these alloys are required to enhance continually to fulfill the socioeconomic requirements and challenges throughout the world. Several strengthening mechanisms have been evolved to enhance the mechanical strength of the Al and its alloys including solid solution strengthening, precipitation strengthening, grain boundary strengthening, work hardening etc (Scattergood et al., 2008). Generally, all the strengthening mechanisms based on this simple basic principle: increase the intrinsic resistance to dislocation motion renders a material harder and stronger. Such obstacles can be grain boundaries, solute atoms, precipitate phase, dislocations etc. The strengthening mechanisms, which are relevant to the present study, are discussed in detail in the following subsections.

2.3.1 Grain boundary strengthening

Grain size refinement is one of the most desirable tool for strengthening the polycrystalline materials, as grain boundaries restrict the motion of dislocations (Youssef et al., 2006). This is due to the fact that the crystallographic orientations in the adjacent grain is different and dislocations cannot slip into another grain of more than a few degrees misorientation. Due to these reasons, during plastic deformation, the dislocations tend to pile-up on their slip planes at the grain boundary (Callister et al., 2007) as shown in Fig. 2.1.

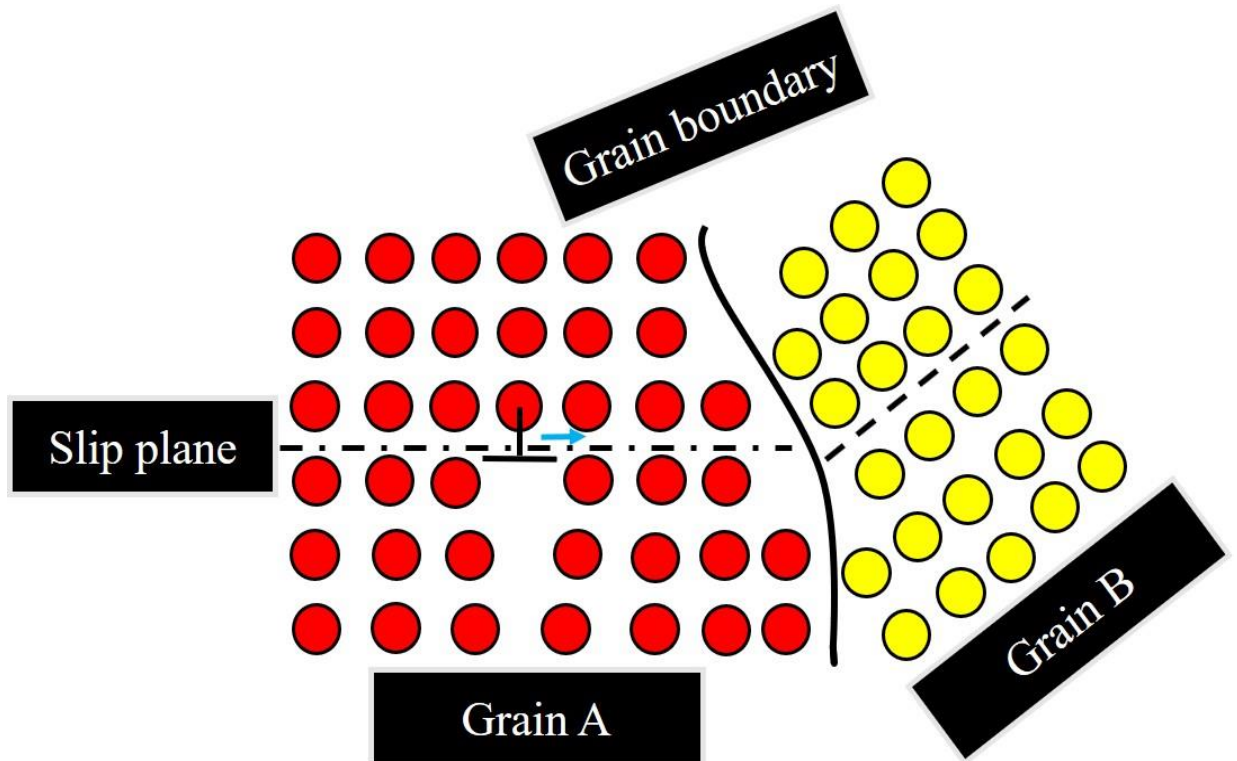


Fig. 2.1: Schematic representation of the grain boundary strengthening: Dislocations approaching a grain boundary and grain boundary acts as a barrier to dislocation motion (Callister et al., 2007).

As the grain size reduces, density of grain boundaries increases, which provide more resistance to dislocation motion. Thus, in the fine-grained materials, much higher stress is needed for further movement of the dislocations thereby strengthening the materials. The effect of grain refinement on yield strength can be described by the well-known Hall-Petch relationship (Dieter, 1986), which is expressed as:

$$\sigma_y = \sigma_0 + \frac{k}{\sqrt{d}} \quad (2.1)$$

Where, σ_y is the yield strength associated with the polycrystalline material, d is the average grain size, σ_0 is the friction stress (20 MPa in case of Al alloys), k is the Hall-Petch constant and reported to 0.12 MPa \sqrt{m} for Al7075 alloy (Shaeri et al., 2016). According to Eq. (2.1), grain size (d) has an inverse relationship with yield strength. So, development of a fine-grained structure during severe plastic deformation (SPD) (Koch et al., 2017; Rajulapati et al., 2008) processes leads to an enhancement of the yield strength as per Hall-Petch relationship.

2.3.2 Solid solution strengthening

Solid solution strengthening is another technique for strengthening the pure metal by incorporating solute atoms of other element(s). Solute atoms added in the parent metal either replace the atoms of the base/parent metal in the crystal lattice (substitutional solid solution) or occupy the interstitial spaces between the solvent atoms in the crystal lattice (interstitial solid solution) without changing the crystal structure. In both cases, crystal lattice of solvent metal gets elastically distorted (Figs. 2.2a & b, respectively) which makes plastic deformation more difficult thereby higher stress is required for further deformation. The size difference between the solute and solvent atoms generate the stress fields around them. The interactions between stress fields due to solute atoms and dislocations result in restriction of dislocation motion, which leads to increase in the strength of the material. Al alloys are mainly alloyed with Cu, Zn, Mg etc. each of which forms the substitutional solid solution. The Hume-Rothery rules describe the factors, which govern the formation of substitutional solid solution. These are (i) size and crystal structure of solute atoms, (ii) electronegativity and (iii) concentration of solute atoms. Moreover, the atomic radius of the solute and solvent atoms must differ by not more than 15%. For good substitutional solid solution, the crystal structures and the valency of solute and solvent must be similar. The following relation is mostly used to describe the solid solution strengthening ($\Delta\sigma_{ss}$) effect on the yield strength of the material due to concentration (C) of solute atoms dissolved in the matrix.

$$\Delta\sigma_{ss} = HC^n \quad (2.2)$$

Where, H & n are constants. Increasing the concentration of the solute atoms will enhance the material strength by impeding more dislocations as compared to low solute concentration (Dieter, 1986).

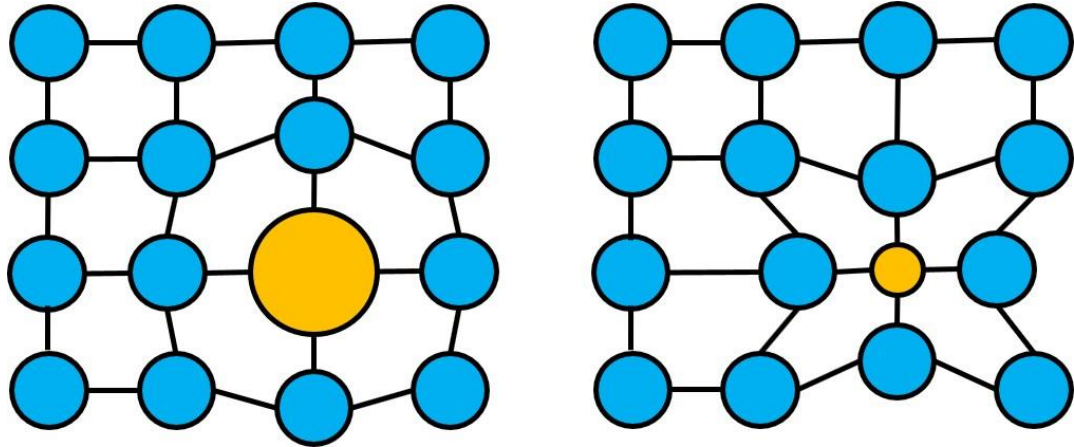


Fig. 2.2: Schematic representation of (a) Substitutional and (b) Interstitial solid solution strengthening (Callister et al., 2007).

2.3.3 Work hardening/ Strain hardening

Strain hardening is the strengthening of the metal/alloy by plastic deformation. During plastic deformation, the dislocation density within the material increases with increasing plastic deformation of a metal (Callister et al., 2007). The higher density of dislocations makes dislocation movement more difficult by the presence of other dislocations. The interaction between the stress fields of the adjacent dislocations leads to strengthening of the material. The relation between yield strength and dislocation density could be estimated by the following equation:

$$\Delta\sigma_D = \alpha G b \rho^{1/2} \quad (2.3)$$

where, α is the constant (depends upon crystal structure) and G , b , and ρ represent shear modulus, Burgers vector and dislocation density, respectively.

2.3.4 Precipitation strengthening

The strength of an age-hardenable alloy could be enhanced by the development of second phase precipitates within the ductile matrix. Precipitation hardening relies on temperature-dependent equilibrium solid solubility characterized by increasing solubility with increasing temperature. After quenching, the excess alloying elements are precipitated out from the supersaturated matrix as second phase. Closely spaced fine precipitates of a second phase, uniformly dispersed within the microstructure, form a strong barrier to dislocation motion. The degree of strengthening resulting from the precipitates strongly depends upon the size, shape and distribution of precipitates, coherency of the precipitates and its volume fraction (Rajulapati et al., 2008). For

dislocations to move in the matrix: they have to either bend around the precipitates or cut through them as shown, respectively, in Figs. 2.3a and b.

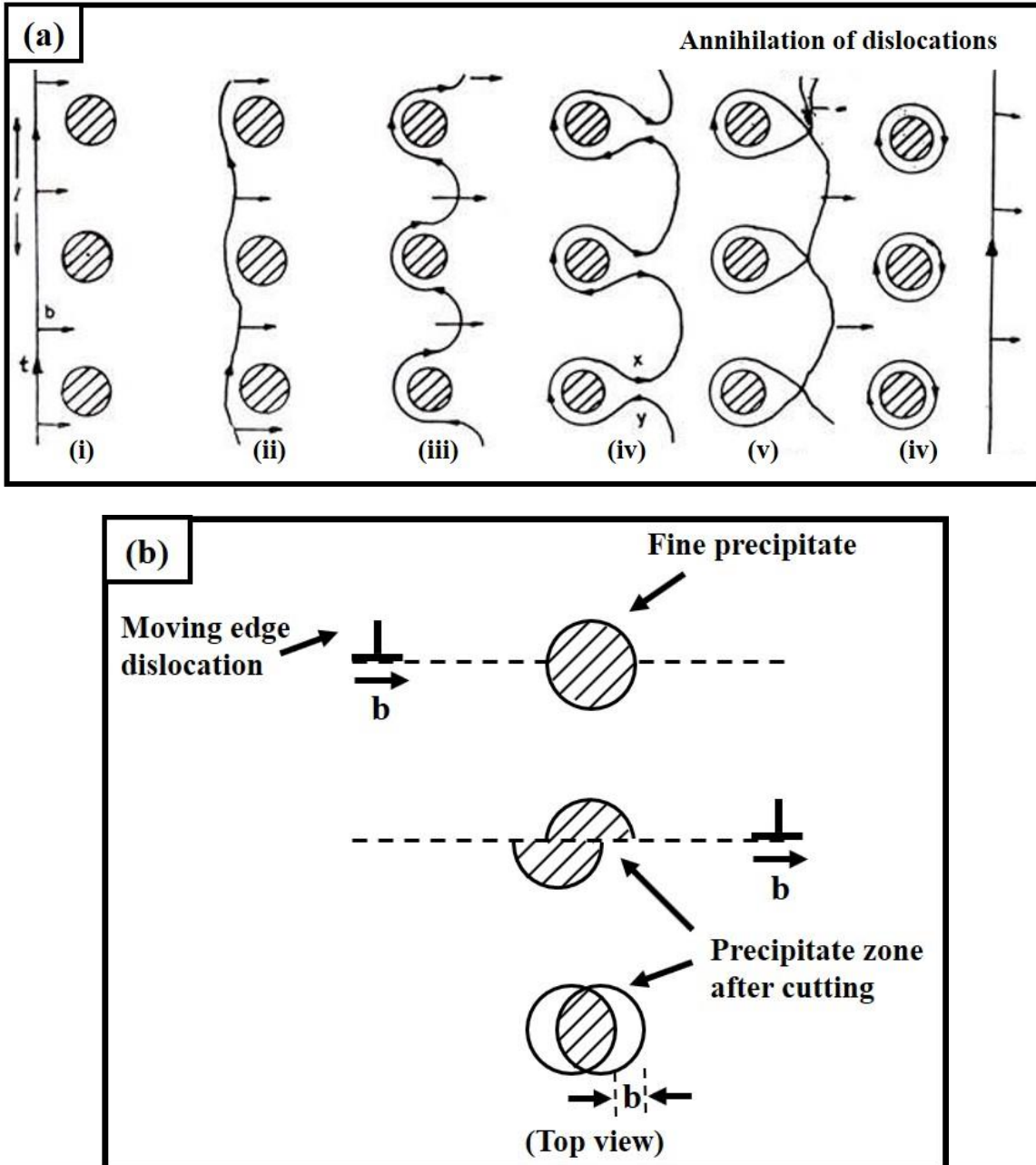


Fig. 2.3: (a) Bowing and bypassing between precipitates and dislocation through Orowan mechanism, (b) shearing of precipitates by moving dislocations through Friedel mechanism (Dieter, 1986).

In case of bending as the applied stress is increased dislocations starts to bow and begin to meet at point X and Y (Fig 2.3a iv). At these points the nature of dislocation is of opposite type as a result they annihilate each other upon interaction leaving behind the loop of dislocation around

the precipitate particles (Fig. 2.3a v). This is called Orowon mechanism. Every time a dislocation passes it leaves behind a loop around the precipitates thus effectively decreasing the distance between the precipitate particles. As a result, next dislocation can only bypass when higher stress is applied. In case of cutting the precipitate by dislocation occurs when dislocation interacts with some fine precipitates or zone. As a result, it offsets the zone by one Burgers vector as illustrated in Fig 2.3b. For this, an additional amount of work done is required to create the additional surface between the precipitate and matrix and stacking faults are also created. These factors contribute to the hardening as they resist the motion of dislocation while cutting the precipitate. In both cases, strength of the material is increases. The shear stress τ , required for a dislocation to move through two nearby obstacles (precipitates) is described as:

$$\tau = Gb/l \quad (2.4)$$

where, G , b and l represent shear modulus, Burgers vector and inter-particle spacing, respectively. So, for the same volume fraction of the second phase, smaller the size of the precipitates, harder for dislocations to pass through them as l is decreased.

2.4 Composite materials

A composite material is a heterogeneous mixture of two or more materials, which have been bounded at a scale that is adequately fine, results in improved properties over the individual material (Liu et al., 2013). Performance of composite materials can be optimized by varying the constituent materials type, their volume fraction, distribution and finally their interaction among them. The two main constitutes of a composite material are the matrix and the reinforcement. The selection of suitable matrix material is mainly determined by the intended application of the composite material, ease of processing, cost factor and availability. The function of matrix material is to hold and maintain relative positions of the embedded phase, give shape of the component and also protect them from chemical and mechanical damage. In addition, when load is applied, the matrix phase should transfer stresses easily with the secondary phase. Optimum combination of matrix and reinforcement properties satisfies a set of operational and manufacturing requirements. The matrix materials can be metals, ceramics or polymers. According to the nature of their matrix, the composite material is classified as: polymer matrix composites (PMCs) (Ray et al., 2006), metal matrix composites (MMCs) (Bachmaier et al., 2012) and ceramic matrix composites (CMCs) (Ouyang et al., 2016). The main purpose of the reinforcement is to strengthen the composite by preventing matrix deformation by mechanical

restraint. Selection of the reinforcement is very important and it includes consideration of properties such as density, elastic modulus, stability at ambient temperature, coefficient of thermal expansion and compatibility with matrix material. Reinforcements are distinguished as particulate fibres, whisker fibres and continuous fibres as per their aspect ratio and morphology.

2.4.1 Metal matrix composites

In a composite, when the matrix phase is metal or its alloy, it is known as metal matrix composites (MMCs). The reinforcing constituent may be another metal or different material, such as a ceramic or organic compound. MMCs are not a single material but a very large family of materials whose main aim is to obtain the judicious combination of toughness and stiffness. By proper selection of reinforcements and manufacturing techniques, the MMCs could offer practical solutions for different sectors including automobile, aerospace, military and medical application. Most of the metallic systems explored in the MMCs for possible practical uses includes Al alloys, Cu alloys, titanium alloys and Mg alloys. But on the basis of usage, Al and its alloys are the dominant choice as matrix material in the MMCs (Al-Aqeeli et al., 2012). Therefore, in the following section, aluminium matrix composites have been discussed in details.

Aluminium matrix composites

Over the years, aluminium matrix composites (AMCs) have become the interesting subject of extensive research because of their outstanding properties such as high strength to weight ratio, high stiffness, superior wear resistance and high thermal stability (Kalaiselvan et al., 2014; Li et al., 2016; Mula et al., 2012; Mallik et al., 2017). The driving force for AMCs manufacturing is tailoring the desirable properties of the matrix and reinforcing materials to achieve better mechanical and other properties in the AMCs; for example, combining the light weight, toughness and ductility of Al alloy with a suitable ceramic particles, which have high wear resistance, high specific stiffness and superior high temperature mechanical properties. The ductile matrix phase reduces the stress concentrations by blunting the cracks through plastic deformation and resulting in improved fracture toughness of the material. Therefore, the AMCs could be useful as potential structural materials to substitute conventional monolithic Al alloys. Moreover, the AMCs have captured the much attention of automotive and aerospace industries because they not only have excellent mechanical properties, but also are economical and environmentally sustainable. They are being used in numerous applications in aerospace and

automobile sectors such as cylinder blocks, drive shaft, rotor vanes etc. Particularly, the SiC reinforced AMCs is being investigated extensively for automotive applications for various parts such as brake drum, cylinder liners, connecting rods, pistons and piston rings (Suryanarayana et al., 2013; Lee et al., 2001). Performance of AMCs depends on composition of the matrix alloy, type of reinforcement, manufacturing methods and processing. Al alloys, specially the age hardenable ones such as the 7xxx series, are the best choice as a matrix material for production of AMCs, because of its enhanced properties (high strength to weight ratio, toughness and good corrosion resistance) compared to other commercially available Al alloys (Atrian et al., 2014). Ceramic materials such as Al_2O_3 , B_4C , MgO , TiC , SiC and TiB_2 are often selected as potential reinforcements for the AMCs. Among the various reinforcements, silicon carbide (SiC) is particularly attractive due to its high specific stiffness, elastic modulus, wear resistance, excellent high temperature stability and low cost (Dey et al., 2014). Furthermore, SiC generally does not react with the matrix material and does not produce undesirable phases. Size, volume fraction of reinforcement and particle-matrix interface characteristics are extremely important factors to characterize the properties of the AMCs.

2.5 Synthesis of metal matrix composites

From the last two decades, the composite materials are showing their benchmarks in various fields of engineering which attract researchers to produce various composites by easy and economical routes. Generally, fabrication methods of MMCs are divided into two main categories, i.e., primary and secondary. Primary processes are used to develop the composite from its ingredient materials. However, the secondary process such as rolling (Lokesh et al., 2014), forging, friction stir processing (Hoziefa et al., 2016), equal channel angular pressing (Manna et al., 2008), hot extrusion (Mousavian et al., 2016) are applied to improve dispersion of reinforcement thereby properties and to alter the shape of the composite to final desired form/shape. Several researchers have found that the above mentioned secondary processes are useful to modify the microstructural constituents and thereby enhance the mechanical properties of the composites (Arab et al., 2014; Ardakani et al., 2014; Krishna et al., 2014; Ramu et al., 2009; Mousavian et al., 2016). At present, bulk size composite reinforced with particulates could be produced by number of primary manufacturing techniques; these include stir casting (Arab et al., 2014), compo casting (Ardakani et al., 2014), ultrasonic casting (Mula et al., 2012), in-situ processing (Krishna et al., 2014), spray forming (Mukhopadhyay et al., 2015), mechanical

alloying (Liu et al., 2013), hot isostatic pressing (Roy et al., 2012), high pressure torsion (Champion et al., 2015), spark plasma sintering (Roy et al., 2007) etc. Among the variety of processing routes, the stir casting is one of the most commonly used and popular technique due to its simplicity, low processing cost, better matrix-particle mixing, near-net shape fabrication of the composites and high production rate (Hashim et al., 1999). It is also preferred as compared to other method because, it has better compatibility with conventional metal processing techniques, no restriction of size, shape and quantity of the production and also it offers dimensional stability of parts. According to Skibo et al. (1988), the production cost of composite material by stir casting process is around 1/3 to 1/2 of the other competitive processes and for large quantity production, it is predicted that the cost will reduce to 1/10th. Shinde et al. (2015) also have demonstrated in his work that the stir casting route is economical and effective way to produce composite in which a dispersed phase is mixed with a molten matrix metal by means of mechanical stirring. Surappa et al. (1997) compared stir casting with the different production techniques on the basis of size, shape, damage to reinforcement, material yield and production cost (Ibrahim et al., 1991), and reported that the stir casting technique is better than the other production methods in all aspects (given in Table 2.1).

Table 2.1: Comparison of stir casting method with other techniques commonly used for MMCs production (Surappa, 1997; Taha, 2001).

Method	Range of size	Damage to Reinforcement	Metal Yield	Cost
Powder metallurgy	Restricted size	Reinforcement fracture	High	Expensive
Squeeze casting	Restricted size	Severe damage	Low	Moderately expensive
Spray casting	Large size	No damage	Medium	Expensive
Stir casting	Larger size	No damage	Very high, >90%	Least expensive

Kumar et al. (2018) developed a low-cost stir casting process for magnesium alloy and its composites. They concluded that the vacuum assisted stir casting is one of the most suitable process for magnesium and its composite development. Mahendra et al. (2007) fabricated AMCs reinforced with fly ash particles by stir casting route and stated a high hardness, high compression & tensile strength and better impact toughness with the increase in reinforcement percentage.

Bhushan et al. (2012) reinforced 10 and 15wt.% SiC particles (20-40 μm) in Al7075 alloy by stir casting process and reported that distribution of SiC particles was excellent in the matrix.

Stir casting is a liquid state technique of composite materials production, in which reinforcement ingredient are mixed into the molten metal by mechanical stirring. The mechanical stirring creates vortex at the surface of the melt, which helps in two ways (i) easy and proper incorporation of the reinforcement particles into the melt and (ii) maintain reinforcement in suspension condition. The prepared composite liquid is then directly cast to the desired shaped mould by simple conventional casting route. By this technique, up to 30% volume fractions of reinforcement can be added into the matrix phase. The schematic representation of stir casting technique is shown in Fig. 2.4.

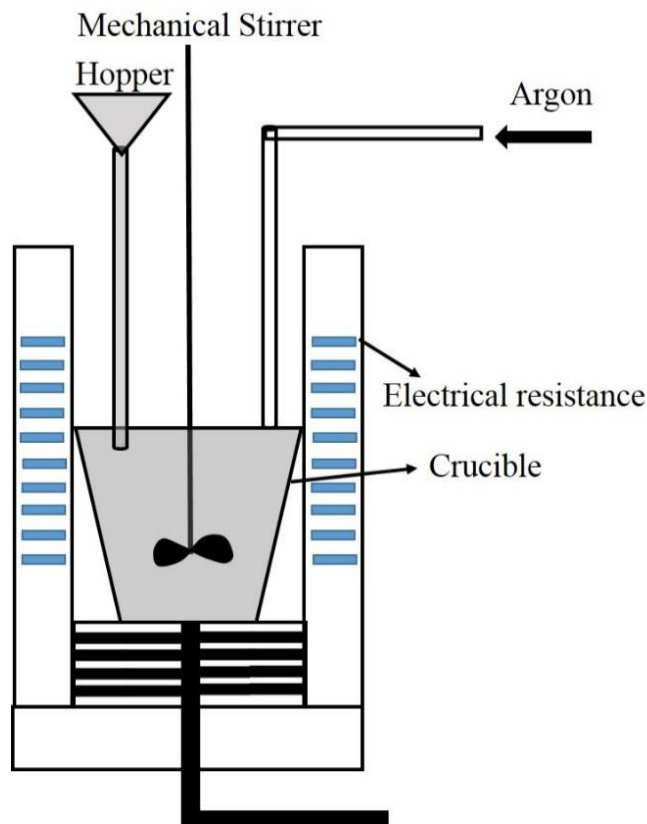


Fig. 2.4: Schematic diagram of stir casting technique.

Key challenges arise during production of MMCs through stir casting process are (i) uniform dispersion of reinforcement within the matrix, (ii) wettability between the particles and matrix phase, (iii) formation of dendritic structure with some casting defects and (iv) settling of the particles during solidification (Hashim et al., 1999). Several researchers have reported that the property of the final product can be enhanced by proper design and effective optimization of the

casting parameters. These parameters include particle addition rate, size & position of the impeller in the melt, stirring speed & time, pouring temperature, pouring system, pre-heated mold temperature etc. (Hashim et al., 1999; Kok, 2005). It has been also reported that preheating of reinforcement particles, addition of Mg to molten Al and coating of SiC particles could improve the wettability between molten Al and SiC particles (Arab et al., 2014; Hashim et al., 2001) thereby improve the properties. Harnby (1997) and Naher et al. (2003) optimized mechanical stirrer designs, such as impeller blade angle, impeller type and speed, for uniform distribution of reinforcement particles. Three blade mechanical stirrer with 60° blade angle is quite popular for uniform distribution. Prabhuet et al. (2006) investigated the influence of stirring speed and stirring time on the particle distribution of stir cast Al-SiC composite. They reported that 600 rpm and 10 min are optimum stirring speed and stirring time to achieve uniform distribution of particles and improve the hardness of Al-SiC composite. Many researchers have reported that the pre-heating of the reinforcement particles before pouring into the molten metal improves wettability and removes moisture problem. Hashim et al. (1999) did the in-depth analysis of the problems associated with stir casting process and suggested some innovative solutions along with list of parameters that may be helpful to resolve those problems. According to Samuel (1993) and Lloyd (1989), for casting defects such as oxide inclusions, particle cluster, porosity etc. improper casting methods are responsible. Agarwala and Dixit (1981) used bottom poring casting method for avoiding the impurities or oxide inclusions from the surface of melt being cast into mold. It is evident from the discussion that with careful control of stir casting parameters decreases the defects in the cast structure up to a certain level but never prevent them. These problems are common to most of the manufacturing techniques, including stir casting.

Various secondary modification and heat-treatment techniques have been proposed to overcome these issues. However, among all of them, friction stir processing (FSP) has been found to be very effective to yield challenging results. Several researchers (Amirizad et al., 2006; Bauri, 2014; Ma et al., 2008) demonstrated that the FSP can be used as an effective tool to homogenize the particle distribution and to refine the grain size in Al based composites. Therefore, the FSP is discussed in details in the next section.

2.6 Secondary processing of AMCs through FSP

The FSP is known to be one of the fast emerging solid-state processing technique for microstructural modification and material processing. The FSP is an upgraded version of the

friction stir welding (FSW) which was originally proposed by Mishra et al. (1999, 2001). The schematic illustration of FSP is depicted in Fig. 2.5.

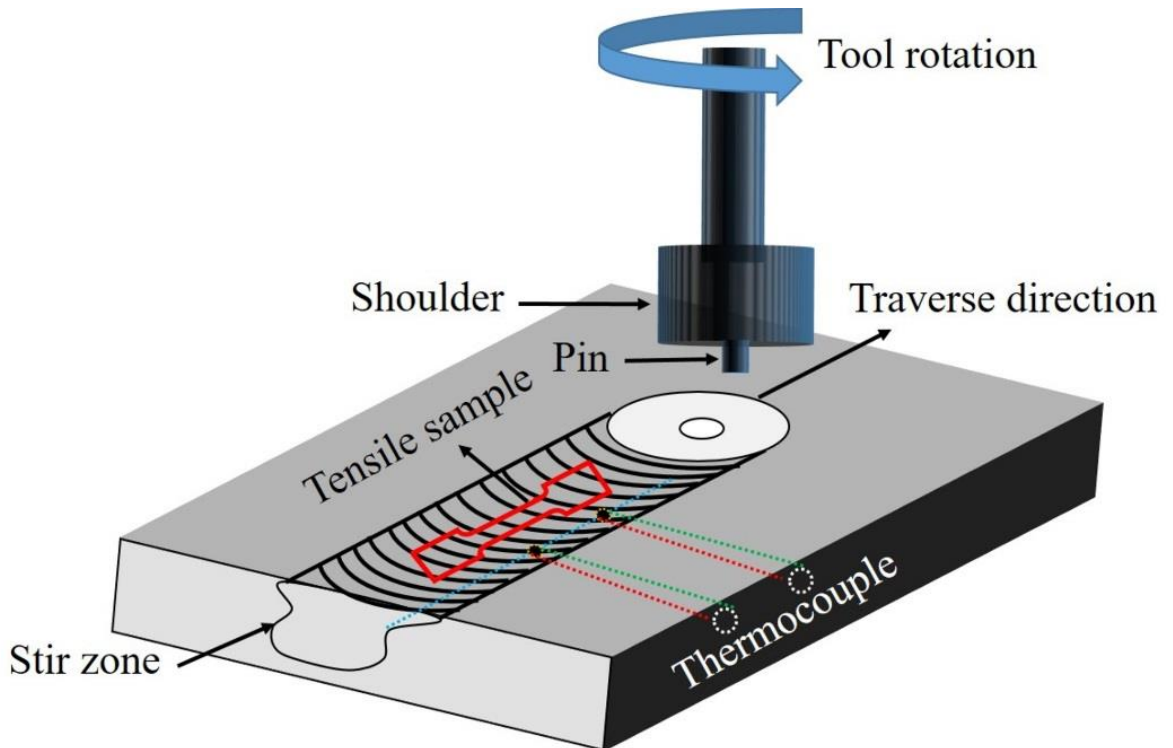


Fig. 2.5: The schematic illustration of FSP.

The basic principle of FSP/FSW follows a simplistic approach: A specially designed non-consumable rotating tool having pin and shoulder is plunged into the workpiece; and then, the tool is traversed along the desired path. The heat energy developed (due to friction between tool and workpiece and plastic deformation of workpiece) is high enough to soften the workpiece (metal) around the pin. The softened material underneath the shoulder is subjected to the combined effect of tool translation and rotation, which moves the material from front to back of the pin (Mishra et al., 2005). The combination of intense plastic deformation and heat generation during the process causes the microstructural refinement thereby homogenizes the distribution of reinforcement particles and removes the inherent casting defects (porosity, particle clustering and agglomeration of particles) from the stir cast composites. These microstructural changes significantly enhance the mechanical properties (ductility, tensile strength and hardness) and wear resistance of the processed material (Cavaliere, 2005; Jarahimoghadam, 2016; Rajan et al., 2016).

The amount of plastic deformation and heat generation is different in different location of the processed zone, due to which three distinct zones could be observed (Mishra et al., 2005); they

are (i) stir zone (SZ) or nugget zone (NZ), (ii) thermo-mechanically affected zone (TMAZ) and (iii) heat-affected zone (HAZ). Different zones formed during FSP are shown in Fig. 2.6.

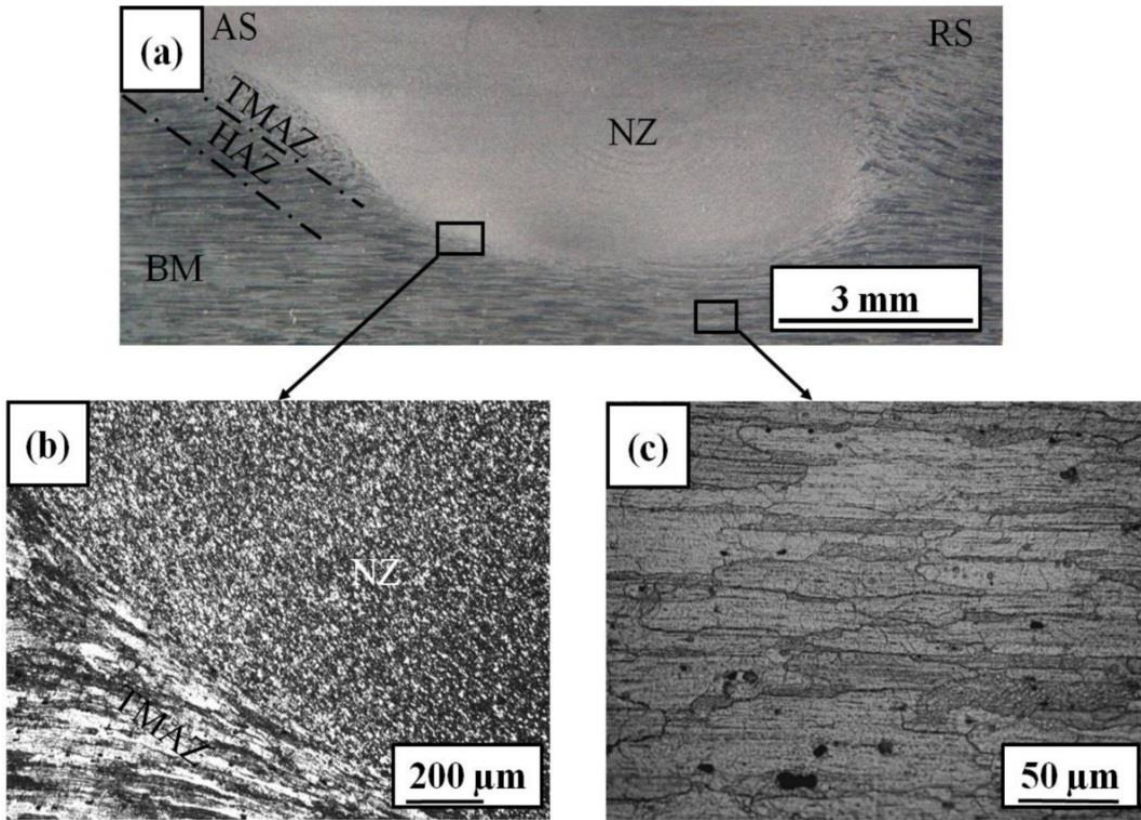


Fig. 2.6: (a) Macrostructure of FSPed sample at 720 rpm-85 mm/min, microstructure of (b) TMAZ and (c) base metal (Al7075 T651). (Kumar et al., 2017)

The region of intense plastic deformation is called as nugget zone. Maximum heat is generated in this zone. Due to intense plastic deformation and high frictional heating during the process, the grains of NZ are fully recrystallized (Azimzadegan et al., 2010; Su et al., 2003). The NZ is usually to pin diameter size or slightly greater than the pin size. Depending upon the variables (processing parameters, geometry of tool, and thermal conductivity of the workpiece), different nugget shapes have been observed. The NZ usually is classified into two types, (i) basin-shaped NZ that has a wider surface at the top as compared to the bottom region and (ii) elliptical NZ that has an onion ring structure (Figs. 2.7a and b). Sato et al. (1999) and Atul et al. (2017) observed the basin shaped NZ on FSP/FSW of Al6063-T5 plate and Al7075-T651 plate, respectively (Figs. 2.6a and 2.7a). They suggested that the upper surface of the workpiece experiences excessive plastic deformation and frictional heating (by the shoulder of the cylindrical tool) thereby a basin shaped NZ with a wide top is generated. While, the elliptical shaped NZ is reported to develop

on FSW of Al7075-T651 by Rhodes et al. (1997) and Mahoney et al. (1998) (Fig. 2.7b). Recently, Ma et al. (2006) performed FSP on cast A356 aluminium and results showed that with same geometry of tool, various shapes of NZ were produced by altering processing parameters. Moreover, nugget shape changes from basin to elliptical with increase in rotation speed. The NZ is surrounded by TMAZ having highly distorted structure due to the stirring by the tool. Recrystallization did not occur in the TMAZ during FSP since there is not sufficient deformation strain generated, which could raise the temperature for recrystallization. However, a grain distortion (elongation) along the direction of flow of material could be observed in the TMAZ (Fig. 2.6b). The TMAZ is generally referred as transition zone, which distinguish the processed zone from the parent material as shown in Fig. 2.6. Beyond the TMAZ, a different zone can be observed which is known as the HAZ. In this region, the sample experiences a thermal cycle but there is no mechanical deformation. The grain size in the HAZ is similar to base metal but thermal cycle affected the precipitate characteristics in a heat treatable aluminium alloy (Mahoney et al., 1998).

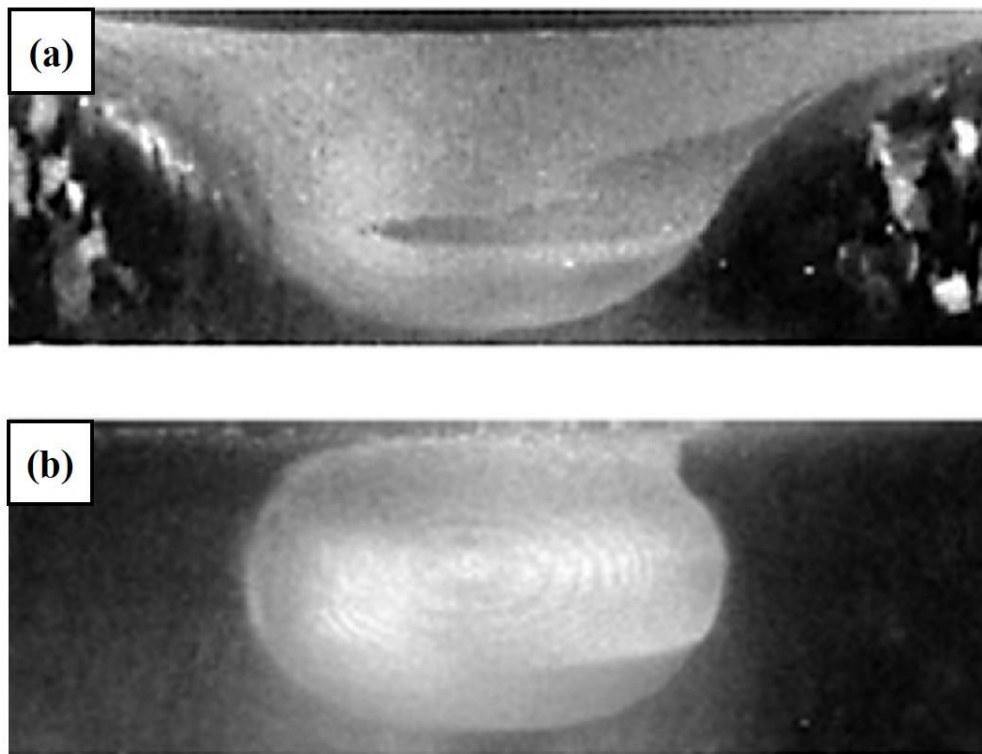


Fig. 2.7: Effect of processing parameters on shapes of NZ in FSP of cast A356 aluminium (a) 300 rpm, 51 mm/min; (b) 900 rpm, 203 mm/min (Ma et al., 2006).

The FSP is a fast emerging technique for microstructural modification and it uses a simple inexpensive tooling; and a readily available machine such as a milling machine can be used to conduct the process. The other advantages of the FSP are: it could be automated for production and a simple fixture to control the cooling rate can be designed. Hence, it is possible to upgrade the FSP method from laboratory scale to the commercialized level. All these features make the FSP easier and less expensive as compared to other SPD methods. Fig. 2.8 shows the potentiality of the FSP as a diversified process (Mishra et al., 2007).

Friction stir processing

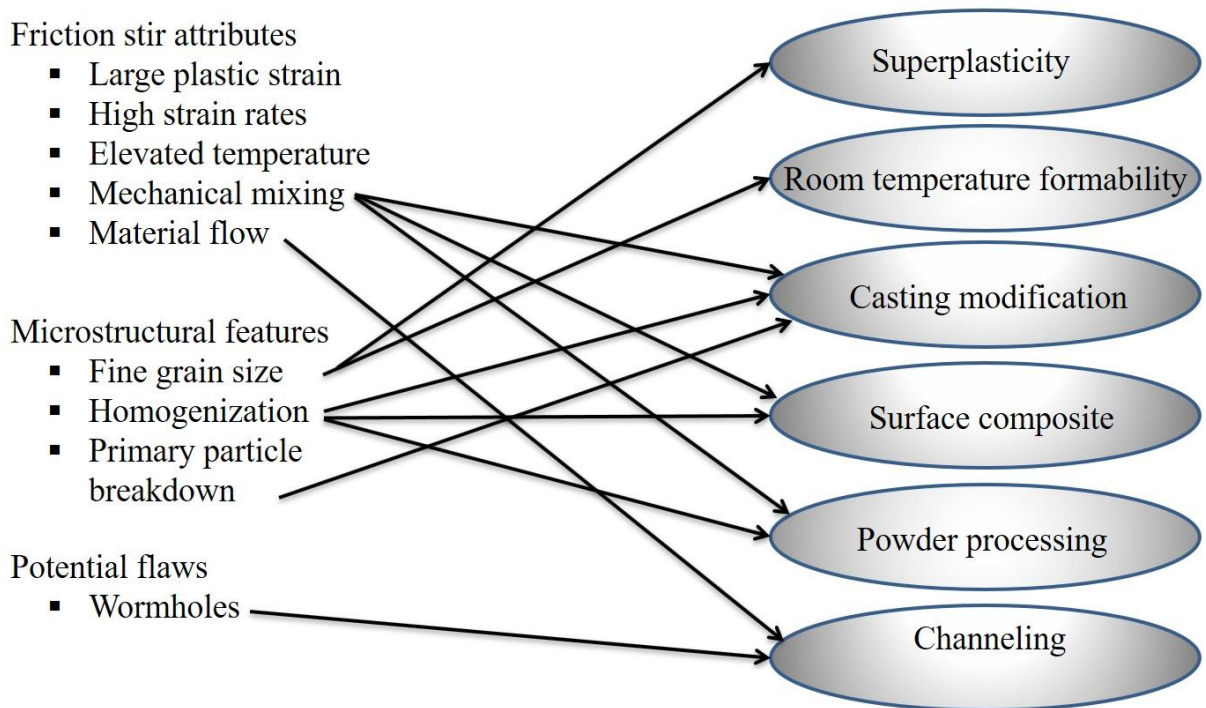


Fig. 2.8: List of attributes and the potentiality of the FSP as a diversified process (Mishra et al., 2007).

2.6.1 Effect of process parameters

Processing parameters of the FSP have great influences on movement as well as flow of material and thermal cycle during the process. Optimizing these parameters plays an important role to achieve defect free fine recrystallized microstructure and thereby final mechanical properties of the processed samples. These parameters fall into three major categories: (i) tool geometry, (ii) machine variables and (iii) cooling condition/rate, which are shown in the flow diagram below (Fig. 2.9).

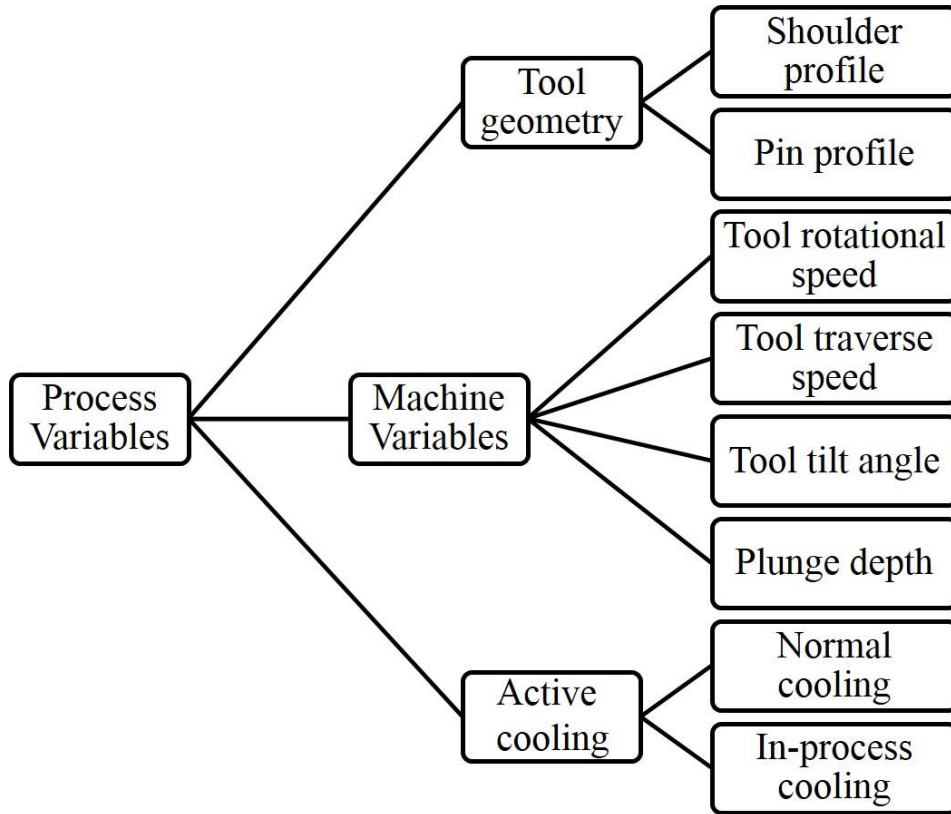


Fig. 2.9: Classification of FSP process variables.

Tool geometry

The FSP is a thermomechanical deformation process in which temperature of the tool generally approach the solidus temperature of the workpiece. Therefore, selection of the tool material as well as design of it should to be carried out carefully. The design of the tool greatly influences the final properties of the processed material. The correct tool material should have sufficient strength at elevated temperature and must maintain dimensional stability during the time of use. The geometry of the tool is a very crucial aspect of the process as it generates the required heat for processing and governs the material flow and thereby processed zone formation (NZ, TMAZ and HAZ) (Kumar et al., 2011). A typical FSP tool consists of two main parts, pin and shoulder as shown in Fig. 2.10. Tool pin is designed to produce frictional and deformational heating with the workpiece at initial stage of tool plunge. Furthermore, it moves the material from front to back of the tool and also helps in uniform dispersion of second phase particles, if any. The processing depth during the FSP mainly depends upon the size of the pin. For improvement of the processed zone, different types of pin profile such as tapered, tapered with threads, cylindrical, cylindrical with thread, square, triangle etc. have been used as shown in Fig. 2.10.

Tool shoulder is designed to serve as reservoir for softened material underneath the shoulder so that it avoids splashing of the plasticized material from the processed region. The shoulder also produces the largest part of the heat required to plasticize the material and provides the necessary downward forging action for consolidation. To improve the friction between shoulder and specimen, different styles of shoulder end surfaces have been used as shown in Fig. 2.10. These include grooves, knurling, concentric circles, scrolls and flat or featureless profile at the end surface of the shoulder. If the shoulder diameter is larger, then the amount of heat input will be higher and vice versa. The shoulder profile includes flat, convex and concave shape. So, to get a defect free processed zone, a correct combination of the size of the shoulder and pin should be chosen. Vijayavel et al. (2014) studied the effect of shoulder diameter to pin diameter (D/d) ratio on mechanical properties of FSPed LM25AA-5% SiCp MMCs and concluded that the D/d ratio of 3 yielded better mechanical properties with defect free processed zone.

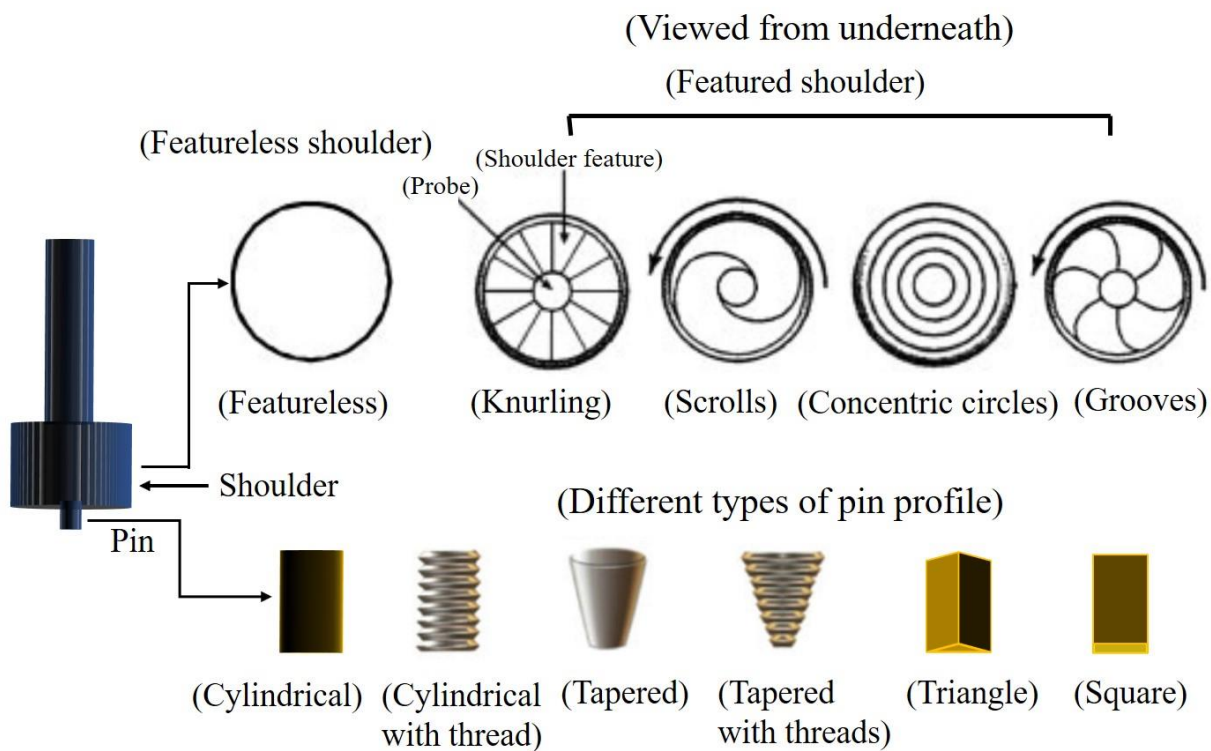


Fig. 2.10: Basic tool geometry along with different types of pin profile and shoulder end surface features (Mishra et al., 2005).

Machine variables

Tool traverse and rotational speed, plunge depth and tilt angle of the tool are the machine variables. Among them rotational speed and traverse speed are very important parameters as they

decide the amount of heat input in the processed zone. In general, the heat input to the work piece is directly proportional to the rotational speed and inversely proportional to the traverse speed. If the ratio of tool rotational speed to traverse speed is high, then the amount of heat input will be higher in the processed zone. Too high heat input can cause a turbulent flow of the material in the processed zone. On other hand, if the ratio of tool rotational speed to traverse speed is low, then the amount of heat input will be low. Insufficient heat input can cause non-uniform flow of processed material during the process and also leads to the formation of defects and voids within the NZ. In both the cases, defective processed zone could be obtained.

In order to simplify the effects of the rotational speed and traverse speed, many studies (Balasubramanian, 2008; Kumar et al., 2017; Liu et al., 2011; Zhang et al., 2015) have been carried out on the optimization of the FSP parameters. For example, Zhang et al. (2015) reported that the mechanical properties of friction stir welded Al-Zn-Mg-Cu Al alloy joints improved with increasing welding speed and decreasing tool rotational speed. Azimzadegan et al. (2010) conducted friction stir welding on AA7075-T6 with various welding parameters and concluded that there was an optimum rotational speed for a given traverse speed to achieve the highest strength and elongation for the stir zone.

Based on the experimental work done on FSW of Al alloys, an empirical relation between maximum NZ temperature (T_{max}) and the process parameters (rotational speed (ω), traverse speed (v)) has been established (Arbegast et al., 1998) :

$$\frac{T_{max}}{T_m} = K \left(\frac{\omega^2}{v \times 10^4} \right)^\alpha \quad (2.5)$$

Where, α and K are the constants, ranges between 0.04–0.06 and 0.65–0.75 respectively, and T_m alloy melting temperature (in Kelvin). The ratio of ω^2 and v is considered as pseudo heat index. In FSW of Al2024 plates (Chen et al., 2015) demonstrated that the relation between the maximum NZ temperature (T_{max}) and the heat index value is in accordance with the Eq. (2.5). The heat input in the processed zone controls the material flow and grain size, which consequently affects the properties of the processed material. To obtain desired microstructural refinement and improved mechanical properties with defect free processed zone, the combination of tool rotational and traverse speed should be effectively optimized. In addition to the tool traverse and rotational speed, other factors like tool tilt angle and plunge depth also affect the evolution of the processed zone; but normally these factors are kept constant (Reddy et al., 2011). A suitable tool

tilt angle and plunge depth helps in proper filling of the key hole created by the moving tool and maintains necessary forging force for proper consolidation.

Effect of cryocooling

The FSP has been established to be an effective means of refining the microstructure and removing various defects from the materials via dynamic recovery and recrystallization. Mechanical properties of Al alloys processed by FSP were reported to improve due to the refinement of microstructure (Jana et al., 2010; Kwon, 2003; Ma et al., 2002; Sato et al., 2001). However, in case of precipitation hardenable alloys, a competition between strengthening due to grain size refinement and softening due to change in precipitate characteristics by FSP is observed (Feng et al., 2013; Kumar et al., 2017.). Many researchers (Chen et al., 2009; Kumar et al., 2017; Mahoney et al., 1998; Rhodes et al., 2003) have studied the precipitates formation characteristics after processing and concluded that, an adverse event of precipitate dissolution or coarsening during the FSP would be the major reason for showing inferior mechanical properties, despite the development of fine grained microstructure. In addition, Xu et al. (2014) have found that fine grains evolved during FSP grow very quickly due to slow cooling rate after FSP. Aforementioned issues associated with the FSP hinder the real purpose of the FSP of enhancing the mechanical properties.

The FSP with active/in-process cooling setup suppresses precipitate coarsening/overaging and arrests the grain growth by reducing the peak temperature, increasing cooling rate and limiting holding time. This tactic can combine the precipitation strengthening and grain size strengthening along with other strengthening mechanisms in age hardenable Al alloys. In recent years, various researchers have applied means of external cooling effect (in-process and submerged) during the FSP/FSW and they concluded that external cooling during FSP is an effective way to enhance the metallurgical characteristics and thereby mechanical properties of the processed materials. For example, Fratini et al. (2009) used a different cooling medium (water, forced air and free air) flowing on the surface of the specimen (AA7075 T6) during FSW and reported that the tensile strength of the joint was superior in the sample processed in water cooling medium. In order to take full benefit of water cooling, Tokisue et al. (2002) conducted submerged FSW on Al6061 alloy and concluded that it is practicable to achieve sufficient torque for welding during underwater FSW. Hofmann and Vecchio also (2005) carried out submerged (underwater) FSP on Al6061-T6 alloy. They found that submerged FSP could attain more grain size refinement

due to faster cooling rate as compared to those of samples FSPed under ambient conditions. Upadhyay and Reynolds (2010) investigated the influence of submerged FSW on the weld properties of Al7050-T7451 joints welded in air, underwater and under sub-ambient liquid medium of -25°C temperature. They reported that there is an increase in the torque required (power consumption/machine capability) for the submerged/sub-ambient welding conditions and the tensile strength of the FSPed samples improved. In order to obtain rapid heat sink during FSP, Chang et al. (2007) designed an efficient cooling system and concluded that the UFG structure with a drastic increase in the microhardness (increment factor of 2.4) could be achieved in Mg-Al-Zn alloy by FSP attached with a rapid heat sink.

In recent years, the FSP with external/in-process cooling has attracted significant attention although the studies are still limited as compared to normal FSP at room temperature. Furthermore, investigation on the influence of in-process cryocooling during FSP of Al7075 alloy and its composites are rarely reported. Therefore, the effect of in-process cryocooling during FSP on the microstructural evolution and mechanical properties of the Al7075 alloy and its composites are studied in detail in this thesis work.

2.6.2 Recrystallization mechanisms during FSP

Microstructural evolution in the NZ is governed by dynamic recrystallization (DRX), which occurred due to intense plastic deformation and high frictional heating (Rajan et al., 2016; Su et al., 2005a; Yadav et al., 2015). Several mechanisms have been proposed for DRX, including continuous dynamic recrystallization (CDRX), geometric dynamic recrystallization (GDRX) and discontinuous dynamic recrystallization (DDRX) (Feng et al., 2011; Gourdet et al., 2003; Humphreys et al., 2004; Jata et al., 2000a; McNelley et al., 2008; McQueen et al., 1991; Mishra et al., 2005; Rhodes et al., 2003). All of these mechanisms lead to grain refinement. However, the exact mechanism of DRX operating during FSP is still debated (Charit et al., 2005). Generally, mechanism of grain refinement mainly depends on the type of metals or alloys. Based on the spatial locations and transient conditions, combination of these models (CDRX, GDRX, DDRX) may all be possible mechanisms during the FSP (Feng et al., 2011; McNelley et al., 2008; Mishra et al., 2005). Various stages of microstructural evolution in these mechanisms (CDRX, GDRX, DDRX) of DRX is schematically shown in Fig. 2.11 (Giribaskar et al., 2008; Jata et al., 2000a; Robson et al., 2010). The DDRX is characterized by generation of new strain free grain structure at high angle boundaries (Fig. 2.11a) (Humphreys et al., 2004).

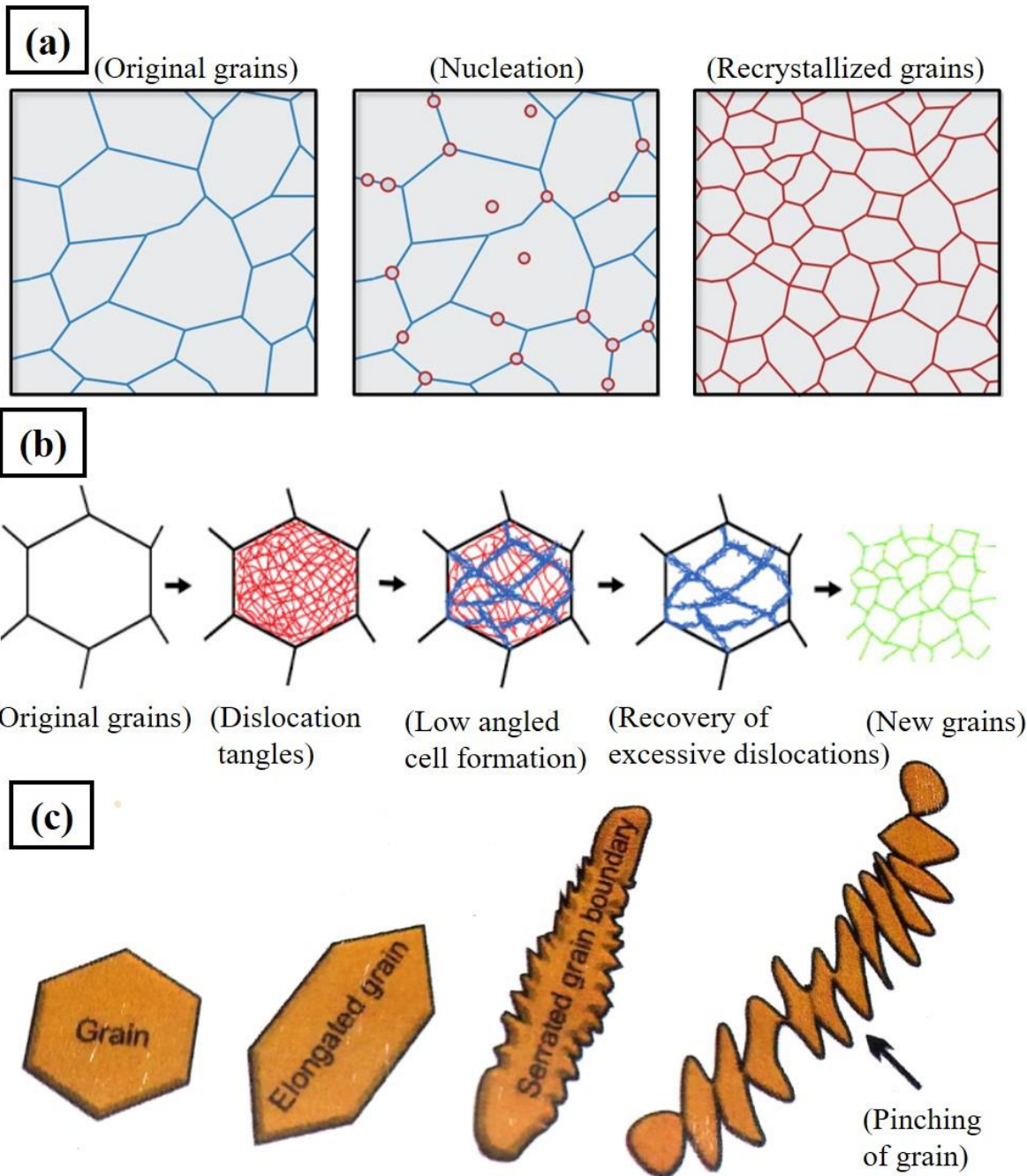


Fig. 2.11: Schematic of various stages of dynamic recrystallization mechanisms (a) DDRX, (b) CDRX and (c) GDRX (Sharma, 2015).

In Al and its alloys, dynamic recovery is observed to precede DDRX because of their high stacking fault energy (McNelly et al., 2008; Raghavan et al., 2014). Jata et. al. (2000a) was the first one who proposed that CDRX is the primary mechanism in refining the grain size during FSW. The CDRX is generally observed in the materials in which dislocation motion is hindered either due to lack of slip systems or by solute drag (Besharati-Givi et al., 2014). The dislocations

rearrange themselves to achieve lower energy configurations, which leads to formation of subgrains structure with low angle grain boundaries. As deformation progress, gradual relative rotation of adjacent subgrains leads to the formation of recrystallized grains with high angle grain boundaries (Fig. 2.11b) (Besharati-Givi et al., 2014). In the GDRX mechanism, a large reduction in cross section during deformation, flattening or elongating the original grains due to combined effect of compression, tension and torsion lead to the formation of serrations at initial grain boundaries (Fig. 2.11c). With further deformation, the original grain thickness is reduced to the thickness of the boundary serrations and causes the serrated boundaries to touch each other and forms newly isolated grains (McQueen et al., 1991; Prangnell et al., 2005).

2.7 National and international status

In recent decades, numbers of processing techniques such as alloying, age-hardening and particulate reinforcement have been evolved to enhance the mechanical as well as other properties of the existing Al alloys with the aims to increase the performance and efficiency of the existing components (Koch et al., 2005; Suryanarayana et al., 2000). Among these, particulate reinforcement followed by the matrix grain size refinement is found to be the most suitable route to improve the wear resistance and mechanical strength without much affecting (sometimes improved) the corrosion resistance of the Al alloys (Boostani et al., 2015; Harichandran et al., 2016; Mosleh-shirazi et al., 2016; Suryanarayana et al., 2013). Refinement of matrix grain size not only improves its yield strength (YS) and fatigue strength, but also enhances the corrosion resistance (Das et al., 2011; Dasharath et al., 2017; Singh et al., 2016). On the other hand, addition of ceramic particles having higher elastic modulus (e.g. 410 GPa for SiC and 171 GPa for Y_2O_3) to the alloy matrix is expected to improve not only the elastic modulus of the material but also its wear resistance (Dieter, 1986). Dasgupta et al. (2010) studied the sliding wear resistance of Al2014 and Al7075 alloys reinforced with 10vol.% SiC particulates (size between 20 and 40 μm). They reported that the Al7075 alloy exhibited a better improvement of wear resistance over the base metal as compared to that of the Al2014 alloy. The abrasive wear rate of the SiC reinforced composites was found to decrease linearly with increase in SiC content (Mondal et al., 2006). Similar results were also reported by other researchers in (Pargunde et al., 2013; Singla et al., 2009; Debnath et al., 2012; Hembrom et al., 2015). The wear rate of Al-Al₂O₃ (400 μm) and Al/SiC (400 μm) composites produced by stir casting reported to decrease significantly with

the addition of reinforcing particles. Al-SiC composites exhibited lower wear rate compared to that of the Al-Al₂O₃ composites (Debnath et al., 2012) processed under similar conditions.

Various processing methods, such as stir casting (Sharma et al., 2013), compoforging (García et al., 2010), ultrasonic casting (Vishwanatha et al., 2016), squeeze casting (Onat et al., 2007), spray decomposition (Su et al., 2004), powder metallurgy (Basariya et al., 2014) etc. have been developed to manufacture aluminium based composites. Singla et al. (2009) proposed two-steps mixing method using stir casting to develop Al-based SiC reinforced (44 µm) composite. The prime objective was to develop a conventional low-cost technique to produce MMCs with homogenous dispersion of ceramic particles. In this method, they first raised the furnace temperature above the liquidus temperature to melt the alloy completely and then allowed to cool down just below the liquidus temperature to keep the slurry in a semi-solid state. At this stage the preheated SiC particles were added and mixed by mechanical stirring manually. After mixing the particles manually, the composite slurry was reheated to a fully liquid state and then automatic mechanical mixing was carried out for about 10 minutes at a normal stirring rate of 600 rpm. They found that the developed method is quite successful to obtain uniform dispersion of reinforcement in the matrix. An increasing trend of hardness (28.5 to 45.5 BHN) and impact strength (12 to 36 N-m) with increase in weight percentage of SiC has been observed. The best results (maximum hardness 45.5 BHN & maximum impact strength of 36 N-m) have been obtained for 25wt.% SiC reinforced composites. Beyond this weight fraction, the hardness value started to decrease as SiC particles starts interacting with each other, which leads to clustering of particles and consequently settling down. Garcia et al. (2010) suggested an alternate technique of compoforging to produce Al-Si alloy based composite reinforced with SiC (38 µm). The compoforging technique is a hybrid technique between the compocasting process and semi-solid forging. This method is reported to be more economical as it reduces production stages, as well as time and energy consumption. This method produced a more or less homogeneous distribution of the reinforced particles. Kok et al. (2005) fabricated the 2024 Al alloy metal matrix composites reinforced with Al₂O₃ particles (having different sizes (16, 32 and 66 µm) with various weight fractions (of 10, 20 and 30) by stir casting method. They reported an optimum condition of the production process with a pouring temperature of 700°C, preheated mold temperature of 550°C, stirring speed of 900 rpm and particle addition rate of 5 g/min. The hardness and the tensile strength of the composites increased with decreasing size and increasing weight fraction of the particulates. Size and volume fraction of reinforcement are also important factors to characterize

the properties of the AMCs. Zabihi et al. (2013) investigated Al-Al₂O₃ (Al powder of 40 μm particle size and Al₂O₃ powder with 3-8 μm particle size) composite strips produced by powder metallurgy and the hot rolling processes. They reported that by increasing reinforcement content in the matrix (from 2 to 4 wt.% Al₂O₃), tensile strength increased from 163 to 196 MPa and hardness increased from 54.8 to 61 BHN; but, the percentage of elongation decreased from 5.5 to 4.7%.

Micron size ceramic particles reinforced in Al and its alloys enhanced the tensile strength of the matrix, but on sacrificing its ductility (Mazahery et al., 2009; Hong et al., 2003). However, use of nanosize reinforcement strengthens the matrix while retaining its good ductility (Ezatpour et al., 2016; Sajjadi et al., 2012; Padhi et al., 2008). For example, Zhang et al. (2015) investigated tensile properties of nanoparticle reinforced (~40 nm) Al2014-SiC composite at elevated temperature and reported that tensile strength of the material improved remarkably without sacrificing its ductility. Mazahery et al. (2009) fabricated the Al-Al₂O₃ (50 nm) nanocomposite by stir casting. The addition of 1.5wt.% Al₂O₃ nanoparticles caused a significant increase in the mechanical properties (23% YS, 58% UTS, 34% hardness) as compared to the base alloy. Yong et al. (2004) fabricated bulk Al matrix nanocomposite by use of ultrasonic nonlinear effects, to achieve uniform dispersion of nanosize SiC particles (≤ 30 nm) in molten Al alloy. From the microstructural examination, it is observed that the nanosize SiC particles are dispersed well in the matrix and the yield strength of A356 alloy was improved more than 50% with only 2 wt.% of nano-sized SiC particles. Reducing the particle size to nanometer range introduces an exceptional change in mechanical properties and gives other strengthening effect because of significant interaction of dislocation with particles (pinning effect). Zener pinning at grain boundaries by the nanoparticles also leads to a highly stable ultrafine grain size, which does not grow significantly after annealing for several hours. Zener pinning is the influence of a dispersion of fine particles on the movement of low- and high angle grain boundaries through a polycrystalline material. Small particles act to prevent the motion of such boundaries by exerting a pinning pressure which counteracts the driving force pushing the boundaries (Mula et al., 2015). Zener pinning is very important in processing of composite materials as it has a strong influence on recovery, recrystallization and grain growth.

Although nanocomposites are very promising for providing excellent properties, but probability of defects formation will also increase using nanosize reinforcement (<100 nm). Because, it is challenging to disperse nanosize particles uniformly within the matrix by most of the production

methods. It is due to the fact that the nanosize particles have large surface area-to-volume ratio thereby higher tendency towards agglomeration and poor wettability in most metallic melts (Boostani et al., 2015; Zhou et al., 2015). In the recent years, several studies have been carried out to reduce aforementioned defects in production of nanocomposites. Several approaches such as rolling (Lokesh et al., 2014), forging, FSP (Hoziefa et al., 2016), equal channel angular pressing (ECAP) (Ramu et al., 2009), hot extrusion (Mousavian et al., 2016) and cross accumulative roll bonding (CARB) (Ardakani et al., 2014) etc. have been applied to improve the microstructure and mechanical properties of cast composites. For example, Arab et al. (2014) used ECAP to modify the microstructure and improve the mechanical properties of Al-SiC (55 μm) cast composites. They reported a significant improvement in the distribution of SiC particles and enhancement of mechanical properties in comparison to the starting cast sample. Ardakani et al. (2014) demonstrated that compocasting followed by CARB was a promising route to develop Al-based nanocomposite. They found that after eight cycles of CARB, ultimate tensile strength and the elongation of the cast nanocomposite improved by 3.22 and 3.28 times, respectively, as compared to the as-cast composite. The improvement is ascribed to the homogeneous distribution of SiC nanoparticles in aluminium matrix without retaining any remarkable porosity and matrix grain size refinement. All of these studies clearly indicate that secondary deformation processes can eliminate casting porosity and improve the distribution of the particles in the Al/Al-alloy composites with a subsequent increase in the mechanical properties. However, most of these SPD methods are comparatively complex and have some major limitations like expensive tooling, design difficulties, low productivity and limitation of sample size produced. These factors make most of the SPD methods challenging to scale up for commercialization (Fuloria et al., 2015; Joshi et al., 2016). In contrast, the FSP has been established as a generic tool for microstructural modification and material processing (Bauri et al., 2011; Gibson et al., 2014; Mishra et al., 2005). It is a single step process; while other SPD techniques require mostly multiple steps/cycles for microstructural modification and homogenizing the distribution of particles in the MMCs.

Ma et al. (2014) demonstrated that the FSP can be used as an effective tool to homogenize the particle distribution in Al-based in-situ composites. Initially, composite had a grain size of 50-100 μm and the synthesized nanosize TiB_2 particles were found to segregate and cluster at the grain boundaries. They reported a considerable grain refinement occurred in the nugget zone (1-5 μm average grain size) along with uniform distribution of the nanosize TiB_2 particles after the

FSP. This resulted in significant improvement in both the ultimate strength and elongation of the composite samples prepared from the NZ. Amirizad et al. (2006) applied the FSW on A356+15%SiCp cast composite and evaluated its microstructure and mechanical properties. They concluded that hardness and tensile properties (yield strength, tensile strength and elongation) of the stir zone improved significantly as compared to that of the base composite. Homogeneous distribution of SiC particles, spheroidization of silicon needles and their dispersion in the matrix, decrease in the micro-porosities, modification of the cast microstructure are the dominant reasons for improvement of the properties in the stir zone. Dinaharan et al. (2019) applied the FSP on AA6061/Al₂Cu cast composite and evaluated its microstructure and mechanical properties. They found that large Al₂Cu particles broke down into fine sized particles due to the severe plastic strain and mechanical impact of the tool. This resulted in significant improvement in both the ultimate tensile strength (280 MPa) and elongation (8%) of the AA6061/15 wt.% Al₂Cu composite samples prepared from the NZ due to the desirable microstructural changes. Chen et al. (2015) also studied the effect of FSP on the microstructure and thermal stability of in-situ AA6063-TiB₂ composite. They reported that the FSP resulted in homogenous redistribution of nanosize TiB₂ particles in the matrix thereby improved thermal stability of the fine-grained in-situ AA6063-TiB₂ composite. The FSPed AA6063-TiB₂ composite had higher average microhardness in the nugget zone due to the refined grain structure, higher dislocation density and uniformly distributed nanosize TiB₂ particles. It shows that casting followed by FSP is a promising route to develop Al-based nanocomposite.

In order to improve the microstructure and mechanical properties, Yang et al. (2015) performed multi-pass FSP on cast A356-Al₃Ti composites. They observed that after multi-pass FSP, both the strength and ductility of the composite samples improved with increasing number of FSP passes. Primary reasons for this improvement were modification and redistribution of Al₃Ti and Si particles, reduced porosity content and substantially matrix grain size refinement after 4-pass FSP. In order to modify microstructure to certain width of the plate, Su et al. (2005b) also performed multi-pass FSP and they produced large-area, bulk size and ultrafine grained aluminium alloy with relatively uniform microstructure using multi-pass FSP with 33 % overlap between the passes. Some researchers (El-Rayes et al., 2012; Johannes et al., 2007) have also reported that the mechanical properties of the processed zone decreased with increasing number of FSP passes. The authors reasoned that the dynamic recrystallization and accumulated heat in

the processed zone due to multi-pass FSP led to coarsening of recrystallized grain size, which deteriorated the strength.

Significance grain growth during the room temperature FSP compelled many researchers to investigate the effect of cooling medium during FSP on metallurgical and mechanical properties of various alloys and composites. Yazdipour et al. (2009) examined the effect of rapid cooling on grain size of NZ during FSP of the Al5083 alloy. They used a mixture of methanol and dry ice for rapid cooling. The mixture was applied immediately behind the FSP tool. The grain size of stir zone dramatically decreased to a size ranging from 80 nm to 0.9 μm , and the hardness of processed region increased. Nia et al. (2014) used rapid cooling during multi-pass FSP of AZ31 Mg alloy. The material was cooled rapidly after every pass to prevent the thermal effects on successive passes. Sharma et al. (2012a) used in-process cooling during FSW of AA7039 aluminium alloy plates using compressed air, normal water and liquid nitrogen. They concluded that the water cooling was more effective in improving the mechanical properties of the FSWed joint than other in-process cooling methods employed. Rouzbehani et al. (2018) studied the metallurgical and mechanical properties of underwater friction stir welds of Al7075 alloy. They have found that the water cooling and an increase in traverse speed impede grain coarsening and increase the volume fraction of precipitates considerably. They concluded that the water cooling was more effective in improving the mechanical properties of the FSWed joint as compared to that of the atmospheric air-cooled samples. Optimum weld strengths of 396 and 360 MPa were obtained in the underwater and air-cooled welds at tool rotational speed of 800 rpm and traverse speed of 50 mm/min. Ashjari et al. (2015) employed the submerged FSP under water to fabricate AA5083-Al₂O₃ surface nanocomposite with enhanced mechanical characteristics. They found that submerged FSP was capable of producing defect-free AA5083-Al₂O₃ nanocomposite. The results show that the submerged FSP could attain more grain size refinement due to faster cooling rate compared to those of samples FSPed under ambient conditions. They reported that the water environment has positive impact on the mechanical properties of the material. Khodabakhshi et al. (2014) investigated the influence of submerged FSP on the mechanical characteristics of Al-Mg-TiO₂ nanocomposites processed in air, water+dry ice medium (-25°C) and liquid nitrogen. They concluded that with increasing the cooling rate during FSP, grain size of stir zone was significantly refined, particularly under cryogenic condition. They attained the ultrafine grained structure (size~200 nm) with a drastic increase in the mechanical strength (150-200%) by FSP under the cryogenic cooling condition. Finally, from the above discussion, it can be concluded

that the FSP is an effective method to modify the microstructure and thus improve the mechanical properties of cast AMCs.

2.8 Research gaps and formulation of problem

An extensive literature survey has been carried out on composite casting methods, secondary processing of the composites and influence of FSP parameters on Al alloys and its composites. The major aim is to develop high strength Al/Al-alloy based MMCs. The important findings from the literature and on the basis of that, the following research gaps are identified to formulate the problems for the present study.

2.8.1 Research gaps

- Very limited literature are available on study of deformation mechanisms and development of ultrafine grained Al7075-SiC nanocomposites developed by stir casting followed modification of cast microstructure by FSP. Most of the studies were focused on the development of micro- or nanosize particles reinforced AMCs
- Porosity, agglomeration, non-uniform distribution of particles are the major problems during fabrication of AMCs.
- Most of the studies were focused on the different fabrication techniques for achieving uniform distribution of reinforcement and thereby good mechanical properties. But secondary microstructural modification technique (FSP) is rarely used.
- Effect of FSP on Al-based nanocomposites, especially on SiC reinforced Al7075 alloy-based nanocomposites has not been carried out.
- In recent years, FSP with external/in-process cooling has attracted significant attention although the studies are still limited as compared to normal FSP at room temperature.
- Furthermore, investigation on the influence of in-process cryocooling during FSP of the Al7075 alloy and its composites are rarely reported.

2.8.2 Formulation of the problem

- Over the years, AMCs have become the subject of extensive research. But, the widespread adoption of the same for the engineering applications has not been successful. This is so as the conventional size particulates reinforced composites encounter various problems such as: (i) ductility/toughness decreases abruptly to much lower range, (ii)

fracturing of particles as well as composites during deformation for further processing i.e., limited workability (iii) poor bonding between the particles/matrix interface and (iv) high cost of production. Addition of nanosize reinforcement strengthens the matrix while retaining its good ductility/toughness.

- The mixing of ceramic nanoparticles uniformly in the bulk Al/Al-alloy matrix is still challenging. Bottom pouring stir casting followed by secondary processing such as rolling, forging, extrusion, ECAP, CARB, FSP etc. is expected to be very effective to distribute nanoparticles homogeneously in the matrix and refining matrix grain sizes.
- Most of the SPD methods are comparatively complex and have some major limitations like expensive tooling, design difficulties, low productivity and limitation of sample size produced. These factors make most of the SPD methods challenging to scale up for commercialization. In contrast, the FSP is a single step process; while other SPD techniques require mostly multiple steps/cycles for microstructural modification and homogenizing the distribution of particles in the cast AMCs.
- As the concept of the FSP being relatively new, there are many areas, which need thorough investigation to optimize the process and make it commercially viable. In order to obtain defect-free fine recrystallized microstructure and thereby desired mechanical properties of the processed samples, certain process parameters like traverse and rotational speed, tool geometry etc. are to be optimized. Numerous efforts have been made to characterize the effects of these process parameters on grain size refinement and control the precipitate kinetics of age hardenable Al-alloys and its composites through physical and mathematical modeling. Active/in-process cooling setup could be useful to suppresses precipitate coarsening/overaging and arrests the grain growth during FSP of age hardenable Al alloys and its composites. This approach can combine the precipitation strengthening and grain size strengthening along with other relevant strengthening mechanisms in age hardenable Al alloys and its composites.

2.9 Objectives of the present research work

Based on the literature review carried out and research gaps identified, the following points are formulated as the primary objectives of the proposed research work.

- Synthesis of Al7075 alloy based composites reinforced with varying wt.% of micro- and nanosize SiC particles using bottom pouring stir casting method with proper control of

casting parameters (such as preheating of reinforcement and mold, optimum stirring speed and time, control argon atmosphere etc.).

- Design the experimental setup to conduct friction stir processing with in-process cryocooling and normal air cooling.
- Optimize the FSP parameters in details to obtain defect-free fine recrystallized microstructure in base alloy and composites. Achieve homogeneous distribution of the reinforcement along with matrix grain size refinement via secondary microstructural modification (FSP) in both the cooling conditions.
- Analyzing the effect of these process parameters on microstructure, mechanical properties, such as hardness, tensile strength (YS, UTS) and wear resistance of the processed composite samples. Prediction of suitable process parameters and cooling condition to achieve best possible mechanical properties through microstructural modification of the micro/nanocomposite.
- Detailed analysis of the deformation mechanisms and different strengthening mechanisms involved in the composites and their individual contribution to the YS to establish the effectiveness of the FSP on the Al7075 alloy and its nanocomposites.

In order to achieve the aims, the overall thesis is organized in five chapters: Introduction (Chapter 1), Literature review (Chapter 2), Materials, experimental and characterization details (Chapter 3), Results and discussion (Chapter 4) and Conclusions (Chapter 5). A flow-chart depicting the interlinking of the chapters and their contribution towards achieving the overall goal is shown in Fig. 2.12.

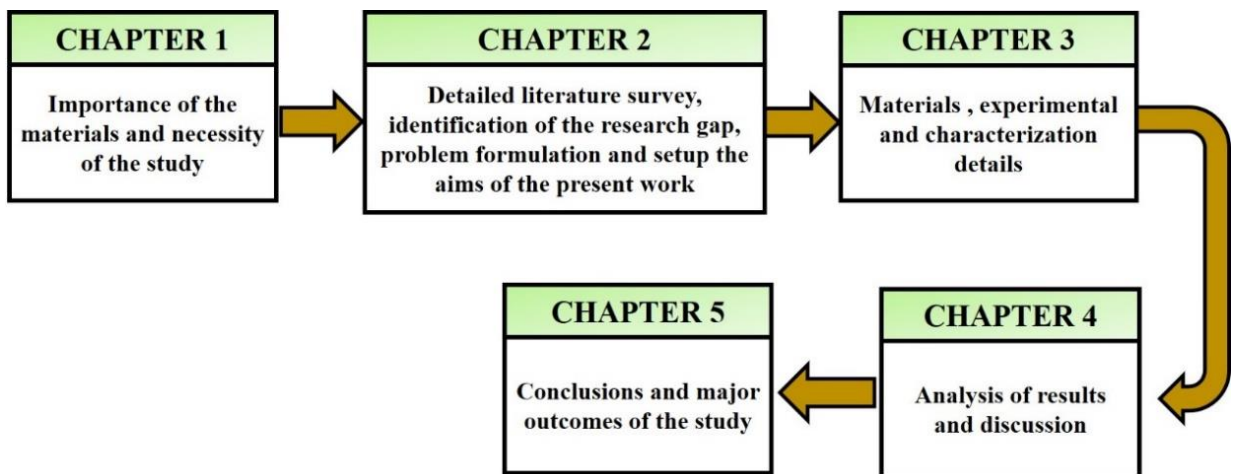


Fig. 2.12: Contribution of each chapter to achieve overall objectives of the present study.

2.10 Plan of the present study

Detailed plan of the present study is summarized in the following flow chart (Fig. 2.13) for the convenience.

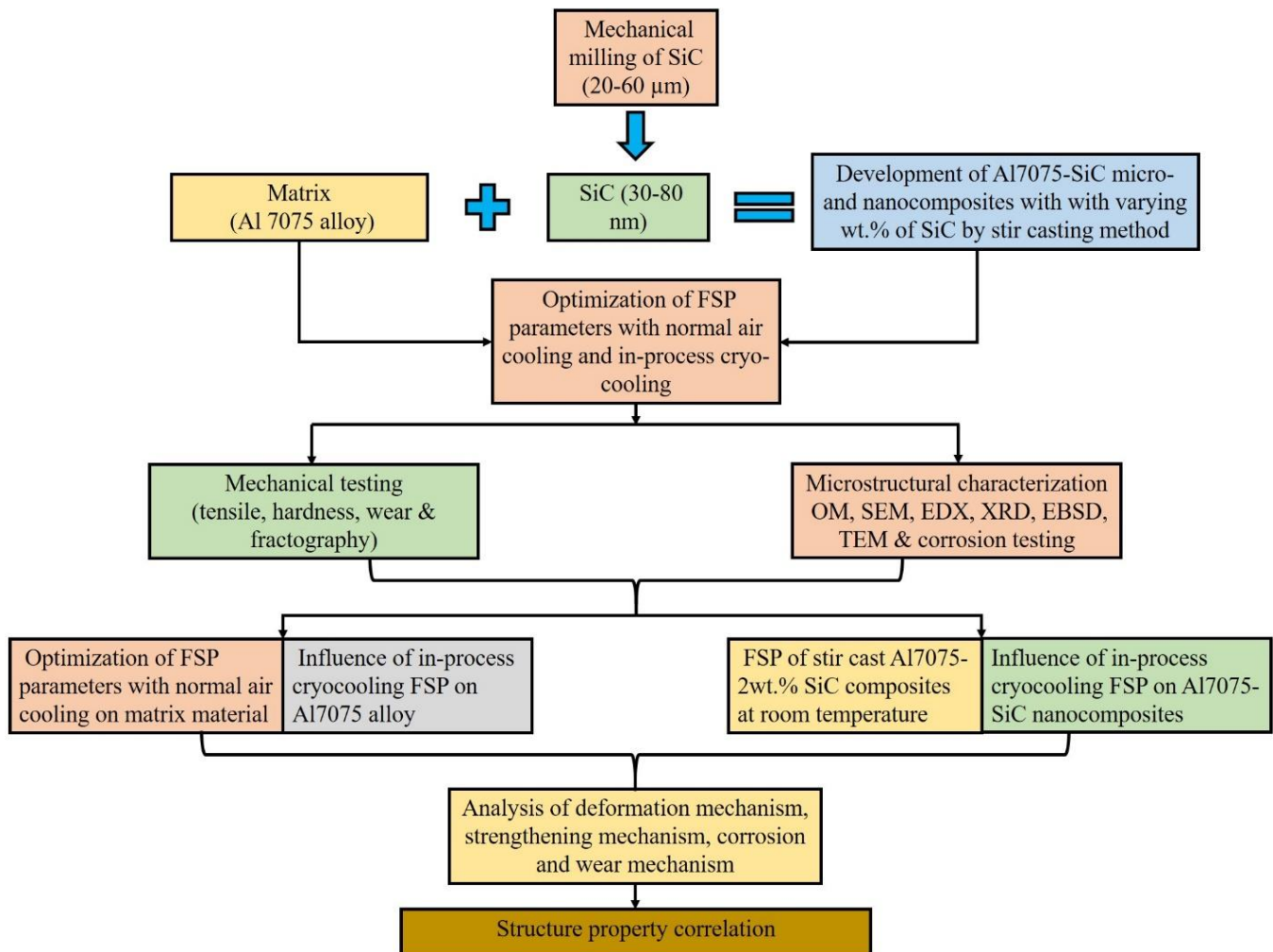


Fig. 2.13: Flow diagram of detailed plan of the present study.

In this chapter, experimental techniques used in the materials synthesis, processing and characterization for the present investigation are described in details. In the present study, Al7075 alloy-based composites reinforced with micro- and nanosize silicon carbide were produced in a bottom pouring stir casting machine. Both Al7075 alloy and Al7075 alloy-based composites have been chosen for the investigation. First, details about material synthesis are provided. This is followed by the detailed description about the experimental setup used to conduct friction stir processing (FSP) with in-process cryocooling and normal air cooling. After that, optimization of the FSP parameters in details are discussed for the Al7075 alloy plate in order to obtain defect-free processed material. Finally, on the basis of the optimized data, FSP of the cast composites with in-process cryocooling and normal air cooling have been conducted with the aim to obtain uniform distribution of reinforcement along with matrix grain size refinement to enhance its mechanical strength, ductility, wear resistance and corrosion resistance simultaneously. After synthesis and processing, the materials were subjected to a series of metallurgical and mechanical characterization techniques. Microstructural evolution was examined through optical microscopy (OM), scanning electron microscopy (SEM) with electron backscatter diffraction (EBSD) and transmission electron microscopy (TEM). The mechanical properties were evaluated by Vickers hardness measurements, tensile and wear testing. Details of the materials, experimental set-up and characterization techniques adopted for the present study are described in in the following sections.

3.1 Material selection

Al7075 alloy plate with a thickness of 6 mm (procured from M/s. Hindalco Industries, India) was used as matrix material for production of aluminium matrix composites (AMCs) in present study. Chemical composition of the alloy obtained by optical emission spectroscopy analysis (Spectrolab, Germany) is given in Table 3.1. Silicon carbide (SiC) powders of particle size 20-60 μm (supplied by Alfa Acer) were used as reinforcement.

Table 3.1: Chemical composition (wt.%) of the alloy obtained by optical emission spectroscopy analysis.

Elements	Zn	Mg	Cu	Cr	Si	Fe	Mn	Ti	Al
wt.%	5.93	2.26	1.43	0.23	0.18	0.18	0.04	0.04	Balance

3.1.1 Preparation of reinforcement

Micron size SiC powder (with particle size of 20-60 μm) was ball milled in a tungsten carbide grinding media using a planetary mill Pulverisette 7 (as shown in Fig. 3.1) for 25 h to produce nanosize SiC particles (particle size of 30-80 nm). The rotation speed of the mill was set at 300 rpm and the ball to powder mass ratio was kept at 15:1. As a process control agent, toluene was poured in the vial before milling. Subsequently, after the milling, size and morphology of the SiC particles was examined by SEM and TEM to assess the particle size. The TEM sample was prepared first by dispersion of small amount of ball milled powder ultrasonically in methanol and then a drop of the dispersed liquid was drop cast on to the carbon coated copper grid of 3 mm diameter using a micro-pipette and allowed to dry up. After that, the sample with carbon coated copper grid was analyzed using TEM. Figs. 3.2a and b, respectively, represent the SEM and TEM images of the as-received (micron size) and ball milled (nanosize) SiC particles.



Fig. 3.1: Planetary ball mill.

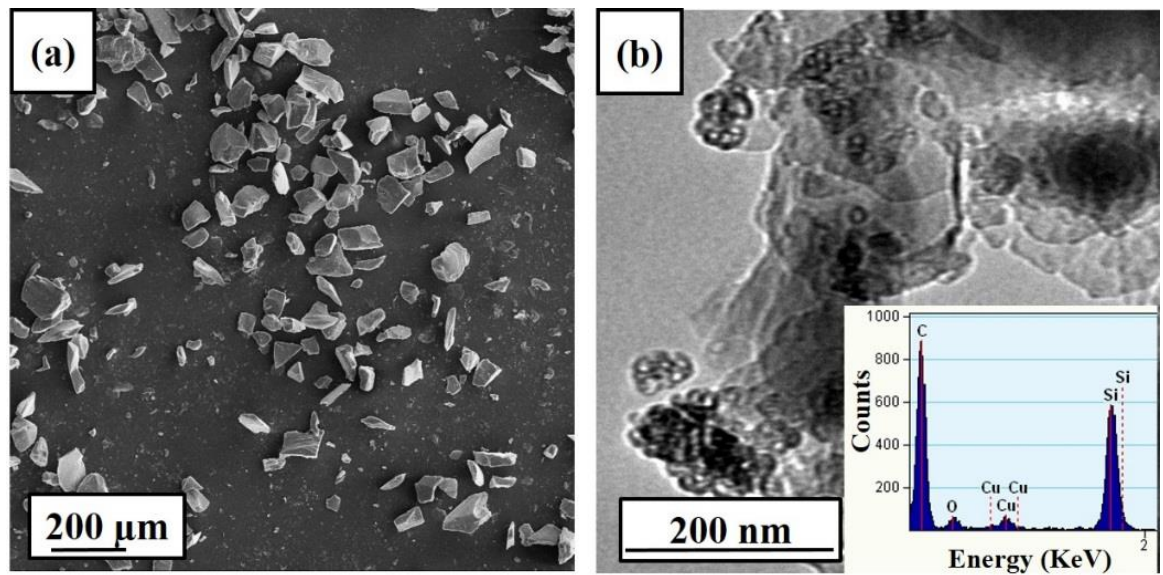


Fig. 3.2: (a) SEM image of as received SiC particles (b) TEM image of 25 h ball milled SiC particles (Kumar et al., 2017).

3.1.2 Synthesis of AMCs

Al7075 alloy-based composites were produced in a bottom pouring stir casting machine equipped with vacuum facility supplied by Swamequip Pvt. Ltd., India. The experimental setup used in the production of the composites is shown in Fig. 3.3. For each casting, an argon gas-controlled resistance heating electric furnace was used to melt one kg of Al7075 alloy. Before charging the furnace, a coating of high temperature paste (wolfrakote) suitable up to 1000°C was applied to the inside wall of the furnace and on the mechanical stirrer to avoid any contamination and to avert sticking of molten material. After holding the melt at 750°C for 30 min, the SiC particles were incorporated in the melt at a feeding speed of 4 g/min. To improve wettability and to remove moisture problem, the SiC powder was preheated for 2 h at 800°C before pouring into the molten metal. After SiC addition, the mechanical stirring was carried out at 600 rpm for 10 min to achieve a distribution of the particles uniformly. Finally, the composite melt was bottom-poured in a steel mold of size 110 mm × 45 mm × 45 mm, which was also preheated to 300°C before casting. The cast composites were allowed to solidify in the mold at room temperature. Throughout the casting process, an argon atmosphere was maintained completely to avoid any oxidation problem. During fabrication of all the compositions, same experimental setup was used and the castings were produced under same conditions. Fig. 3.4 shows the cast ingots of pure Al7075 alloy and its composites.

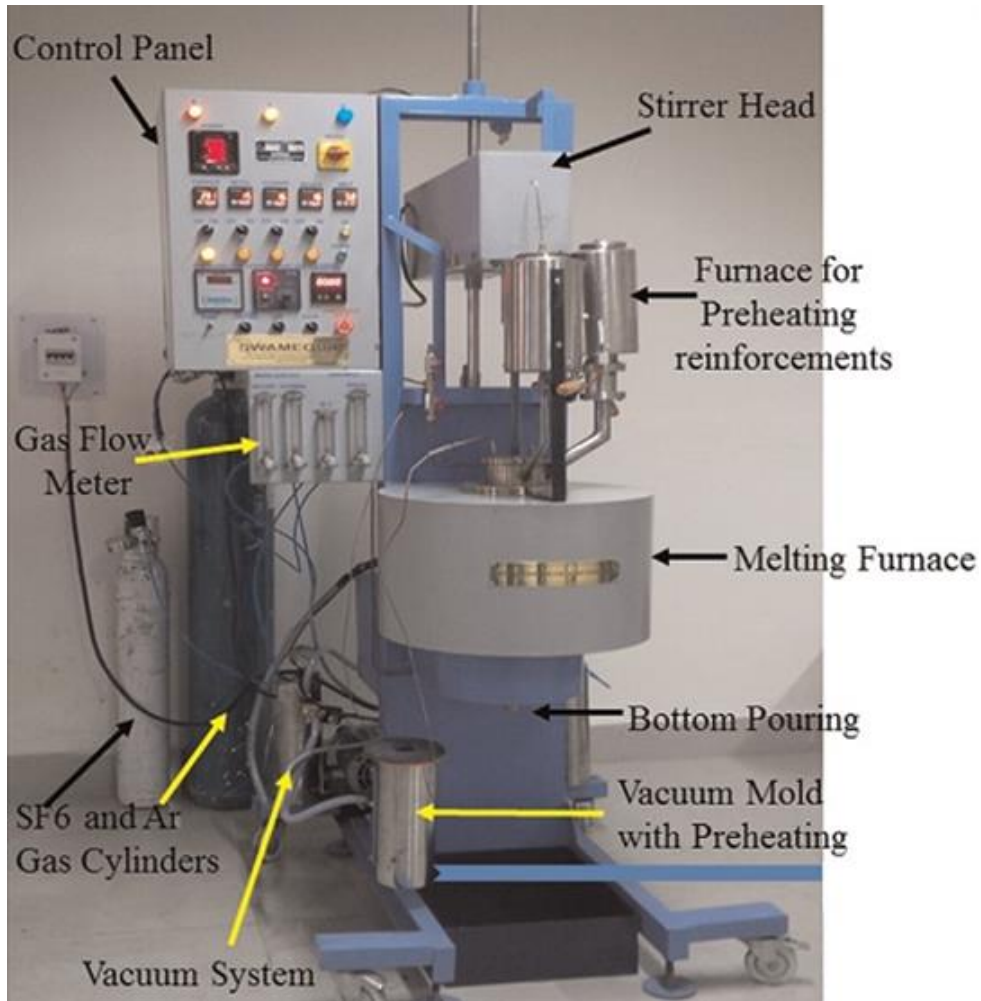


Fig. 3.3: Schematic image of bottom pouring stir casting machine.

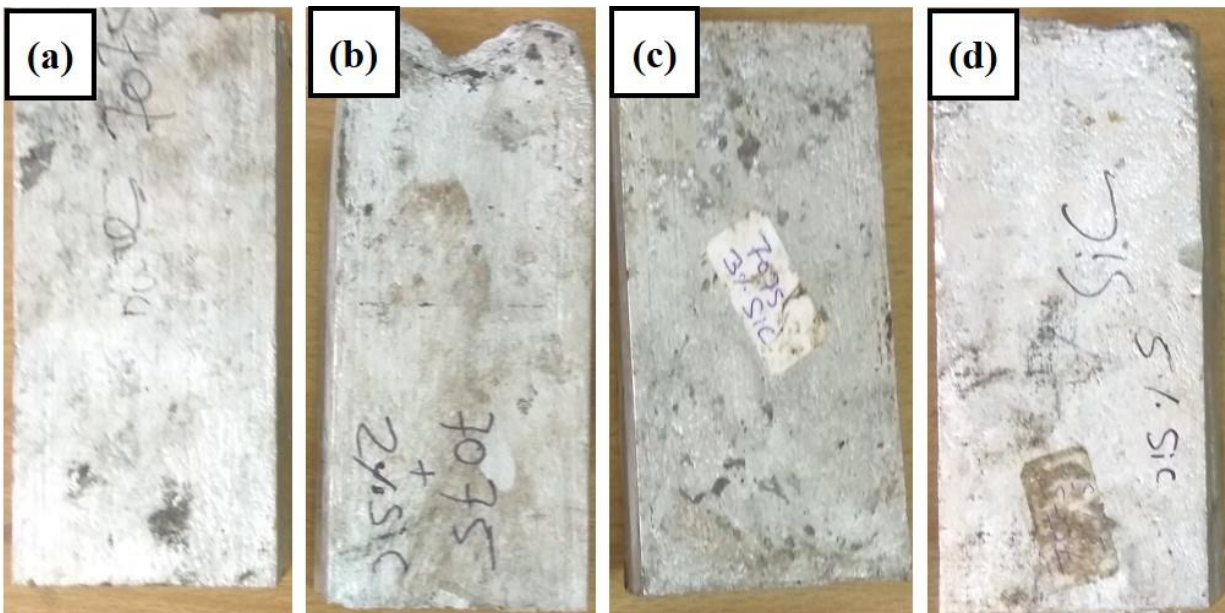


Fig. 3.4: (a) As cast Al7075 alloy (b) Al7075-2wt.% SiC nanocomposite, (c) Al7075-3wt.% SiC nanocomposite and (d) Al7075-5wt.% SiC nanocomposite.

3. 2 Experimental techniques

3.2.1 Friction stir processing setup

An indigenously made vertical milling machine was modified to carry out the FSP experiments. A 3-horsepower motor mounted on the top of the machine allows to attain eight adjustable spindle speeds. Spindle speed can be changed by changing the position of the V-belt in the four slot cone pulleys. The traverse speed and the plunge depth of the tool could be adjusted with the help of the semi-automatic adjustable table (hydraulic power pack controlled). The table has 3-axis movements; vertical (tool plunge), horizontal (traverse speed) and cross (overlap). The cross and vertical motion of the table were governed manually. The tool can be swiveled from 50° to 50° by tilting the spindle head. The photograph of the FSP setup is shown in Fig. 3.5.



Fig. 3.5: Photograph of friction stir processing machine used in this work.

The as-received material and the cast ingots were cut into rectangular pieces of required size to carry out the FSP operation. The rectangular plates were cleaned thoroughly by using emery papers and acetone to remove oxide layer, burrs and surface discontinuity, if any. The specimen was firmly clamped to the working table of the FSP machine by adjustable fixture. In this study, FSP was carried out at two different conditions: (i) normal air cooling (NAC) and (ii) in-process cryocooling (IPC). For the FSP with NAC condition, the conventional fixture made out of hardened steel was used and is shown in Fig. 3.6a. For the FSP with IPC condition, an indigenously designed and fabricated fixture was used (Fig. 3.6b). The fixture has the configuration of a hollow rectangular chamber below the bottom surface of the backing plate. The backing plate of the fixture was made of copper because of its high thermal conductivity. A chilled mixture (-30°C) of liquid nitrogen and methanol ($\text{LN}_2+\text{CH}_3\text{OH}$) was used to flow continuously through the hollow rectangular chamber of the backing plate during FSP with IPC condition. Fig. 3.7 shows the magnified photograph of hollow fixture used for FSP in IPC condition along with schematic diagram of the same to show the hollow rectangular chamber below the copper plate.

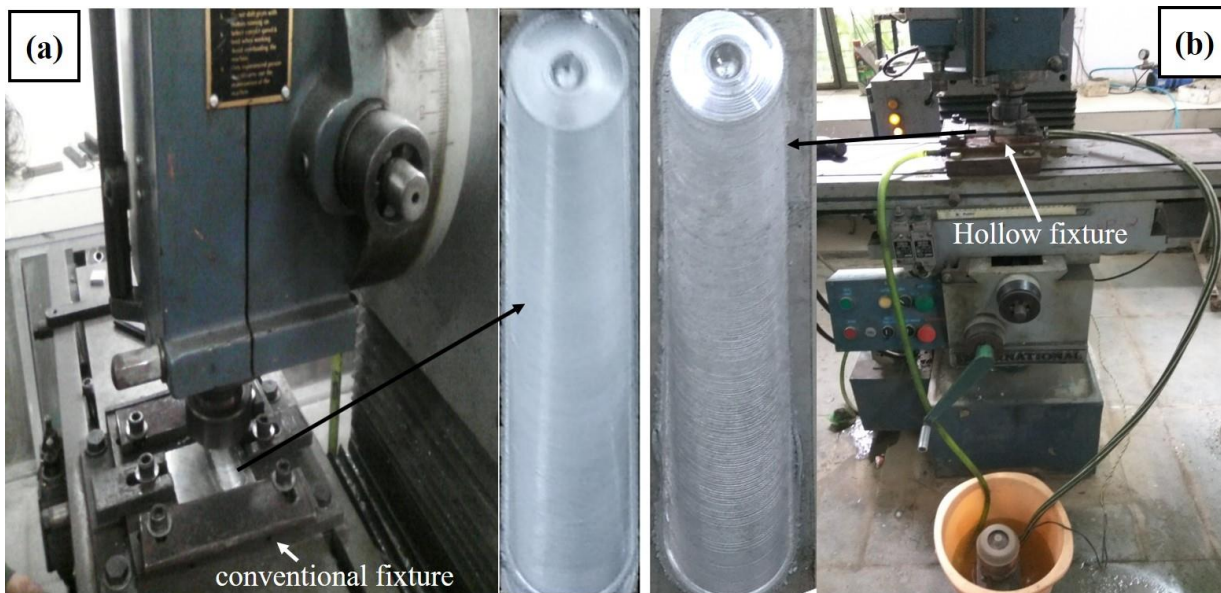


Fig. 3.6: Experimental setup used in this study along with surface appearance of the samples after FSP: (a) normal air cooling (b) in-process cryocooling.

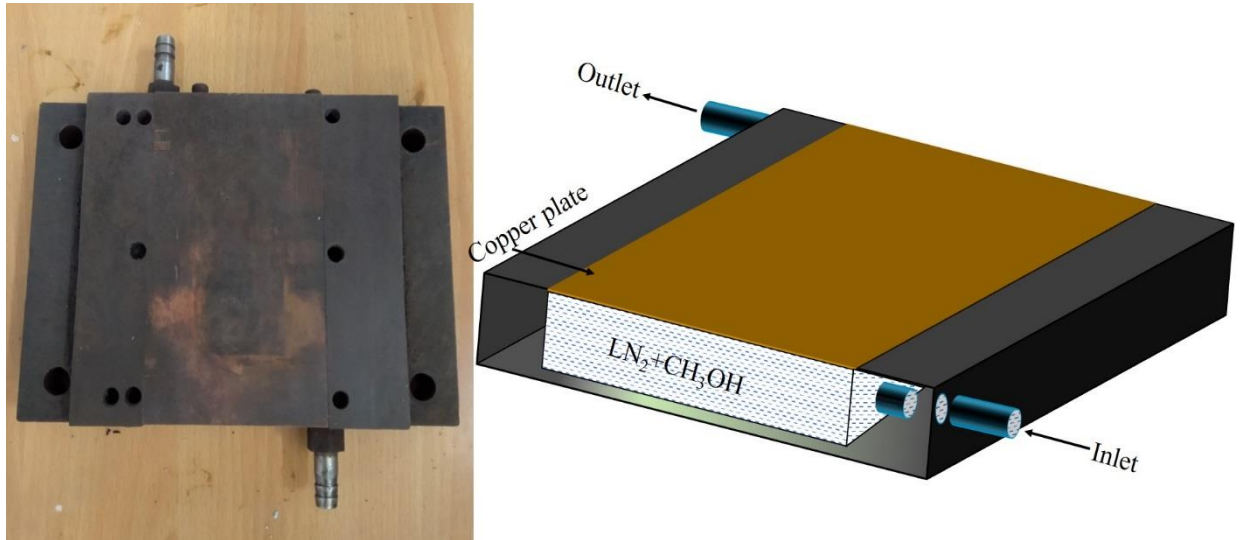


Fig. 3.7: Photograph of the hollow fixture along with schematic drawing.

Selection of FSP parameters

A specially designed non-consumable tool (made up of D2 die steel with concave shoulder of 25 mm diameter and a cylindrical threaded pin of 6 mm diameter and 4 mm length) with a hemispherical shape at the bottom was used for the FSP. Fig. 3.8 shows the schematic drawing of tool used for the present study. As the FSP parameters have great influences to produce defect free recrystallized microstructure and thereby final mechanical properties of the processed samples. The FSP parameters (rotational speed, traverse speed and geometry of tool) were optimized to obtain defect free processed samples. For this purpose, several numbers of trials have been carried out with the different combination of rotational speed (508, 720 and 1025 rpm) and traverse speed (25, 45, 65, 85, 100 and 150 mm/min) with a fixed tilt angle of 1.5° to the vertical axis. The optimized result in terms of defect-free processed zone with refined microstructure was obtained for the traverse speeds of 25, 45, 65 and 85 mm/min at a rpm of 720 only for the as received material (Al7075). Whereas, in case of the composite materials, the defect free processed region with uniform distribution of SiC particles and refined microstructure was achieved only at 1025 rpm at a traverse speed of 25 mm/min. The tool plunge depth was kept constant for all the samples.

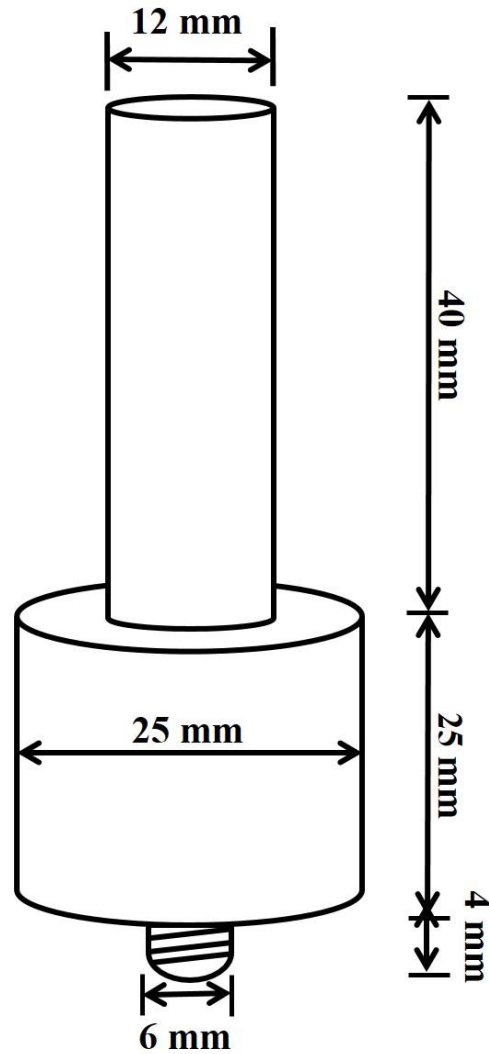


Fig. 3.8: Schematic drawing of tool used for this study.

Temperature measurement

Temperature profile of the nugget zone (NZ) during the FSP of all samples was measured using a K-type thermocouple. For plunging the thermocouples, two holes of 1.5 mm diameter were drilled to a depth of 13 mm from the edge of the plate. The K-type thermocouples with 0.8 mm diameter tip were fitted into the machined grooves as shown in Fig. 3.9b. The distance between the thermocouple tip and center line of the processing zone was around 3 mm. Fig. 3.9a shows the schematic diagram of the positions of thermocouples during temperature measurements. A computer aided data logger system with eight channels was used for recording the temperature profiles using the thermocouples at a sampling interval of 0.5 s during processing (Fig. 3.9c).

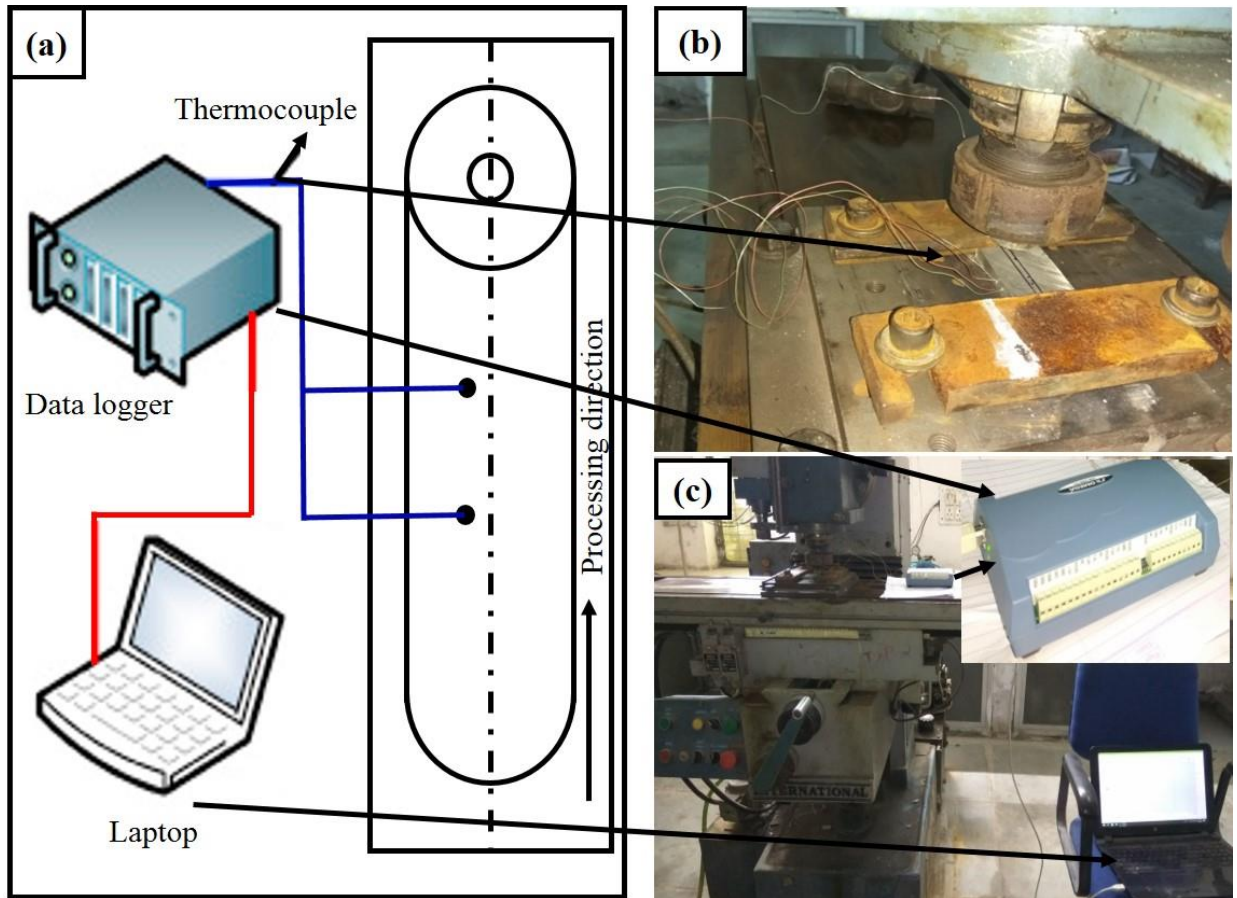


Fig. 3.9: (a) Schematic representation of the temperature measurement system, (b) Photograph of the K-type thermocouples fitted into the FSP sample and (c) Photograph of the data logger connected with computer and thermocouples for temperature measurement.

3.3 Microstructural investigation

Several microstructural characterization techniques were used to examine the microstructural evolution during FSP at various processing conditions. The major microscopy techniques used are optical microscopy (Leica DMI 5000 M), scanning electron microscopy (Make: ZEISS, Model: 51-ADD0048) equipped with EBSD and transmission electron microscopy (FEI Technai 20 G2S-Twin TEM). The steps involved in precise sample preparation for metallographic examination includes sectioning, grinding, paper polishing, cloth polishing, normal and electro-etching. Transverse sections of the processed zone were taken for microstructural investigation.

3.3.1 Optical microscopy

An optical microscope with an image capturing software was used to characterize the microstructure of the as-received, solution treated, as-cast and friction stir processed (FSPed) samples at low magnification. In order to observe the microstructure, standard metallographic procedures were followed to prepare the metallographic samples. All the processed samples were sliced from cross section perpendicular to the tool traversed using a high speed diamond cutter (Buehler IsoMet 4000) as shown in Fig. 3.10. Then, the samples were cold mounted for polishing. Initially, the cold mounted sample was flattened on a belt grindier with an abrasive belt of 120 grit size. After grinding, the specimen was polished with different grades of emery papers ranging from 320, 800, 1200, 1500, 2000 grit size successively. The sample was rotated by 90° after polishing on each paper for effective removal of scratches from the surface. The specimen was washed thoroughly with water and acetone after each polishing step to remove loose particles attached with the sample. After paper polishing, the sample was finally polished on a velvet cloth smeared with 0.75 µm magnesium oxide slurry in the rotating disc polishing machine. The mirror polished sample was cleaned and then etched with modified Keller's reagent (10 mL HF, 15 mL HCL, 25 mL HNO₃, and 50 mL H₂O) to reveal the microstructural features under light microscope (Fig. 3.11).



Fig. 3.10: Photograph of high speed diamond cutter IsoMet 4000.

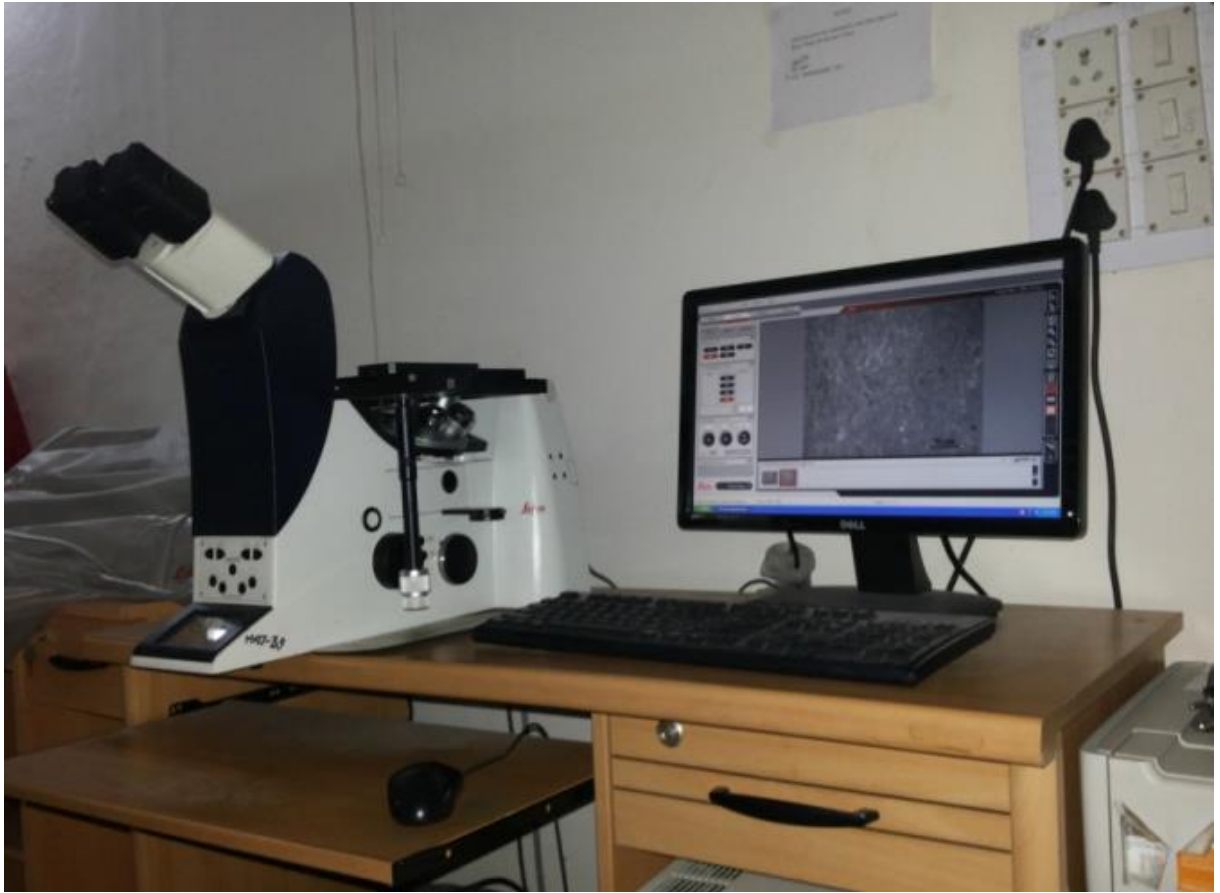


Fig. 3.11: Leica DMI 5000 M inverted optical microscope.

3.3.2 Scanning electron microscope (SEM) and Electron backscatter diffraction (EBSD)

SEM was used to characterize the microstructure at high magnification as well as fractured surface morphology after tensile test. The samples were examined using both secondary electron (SE) imaging and backscattered electron (BSE) imaging modes. The SE imaging with proper accelerating voltage was used for the best possible resolution. The SEM equipment was attached with energy dispersive spectrometer (EDS) and EBSD detectors. The EDS is an analytical technique used to study the quantitative measurement of elements as well as element mapping and on the basis of that approximate stoichiometry of the samples is estimated. The EBSD is a qualitative as well as quantitative microstructural investigation technique, which uses electron backscatter diffraction patterns/Kikuchi bands to examine the crystallographic orientations, grain structure, misorientation of grains and the texture of the material. It provides the information about the fraction of recrystallized/deformed grains. Therefore, the recrystallization mechanisms operating during processing/deformation could be established through quantitative measurement of low and high angle grain boundaries present and their distribution in deformed state. Therefore, in this work, the samples of Al7075 alloy and its

composites after normal and in-process cryocooling FSP were characterized using the EBSD technique. The photograph of the SEM equipped with EBSD can be seen from Fig. 3.12. The EBSD measurement was done by placing a flat, highly polished sample in the SEM chamber at an angle of approximately 70° to the incident electron beam. Fig. 3.13 shows the schematic representation of the EBSD setup. The EBSD detector consists of a compact lens and a charge couple device (CCD) camera equipped with phosphor screen. When interaction between the electron beam and the atomic lattice within the material satisfy the Braggs condition, an EBSD pattern/Kikuchi bands is formed. These patterns are systematically collected and analyzed by specialized computer software using an optimized Hough transform. By indexing each pattern, orientation maps, grain size and texture of the material can be obtained. The EBSD samples were made first by following standard metallographic polishing procedures for sample preparation. Finally, the samples were electropolished in a solution of 20% perchloric acid + 80% methanol for 90 s at -30°C and at a potential difference of 12 V. The EBSD scan was conducted at a step size of $0.2\ \mu\text{m}$ with frame size of about $150\ \mu\text{m}\times 150\ \mu\text{m}$. Further, the scan was analyzed by using TSL OIM software.

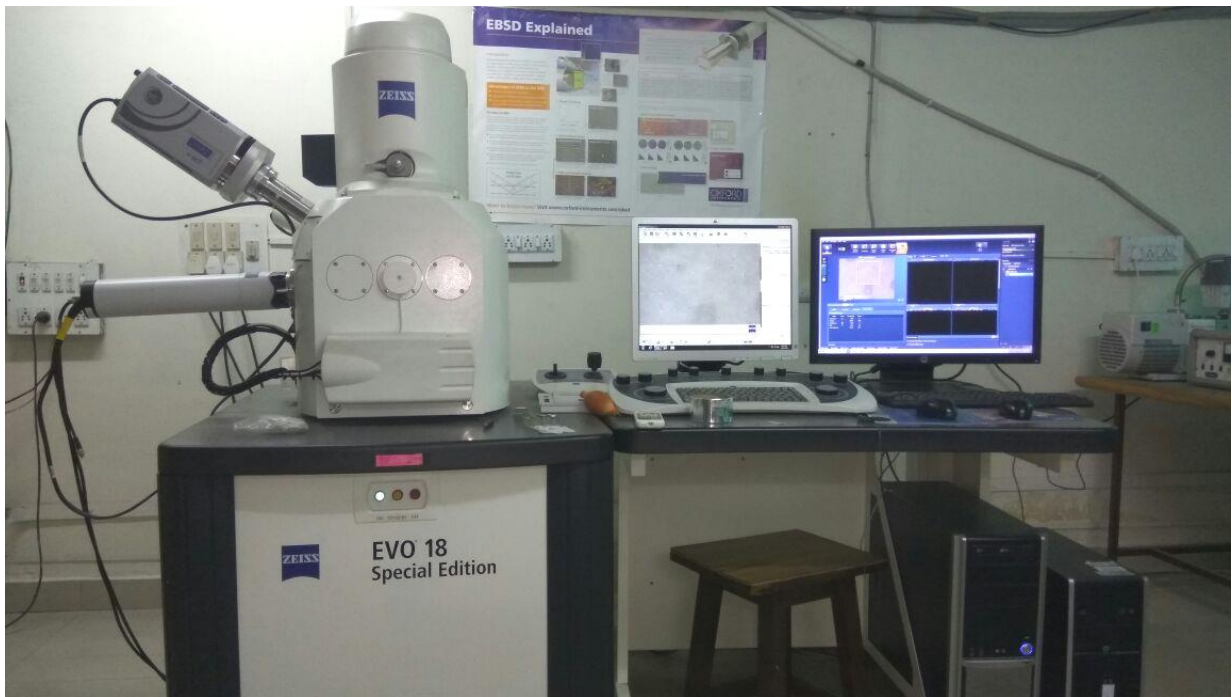


Fig. 3.12: Photograph of the SEM (ZEISS 51-ADD0048).

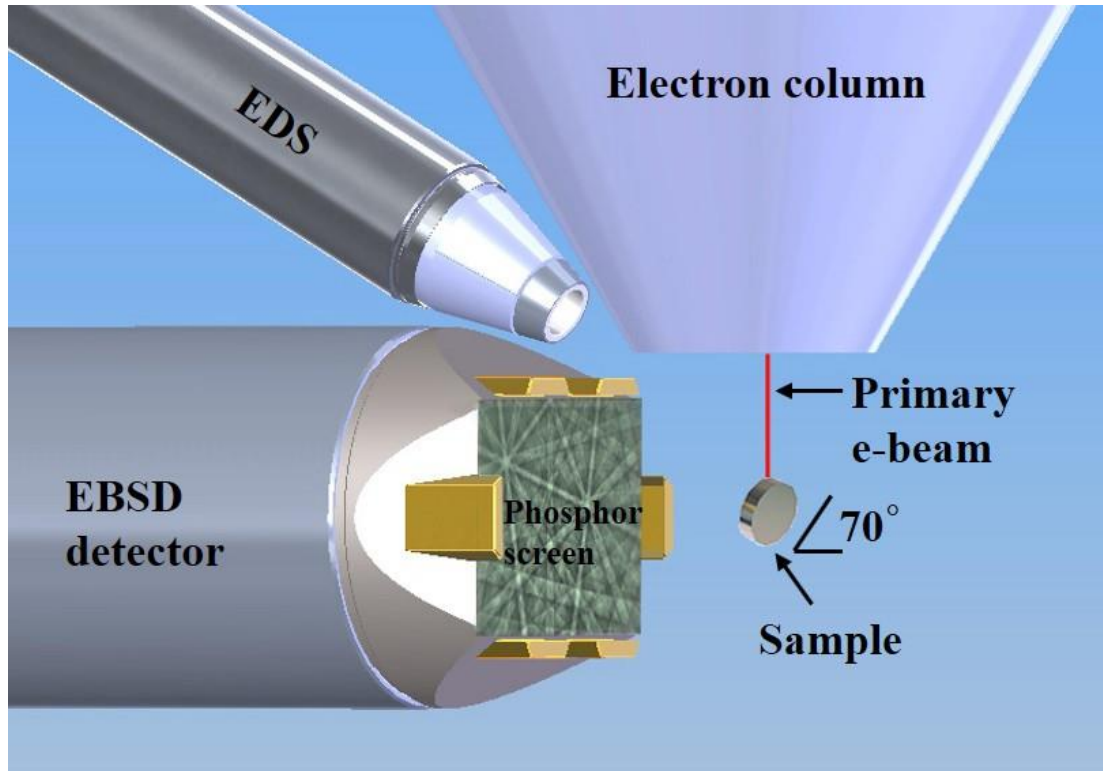


Fig. 3.13: Schematic representation of the EBSD setup.

3.3.3 Transmission electron microscopy (TEM)

The microstructural observation was made with TEM to look into the microstructural features at a significantly higher magnification. The transmission electron microscope can magnify the image of specimen in the range of 10 nm or less to observe the submicron and nanometer level features by imaging and electron diffraction. In present work, TEM was used to study the extent of grain refinement (grain size and their orientations), precipitate characteristics (size, shape and distribution of precipitates) and distribution of the SiC nanoparticles in the matrix through imaging (bright field and/or dark field) and selected area electron diffraction patterns. The TEM samples were made first by paper polishing of the samples to produce 100 μm thin foil and then 3 mm circular discs were extracted from the foil by Gatan punching tool (Fig. 3.14a). The disk was thinned down to 30 μm by dimple grinding (Fig. 3.14b) (Fischione 200) and then subjected to twin-jet electropolishing (FEI twin jet electropolisher) using a solution of 10% perchloric acid + 90% methanol at -30°C using 30 V potential difference (Fig. 3.14c). The detailed microstructural investigation was carried out using FEI Technai 20 G2S-Twin TEM (Fig. 3.15).

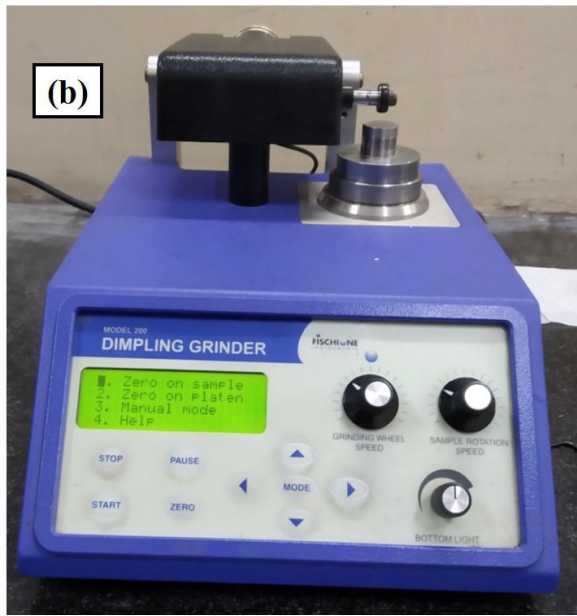


Fig. 3.14: Photograph of the TEM sample preparation unit (a) Gatan punching tool (Model: 656 punch), (b) Dimple grinder (Model: Fischione 200) (c) Twin jet electropolisher.



Fig. 3.15: Photograph of the FEI Technai 20 G2S-Twin TEM.

3.4 Mechanical testing

3.4.1 Vickers hardness measurement

Hardness testing is a quick and simple method of determining the resistance offered by a material to plastic deformation. The hardness values of the material under different processing conditions were measured by Vickers hardness indentation test. In Vickers hardness test, a square-based diamond pyramid indenter with 136° angle between its opposite faces was used. Fig. 3.16 shows the photograph of Vickers hardness testing equipment (FEI-VM50) used to measure the hardness values. The specimens for hardness testing were sliced from the transverse cross section of the processed zone. Prior to hardness testing, the samples were well polished in order to produce flat and parallel surface for indentations. Vickers hardness values were evaluated by applying a constant 5 kg load for a dwell time of 15 s. An average of 10

indentation measurements has been reported for each hardness value with a standard deviation in parenthesis.



Fig. 3.16: Photograph of the FEI-VM50 Vickers hardness tester.

3.4.2 Tensile testing

Uniaxial tensile tests were performed at room temperature in order to study the mechanical behavior of the materials processed under different conditions. The specimens for tensile testing were extracted from the processed zone along the FSP direction (Fig. 2.5) as per the ASTM: E8 sub-size standard with 12.5 mm gauge length. The schematic diagram and picture of actual tensile specimen are shown in Fig. 3.17. The tensile tests were carried out using S-Series, H25K-S (Model 3367) universal testing machine with a constant crosshead speed of 1 mm/min (strain rate = 0.08/min). To ensure the reproducibility of the tensile results, minimum 3 tensile samples were tested for each condition. Photograph of S-Series, H25K-S tensile testing machine used in this work is shown in Fig. 3.18.

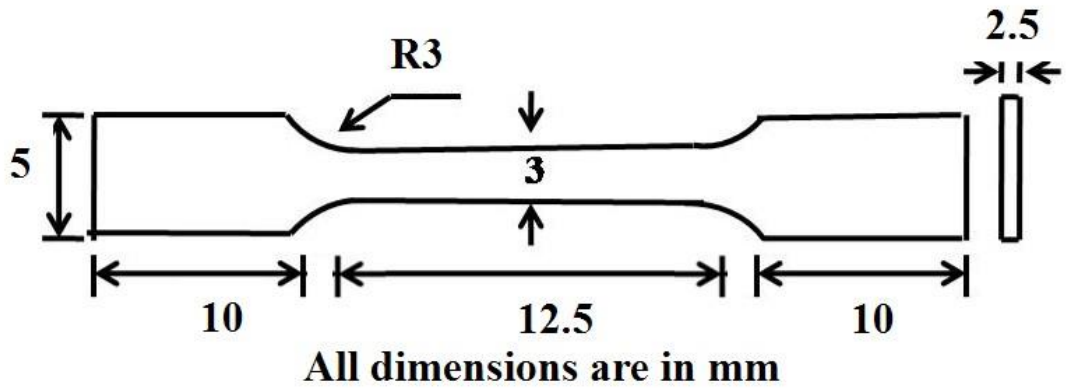


Fig. 3.17: Schematic drawing and photograph of a tensile specimen.



Fig. 3.18: The picture of the S-Series, H25K-S tensile testing machine.

3.4.3 Wear testing

The wear characteristics of the Al7075 alloy, as-cast composites and FSPed samples were investigated using a pin-on-disc tribometer (TR-201E-M2, DUCOM, Bangalore, India). The

wear testing system is shown in Fig. 3.19. There are two possible configurations for the wear test: (i) the pin is made of the material to be tested and the disk is made of a hard material, (ii) in the second configuration, the disk is made of the material to be tested and the pin is usually made by a harder material.

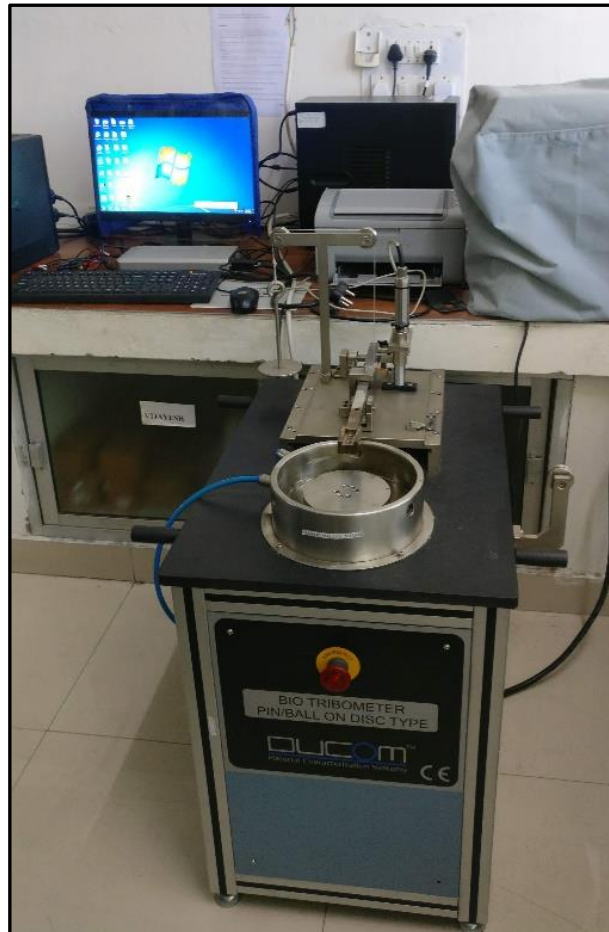


Fig. 3.19: Photograph of the pin-on-disc tribometer (TR-201E-M2, DUCOM, India).

In first set of experiment, the rotating part was the sample and the pin was a stainless steel ball of 10 mm in diameter. The specimens for wear test were prepared by polishing up to 1500 grit size emery papers followed by cleaning with acetone. Sliding wear tests were conducted with an applied normal load of 20 N at a rotation speed of 500 rpm in ambient conditions. The tests were conducted for a period of 30 minutes maintaining a track diameter of 3 mm. The coefficient of friction was calculated from the ratio of the frictional force to the normal load. A real time coefficient of friction was generated using an electronic sensor, which automatically records the frictional force induced between the steel ball and the sample. The surface profile of the worn disk samples was analyzed after measuring the depth and width of the wear scars

using a profilometer (SJ 400, Mitutoyo, Japan) as shown in Fig. 3.20. At least 3 tracks for each condition and 10 orthogonal measurements per track were made to obtain an average value of the width and depth of the wear scar. These results were used for calculation of wear volume loss. The wear volume loss (V_d) in the disk was calculated by using the following formula:

$$V_d = 2\pi \times r \times W \times D \quad (3.1)$$

where, r is the radius of the wear track, and D & W are the depth and width of the wear track, respectively.



Fig. 3.20: Photograph of the SJ 400, Mitutoyo, profilometer.

In second set of experiment the rotating part was the counterpart material made of EN 31 steel and specimen was the cylindrical pin of 4 mm diameter. A wire electric discharge machining was used to extract the cylindrical specimens of 4 mm diameter from the processed region. A specially designed and fabricated specimen holder was used to hold the wear pin (which is the sample itself) against the rotating counter body (made of EN 31 steel having $0.2 \mu\text{m}$ surface roughness & 65 HRC). All the tests were conducted by applying a normal load of 20 N and sliding speed of 1.674 m/s, maintaining a constant track radius of 40 mm. After completion a sliding distance of 2000 m, the samples were cleaned with acetone. The dried samples were weighed to calculate the mass loss due to wear. The specimen weight was measured by using

an electronic weighing balance (ML204/A01, Mettler Toledo, Switzerland) with a least count of 0.0001 g (Fig. 3.21). The abraded surfaces were further characterized by using SEM to analyze surface morphology and to investigate the wear mechanisms.



Fig. 3.21: Weighing machine with density kit setup (ML204/A01, Mettler Toledo, Switzerland).

3.5 Corrosion testing

To examine the corrosion performance of the Al7075 alloy, as-cast composites and FSPed samples, potentiodynamic polarization experiments were carried out in a 3.5 wt.% NaCl de-aerated solution at room temperature. The corrosion test was conducted on well-polished samples of $15 \times 15 \times 6 \text{ cm}^3$ size, which was extracted from top nugget domain of the FSPed sample. Potentiodynamic polarization measurement was carried out using a Gamry potentiostat (Model: Interface1000) setup as shown in Fig. 3.22. The polarization test was performed in a three-electrode flat cell setup, in which a platinum mesh was served as the counter electrode, a saturated calomel electrode (SCE) was used as a reference electrode and the specimen was served as a working electrode. The working electrode was placed in a flat cell in such a way that only $\sim 0.785 \text{ cm}^2$ area of the sample was exposed to the corrosive environment. Before potentiodynamic test, the samples were kept immersed in the electrolyte for 30 min to obtain a

steady open circuit potential (OCP). The polarization measurements were carried out from -250 mV in cathodic direction to +250 mV in anodic direction with respect to the OCP at a scan rate of 0.2 mV/s. Corrosion current density (i_{corr}) and corrosion potential (E_{corr}) have been calculated from the polarization curves using the Tafel extrapolation method. On the polarization curve, straight line portions of the anodic and cathodic curves were extrapolated and the intersection point of the extrapolated lines gives i_{corr} and E_{corr} values, respectively, from the X and Y axes. After the corrosion test, morphology of the corroded surface of each region has been analyzed using SEM to discuss the nature of corrosion attack.

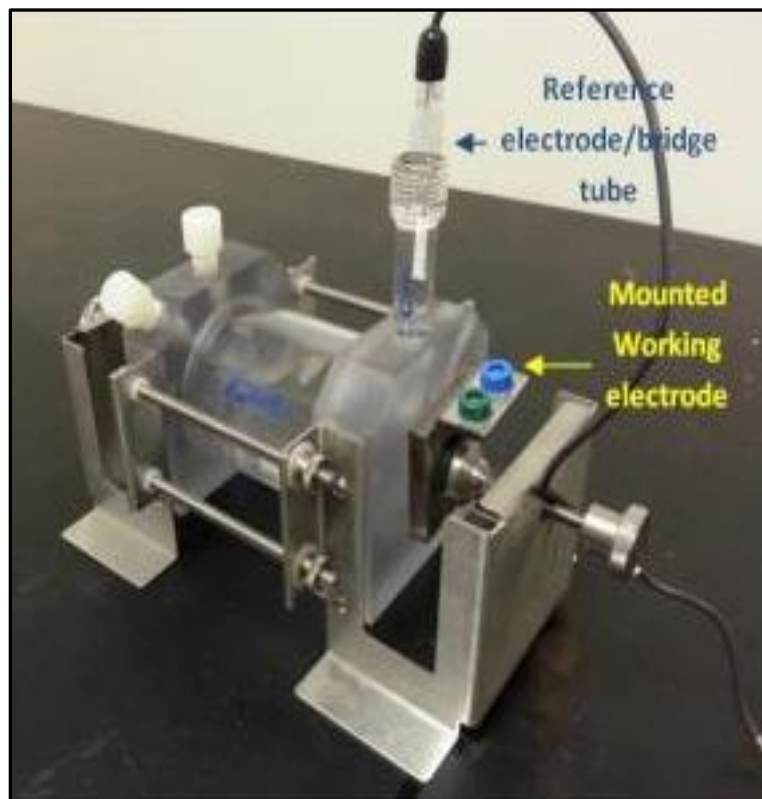


Fig. 3.22: Grammy potentiodynamic polarization setup.

The detailed results, their analysis and in-depth discussion have been described in this chapter. The major findings of the study and their analysis with explanation have been summarized in the subsequent sections.

4.1 FSP on Al7075 alloy and its analysis

In the present study, friction stir processing (FSP) is used as a secondary processing method for microstructural modification of Al7075 alloy and Al7075-SiC composites and thereby improvement of their mechanical properties. Hence, optimization of FSP parameters is carried out to achieve defect-free processed zone for the base alloy, i.e. Al7075 alloy and this chapter examines the effect of processing parameters solely on the microstructural modification and mechanical properties of the same (i.e. Al7075). It is known that the FSP parameters have great influences to produce defect-free fine recrystallized microstructure and thereby final mechanical properties of the processed samples. For this purpose, Al7075 alloy plate was friction stir processed using different combination of traverse speeds (25, 45, 65, 85, 100 and 150 mm/min) and rotational speeds (508 and 720 rpm) in order to investigate their influence on the microstructure, mechanical properties and corrosion resistance, which are discussed in the following sub-sections.

4.1.1 Microstructural characterization

It is to be noted that the FSP was carried out at two (2) different rotational speeds of 508 and 720 rpm at different traverse speed (25, 45, 65, 85, 100 and 150 mm/min). But it was not possible to produce any defect-free processed sample (processed zone) by FSP with 508 rpm at any traverse speed used. Therefore, further study was not conducted for the samples processed with 508 rpm. The macrostructure of the sample friction stir processed (FSPed) at 720 rpm at a traverse speed of 85 mm/min is shown in Fig. 4.1. Similar basin-shaped nugget zones (NZs) without any defect were also obtained for the samples FSPed at 25, 45 and 65 mm/min traverse speed at the same rpm (i.e. at 720). Intense plastic deformation caused by tool stirring resulted in the formation of nugget zone (NZ), thermomechanically affected zone (TMAZ) and heat-affected zone (HAZ) in FSPed region as shown in Fig. 4.1a. It can be noticed that the NZ has a wider surface at the top as compared to the bottom region. Since during processing, the upper surface of the workpiece

experiences excessive plastic deformation as well as frictional heating (by the shoulder of the cylindrical tool), a basin-shaped NZ with a wide top is generated (Ma et al., 2006). Microstructures of the transition zone (between base metal and FSPed region, processed at 720 rpm at 85 mm/min traverse speed) and the base metal (BM) are shown in Figs. 4.1b and c, respectively. The NZ is surrounded by TMAZ having highly distorted structure due to the stirring by the tool. Recrystallization did not occur in the TMAZ during FSP since there was not sufficient deformation strain generated, which could raise the temperature for recrystallization to occur. However, a grain distortion (elongation) along the directional flow of material could be observed in the TMAZ. Microstructure of the BM in Fig. 4.1c does not show any indication of deformation and/or recrystallization. In the following section, detailed microstructural analysis has been described for the NZ in comparison with that of the BM to correlate the mechanical properties before and after the FSP.

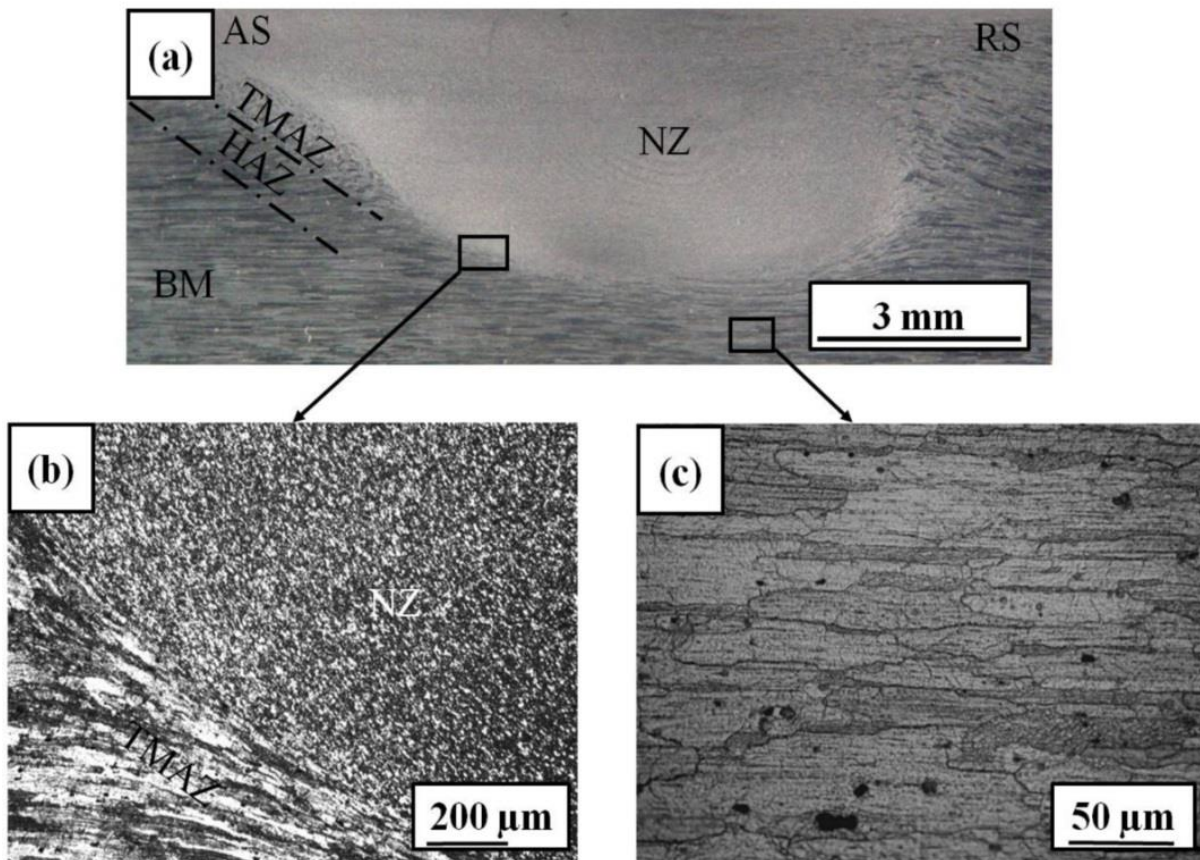


Fig. 4.1: Macrostructure of (a) FSPed sample at 720 rpm-85 mm/min, microstructure of (b) TMAZ and (c) BM.

Figures 4.2a-d show the microstructures of the NZs (from the central regions) of the different samples processed at different traverse speeds at 720 rpm. It can be noticed that fine and equiaxed grains are produced in the NZs for all the processed specimens. This is due to the fact of dynamic recrystallization of the deformed structure caused by intense plastic deformation and high frictional heating during the process (Hassan et al., 2003; Su et al., 2005a). It can also be observed that the increase in the traverse speed from 25 to 85 mm/min (at a constant rotational speed of 720 rpm) gradually decreased the recrystallized grain size. The average grain size was calculated from at least 200 grains (Figs. 4.2a-d) using a linear intercept method.

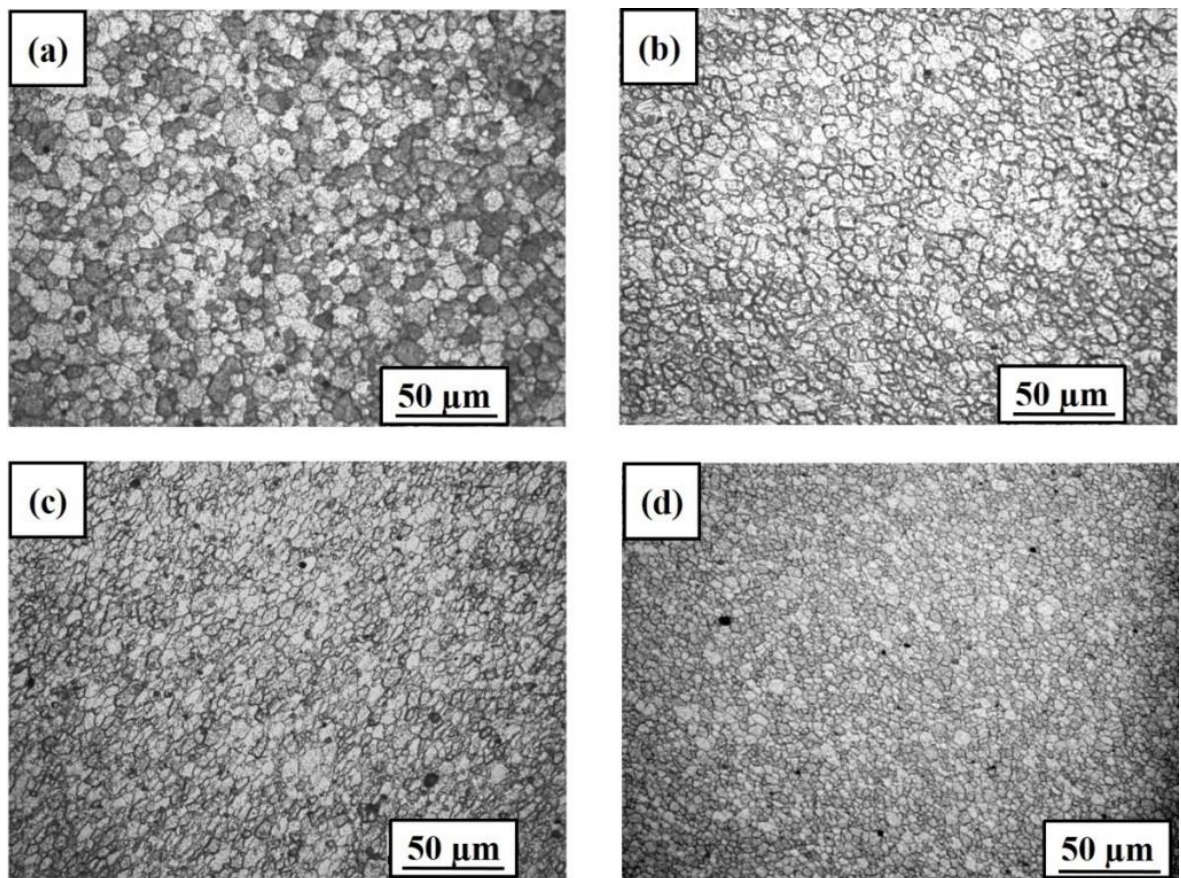


Fig. 4.2: Microstructures of the center of the NZ at (a) 720 rpm-25 mm/min, (b) 720 rpm-45 mm/min, (c) 720 rpm-65 mm/min and (d) 720 rpm-85 mm/min.

The average grain size was found to be $\sim 7 \mu\text{m}$ (Fig. 4.2a) when the sample was processed at a traverse speed of 25 mm/min. The recrystallized grain size decreased gradually with an increase in the traverse speed of the processing, and the lowest grain size was estimated to be $\sim 3 \mu\text{m}$ (Fig. 4.2d) for the sample processed at 85 mm/min. The variation of average grain size as a function of traverse speed is shown in Fig. 4.3. The result obtained in the present study is consistent well

with the various previous studies reported in (Buchibabu et al., 2016; Golezani et al., 2015). The grain size of the NZ is affected mainly by two thermomechanical factors, i.e., heat input and degree of plastic deformation during FSP (Golezani et al., 2015; Mishra et al., 2014). Increasing the traverse speed at a constant rpm leads to a decrease in the amount of heat input per unit length (Kim et al., 2006). Hence, coarsening of the recrystallized grains is restricted due to decrease in the heat input at higher traverse speed.

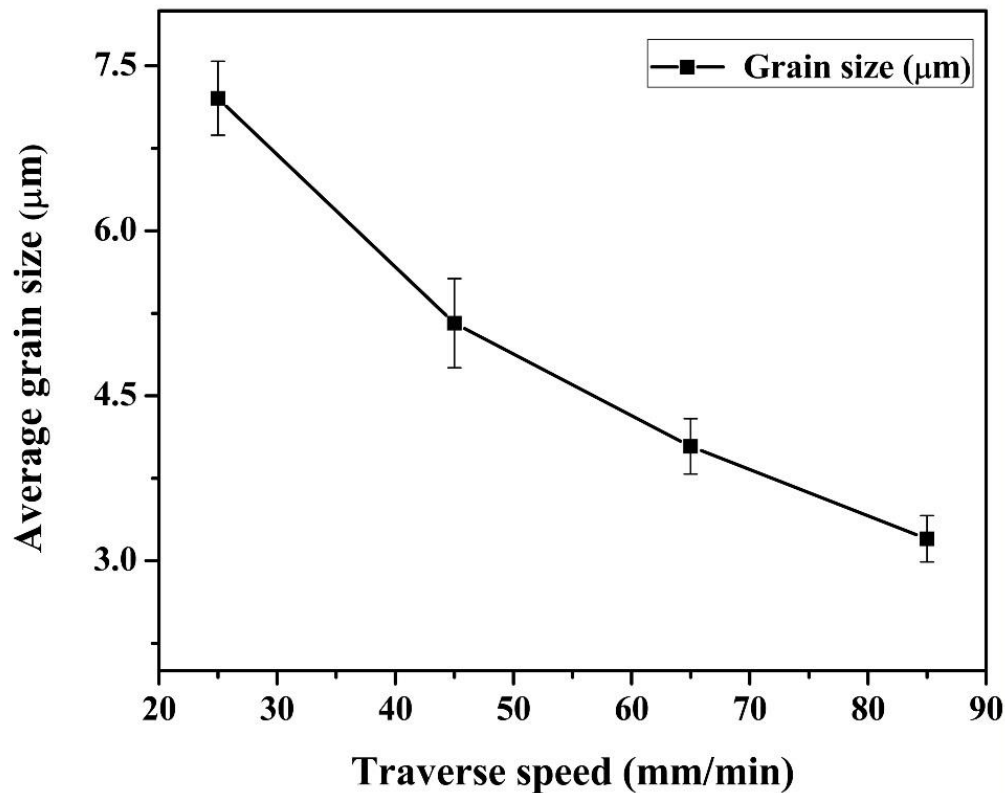


Fig. 4.3: Effect of traverse speed on grain size.

Detailed microstructural analysis was performed by transmission electron microscopy (TEM) to look into the characteristics and morphology of the precipitates formed before and after the FSP of the Al7075 alloy samples. TEM micrograph of the base alloy shows that the precipitates are segregated along the grain boundary as well as in the grain interior (Fig. 4.4a). It is worthwhile to mention that the material (Al7075) used in this study was in the T651 condition. The strengthening precipitates in Al7075 alloy in the T651 temper condition are well established as η' , $\text{Mg}(\text{Zn,Cu,Al})_2$ and the grain-boundary precipitates as η , MgZn_2 and/or $\text{Mg}_3\text{Zn}_3\text{Al}_2$ according to the literature (Jata et al., 2000b; Su et al., 2003).

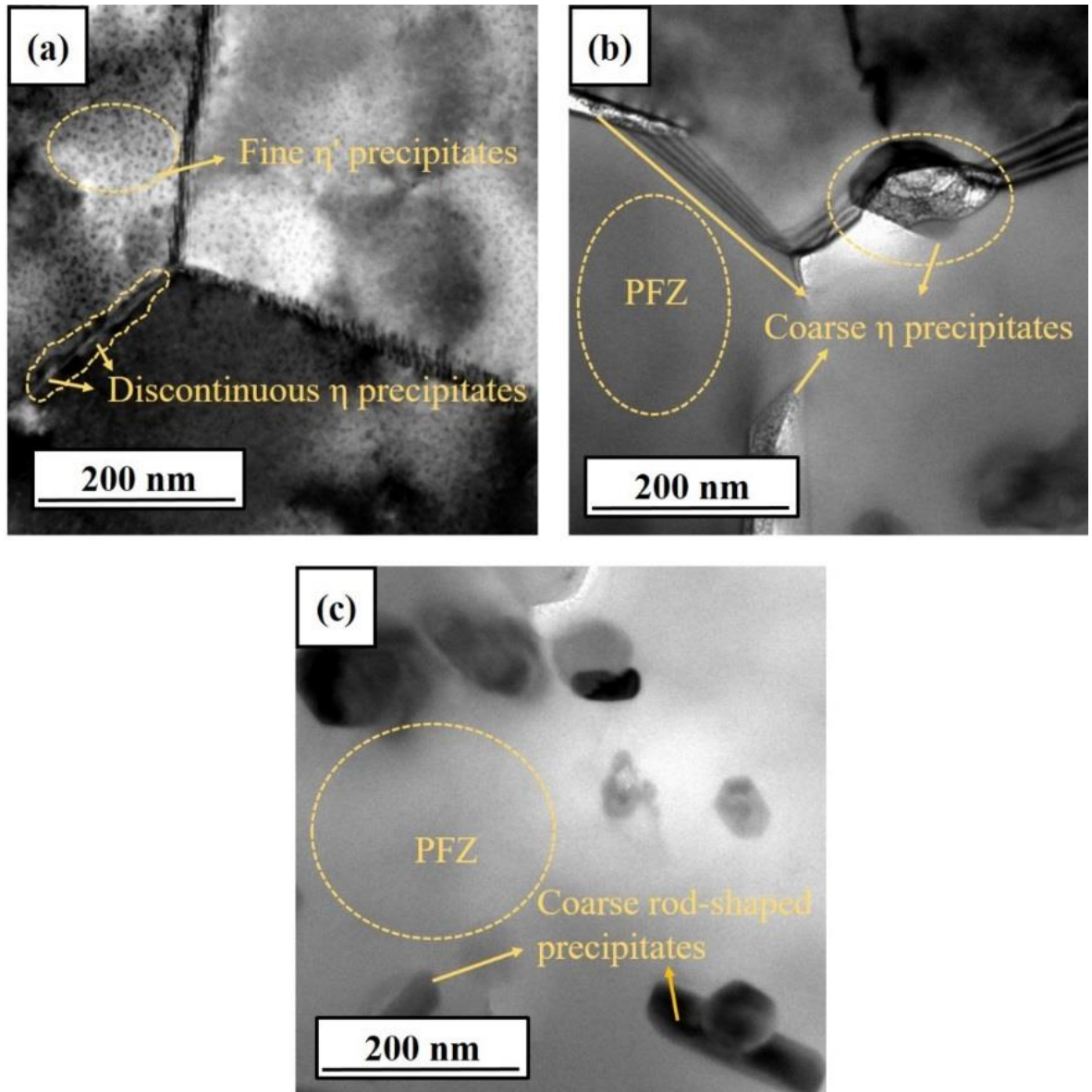


Fig. 4.4: TEM micrographs of (a) BM, and (b) and (c) NZ of the FSPed sample at 720 rpm-85 mm/min.

The fine η' precipitates with a size of ~ 10 nm are found to be distributed diffusely within the grain (Fig. 4.4a); whereas, discontinuous η precipitates of size (25-50 nm) are evident along the grain boundary (Fig. 4.4a). After the FSP, precipitate morphology in the NZ was found to change, which can be observed in Figs. 4.4b & c. It can be clearly observed from the TEM image (shown Fig. 4.4b) that some larger size η precipitates of ~ 150 nm are segregated mostly along the grain boundaries in contrast to the size of 25-50 nm before the FSP. Also, some relatively smaller size η precipitates of ~ 50 nm could be seen within the grains (Fig. 4.4c). It can be noted that the grain boundary precipitates are coarser with greater separation, and there is a precipitate-free zone,

approximately of 50-100 nm wide adjacent to the grain boundaries (Fig. 4.4b). The density of precipitates in the NZ after the FSP is found to be much less because of the coarsening of the same (Fig. 4.4c). Many researchers have reported that the temperature could be raised to ~470 °C during the FSP of Al alloys (Mahoney et al., 1998; Mishra et al., 2005). Although this temperature is high enough to dissolve the precipitates in the matrix during FSP, only fractional dissolution is possible due to the very short duration available for the dissolution. The remaining precipitates are subjected to go through coarsening resulting in larger size and few numbers of precipitates within the recrystallized equiaxed grains. Similar observation is also reported in previous studies (Zhang et al., 2015).

4.1.2 Mechanical properties

Mechanical properties of the samples friction stir processed under different conditions have been evaluated through measurements of hardness and uniaxial tensile testing. The hardness values in the NZs of different samples were measured and the average values (with their standard deviation) are shown in Fig. 4.5.

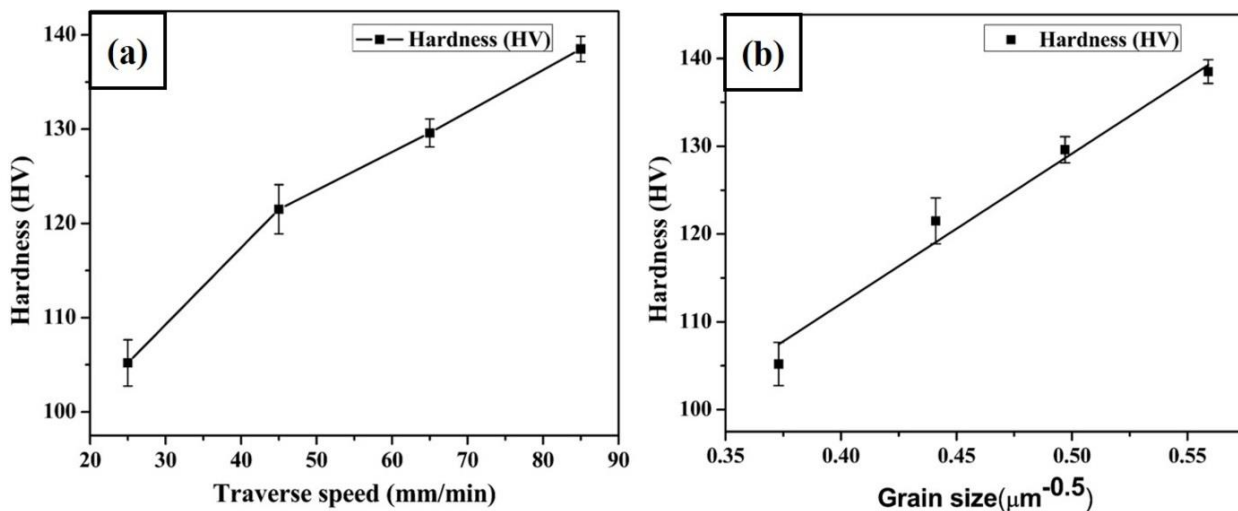


Fig. 4.5: (a) Variation in hardness of NZs with traverse speed and (b) Variation in hardness of NZs with inverse of the square root of grain size.

From the hardness results (Fig. 4.5a), two important points can be noted: firstly, the BM in the as-received state has the highest hardness of 180 HV, as it was in age-hardened (T651) condition. Secondly, among the friction stir processed samples, the hardness value is found to increase with increasing the traverse speed of processing at constant rotational speed (Fig. 4.5a) and the maximum hardness value achieved is 138 HV, which is less than that of the BM (i.e. 180 HV).

Figure 4.5a shows that the average hardness value increases from 105 to 138 HV as the traverse speed increases from 25 to 85 mm/min. Figure 4.5b shows the Hall-Petch type of plot between the hardness (H) and the inverse of the square root of grain size ($d^{-0.5}$) for the FSPed samples. A linear relationship could be obtained (as indicated in Fig. 4.5b) which establishes the validity of Hall-Petch relationship. Extrapolation of the plot could result a hardness value of 43 HV, which corresponds to a hardness value for the grain boundary-free condition ($\approx H_0$) as per Hall-Petch relationship; whereas, slope of the plot gives the Hall-Petch constant, $K_H \approx 171 \text{ HV}\mu\text{m}^{1/2}$. Therefore, the hardness values of the FSPed samples are found to corroborate well with the resultant grain size as per the Hall-Petch relationship (Fig. 4.5b). In an age-hardenable Al alloy, the hardness profile mainly depends on grain size of the matrix and morphology & interface characteristics of the precipitates. These factors depend on the amount of heat input per unit length, consequent temperature generated and cooling rate during and after the FSP. Increasing traverse speed (at a constant rpm) leads to a decrease in the amount of heat input per unit length. This results in faster cooling of the sample. Hence, at higher traverse speed, there is less chance of coarsening of the recrystallized grains as well as the remnant precipitate particles. This leads to the increase in the hardness.

Figure 4.6 shows typical engineering stress-strain curves for the BM and FSPed specimens processed at different traverse speeds with a constant rpm of 720. It can be noted that there is a significant decrease in the yield strength (YS) and ultimate tensile strength (UTS) for all the FSPed samples in comparison to that of BM in T651 condition. Consequently, the ductility is found to increase (14-42% increase) with decrease in the strength (i.e. YS/UTS). The maximum elongation of 20% is noted in the sample processed at a traverse speed of 65 mm/min as compared to 14% elongation of the BM. The decrease in the YS/UTS and increase in the ductility after FSP can be correlated with the microstructural features (obtained by TEM) of the corresponding sample. In BM at T651 condition, the alloy yields with the maximum strength mainly due to the presence of coherent/semi-coherent precipitates distributed uniformly within the matrix. After the FSP, the precipitates are subjected to partial dissolution and/or overaging as discussed earlier in the microstructural description. Therefore, the strengthening effect due to the precipitation hardening is mostly lost due to the formation of larger size overaged incoherent precipitates. It is to be noted that the YS and UTS gradually enhanced with increase in the traverse speed. For example, the YS and UTS are found to increase from 236 to 366 MPa (55% increase) and 278 to

421 MPa (51% increase), respectively, when the traverse speed increased from 25 to 85 mm/min. The increase in the YS of the FSPed samples processed at higher traverse speed is attributed to the formation of finer grains in the NZs (Fig. 4.2). It is well known that the YS increases with decrease in the grain size as per the Hall-Petch equation. The grain size strengthening effect increases with the increase in the traverse speed. The key strengthening mechanisms involved in Al7075 alloy mainly include grain size refinement, precipitation strengthening and a bit of dislocation hardening. But, in the age-hardenable alloys after the FSP, the dislocation density generally decreases to a lower level as compared to that of the BM (Rhodes et al., 1997). Before the FSP, the BM was in the age-hardened (T651) condition. On the other hand, strain-free recrystallized fine grains are developed during the FSP via dynamic recrystallization. During the FSP, the temperature of the Al alloy (work-piece) increases to a value of ~ 470 °C, which is higher than its recrystallization temperature (Mahoney et al., 1998; Mishra et al., 2005). Therefore, the dislocation density is expected to decrease to a very low level in the FSPed samples as compared to that of the BM. Woo et al. (2008) also reported that the dislocation density decreased in Al6061 alloy after the FSP. Therefore, in the FSPed samples, the dislocation strengthening contribution to the YS could be very small as compared to the contribution from the grain size strengthening or precipitation hardening (Woo et al., 2008). In the present study, the Al7075 alloy samples were subjected to dynamic recrystallization during FSP due to intense plastic deformation and high frictional heating. This subsequently results in a fine grain structure followed by faster cooling after the FSP. On the other hand, the precipitation strengthening played a reverse role in the present study. As it has been discussed earlier that the temperature in the NZ could reach in the range of solutionizing temperature (~ 470 °C) and due to that, there was partial dissolution of the precipitate particles in the matrix and the remaining particles were undergone overaging to produce incoherent second phase(s) particles. Therefore, there is softening of the NZ relative to the BM due to the dissolution and overaging of the precipitates. Overall, the increase in the YS due to the grain size refinement cannot offset the decreased in the same (YS) due to the softening effect.

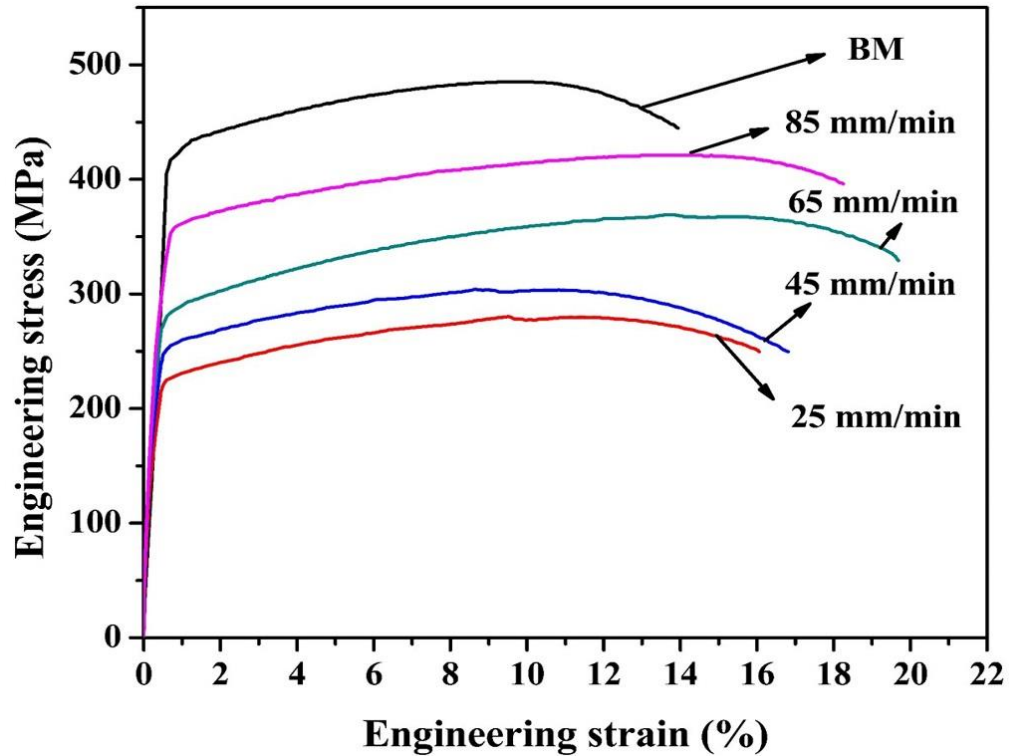


Fig. 4.6: Engineering stress-strain curves for BM and FSPed samples at different conditions.

The fractured surface of the tensile samples was analyzed by scanning electron microscopy to realize the failure mode under uniaxial loading. It can be noticed that the fractured surface of the BM (Fig. 4.7a) after tensile test consists of large number of cleavage facets and few numbers of dimples separated by tearing edges and cracks, which are mostly indicative of brittle dominated fracture. Fractured surface of the specimen processed at lower traverse speed (25 mm/min) shows little more number of smaller size dimples. The grain size decreased after the FSP and larger size precipitates could be observed along the grain boundary region. The breakage of secondary precipitates at grain boundary region initiated the formation of microvoids, which coalesced to cause failure. Size of the second-phase particles decreased with the increase in the traverse speed due to less heat input. Figure 4.7c reveals a large number but smaller size dimples throughout the fractograph. This is attributed to the grain size refinement and less coarsening of the second-phase particles (Zhang et al., 2015). It can be noticed that none of the FSPed samples shows any cleavage kind of facets and major cracks. This indicates that the failure mode changes to ductile appearance fracture for the FSPed samples from the brittle dominated failure in the BM.

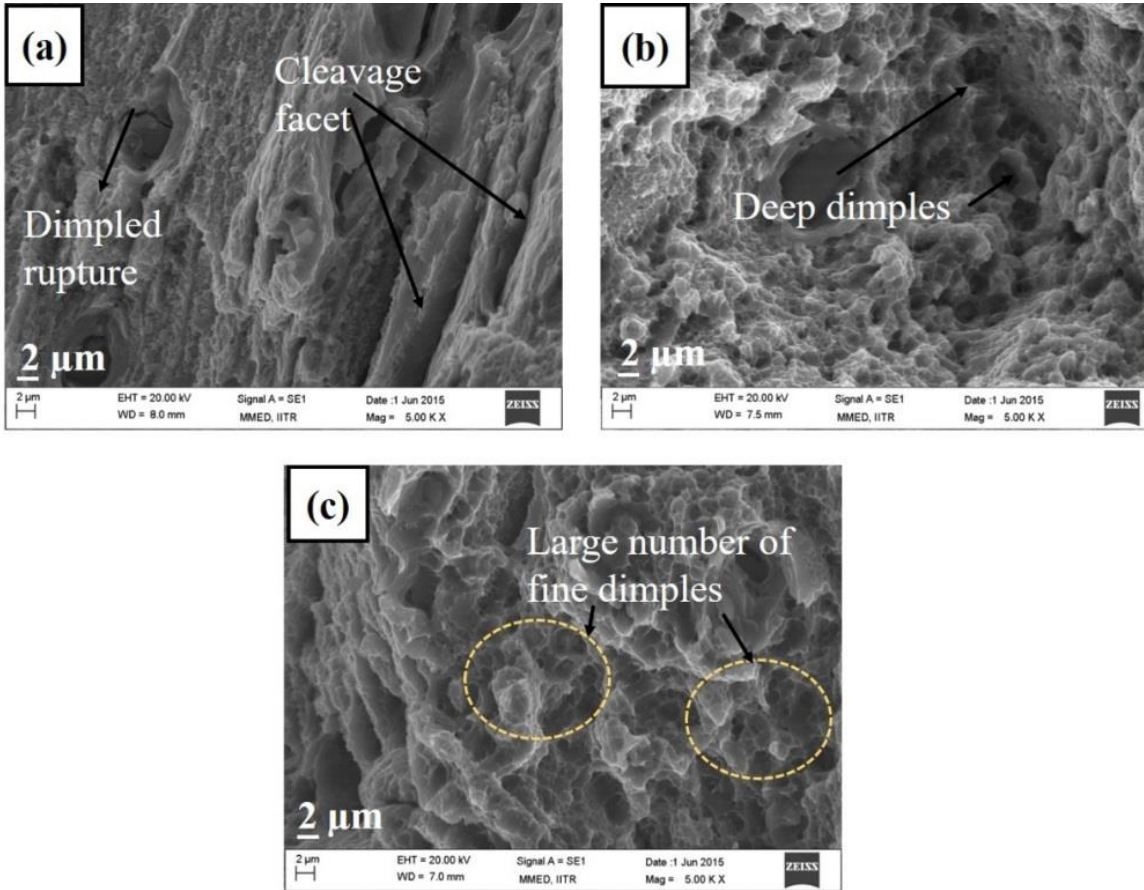


Fig. 4.7: SEM fractographs of (a) BM, (b) FSPed at 720 rpm-25mm/min and (c) FSPed at 720 rpm-85mm/min.

4.1.3 Wear characteristics

The variation of friction coefficients of the BM and FSPed samples against a steel ball (counter body) as a function of sliding time is shown in Figs. 4.8a-e. In the initial stage of sliding for all the specimens, the coefficient of friction increased rapidly to a peak value and thereafter attained a steady state. An increase in the friction coefficient in the initial stage can be triggered due to an increase in the frictional force which is required to overcome the highly adhesive contact between the test surface and the counter body (Huq, 1997). The large fluctuation of the friction coefficient (observed in all the curves as shown in Figs. 4.8a-e) can be attributed to the periodical accumulation and elimination of wear debris on the worn track (Barmouz et al., 2011; Mahmoud et al., 2010). The friction coefficients of all the specimens are found to be very close to each other. It can be noticed that (Fig. 4.8) the average steady-state friction coefficient varies from 0.39 to 0.32 as the traverse speed increases from 25 to 85 mm/min during the FSP.

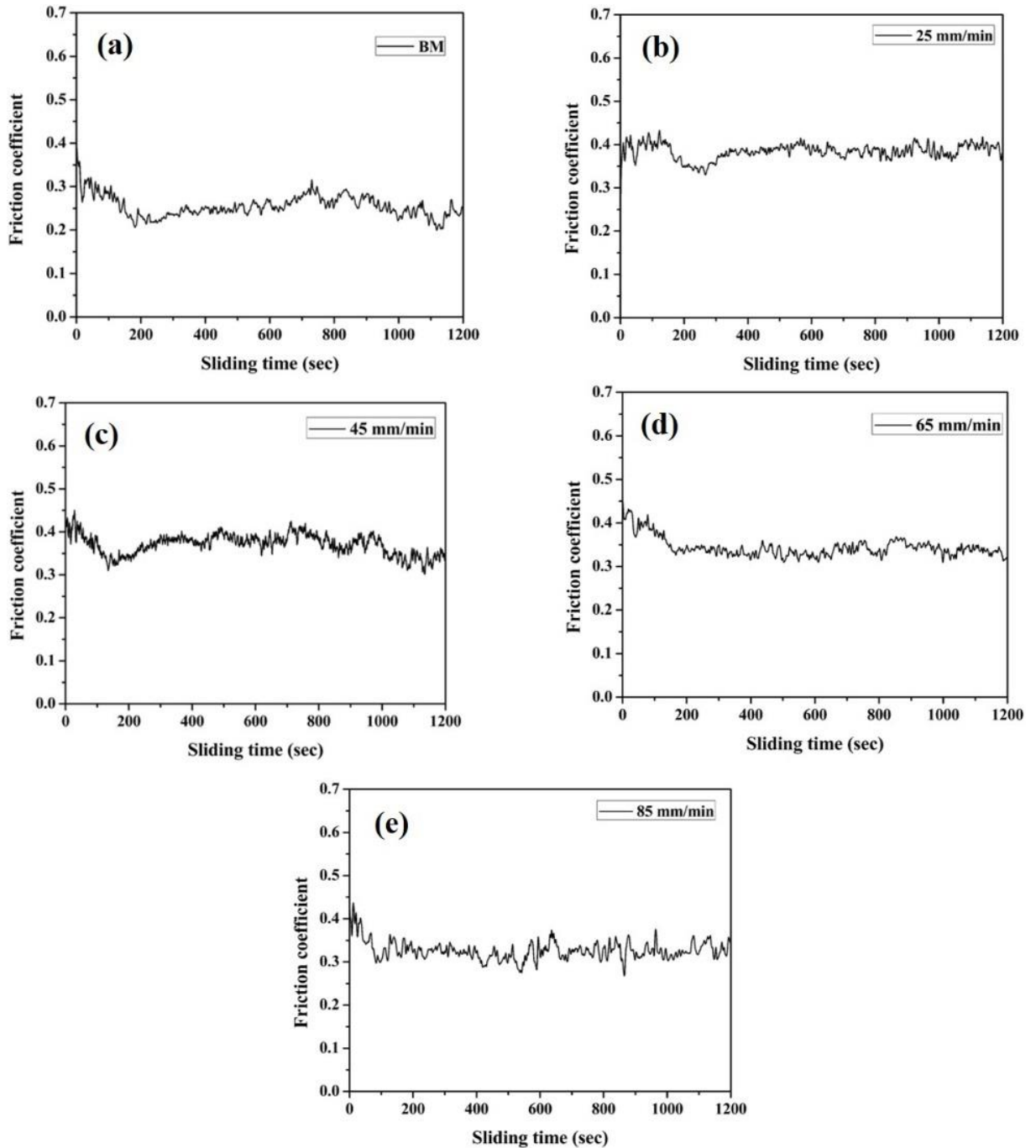


Fig. 4.8: Variation of friction coefficient with sliding time for (a) BM, (b) FSPed sample at 720 rpm-25 mm/min, (c) FSPed sample at 720 rpm-45 mm/min, (d) FSPed sample at 720 rpm-65 mm/min and (e) FSPed sample at 720 rpm-85 mm/min.

The friction coefficients of the samples processed at 45 and 65 mm/min traverse speed could be approximately 0.38 and 0.34, respectively. The main attributes of the frictional behavior of the metallic material are abrading action of wear debris, adherence of material on the counter body and stability of the tribolayer. The reduction in the friction coefficient is ascertained to the

increase in the hardness of the FSPed samples (processed at higher traverse speed), which decreases the adhesive wear. This is also corroborated well with the appearance of worn surface of the corresponding sample examined by SEM (discussed later).

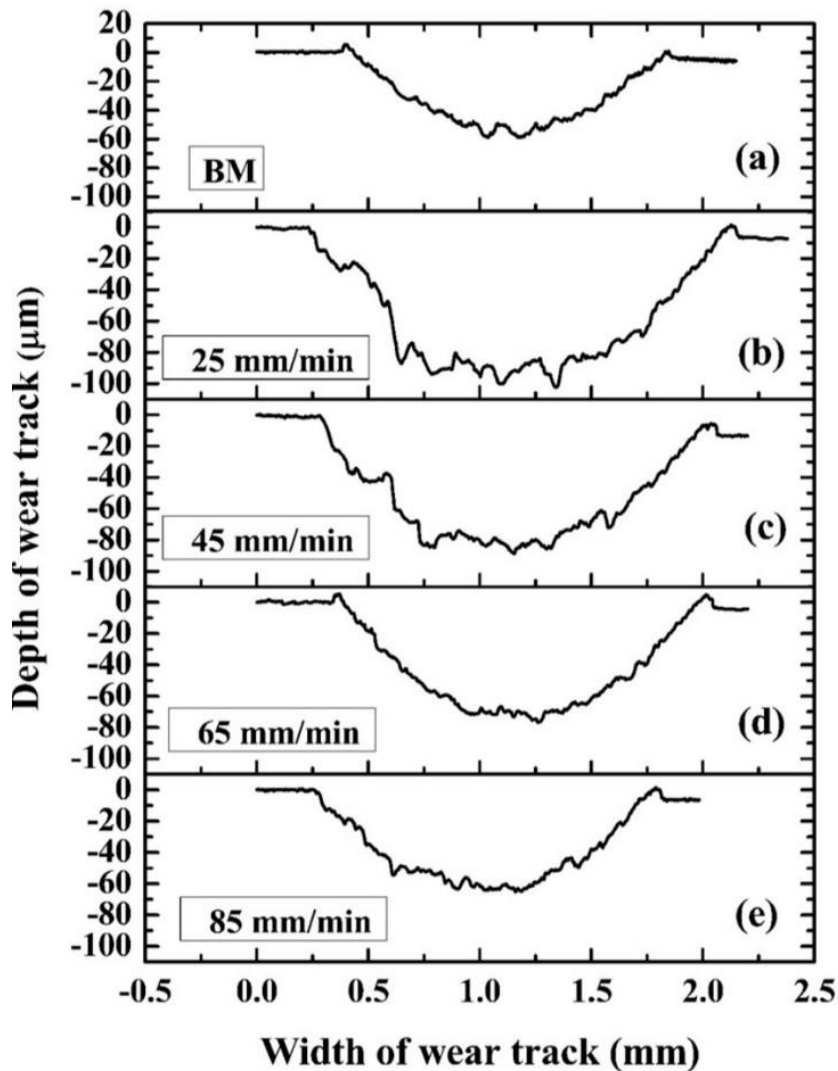


Fig. 4.9: Surface profiles of wear scars for (a) BM and (b) FSPed sample at 720 rpm-25 mm/min (c) FSPed sample at 720 rpm-45 mm/min, (d) FSPed sample at 720 rpm-65 mm/min and (e) FSPed sample at 720 rpm-85 mm/min.

The cross-sectional profiles of the wear tracks acquired in the transverse direction of sliding are shown in Figs. 4.9a-e. It shows that the average depth of the wear tracks varies between 55 and 90 µm, and the width of the wear tracks varies between 1.44 and 1.9 mm. It can be noticed that a decrease in the wear track width as well as wear depth could be observed with the increase in the traverse speed of the processing. The FSPed sample processed at 25 mm/min traverse speed showed a greater damage in the wear track (Fig. 4.9b) as compared to that of the samples

processed at higher traverse speed (Figs. 4.9c-e). The BM shows the lowest depth and width of the wear scar, which indicates the minimum damage to the surface. This trend is consistent with the increase in the hardness values of the corresponding samples.

Wear volume data of the BM and FSPed samples have been evaluated and plotted as a function of traverse speed as shown in Fig. 4.10. It is well known that the hard materials are more resistant to wear than a soft metal under the same frictional conditions (Deuis et al., 1996; Mazaheri et al., 2013). The influence of hardness on the wear volume is defined by Archard's equation (Mazaheri et al., 2013) as follows:

$$Q = K \frac{W}{H} \quad (4.1)$$

where, W is the load applied, Q is the volume worn per unit sliding distance, H is the hardness of the sample and K is the wear coefficient, which can be obtained from Fig. 4.8. According to Eq. (4.1) and Fig. 4.8, it is obvious that the volume loss is inversely proportional to the hardness of the material. In the present study, it is found that the wear volume of the BM is much lower as compared to that of the FSPed samples, whereas, the wear volume gradually decreases with the increase in the traverse speed of the FSP. The decrease in the hardness of the FSPed samples can be explained by the fact of overaging and/or dissolution of the precipitate particles within the matrix. Overaging followed by coarsening of the precipitates produces incoherent large size precipitate particles. Therefore, the overaging and dissolution due to solutionizing during FSP both resulted in the decrease of the hardness and led to significant loss of the strength of the material. And after the FSP, an increase in the strength due to the decrease in the grain size could not able to compensate the loss of the strength due to the softening effect by overaging and solutionizing. The BM exhibits the lowest wear volume of 0.72 mm^3 , which could be attributed to the highest hardness of the material (180 HV), whereas, the wear volume for the FSPed samples is much higher and lies in the range of $0.874\text{-}1.432 \text{ mm}^3$. It could be observed that the wear volume gradually decreases with the increase in the traverse speed of the FSP. This is attributed to the increase in the hardness due to the grain size reduction at higher traverse speed. After the FSP, the minimum wear volume of 0.874 mm^3 is obtained for the sample FSPed at 85 mm/min traverse speed. This is also corroborated with the highest hardness value (138 HV) among the FSPed samples. The minimum wear is ascertained to the maximum grain size refinement achieved and least deterioration of the precipitate (least coarsening) at the higher

traverse speed (Liu et al., 2011; Thangarasu et al., 2014). These results are also consistent with the profilometric results as discussed earlier (Fig. 4.9).

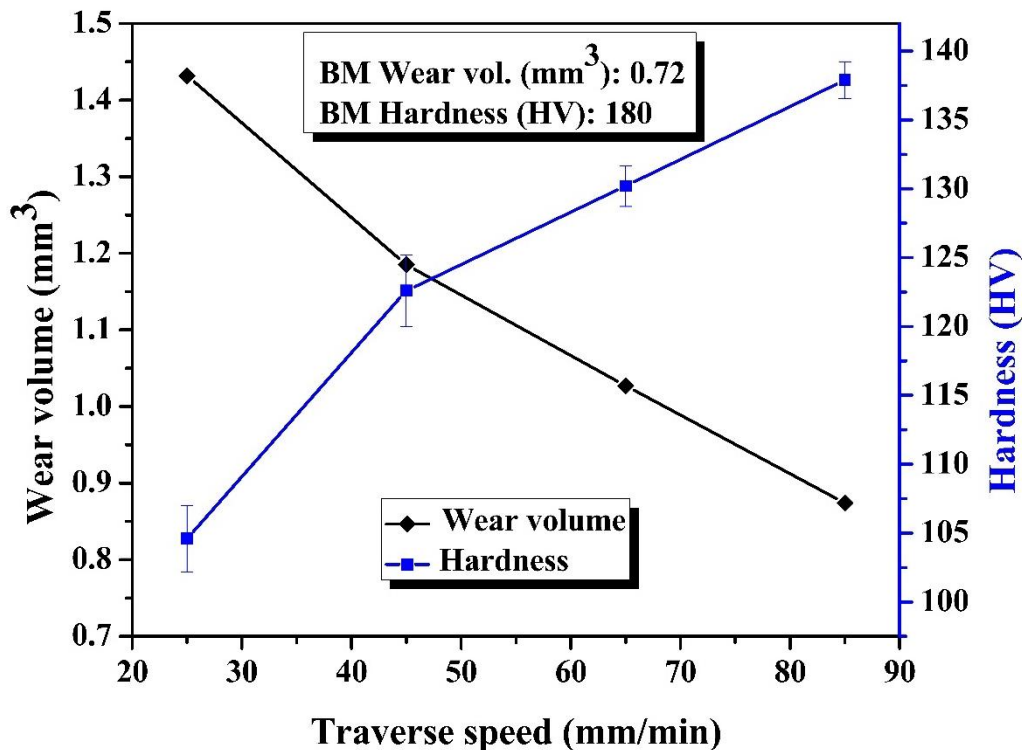


Fig. 4.10: Effect of traverse speed on wear volume of FSPed samples.

To identify the type of wear mechanisms involved, the worn surfaces of the BM and FSPed samples (Fig. 4.11) have been analyzed by SEM. Evidence of metal flow and deep grooves on the worn surface (shown in Figs. 4.11b, c) is the clear indication of the adhesive and abrasive wear. The worn surface of the BM appears comparatively smoother, and some shallow grooves are formed on them as compared to the large number of deep grooves in the FSPed samples (in Figs. 4.11b, c). It is evident that the extent of adhesive and abrasive wear in the BM decreased due to a relatively lower coefficient of friction and higher hardness value of the BM. At lower traverse speed, the degree of groove formed on the worn surfaces of the FSPed samples is quite larger and undergone severe plastic deformation. This may be due to the debris particles, which entrapped between the ball and the surface, producing deeper cut on the sliding surfaces (Fig. 4.11b). The extent of grooving in the worn surfaces of the FSPed samples is found to decrease with an increase in the traverse speed. The improvement in the wear resistance at higher traverse speed can be attributed to the enhancement of hardness due to the microstructural refinement. It is known that under abrasive wear conditions, the wear of the material is reduced with increase

in the hardness (Deuis et al., 1996). The EDS analysis was performed on the worn surface of all the samples, and the EDS results (a representative result shown in Fig. 4.11d) show almost the same results. The EDS analysis made on the worn surface shows the presence of oxygen peak indicating bit oxidation of the worn surface. A typical EDS result for the sample processed at a traverse speed of 85 mm/min is shown in Fig. 4.11d. The oxidation of the worn surface leads to further material loss from the surface of the sample (Sert et al., 2014).

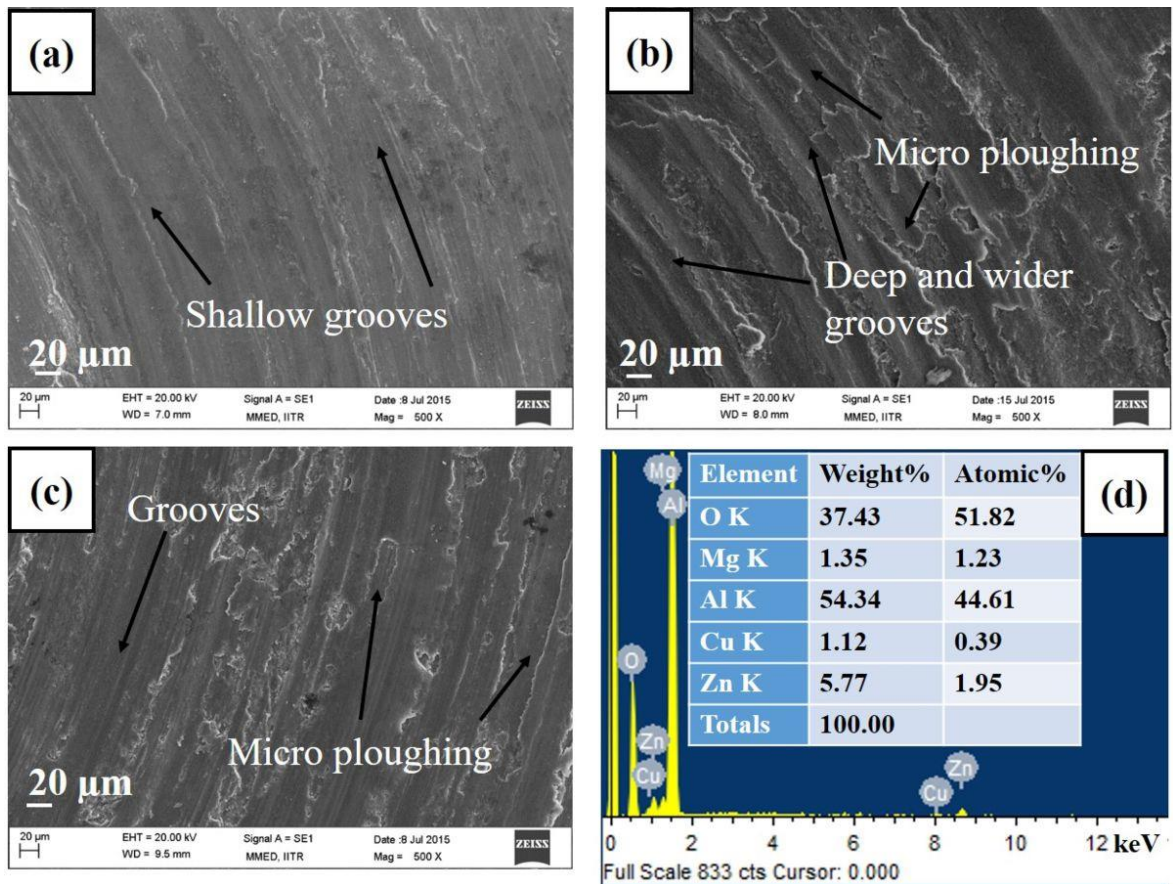


Fig. 4.11: SEM micrographs of worn surfaces of (a) BM, (b) FSPed sample at 720 rpm-25 mm/min, (c) FSPed sample at 720 rpm-85 mm/min and (d) EDS analyses of the sample FSPed at 720 rpm-85 mm/min.

4.1.4 Corrosion behavior

The potentiodynamic polarization curves of the BM and FSPed samples are shown in Fig. 4.12. The corresponding E_{corr} and i_{corr} values were acquired from the corresponding polarization curve using the Tafel extrapolation method (Fontana, 2005). Figure 4.12 shows that the corrosion resistance of the FSPed samples is inferior in comparison with that of the BM. The BM exhibited a corrosion potential (E_{corr}) of approximately -1.025 V, whereas the E_{corr} values of the FSPed

samples lie in the range of -1.05 to -1.07 V. It can be observed that the FSPed sample processed at a traverse speed of 25 mm/min shows better corrosion resistance (E_{corr} , -1.05 V) among all the FSPed specimens. This can be explained in the light of microstructural features of the corresponding sample. At lower traverse speed (25 mm/min), the grain size refinement was not very effective and average grain size produced is ~ 7 μm (Fig. 4.2a). On the other hand, very fine grain size (av. size ~ 3 μm) could be achieved when the FSP was conducted at higher traverse speed, e.g., 85 mm/min (Fig. 4.2d). Therefore, the sample processed at lower traverse speed (e.g., 25 mm/min) contains comparatively less amount of grain boundary area as compared to that of the sample processed at 85 mm/min. Hence, the overall surface reactivity decreases due to the less grain boundary area available for the relatively coarse grained sample. Therefore, it can be concluded (from Fig. 4.12) that among the FSPed samples, the corrosion resistance is superior for the sample processed at 25 mm/min. Although E_{corr} and i_{corr} values of the FSPed samples are close to each other, the BM shows significantly nobler E_{corr} value and less i_{corr} as compared to that of the FSPed samples. This implies that the BM is much resistant to corrosion than that of the FSPed samples. The inferior corrosion resistance of the FSPed samples can be ascertained to the more grain boundary structure (refinement of grain size) and alteration of precipitate morphology (Proton et al., 2013) due to high temperature involved during the FSP. The overall surface reactivity increases due to the increase in the grain boundary area (Proton et al., 2013). Thus, the fine grain structure is thermodynamically susceptible to corrode faster and leads to poorer corrosion resistance than the BM (Kim et al., 2001). It is to be noted that the main strengthening precipitates in the Al7075 alloy are η (MgZn_2 and /or $\text{Mg}_3\text{Zn}_3\text{Al}_2$) and η' $\text{Mg}(\text{Zn,Cu,Al})_2$. The TEM characterization revealed that these precipitates are coarsened and/or overaged during the FSP. Some precipitate-free zones (PFZs) along with the coarse precipitates at the grain boundary regions could be seen throughout the microstructures (Figs. 4.4b, c). The coarsening of the precipitates causes depletion of solutes from the matrix surrounding the growing precipitates, and this leads to development of solute-depleted zones (SDZs). The PFZs and SDZs are more reactive than the matrix with saturated solutes and cause more intergranular attack (Jariyaboon et al., 2010). Similar kind of corrosive behavior was also reported in friction stir welded AA7039 alloy by Sharma et al. (Sharma et al., 2012b).

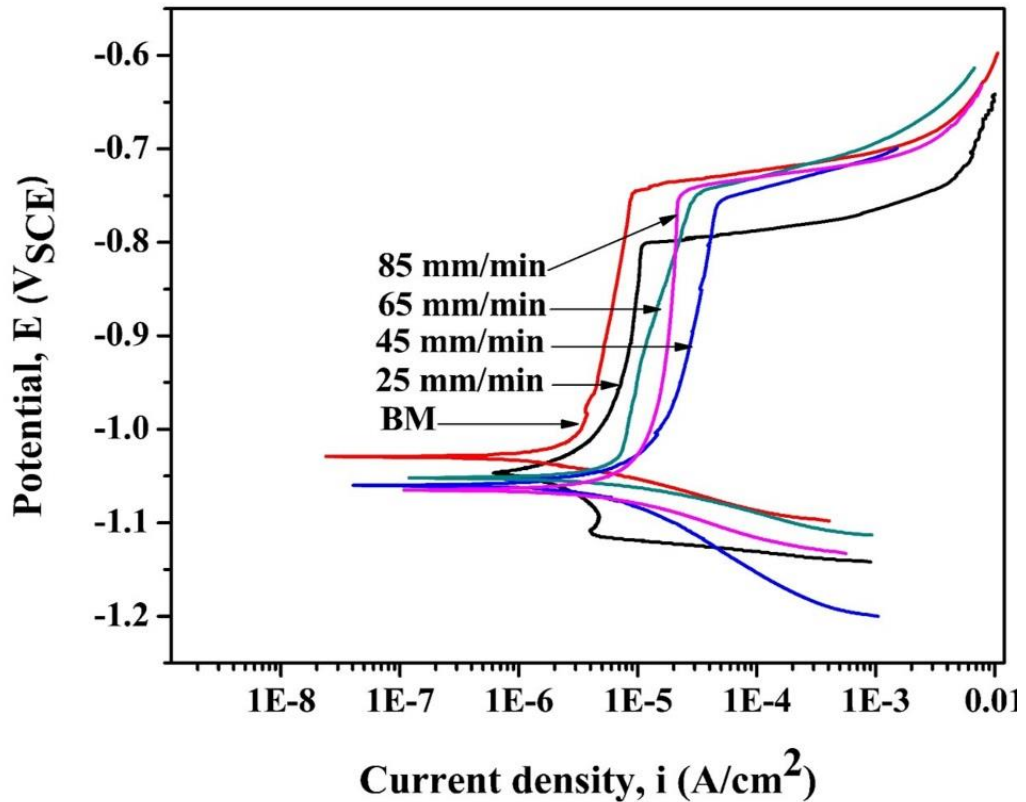


Fig. 4.12: Potentiodynamic polarization scans for BM and FSPed samples at different conditions.

Figures 4.13a and b show the corroded surface images of the BM and FSPed sample (processed at 85 mm/min) after potentiodynamic polarization test in 3.5% NaCl solution. Figure 4.13b shows that the intergranular corrosion combined with localized pitting dissolution could be the dominant corrosion mechanisms observed in the FSPed sample. On the other hand, only the pitting corrosion could be observed with no noticeable intergranular corrosion in the BM (Fig. 4.13a). The pitting occurs due to the development of local corrosion cells between the surrounding matrix and second-phase particles, which are anodic with respect to the surrounding matrix in Al7075 alloy (Liu et al., 2015). The potential difference between intermetallic phases and alloy matrix is the main driving force for the localized corrosion (Cavanaugh et al., 2014), and the η and η' precipitates in the Al7075 alloy (containing Al, Zn and Mg) are anodic relative to the surrounding matrix leading to severe microgalvanic coupling corrosion (i.e., pitting). On the other hand, the intergranular corrosion is mainly influenced by the potential difference between the matrix and grain boundary area as well as by the size and shape of the precipitate phases (Fontana, 2005). A wider PFZ always promotes propagation of the intergranular corrosion (Jariyaboon et al., 2010; Liu et al., 2015). The PFZs and coarse precipitates with different morphologies (Figs. 4.4b, c) developed in the FSPed sample might have resulted in the increased

anodic reactivity than that in the BM. Therefore, the FSPed sample was more susceptible to intergranular corrosion (Sharma et al., 2012b).

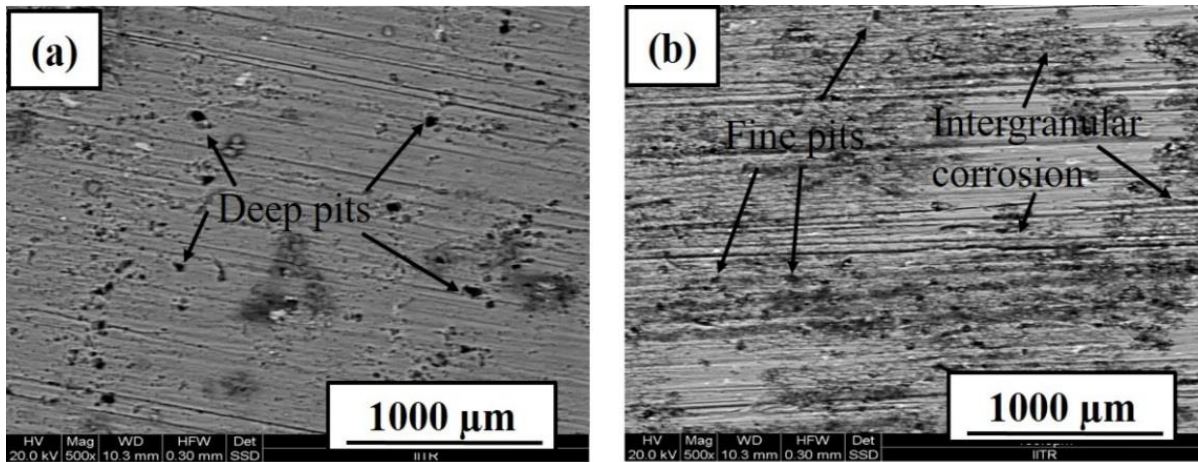


Fig. 4.13: SEM micrographs of corroded surfaces of (a) BM and (b) FSPed sample at 720 rpm-85 mm/min.

4.1.5 Summary

In this investigation, Al7075-T651 alloy plate was friction stir processed using different combination of processing parameters in order to investigate their influence on the microstructure, mechanical properties and corrosion resistance. Following conclusions can be made as the major outcome of the present study:

- a) Defect free processed zone could be produced at different traverse speed of 25-85 mm/min at a constant rotation of 720 rpm. The NZ exhibited a recrystallized fine grain structure and the average grain size decreased with an increase in the traverse speed from 25 to 85 mm/min. This is due to the lesser amount of heat input at higher traverse speed. As a result, the yield strength (as well as UTS) and hardness of the FSPed samples increased gradually with an increase in the traverse speed.
- b) After the FSP, two major observations are obtained: (i) softening of the NZ relative to the BM due to partial dissolution and/or overaging of precipitate particles and (ii) grain size refinement due to the dynamic recovery and recrystallization during the FSP. The increase in the yield strength (YS) due to decrease in the grain size could not able to offset the decrease in the strength (i.e. YS) due to the precipitate coarsening (overaging) and/or dissolution.

- c) The BM exhibited a better wear resistance as compared to that of the FSPed samples, because of the dissolution of solutes and/or overaging of precipitate particles during the FSP. The grain boundary strengthening (i.e. grain size refinement) could not able to compensate the lacking of the wear resistance due to the softening effect.
- d) The FSPed sample processed at 720 rpm-85 mm/min traverse speed was found to more susceptible to corrosion as compared to that of the BM. This is because of more reactivity of the FSPed samples due to larger grain boundary area available, dissolution of solutes and coarsening of the precipitate particles.

4.2 FSP on Al7075-2wt.% SiC composites developed by stir casting

4.2.1 Optimization of the FSP parameters for cast AMCs

In this section, effect of the FSP parameters on as cast Al7075-2wt.% SiC composites have been investigated and the parameters have been optimized to produce defect-free processed zones for the cast composites. As the concept of FSP is relatively new, therefore, initially, Al7075-T651 alloy has been exploited to optimize the process parameters in details to obtain defect-free fine recrystallized microstructure, which has been described in the earlier section 4.1. In order to optimize the FSP parameter for as cast composites, several numbers of trials have been carried out with the different combination of traverse speeds (25, 50 and 100 mm/min) and rotational speeds (720 and 1025 rpm) with a fixed tilt angle of 1.5° to the vertical axis. After each trial, for each combination of process parameters, the friction stir processed sample was cross-sectioned and inspected visually and under optical microscope. Fig. 4.14 shows macrostructures of some unsuccessful/defective FSPed samples produced due to insufficient heat input or inadequate material flow at different combination of processing parameters.

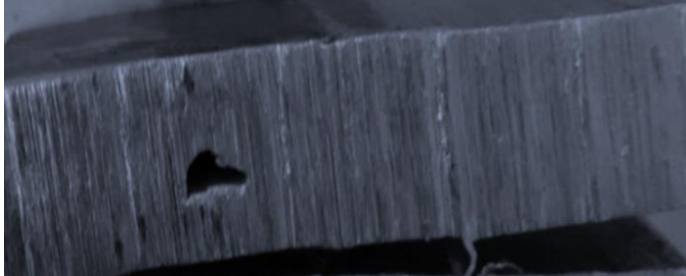



Macrostructure	FSP parameters
	Rotational speed: 720 rpm Traverse speed: 50 mm/min
	Rotational speed: 1025 rpm Traverse speed: 100 mm/min
	Rotational speed: 1025 rpm Traverse speed: 50 mm/min
	Rotational speed: 1025 rpm Traverse speed: 25 mm/min Defect free structure.

Fig. 4.14: Macrostructure of the samples at different FSP parameters.

Defects in the processed zone occurs mainly due to the improper selection of process parameters. In composite materials, reinforcement phase hinders the material flow during the processing. If process parameters are not optimum then it could also increase chances of defect formation. In the present study, i.e. the FSP of Al7075-2wt.% SiC, the optimized result in terms of defect-free processed zone (with refined microstructure) was obtained for the traverse speed of 25 mm/min at an rpm of 1025 only. This indicates that more heat input is essential for the FSP of the composites than that of the BM (i.e. Al7075 alloy). The more heat input is provided by increasing the rpm and decreasing the traverse speed of the tool. Stitched optical images of friction stir processed Al7075-2wt.% SiC microcomposite is shown in Fig. 4.15. In this case, no visual as

well as microscopic level defects were found on the surface as well as traversed section when sample was investigated under light microscope (Fig. 4.15a). Optical image of the as-cast composite is shown in Fig. 4.15c. The micrograph of the as-cast sample is characterized by the presence of dendritic structure with some casting defects, such as porosities. Fig. 4.15d clearly shows the transition zone, which distinguishes processed zone from the as cast structure. This transition zone is generally referred to as the thermomechanically affected zone (TMAZ). The TMAZ is characterized by highly distorted structure due to the stirring by tool. Fig. 4.15b shows the magnified image of the central region of the nugget zone (NZ). The significant breakdown of the dendritic cast structure could clearly be seen in the highly magnified micrograph. By comparing the micrographs of the as cast and friction stir processed composite (Figs. 4.15b and c), it can be seen that the FSP induced a significant grain refinement due to dynamic recrystallization of the as cast composite structure.

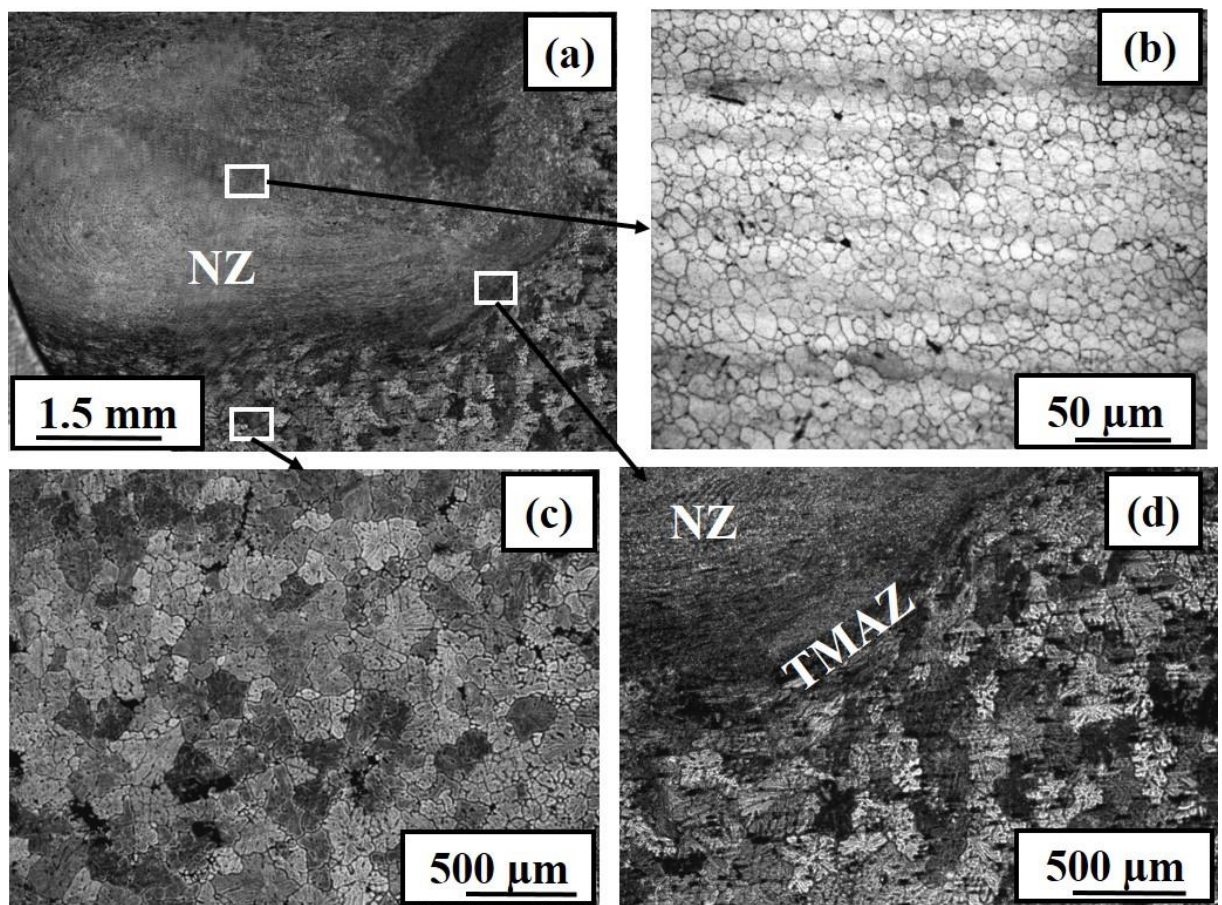


Fig. 4.15: (a) Stitched optical micrograph of Al7075-2wt.% SiC microcomposite, FSPed at 1025 rpm-25 mm/min, (b) magnified view of NZ, (c) as-cast Al7075-2wt.% SiC microcomposite and (d) TMAZ

4.2.2 FSP on stir-cast Al7075-2wt.% SiC micro- and nanocomposites

The processing parameters have been chosen in safe workable regions as per the optimized data to produce defect-free processed zone. The FSP conditions (i.e. 1025 rpm, 25 mm/min traverse speed) were kept same for both micro- and nanocomposites for comparisons of the results. Detail experimental schedules have been discussed in the experimental section. Aim of the FSP is to modify the as-cast composites microstructure thereby enhancing its mechanical strength, ductility, wear resistance and corrosion resistance simultaneously for its practical applicability. A systematic study on microstructural evolution (at mesoscale and microscale) has been evaluated by optical and transmission electron microscopy. The mechanical properties were evaluated by Vickers hardness measurements, tensile and wear testing. To analyze the mechanical properties, detailed investigation of strengthening mechanisms, such as grain size refinement, precipitation strengthening and/or Orowan strengthening and particle/matrix interface characteristics before and after FSP have been discussed.

4.2.2.1 Microstructural characterization

Figures 4.16a and b, respectively, represent the SEM and TEM images of the as-received (micron size) and ball milled (nanosize) SiC particles. It is observed that (Fig. 4.16a) the as-received SiC particles have sizes in the range of 20-60 μm . However, the TEM analysis revealed that the average particle size of the 25 h ball milled SiC powder is in the range of 30-80 nm (Fig. 4.16b). An energy dispersive x-ray spectroscopy (EDS) analysis (shown in the inset of Fig. 4.16b) has been carried out on such particles and approximate quantitative analysis of the particles shows ~54at.% carbon (C) and ~46at.% silicon (Si). The approximate stoichiometry of these elements confirms these as SiC particles. The as-received SiC powders were used to produce Al7075-2wt.% SiC microcomposite (MC2), and the nanosize SiC powders were reinforced to produce Al7075-2wt.% SiC nanocomposite (NC2) both by stir casting process. The SEM micrograph of the as-cast MC2 and NC2, respectively are shown in Figs. 4.16c and d.

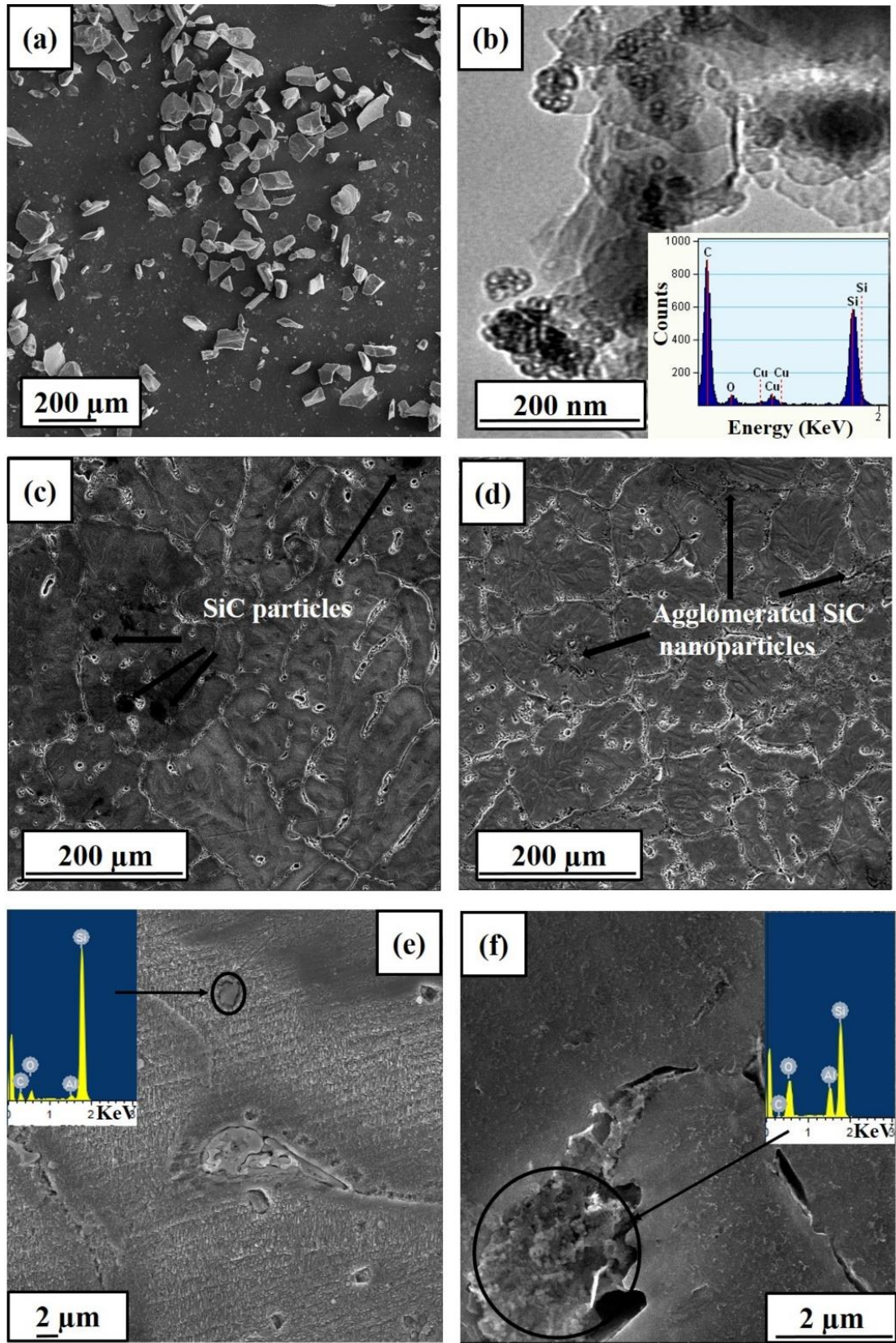


Fig. 4.16: (a) SEM image of as received SiC particles (b) TEM image of 25 h ball milled SiC particles; SEM (SE) images of the as-cast (c) MC2 and (d) NC2; magnified SEM (BSE) images of the as-cast (e) MC2 and (f) NC2.

Images shown in Figs. 4.16c & d were recorded after proper etching with the Keller's reagent. Since Figs. 4.16c & d are the images of as-cast Al7075-2wt.% SiC micro- and nanocomposites, the grain boundary is not properly developed/revealed in the as-cast state. However, it can be seen from Figs. 4.16c and d that SiC particles (both micron- and nanosize) are segregated along the interdendritic region and distribution of the particles seems to be inhomogeneous in the as-cast condition. Both the as-cast composites are observed to be a dendritic structure with some casting defects, such as porosities. Formation of the porosity in the stir cast AMCs can be accredited to the poor wettability of the reinforced particles (i.e. SiC) with the melt and air entrapment between the particles (Akbari et al., 2015). Figures 4.16e and f show the magnified SEM images with EDS analysis of the MC2 and NC2, respectively. The agglomeration of both micron and nanosize SiC particles at grain boundary area could clearly be seen in the highly magnified micrographs. The EDS peak analysis obtained from the encircled areas of the Figs. 4.16e and f also confirm the presence of SiC particles in the agglomerated form.

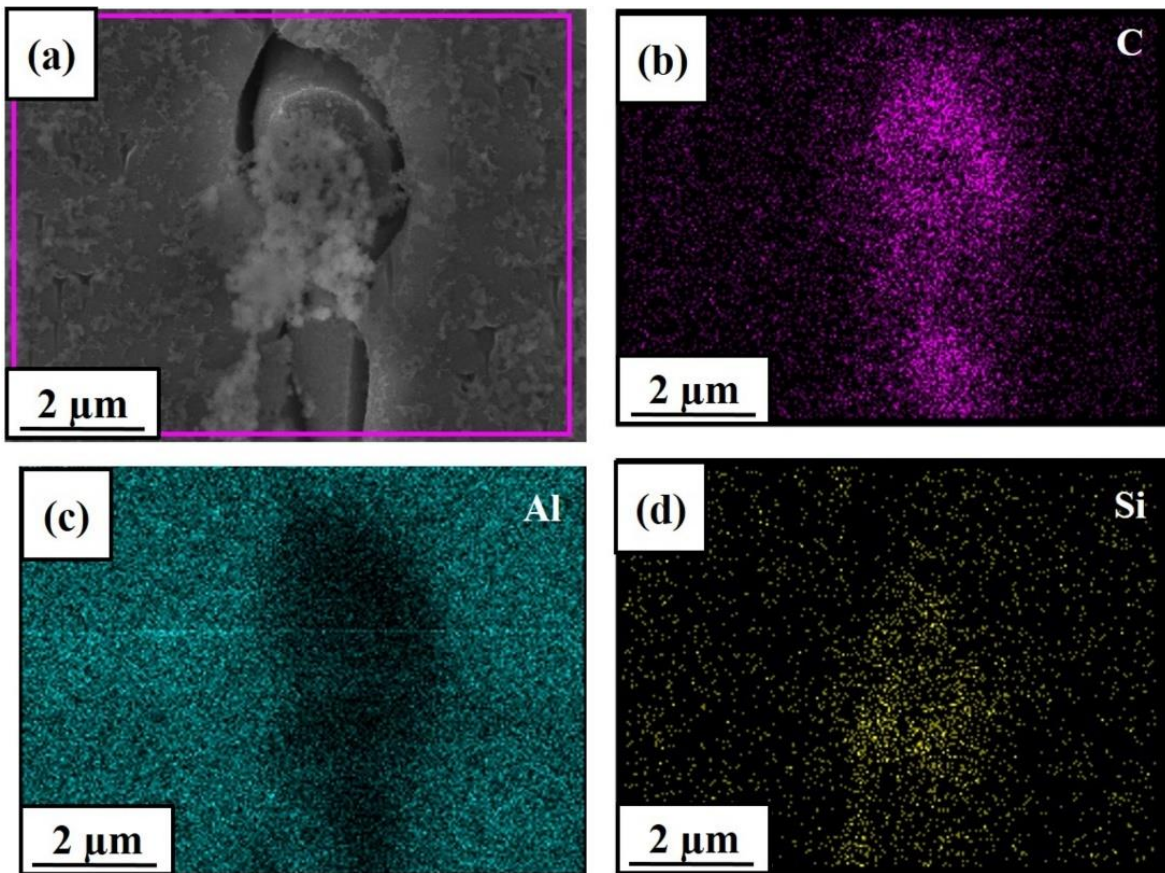


Fig. 4.17: SEM image with EDS mapping of as-cast Al7075-2wt.% SiC nanocomposite: (a) Micrograph, (b) EDS mapping of C, (c) EDS mapping of Al and (d) EDS mapping of Si.

During solidification, SiC particles are pushed ahead by solidification front, so micron- and nanosize SiC particles predominantly located in the interdendritic regions in both the as-cast composites. To identify the distribution of micron and nanosize SiC particles in the as-cast composites, SEM-EDS elemental mapping (for Al, Si and C elements) was carried out for both Al7075-2wt.% SiC micro- and nanocomposites. Figures 4.17 and 4.18 represent the microstructures along with elemental mapping for the C, Si and Al of the NC2 and MC2, respectively.

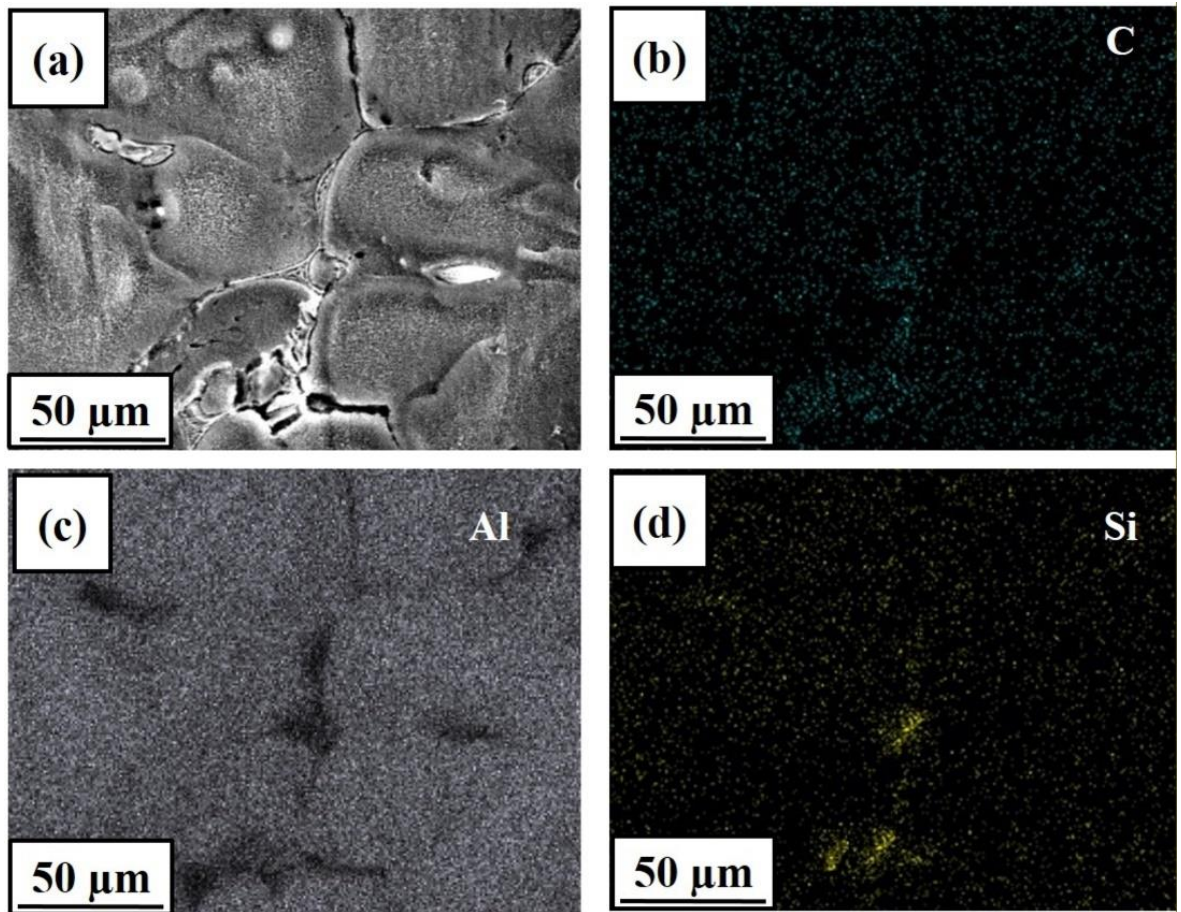


Fig. 4.18: SEM image with EDS mapping of as-cast Al7075-2wt.% SiC microcomposite: (a) Micrograph, (b) EDS mapping of C, (c) EDS mapping of Al and (d) EDS mapping of Si.

The elemental mapping shows that the distribution of C and Si are denser at grain boundary areas for both the composites, which indicates the inhomogeneous SiC particles distribution in the as-cast conditions. In Fig. 4.17, the presence of C rich zones than that of the Si may be due to the experimental factors such as C contamination from the carbon-tape used for sample mounting and adjacent $K\alpha$ lines overlapping of C, nitrogen (N) and oxygen (O) (N, O present as residual gas). The NC2 showed a quite finer grain size than that of the MC2. Average grain size of the

MC2 is $\sim 190 \mu\text{m}$ (Fig. 4.16c) in comparison to $135 \mu\text{m}$ for the NC2 (Fig. 4.16d). This can be ascribed to the existence of nanosize SiC particles in the melt, which provide more nucleation sites and consequently finer grain structure was developed in comparison to that of the MC2. Some researchers also reported similar kind of observation in their works (Ezatpour et al., 2016; Hoziefa et al., 2016; Vishwanatha et al., 2017).

In order to improve the distribution of particulates, the as-cast composites were subjected to FSP at a rotational speed of 1025 rpm and at a traverse speed of 25 mm/min. Figures 4.19a and b show the microstructures of the FSPed Al7075-2wt.% SiC micro- and nanocomposites, respectively. It can be noticed that the FSP leads to the significant breakdown of the dendritic cast structure developing a uniform dispersion of SiC particles and complete elimination of casting defect.

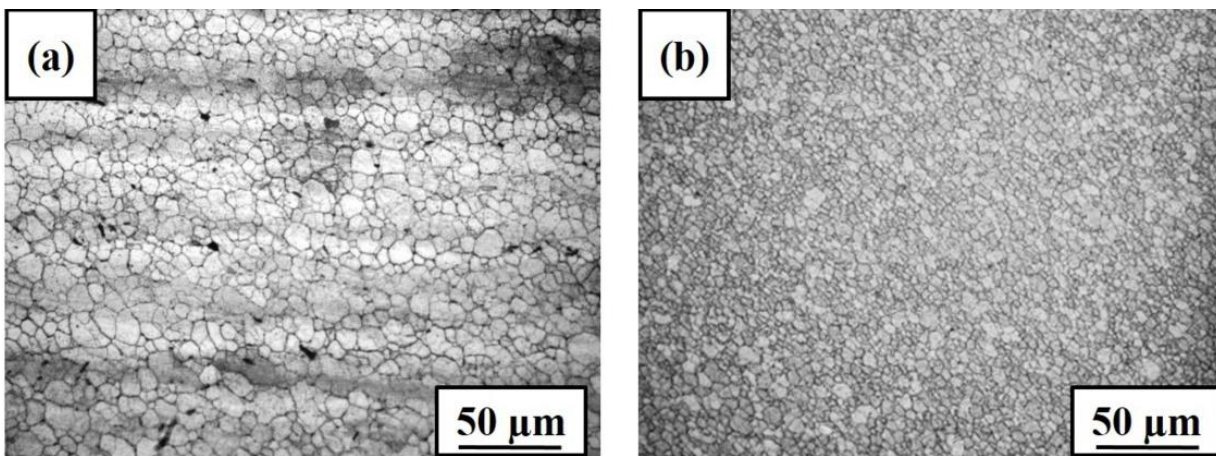


Fig. 4.19: Optical images of friction stir processed (a) Al7075-2wt.% SiC microcomposite and (b) Al7075-2wt.% SiC nanocomposite.

Figures 4.20 and 4.21 display the magnified SEM images and corresponding elemental mapping of Si, C and Al of the FSPed Al7075-2wt.% SiC micro- and nanocomposites, respectively. By comparing the EDS mapping images and the corresponding SEM image of the FSPed MC2 (Fig. 4.20), it can be seen that the micron size SiC particles are more or less evenly distributed in Al matrix after the FSP (except a large SiC particle in the central region) as compared to the cast MC2 (Fig. 4.18). On the other hand, in the FSPed NC2 (Fig. 4.21), the reinforced particles are uniformly distributed and no elemental (i.e. C and Si) rich zone has been detected. This validates homogeneous distribution of SiC nanoparticles after the FSP.

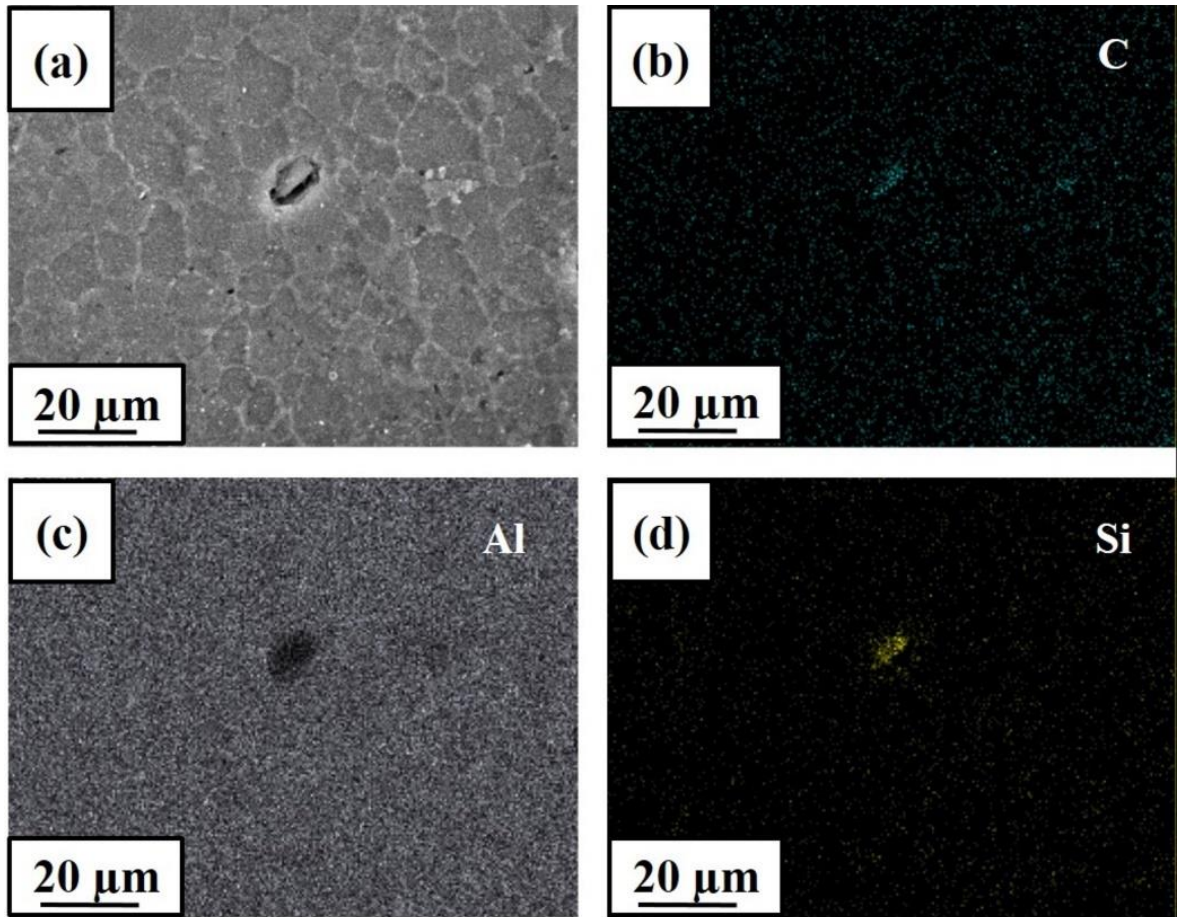


Fig. 4.20: SEM image with EDS mapping of FSPed Al7075-2wt.% SiC microcomposite: (a) Micrograph, (b) EDS mapping of C, (c) EDS mapping of Al and (d) EDS mapping of Si.

Moreover, magnified SEM images of the FSPed composites in Figs. 4.20a & 4.21a clearly reveal that the casting defects are almost eliminated after the FSP. This is attributed to the intense plastic deformation and frictional mixing, which led to the dynamic recrystallization in the nugget zone (Rajan et al., 2016; Su et al., 2005a; Yadav et al., 2015) thereby changing the microstructure. By comparing micrographs of the as-cast and FSPed composites (Figs. 4.16c,d, and Figs. 4.19a,b), a considerable decrease in the grain size could be observed for both the composites (Al7075-2wt.% SiC micro- and nanocomposite) after the FSP. The average grain size was determined from at least 200 grains from the optical micrographs (such as shown in Figs. 4.19a and b) using linear intercept method.

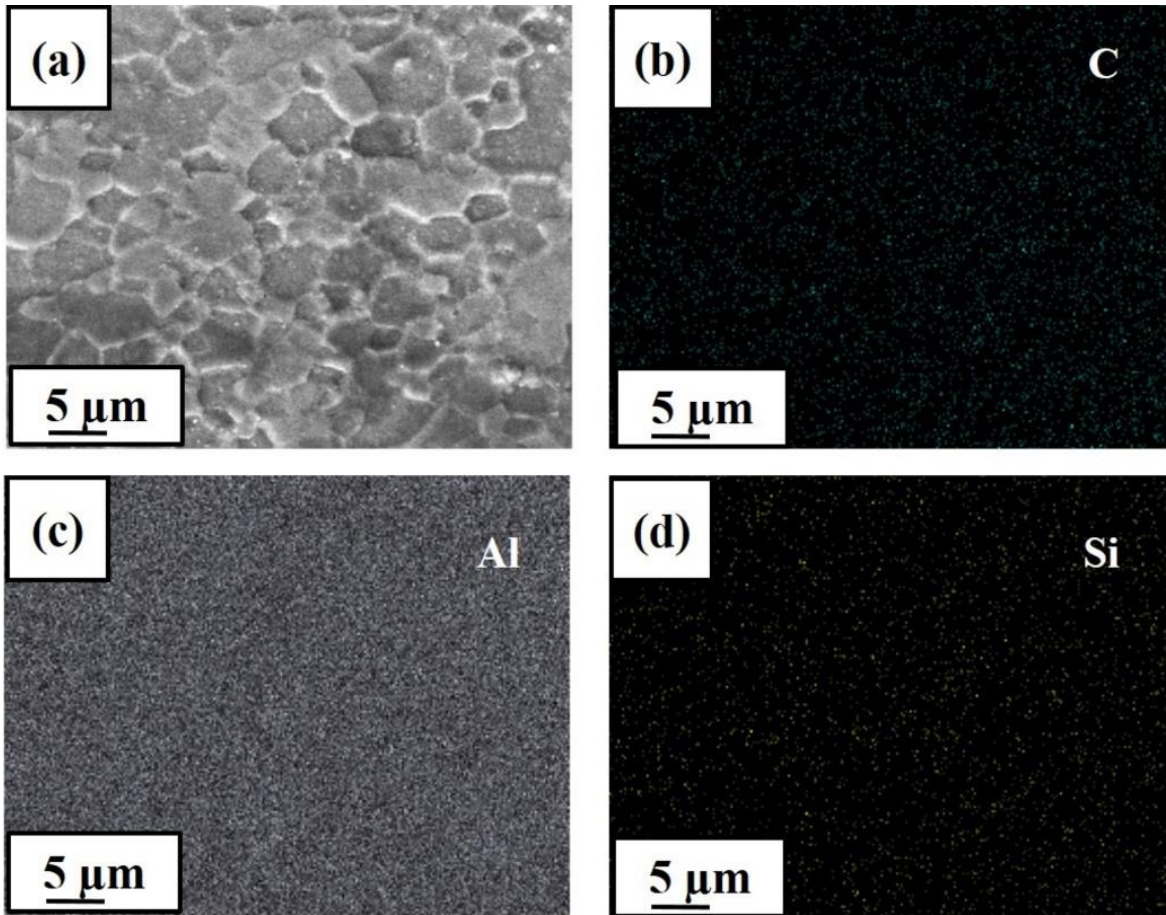


Fig. 4.21: SEM image with EDS mapping of FSPed Al7075-2wt.% SiC nanocomposite: (a) Micrograph, (b) EDS mapping of C, (c) EDS mapping of Al and (d) EDS mapping of Si.

The average grain size of the MC2 and NC2 after the FSP was found to be $\sim 9 \mu\text{m}$ and $\sim 4 \mu\text{m}$, respectively. Some researchers already reported that during FSP, the temperature of the specimen rises to approximately $470 \text{ }^\circ\text{C}$ (Mahoney et al., 1998; Mishra et al., 2005), which is greater than its (i.e. Al alloy) recrystallization temperature. At this temperature ($\sim 470 \text{ }^\circ\text{C}$), the recrystallized grains are prone to grow (Mishra et al., 2005) and develop a coarse grained structure. The SiC particles distributed in the matrix hinder the movement of dislocations as well as grain boundaries and thus restrict the grain coarsening by pinning effect (Asadi et al., 2010; Sun et al., 2011). Pinning effect of the grain boundary has been intensified further with the reduction of the particle size as the number of SiC particles increases having same weight fraction of the micron- and nanosize particles. As a result, the NC2 has developed a smaller size grains.

The microstructure of the FSPed NC2 was further examined by using TEM. The TEM allows a better understanding of the distribution, especially of the nanosize SiC particles and precipitates

formed within the matrix after the FSP of the NC2. Fig. 4.22a shows the TEM image of the Al7075-2% SiC nanocomposite after FSP. As shown in Fig. 4.22a, the matrix contains two types of second phase particles, i.e. nanosize SiC particle and precipitates, which can be differentiated by their morphologies. The second phase particles with rounded shape (produced due to ball milling) and clear contrast are identified as SiC. The average size of the SiC particles could be estimated to be ~60 nm, which was evenly distributed within the grains: segregated nanoparticles at grain boundaries have not been observed. However, elongated rod-shaped precipitates were identified as η phase (MgZn_2 and/or $\text{Mg}_3\text{Zn}_3\text{Al}_2$) (Zhou et al., 2016). These precipitates have a size between 50 to 100 nm. The formation of coarse η precipitates after the FSP and distribution of nanosize SiC particles within the Al matrix can be confirmed from the existence of extra partially revealed rings/spots in the selected area electron diffraction (SAED) pattern as indicated in Fig. 4.22b. It (Fig. 4.22b) shows typical SAED pattern corresponding to the TEM image displayed in Fig. 4.22a. The SAED pattern shows the discontinuous ring with spots of Al (220) (200) and (111) planes, and the weak diffraction spots are detected to be from SiC (103) and η (201). These results confirm that the nanoparticles (i.e. SiC) are incorporated well into the matrix of the NC2. Gazawi et al. (2015) stated a similar type of findings in the nanosize SiC particles reinforced Al matrix composite produced through powder metallurgy route.

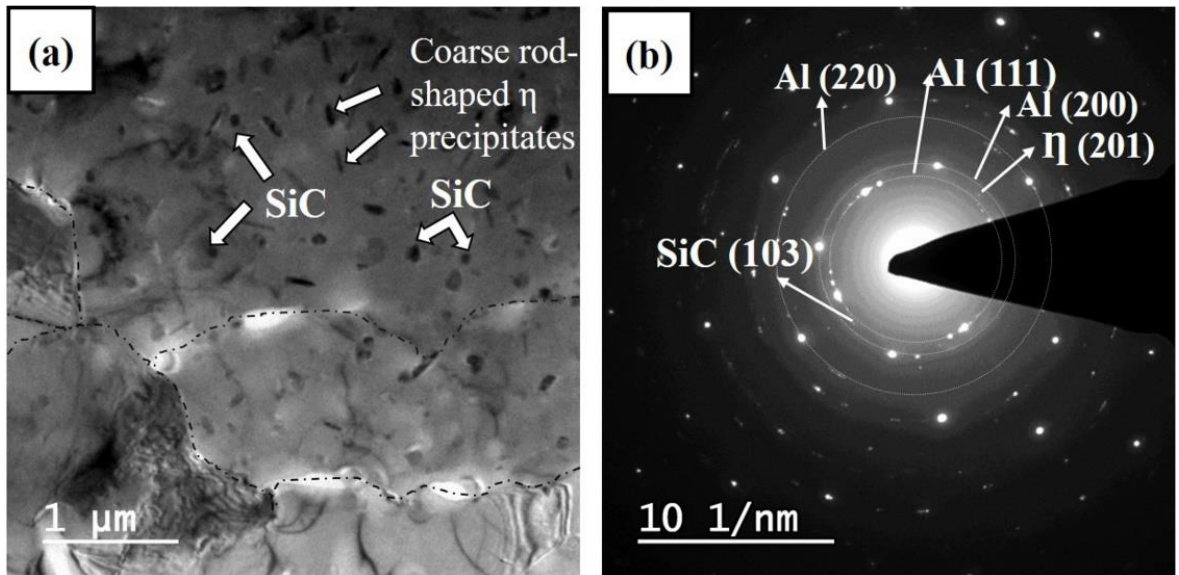


Fig. 4.22: Bright field TEM image of (a) FSPed Al7075-2wt.% SiC nanocomposite and (b) SAED pattern corresponding to the TEM image.

4.2.2.2 Mechanical properties

Mechanical behavior of the as-cast and FSPed composite samples were investigated by tensile test and Vickers hardness measurements. Fig. 4.23 demonstrates the hardness of the as-cast and FSPed composites. An average of 6 indentation measurements has been reported for each hardness value with a standard deviation in the parenthesis. The average hardness of the as-cast MC2 and NC2, respectively, are estimated to be 78 HV and 88.5 HV. The hardness value of the as-cast MC2 is found to be lower than that of the as-cast NC2. As discussed above (section 4.2.2.1), this may be due to the grain size refinement occurred in NC2 because of the more heterogeneous nucleation sites (i.e. nanoparticles) available during the solidification of it (Fig. 4.16). After the FSP, a considerable enhancement in the hardness value is obtained for both Al7075-2wt.% SiC micro- and nanocomposites, and these are found to be 101 HV and 121 HV, respectively. The increase in the hardness values is attributed to the remarkable microstructural refinement, improved homogeneity of particles distribution and closure of the microporosity by the FSP. Similar trends of the results were also reported by other researchers (Alidokht et al., 2011, 2012). Moreover, it is also noticed that the FSPed NC2 specimens have a higher hardness than that of the FSPed MC2 samples. Reinforcing the particles in the matrix leads to strengthen the material in two ways: the first one is due to the hard nature of SiC particles and the second one relates to the grain boundary pinning by the particulates (Jamalian et al., 2016), which develops fine grain structure. Grain boundary pinning is further intensified by decreasing the SiC particles size and it leads to increase in the hardness values for the NC2. The hardness of the FSPed composite is found to consistent with the corresponding grain size (Fig. 4.19) and tensile properties (shown in Fig. 4.24, discussed later). Moreover, it can be noted that in the as-cast state, the standard deviation in the hardness is noticeably higher in comparison to that of the FSPed samples. This is due to the agglomeration and non-uniform SiC particles distribution and presence of residual porosities in the cast composites.

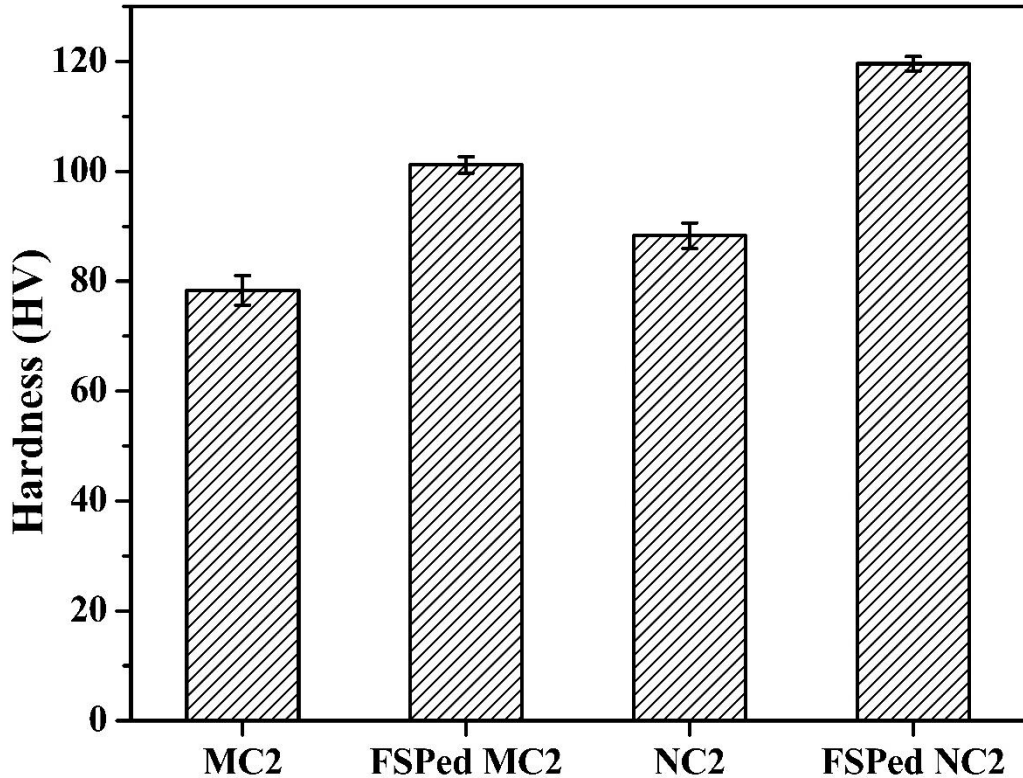


Fig. 4.23: Variation in hardness of composites in the as-cast state and after the FSP.

Fig. 4.24 shows the engineering stress–engineering strain plots for the as-cast and FSPed composite samples. At least 3 samples of each condition were tested to ensure the reproducibility of the tensile data. Fig. 4.24a shows the representative engineering stress–strain curves for the FSPed NC2 samples to indicate the variation of tensile strength of the composites. For comparison, the tensile test results of the as-cast and FSPed samples are tabulated in Table 4.1. By comparing the engineering stress–strain plots of the as-cast MC2 and NC2 samples (Fig. 4.24b), it reveals that the addition of nanosize particles by stir casting process does not show any major impact on the tensile properties, i.e., the cast NC2 sample does not indicate any significant benefit on the tensile properties over the MC2 tensile results. A slight increase in the UTS (i.e. from 111 to 139 MPa) as well as %elongation (from 1.3% to 2.2%) has been observed for the NC2 sample as compared to that of the MC2 specimen. Optimal utilization of the strengthening potential of the nanosize SiC particles (Orowan strengthening) in the as-cast condition is hindered due to the severe agglomeration nature of nanoparticles, which lead to the particle clustering and formation of porosities during solidification (Hoziefa et al., 2016).

Table 4.1: Tensile properties and Vickers hardness values of the Al7075-2wt.% SiC micro- and nanocomposites before and after the FSP. Improvement of the mechanical properties has been compared with that of the previous studies.

Materials	Processing conditions	Hardness (HV)	0.2% Proof stress (MPa)	Elongation to failure (%)	UTS (MPa)	Enhancement in UTS (%)	Ref.
Al7075-2% SiC microcomposite	As cast	78±2.7	61±9	1.3±0.3	111±12	233	Present
	FSPed	101±1.5	284±6	18.6±1.2	370±8		
Al7075-2% SiC nanocomposite	As cast	88.5±2.3	80±8	2.2±0.5	139±10	189	Present
	FSPed	121±1.3	312±5	21±1.4	402±9		
AA7075-9wt.% TiB ₂ in-situ composite	As cast	125	-	3.4	287	18.5	(Rajan et al., 2016)
	FSPed	160	-	2.5	340		
Al-5TiB ₂ in situ composite	As cast	38±7	80	11	103	49.5	(Yadav et al., 2015)
	FSPed	51±2	124	20	154		
AA2024-Al ₂ O ₃ nanocomposite	As cast	101±11	48	0.3	48	504	(Hoziefafa et al., 2016)
	FSPed	120	199±5	7.2±1.5	290±30		
In-situ TiB ₂ /AA6063 composites	As cast	-	128±20	5.7±2	187±20	47	(Ma et al., 2014)
	FSPed	-	187±15	11.8 ± 3	275±10		

After the FSP, simultaneous improvement in the mechanical strength and ductility is observed (Fig. 4.24c) for both the composites as compared to that of the as-cast state of the corresponding sample. The UTS of the NC2 is found to increase from 139 MPa (as-cast specimen) to 402 MPa (after FSP) and the %elongation increases from 2.2% to 21%. The UTS of the MC2 is found to increase from 111 MPa (as-cast specimen) to 370 MPa (after FSP) and the %elongation increases from 1.3% to 18.6%. Such improve in the mechanical strength and ductility of the FSPed Al7075-2wt.% SiC micro- and nanocomposites are highly attractive for practical applications. The enhancement of the ductility and strength simultaneously is indorsed to the combined effect of grain refinement persuaded by dynamic recrystallization during the FSP and better Orowan strengthening due to the homogenization and redistribution of the SiC particles homogeneously (Cavaliere, 2005; Sahraeinejad et al., 2015). Development of finer grains after the FSP contributes to the improvement in the strength as per Hall-Petch relation.

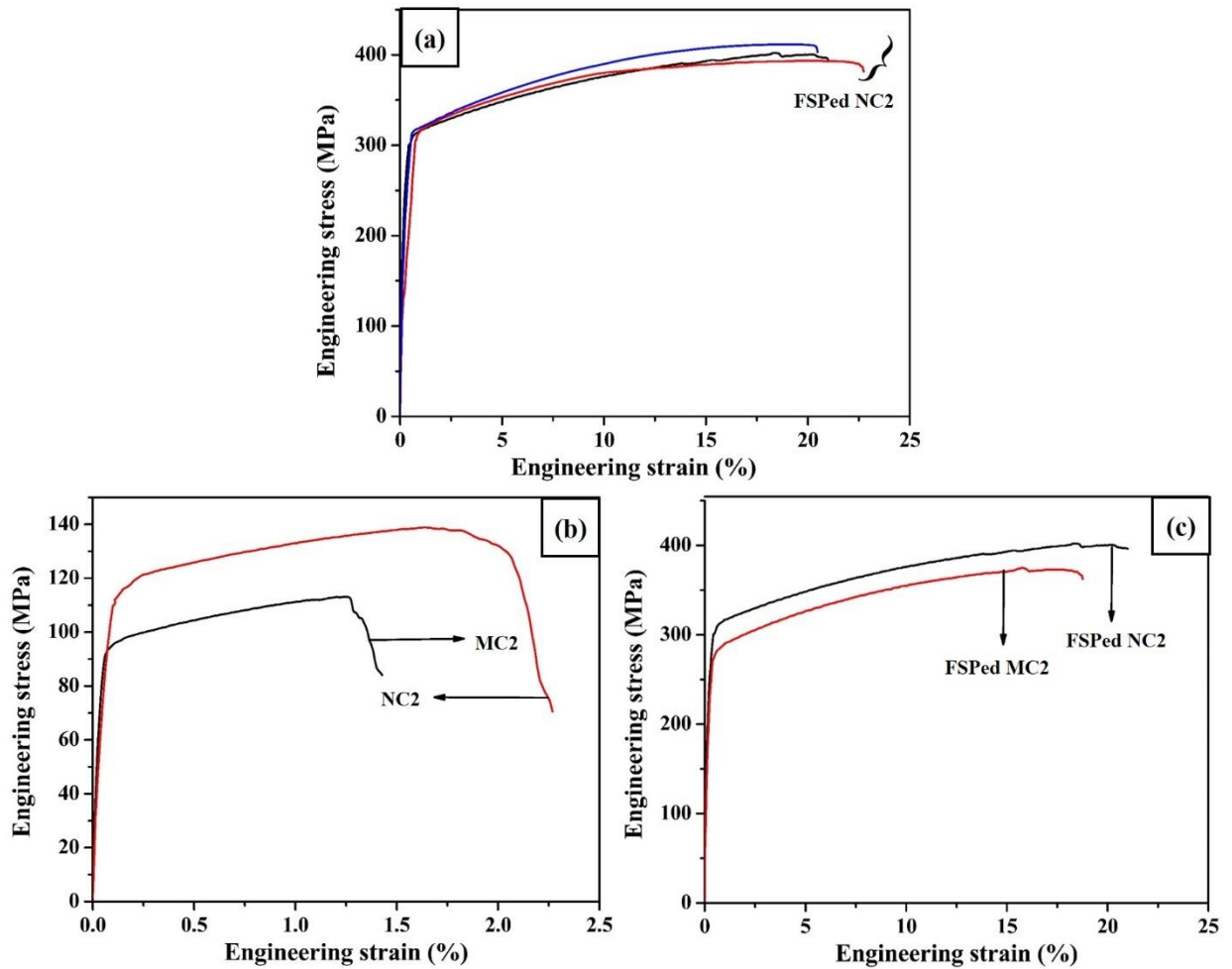


Fig. 4.24: (a) Representative stress-strain curves for the FSPed NC2 to indicate the variation of tensile strength of the composite samples; stress-strain curve of (b) the as-cast Al7075-2wt.% SiC micro- and nanocomposites and (c) FSPed Al7075-2wt.% SiC micro- and nanocomposites.

The significant improvement of the elongation to failure is ascribed to the breakage of the cast dendritic structure and development of well-defined grain structure, elimination of segregation/agglomeration of SiC particles and other casting defects. The tensile strength of the FSPed NC2 is observed to be higher in comparison to that of the FSPed MC2. This is due to the difference in the reinforcement size: for the same weight fraction of the particles, the nanosize SiC particles will have more in numbers and thereby lower inter-particle distance, which shows a strong influence on the Orowan strengthening. In addition, as discussed in the microstructural section earlier, the nanosize SiC particles impede the grain growth during FSP developing smaller size recrystallized grains.

Fractography study after the tensile tests was conducted using SEM to relate the type of fracture mode under uniaxial loading. Fig. 4.25 shows the fractographs of the as-cast and FSPed samples.

The fractured surface of the as-cast composites (both micro- and nanocomposite in Fig. 4.25a,b), exhibited a dendritic structure, lack of matrix continuity and presence of associated porosities. It is widely accepted that the existence of such type of defects restricts the plastic deformation capability of the matrix strongly (Hoziefa et al., 2016; Shen et al., 2016). The low elongation to failure, as seen in the stress-strain curve (Fig. 4.24b), is the consequence of the premature fracture due to the debonding in the particle/matrix interface. As a result, the composites behave like brittle materials. In fact, dimples are not observed from the fractured surface. However, a completely different fractured morphology could be observed after the FSP of the composites (Figs. 4.25c,d). The fractured surface of the FSPed composites shows deep and well-defined dimples, which are concomitant to the modified SiC particles distribution within the matrix, formation of recrystallized grains with refined morphology and elimination of porosities. In addition, a noticeable change in the dimples size can be observed between the FSPed Al7075-2wt.% SiC micro- and nanocomposites. The dimples are coarser in the FSPed MC2 (Fig. 4.25c) as compared to that of the FSPed NC2 (Fig. 4.25d). The void size is found to decrease in case of the FSPed NC2 (Fig. 4.25d) due to the existence of refined grain structure and reinforcement of the nanosize SiC particles. Such microstructural changes possibly reduced the possibility of premature failure, which led to the enhanced ductility and strength of the FSPed composites (Yang et al., 2015) in comparison to that of the as-cast structures. It can be noticed that the overall fractured morphology of the FSPed samples does not show any interdendritic debonding, major cracks and microporosity. Thus, the brittle appearance fracture mode in the as-cast condition is shifted to the ductile dominated fracture after the FSP of the composites.

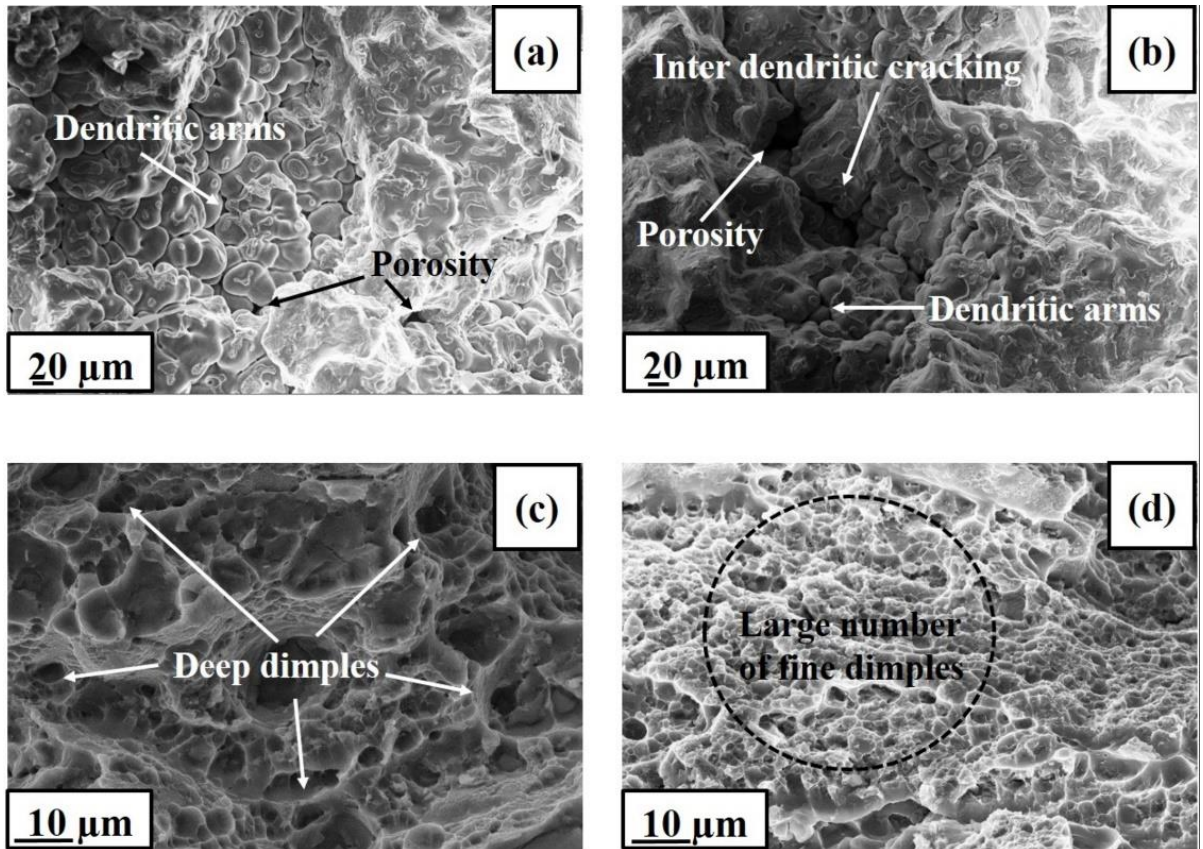


Fig. 4.25: SEM micrographs of the tensile fracture surface of (a) as-cast Al7075-2wt.% SiC microcomposite, (b) as-cast Al7075-2wt.% SiC nanocomposite, (c) FSPed Al7075-2wt.% SiC microcomposite and (d) FSPed Al7075-2wt.% SiC nanocomposite.

4.2.2.4 Wear characteristics

Tribological properties are extremely important for the composite materials. Hence, to evaluate the tribological behavior of the as-cast and FSPed composites, pin-on-disc wear tests were conducted. Fig. 4.26 indicates the change in weight loss of the MC2 and NC2, before and after the FSP. The as-cast MC2 specimen shows comparatively higher weight loss than that of the other samples. It could be noted (from Fig. 4.26) that the wear loss of the as-cast NC2 specimen is slightly lower as compared to the as-cast MC2 specimen, which corresponds to better wear resistant of the NC2. The enhancement in the wear resistance of the as-cast NC2 is ascribed to the development of finer grains than that of the cast MC2 (as discussed in the microstructural section, Fig. 4.16). Furthermore, incorporation of SiC nanoparticles into the matrix leads to the reduction of the real (actual) contact area. These changes in the microstructure substantially influence the wear behavior of the composites. The enhancement of the wear resistance could also be ascribed to the enhancement of the hardness due to the modification of the microstructure.

The obtained result is in agreement with the trend observed for the hardness values of the corresponding specimens (Fig. 4.23). Besides, as could be noted from Fig. 4.26, the wear loss of the as-cast composites is reduced considerably after the FSP. The vast reductions in the wear loss of the FSPed composites as compared to that of the as-cast materials can be ascribed to the better dispersion of the hard micron- and nanosize SiC particles within the matrix and proper bonding (Alidokht et al., 2012; Rajan et al., 2016; Rejil et al., 2012). Uniform dispersion of the SiC particles reduces the real (actual) contact area between the sample and the counter body, thereby improving the dry sliding wear properties. Such beneficial effect is further increased owing to the reinforcement of SiC nanoparticles in the matrix.

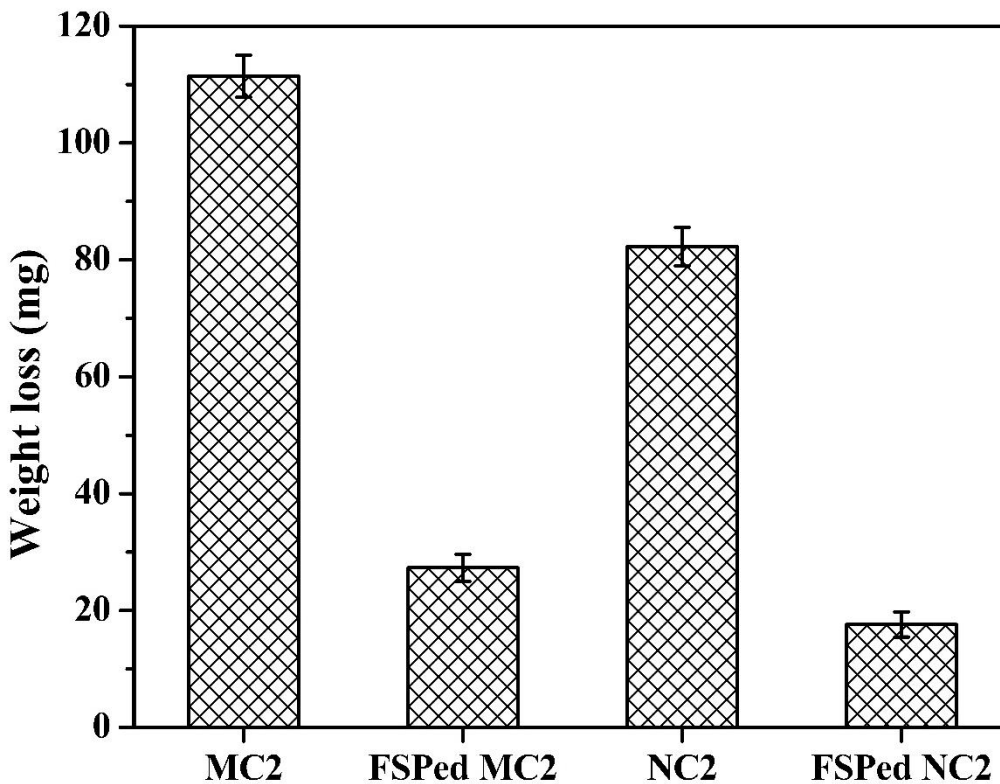


Fig. 4.26: Variation in weight loss of composites in the as-cast state and after the FSP.

The worn surfaces of the as-cast and FSPed composites were analyzed under SEM to recognize the type of wear mechanisms involved. Figs. 4.27a & b, respectively, show the SEM images of the worn out surfaces of the as-cast Al7075-2wt.% SiC micro- and nanocomposite samples. As illustrated, the as-cast composites exhibit plastic deformation bands along the direction of the sliding and partial irregular pits, which are the clear evidence of the abrasive and adhesive wear. The removal of particles cluster from the matrix during sliding creates pits. Microstructural inhomogeneity and poor particle-matrix interface characteristics are responsible for the pit

formation. Figures 4.27c,d show the worn surfaces of the FSPed Al7075-2wt.% SiC micro- and nanocomposite samples. The worn surfaces are appeared comparatively smoother and are comprised of some shallow grooves with a slight plastic deformation on the grooves' edges. No craters are evident on the worn out surfaces owing to the uniform SiC particles distribution within the matrix. These results indicate that the wear mode gradually has modified to abrasive wear from the adhesive type. The enhancement in the wear resistant behavior of the FSPed composites can be ascribed to the improvement in the hardness values due to the refinement of matrix structure, uniform SiC particles distribution after the FSP, increase the bonding between matrix and particles and elimination of the casting defects such as porosities. It is widely known that with increasing the hardness value, wear loss of the material decreases under abrasive wear conditions (Alidokht et al., 2012).

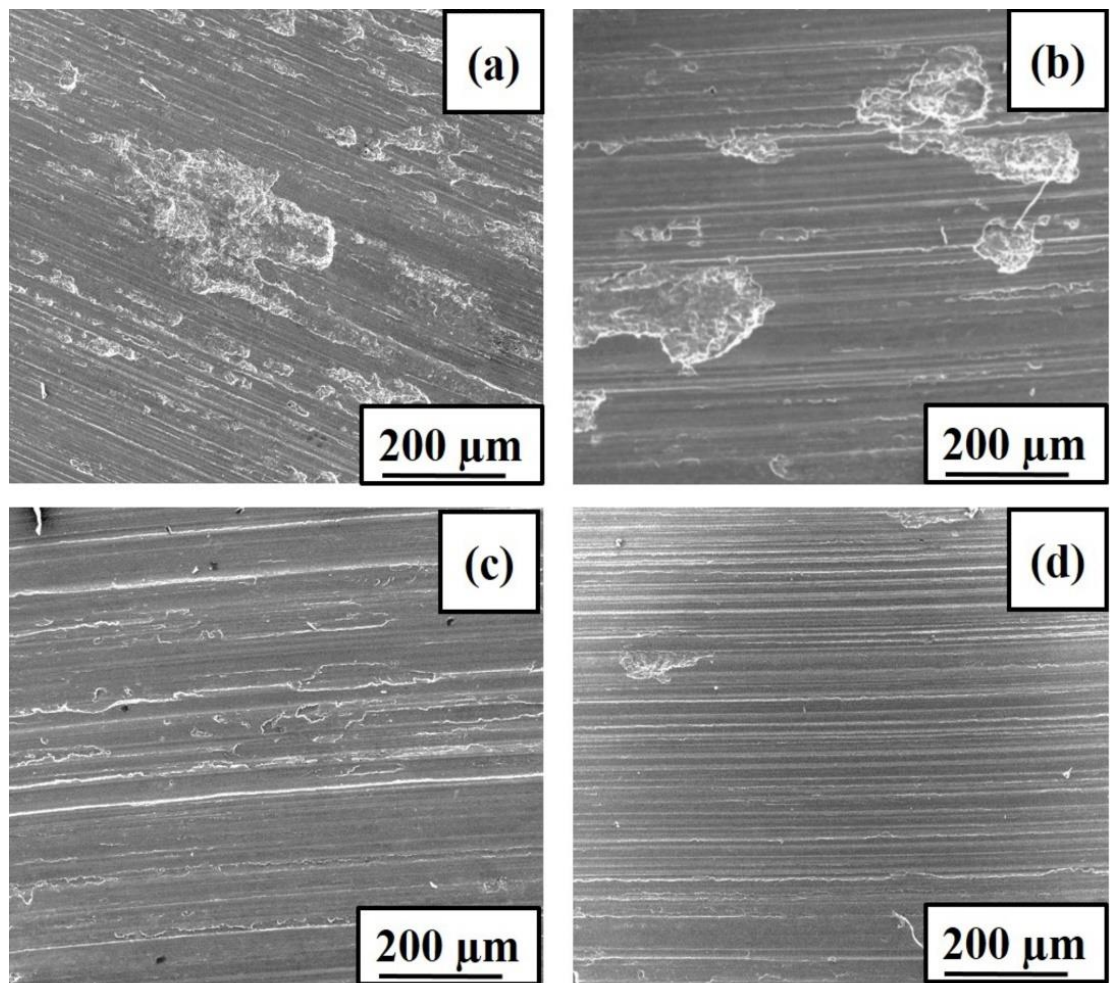


Fig. 4.27: SEM micrographs of the worn surface of (a) as-cast Al7075-2wt.% SiC microcomposite, (b) as-cast Al7075-2wt.% SiC nanocomposite, (c) FSPed Al7075-2wt.% SiC microcomposite and (d) FSPed Al7075-2wt.% SiC nanocomposite.

4.2.5 Corrosion behavior

The electrochemical polarization curves for the as-cast and FSPed composites are displayed in Fig. 4.28. Tafel extrapolation method was used to determine the values of corrosion current density (i_{corr}) and the corrosion potential (E_{corr}) from the corresponding polarization plots (Fontana, 2005). The pitting potential (E_{pit}) has been calculated from the anodic polarization curves of the corresponding polarization plots. Table 4.2 summarizes the various electrochemical parameters obtained from the Tafel plots (Fig. 4.28).

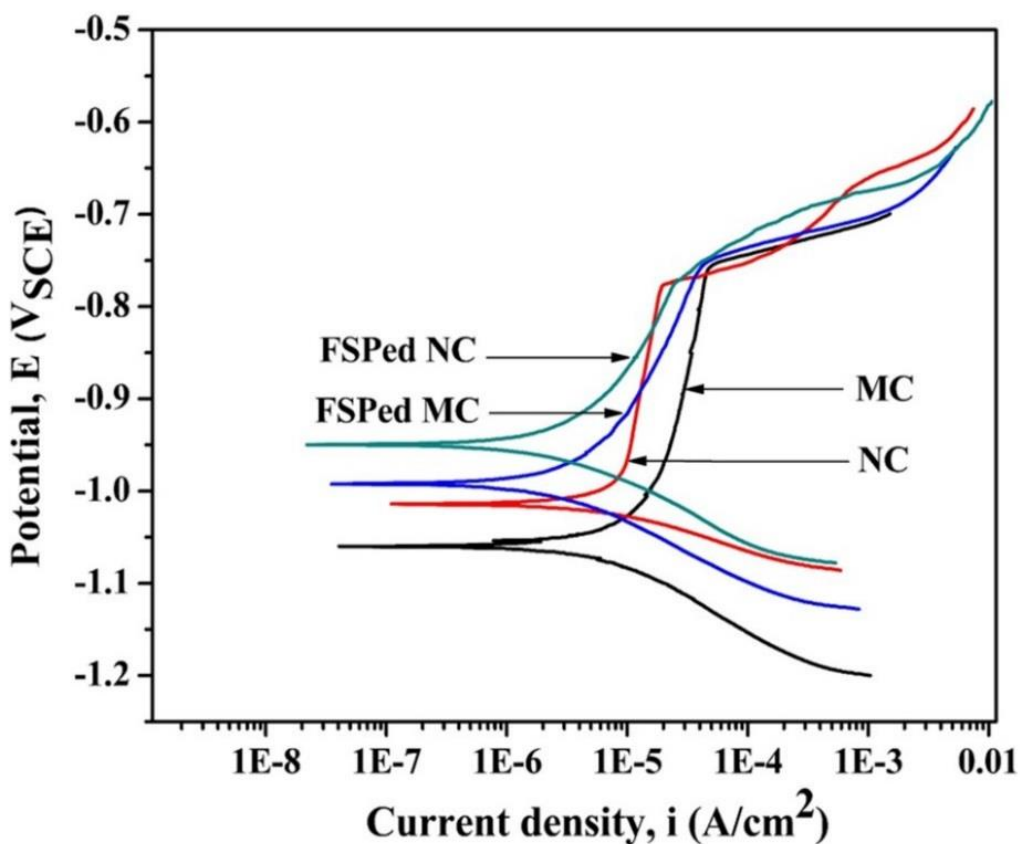


Fig. 4.28: Potentiodynamic polarization curves for the as-cast and friction stir processed Al7075-2wt.% SiC micro- and nanocomposites.

The E_{corr} values of the as-cast MC2, as-cast NC2, FSPed MC2 and FSPed NC2 samples are found to be -1060 mV, -1010 mV, -992 mV and -950 mV, respectively. Moreover, the i_{corr} is determined to be 12.4 , 7.46 , 3.86 and 2.52 μAcm^{-2} , respectively, for the as-cast MC2, as-cast NC2, FSPed MC2 and FSPed NC2 samples. The corresponding E_{pit} values are found to be -758 mV, -776 mV, -755 mV and -750 mV, respectively, for the as-cast MC2, as-cast NC2, FSPed MC2 and FSPed NC2 samples. It is found that (Fig. 4.28) the corrosion potentials of both the micro- and nanocomposite samples in the as-cast condition are very high. This could be due to

the microstructural inhomogeneity and poor particulate-matrix interface characteristics. This type structure is very common in the cast AMCs and facilitates pit initiation which promotes corrosion (Nunes et al., 1995). The slightly improved corrosion resistance of the as-cast NC2 could be ascribed to the presence of more number of inert SiC particles as compared to that of the as-cast MC2 (as for the same volume fraction of the reinforcement, nanosize SiC will have larger numbers than that of the micron size SiC). Therefore, the nanosize inert SiC particles could cover reasonably more active metallic surface area opened to the corrosive solution and leading to interruption of the continuity of the matrix channels. So, effectively a less active surface area would be available for the corrosion to occur, which could practically lead to less corrosion for the NC2 samples. The enhancement in the corrosion resistance of the AMCs due to the reinforcement of smaller size SiC particles was also reported previously by some researchers (Mahmoud et al., 2012; Zakaria, 2014). It can be seen from Fig. 4.28 that the E_{corr} of both the micro- and nanocomposite samples were shifted towards noble direction after the FSP. This can be explained in the light of the microstructural features of the corresponding sample after the FSP. As discussed earlier, during FSP, intense heating and frictional mixing refine the microstructure and remove the inherent casting defects (such as porosity, particle clustering and non-uniform distribution of reinforcement) from the as-cast structure. The FSP leads to the uniform SiC particles distribution, decreases surface porosities and enhances the bonding between particle-matrix interfaces. Most importantly, the FSP leads to a substantial grain size refinement. In this work, the grain size (average) reduced to $\sim 9 \mu\text{m}$ and $\sim 4 \mu\text{m}$ (Fig. 4.19) for the MC2 and NC2, respectively. The Cl^- concentration/grain boundary area is reduced for the fine-grained structure of the same material due to the increase in the grain boundary area as compared to its coarse-grained counterpart (Inturi et al., 1992; Kumar et al., 2015). Thus, it leads to the lesser current density. These microstructural changes reduce the driving force for corrosion and promote the formation of a uniform and strongly adhering passive layer, which leads to the enhancement of the corrosion resistance. Such beneficial effect is further improved by decreasing the reinforced particles size as observed in this work as well as reported in other work (Mosleh-Shirazi et al., 2015). The obtained result is consistent well with that reported by Singh et al. (Singh et al., 2016) for the ultrafine grained Al2024 alloy processed through cryoforging. Moreover, the reduction of the surface porosities and proper particle-matrix interface bonding after the FSP also can increase the corrosion resistance.

Table 4.2: Electrochemical parameters obtained from Tafel plots of both the as-cast and FSPed composites.

Materials	conditions	E_{corr} (mV)	i_{corr} (μAcm^{-2})	E_{pit} (mV)	OCP (mV)
Al7075-2% SiC microcomposite	As cast	- 1060±9	12.4±2.3	- 758±5	- 949
	FSPed	- 992±5	3.86±1.5	- 755±8	- 877
Al7075-2% SiC nanocomposite	As cast	- 1010±10	7.46±2.8	- 776±5	- 835
	FSPed	- 950±5	2.52 ±1.2	- 750±10	- 827

4.2.6 Summary

In this work, Al7075 alloy composites reinforced with 2wt.% micron- and nanosize SiC particles were manufactured by stir casting route. After that, the FSP was used as a secondary processing technique to modify the cast microstructures with the aims to improve the mechanical properties and corrosion resistance of the stir cast composites simultaneously. The major outcomes of this work could be concluded as follows:

- a) Al7075 alloy based micro- and nanocomposites (2wt.% SiC reinforcement) were successfully manufactured by stir casting route. The cast composites, both micro- and nanocomposites, showed poor mechanical strength and very low level of ductility due to the presence of dendritic structures, inhomogeneously distributed SiC particles along interdendritic regions and casting defects such as porosities in the matrix.
- b) The FSP led to modify the cast microstructure into uniformly distributed SiC particles within the matrix of refined grain structure with reduced casting defects. Thus, the vast improvement of the tensile strength (~190%) and elongation (854%) simultaneously for the FSPed nanocomposite (as compared to that of the as-cast counterpart) are mainly due to the microstructural modification arisen after the FSP. The strengthening mechanisms involved in such composite structures are analyzed to be the grain boundary strengthening (i.e. Hall-Petch strengthening), Orowan strengthening through nanosize particle reinforcement and precipitation hardening (η phase).

- c) The FSPed NC2 showed superior wear resistance in comparison to that of the as-cast state of the same. This is ascribed to the improved hardness, refined matrix grain size, uniform distribution of nanosize SiC particles and enhanced bonding between the particles-matrix interface.
- d) Corrosion potentials (i.e. E_{corr}) of the Al7075-2wt.% SiC micro- and nanocomposite samples were shifted towards noble direction after the FSP. This can be ascribed again to the modification of the microstructural features comprising with a uniform distribution of SiC particles, reduced surface porosities, refinement of grain size and increased particles-matrix interface bonding characteristics after the FSP. Such beneficial effects became more intense (i.e. shifting towards more noble E_{corr}) when the particle size (reinforced in the composite) decreased from micron to nanometer scale.

4.3 Cryo-FSP on Al7075 alloy and its analysis

The FSP has been established as a generic tool as well as technique for microstructural modification and material processing, as it could provide more intense plastic deformation as well as higher strain rates than other SPD methods. However, the FSP of heat treatable aluminum alloys is reported to deteriorate strength properties in spite of huge grain size refinement due to coarsening or dissolution of the strengthening precipitate(s). To overcome these constraints, present work investigates an effective way of heat rejection from the processing zone of solutionized Al7075 alloy plate to control the precipitate evolution besides the grain size refinement during FSP. The FSP was carried out with standardized process parameters (i.e. 720 rpm, 65 mm/min traverse speed) under two different cooling environments: (i) at normal air cooling (NAC) and (ii) in-process cryocooling (IPC), which is achieved by rushing a chilled mixture ($-30\text{ }^{\circ}\text{C}$) of liquid nitrogen and methanol through the bottom surface of the backing plate. Detail experimental schedules have been discussed in the experimental section. Figure 4.29 shows the schematic illustration of the in-process cryocooling FSP experimental setup with FSPed sample. Microstructural evolution was examined through optical, scanning and transmission electron microscopy and electron backscatter diffraction to confirm the grain size and morphology of precipitate(s) formed. Tensile test and Vickers hardness measurement were used to evaluate the effects of IPC during FSP of the samples. The results have been analyzed in

terms of working temperature, strain rate, Zener–Holloman parameter Z , precipitate interface characteristics and its strengthening effect, Hall–Petch strengthening due to grain size reduction and trade-off between them.

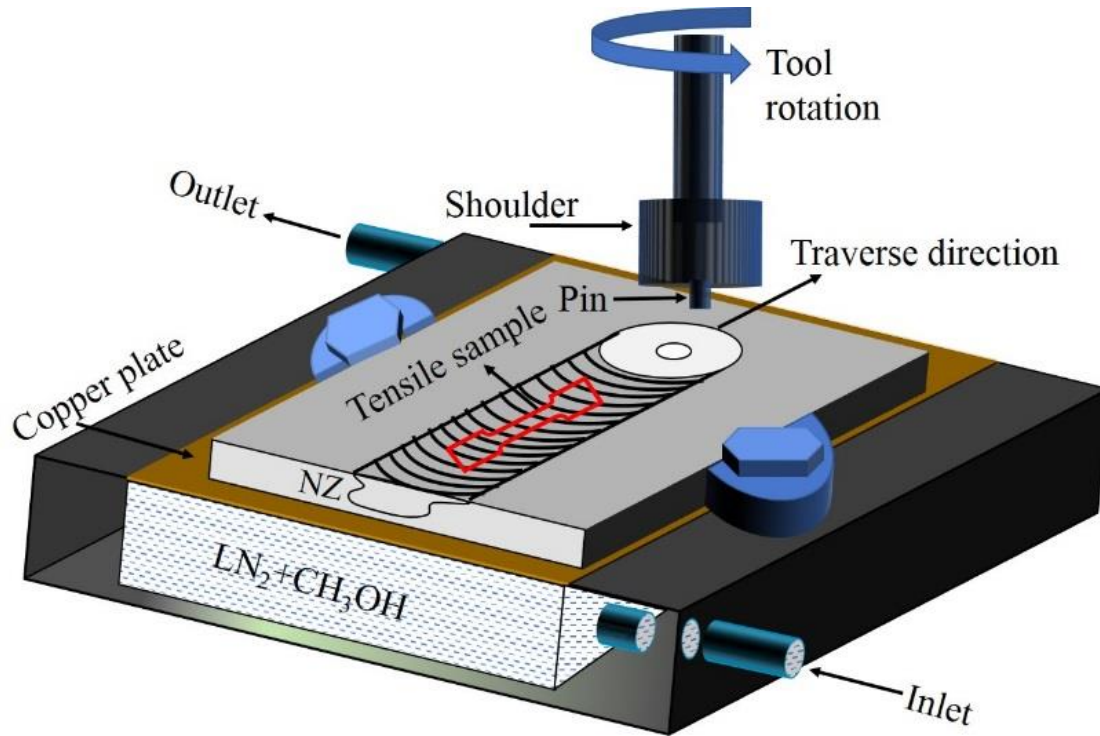


Fig. 4.29: Experimental setup used in this study along with surface appearance of the samples after FSP: (a) normal air cooled (b) in-process cryocooled.

4.3.1 Microstructural characterization

Figure 4.30 illustrates the optical images from cross-sections parallel to the rolling direction of the solution treated (ST) and the FSPed samples of Al7075 alloy, both in the NAC and IPC conditions. The ST-Al7075 alloy samples have exhibited large size elongated grains showing a typical rolled structure (Fig. 4.30a). Moreover, black irregular-shaped spots present in the microstructure are likely to be Al-Cu intermetallic containing iron- and silicon (i.e. Al_7Cu_2Fe , $Al_{12}Fe_3Si$), which are very resistant to dissolution as also reported in literature (Ayer et al., 1985; Orozco-Caballero et al., 2016; Rometsch et al., 2014). Figures 4.30b and c show microstructures of the nugget zone (NZ) for the normal and in-process cryocooled FSPed samples, respectively. It is evident that microstructures in the NZs of both the FSPed conditions were significantly refined as compared to that of the ST sample. Intense plastic deformation and high frictional heating during the FSP led to the dynamic recrystallization in the NZs thereby large amount of

grain refinement occurred (Mishra et al., 2005; Su et al., 2005a). In order to observe the microstructural details in the NZs of the FSPed samples, EBSD analysis was carried out for both type of samples.

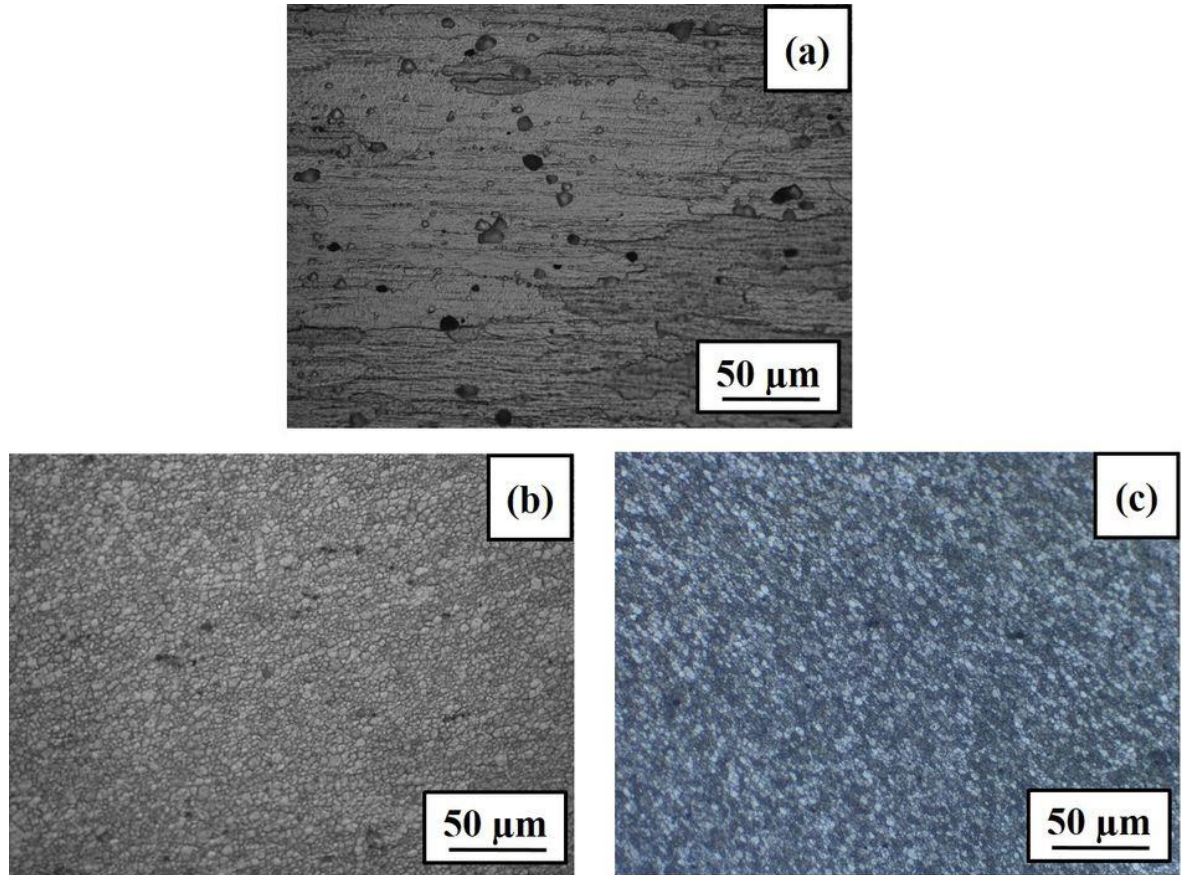


Fig. 4.30: Optical micrographs of the (a) ST base metal, (b) FSPed sample with NAC and (c) FSPed sample with IPC.

Figures 4.31a and b depict the IPF (inverse pole figure) EBSD maps along with distribution of grain size as a function of area fraction, respectively, for the normal and in-process cryocooled FSPed samples. The various color contrast in the EBSD maps are related to different orientations of the grains (Chakrabarty et al., 2014). The average grain size of the sample, processed with IPC setup was found to be 2.4 μm as compared to 4.7 μm for the FSPed sample with NAC condition. From grain orientation spread chart (Fig 4.31), it could be seen that after the FSP (NAC state) nearly 50% of the grains have misorientation less than 3 degrees indicating very low disorder inside the grains, which is a characteristic of a recrystallized grain. In case of IPC condition, 67% of grains have GOS misorientation of less than 3 degree. With more strain and at moderate temperatures (IPC condition), these deformed grains further increase their boundary

misorientation by recovering the grain interiors along with secondary processes like strain induced boundary migration to develop final grain structure and texture (Sakai et al. 2014).

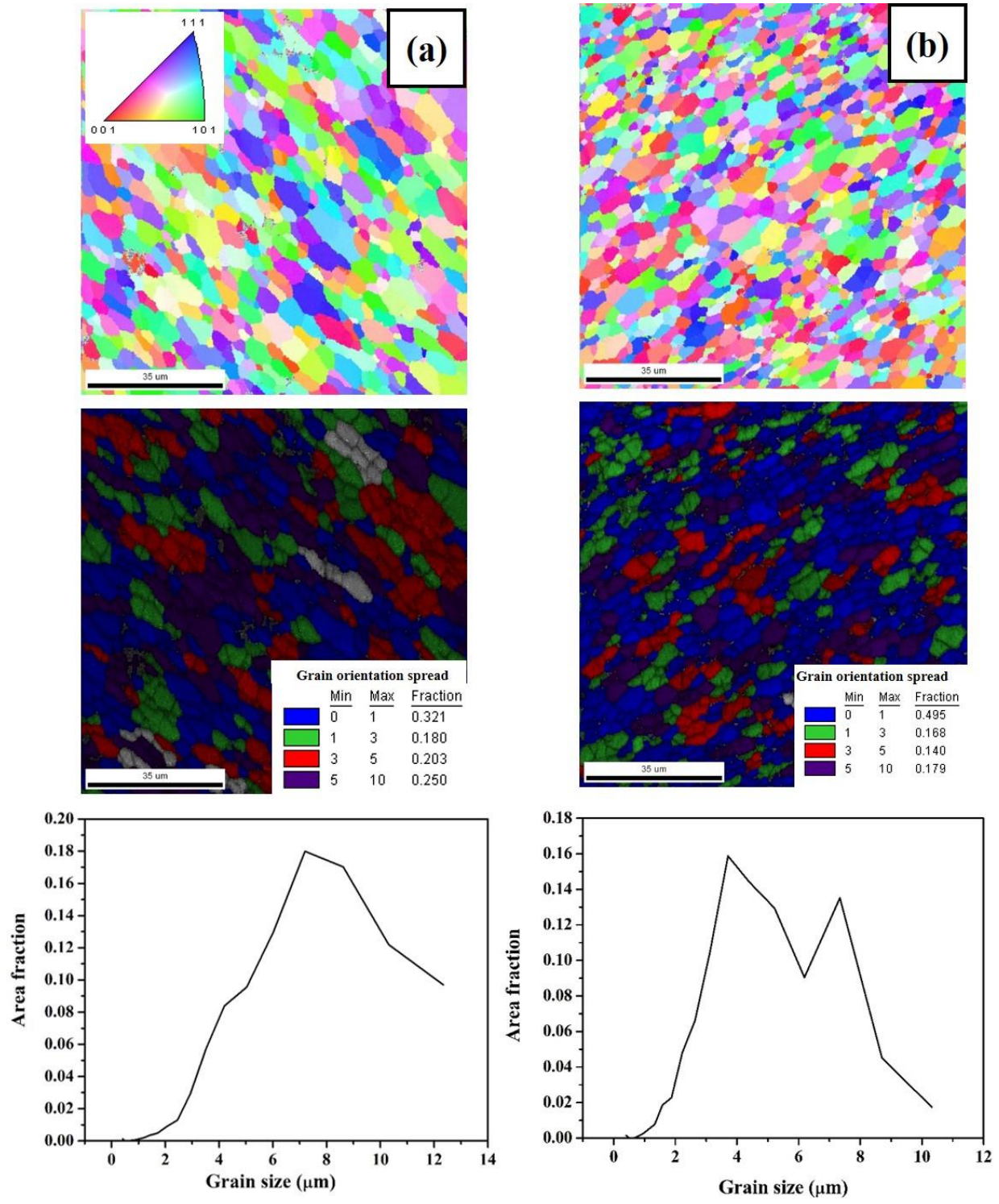


Fig. 4.31: Typical EBSD maps, grain orientation spread and distribution of grain size as a function of area fraction for (a) FSP with NAC and (b) FSP with IPC condition.

As reported in the literature, the degree of deformation or strain rate ($\dot{\epsilon}$) and the heat input or deformation temperature (T) are the two important thermomechanical factors, which affect the resulting grain size of the NZ during FSP. For estimating the average strain rate ($\dot{\epsilon}$) during FSP, Chang et al. (2004) proposed a torsion-type deformation equation as follows:

$$\dot{\epsilon} = k \frac{\pi \omega r_e}{L_e} \quad (4.2)$$

Where, L_e and r_e denote the effective depth and radius of the dynamically recrystallized zone (NZ), respectively. k is a constant which is normally taken as 1 (Chang et al., 2004) and ω is the rotational speed of the tool. Measured values of L_e and r_e for NAC condition are 4.15 and 3.48 mm; whereas, in case of the IPC condition, these values are found to decrease to $L_e = 3.94$ mm and $r_e = 3.05$ mm. This is attributed to the rapid removal of heat from the processed zone during FSP with IPC condition, which decreased the NZ size (L_e & r_e). Since strain rate is inversely proportional to the L_e and directly proportional to the r_e [Eq. (4.2)], the reduction in the values of these two factors in the IPC situation do not affect the strain rate noticeably. The calculated strain rate ($\dot{\epsilon}$) values [using Eq. (4.2)] for both the conditions are listed in Table 4.3 for convenience.

Temperature profile during FSP at different cooling conditions is shown in Fig. 4.32. It can be noticed that the maximum temperature recorded for NAC condition is 461°C and for IPC situation it is 384 °C. In case of SPD processing of age-hardenable alloys, the deformation temperature determines the rate of the nucleation of new grains; whereas, the post-processing cooling rate controls the kinetics of both precipitation and growth. Therefore, in case of age-hardenable alloys, optimized processing conditions with effective cooling rate is the key factor for developing fine grained microstructure with fine precipitates thereby yielding better mechanical properties by FSP. Therefore, in the present study, the FSP with IPC condition shows better grain refinement due to the less maximum temperature (384°C) achieved than that of the NAC condition (461°C).

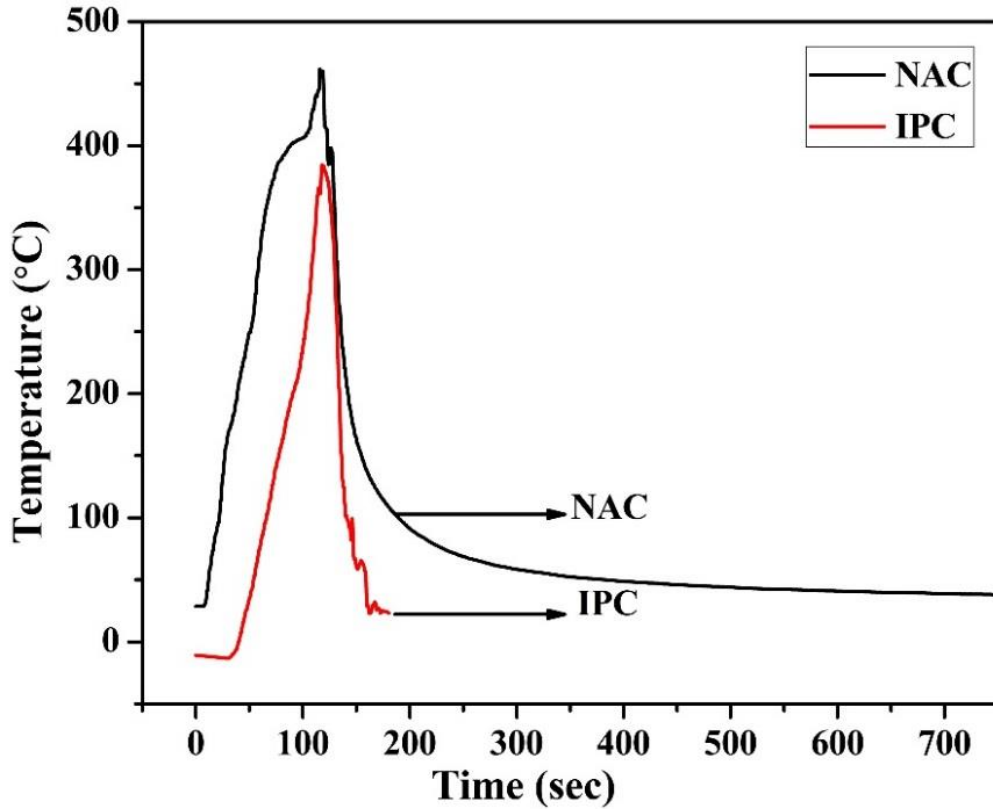


Fig. 4.32: Temperature profile recorded during FSP with IPC and NAC condition.

The combined effect of the deformation temperature and strain rate on grain size could be explained by the Zener-Hollomon parameter (Z) described as:

$$Z = \dot{\epsilon} \exp\left(\frac{Q}{RT}\right) \quad (4.3)$$

Where, R is the gas constant (8.314 J/mole K), Q denotes the activation energy (142 kJ/mole) (Charit et al., 2005; Morishige et al., 2010) and T is the deformation temperature. The calculated value of Z parameter for both the processing conditions is given in Table 4.3. The Z parameter is related to the recrystallized grain size (d) by the following equation:

$$\ln d = A - B \ln Z \quad (4.4)$$

Where, A and B are constants. Values of Z parameter and d are used to quantify the constants A and B , and the estimated values are found to be 8.36 and 0.255, respectively. From Eq. (4.4), it is evident that, with increasing the value of Z parameter, grain size (d) decreases. When the FSP was conducted with IPC setup, the heat generated in the processing zone was very quickly taken away by circulating a cryogenic liquid mixture than done in the NAC condition. Thus, low

deformation temperature is maintained during the FSP in IPC condition. According to Eq. (4.3), Z parameter is a function of strain rate ($\dot{\epsilon}$) and deformation temperature (T). Therefore, the lower value of T with almost constant values of $\dot{\epsilon}$ results in higher value of Z parameter which has led to develop smaller size grains in the IPC condition. Moreover, the FSP with IPC setup also arrests the grain growth by reducing the duration of peak temperature in the NZ. Similar results were also reported in several previous research works (Ashjari et al., 2015; Xue et al., 2011).

Table 4.3: Measured values of temperature, calculated values of the strain rate ($\dot{\epsilon}$) and Z parameter for the samples FSPed with IPC and NAC conditions.

Processing condition	ω (r.p.m.)	Strain rate (s^{-1})	Deformation temperature ($^{\circ}C$)	Z parameter (s^{-1})
NAC	720	31.6	461	4.1×10^{11}
IPC	720	29.2	384	5.7×10^{12}

Transmission electron microscopy was used to study the extent of grain refinement and precipitate characteristics of the NAC and IPC conditions. In case of Al7075 alloy, the precipitate evolution would take place in the following sequence:

Supersaturated solution \rightarrow Guinier Preston (GP) zones \rightarrow η' precipitates \rightarrow Stable η precipitates.

GP zones are basically solute rich spherical regions (less than 10 nm in size) that are coherent to the matrix. The η' precipitate of the order of 10-50 nm is demarcated as the intermediate phase, which is semi-coherent to the matrix and has a hexagonal crystal structure with plate like morphology; whereas, incoherent stable η precipitate >100 nm size has both plate like and lath type morphology (Jin-Feng et al., 2008; Park et al., 1983; Raghavan, 2015).

Scanning TEM images of the FSPed samples in NAC condition show the recrystallized grain structure with a grain size of the order of 4-5 μm (Figs. 4.33a and b). In case of the FSP with NAC condition, heat evolved during the process is sufficient enough for η' precipitates to coarsen and form stable η phase. Particles of size more than 200 nm are found to form inside the grains along with discontinuous particles at the grain boundaries (Figs. 4.33a and b). While a dense distribution of fine η' intermediate precipitates, which are semi-coherent to the matrix, are developed (Figs. 4.33c and d) in the sample FSPed with IPC condition. In this sample, the average grain size is found to be 2.4 μm with precipitate sizes in the range of 20-30 nm. These precipitate

sizes are critical enough for effectively arresting the dislocation movement, which could yield high strength.

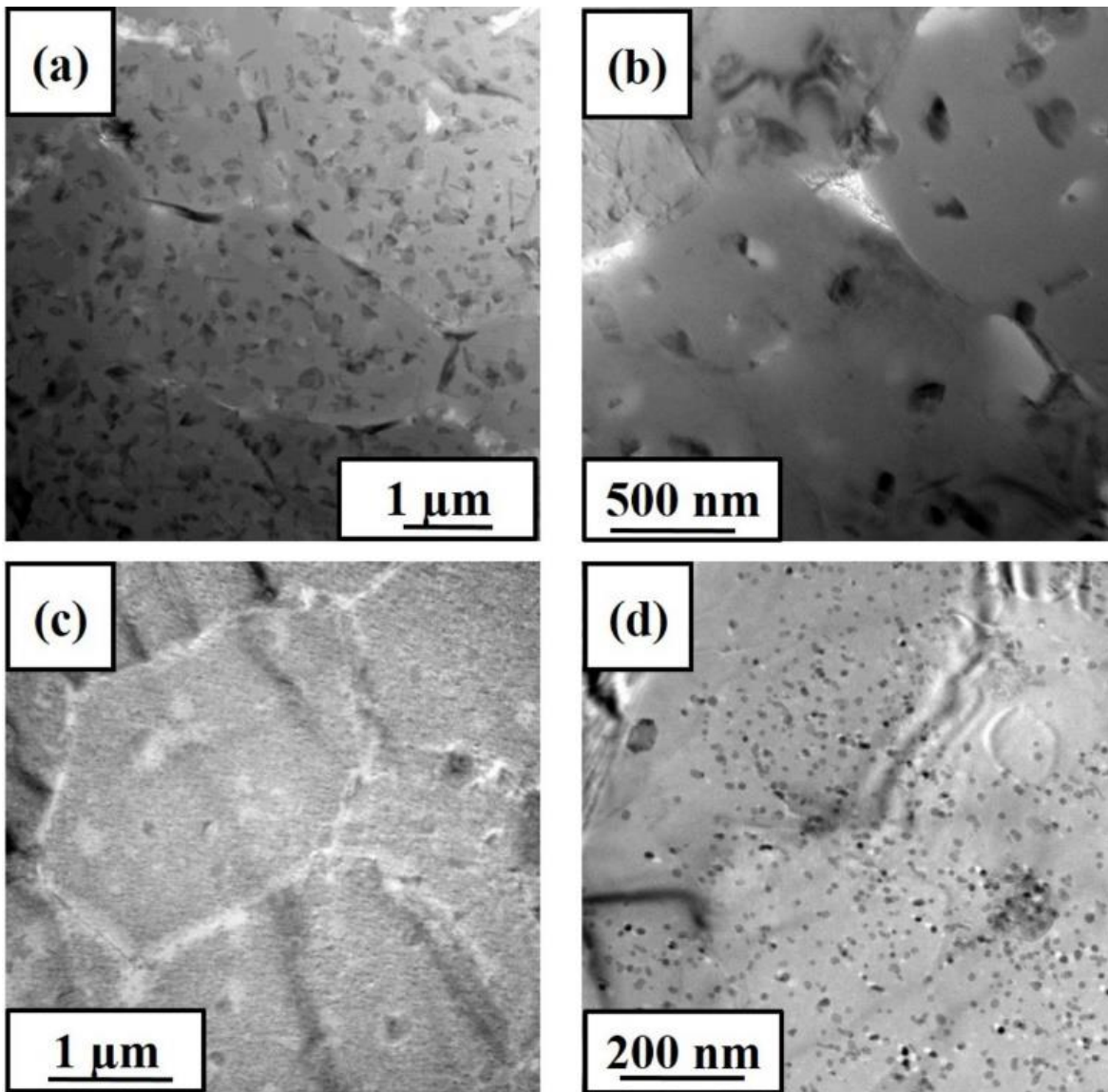


Fig. 4.33: TEM micrographs of FSPed sample processed with (a and b) NAC and (c and d) IPC condition.

4.3.2 Mechanical properties

To evaluate the effect of the IPC on the mechanical properties of the FSPed samples, uniaxial tensile tests as well as hardness measurements were carried out. Figure 4.34 depicts the hardness values of the ST base metal and FSPed samples processed under different cooling environments. An average of 6 readings was reported for each hardness value with a standard deviation in the parenthesis. The hardness value of the starting material was found to be 97 HV only. For the age-

hardenable Al7075 alloy, the hardness value of 97 HV is very low, which is attributed to the dissolution of most of the strengthening precipitates due to solutionizing treatment.

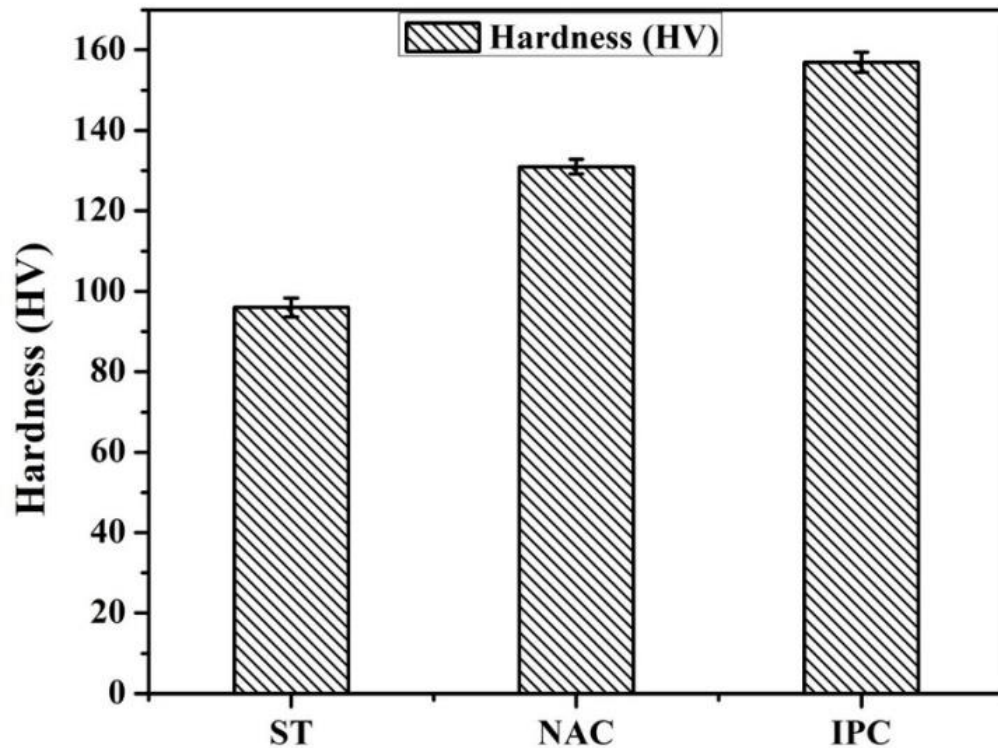


Fig. 4.34: Variation of hardness for different process conditions.

As could be seen from Fig. 4.34 that the FSPed samples in both conditions (NAC and IPC) exhibited significant improvement in the hardness as compared to the ST base metal. Such improvement in the hardness values is ascribed to the significant grain size refinement and re-precipitation of strengthening phase after FSP. These results are consistent with the trends reported by other investigators (Cao et al., 2017; Upadhyay et al., 2010). Furthermore, it is to be noted that average hardness value of the NZ for specimen processed under IPC condition is quite high (157 HV) and this is higher than that of the FSPed sample (131 HV) in the NAC condition. This is ascribed to the fact that, the FSP with IPC setup suppresses precipitate coarsening/overaging and arrests the excessive grain growth by reducing the peak temperature, increasing cooling rate and limiting post-FSP cooling time. This leads to an increase in the hardness value. Moreover, the fine precipitates formed in the IPC condition arrest the dislocation movement resulting in higher hardness. Overall, the hardness values of the processed samples under different processing environments are well-corroborated with the microstructural characteristics (Fig. 4.30) and tensile properties (Fig. 4.35, discussed later).

Figure 4.35 shows the typical engineering stress-strain curves of the ST base metal and FSPed samples processed with and without in-process cryocooling at a constant rpm and traverse speed. It can be noticed that the starting material exhibited low yield strength (214 MPa) and ultimate tensile strength (308 MPa) with ~22% elongation due to its solution treated state. From Fig. 4.35, it can be observed that the both NAC and IPC FSPed samples showed remarkable enhancement in the YS and UTS, while the ductility (22.8%) is improved in case of the IPC condition and there is slight decrease in the ductility (~19%) under NAC condition in comparison to that of ST base metal. The enhancement in the tensile properties of the FSPed samples is highly correlated to microstructural features evolved after the FSP. As discussed before in microstructural section, the key differences in the microstructure of the starting material and processed samples are grain size and precipitate(s) characteristics. The mechanical strength (i.e. hardness, YS, UTS) of the age-hardenable Al alloys mainly depends upon grain size and strengthening precipitates characteristics. Since, the starting material for the FSP was in solution treated condition, it is expected that the strengthening precipitates are mostly dissolved in the matrix (i.e. matrix in super-saturated state). As mentioned before, the FSP causes intense plastic deformation at elevated temperature in the NZ which leads to generation of fine recrystallized grain structure with re-precipitation of metastable precipitates. Therefore, the overall strength achieved by the FSPed samples is mainly dominated by the grain boundary (Hall-Petch) strengthening and precipitation strengthening effects. The effect of grain refinement on yield strength can be described by the well-known Hall-Petch relationship (Dieter, 1986) expressed as:

$$\sigma_y = \sigma_0 + \frac{k}{\sqrt{d}} \quad (4.5)$$

Where, σ_y is the yield strength associated to grain refinement, d is the average grain size, σ_0 is the friction stress (20 MPa), k is the Hall-Petch constant and reported to 0.12 MPa \sqrt{m} for Al7075 alloy (Shaeri et al., 2016). According to Eq. (4.5) grain size (d) has an inverse relationship with yield strength. So, development of a fine grained structure during FSP leads to an enhancement of yield strength as per Hall-Petch relationship. The enhancement in the yield strength due to Hall-Petch strengthening is calculated to be ~98 and 75 MPa, respectively, for FSPed specimens with IPC and NAC conditions. It is also noticeable (from Fig. 4.35) that the FSP with IPC condition has led to more consistent enhancement of strength and ductility both in comparison to the FSP with NAC condition. For instance, the FSPed sample under IPC condition exhibited a tensile and yield strength of 535 MPa and 384 MPa, respectively, with 22.8% elongation. While for FSP

with NAC condition, the tensile and yield strength increased to 377 and 305 MPa, respectively, with 18.9% elongation. Hence, extra enhancement in the IPC condition could be related to the positive influence of the controlled temperature distribution during FSP and effective cooling rate, which led to the formation of fine semi-coherent η' precipitates (20-30 nm) along with the development of very fine matrix grains (2.4 μm). The evolution of fine precipitates (20-30 nm) after the FSP with IPC condition poses obstacles against dislocation movement, which consequently increases the strength. The precipitation strengthening effect on the yield strength of Al alloys could be estimated by Orowan-Ashby equation (Dieter, 1986), described as:

$$\Delta\sigma_{ppt} = \frac{0.13 Gb}{\lambda} \ln\left(\frac{r}{b}\right) \quad (4.6)$$

Where, G , b , r and λ represent shear modulus, Burgers vector, radius of the precipitates and inter-particle spacing, respectively. As reported in the literature (Ma et al., 2014), the shear modulus (G) for Al7075 is 26.9 GPa and magnitude of the Burgers vector (b) for fcc metals is 0.286 nm. The yield strength increment from the precipitation strengthening is calculated to be about 187, and 55 MPa, respectively, for the FSPed specimens with IPC and NAC conditions. So, it can be noted that the contribution of precipitation strengthening mechanism is higher in the sample FSPed with IPC condition as compared to that of the FSPed sample with NAC condition. Moreover, a considerable enhancement in the uniform elongation with IPC condition (20% as compared to <15% for NAC) is ascribed to the development of nanosize η' precipitates (20-30 nm). The work hardening capacity is increased by these extremely fine dispersed η' precipitates, which hinder dislocation motion.

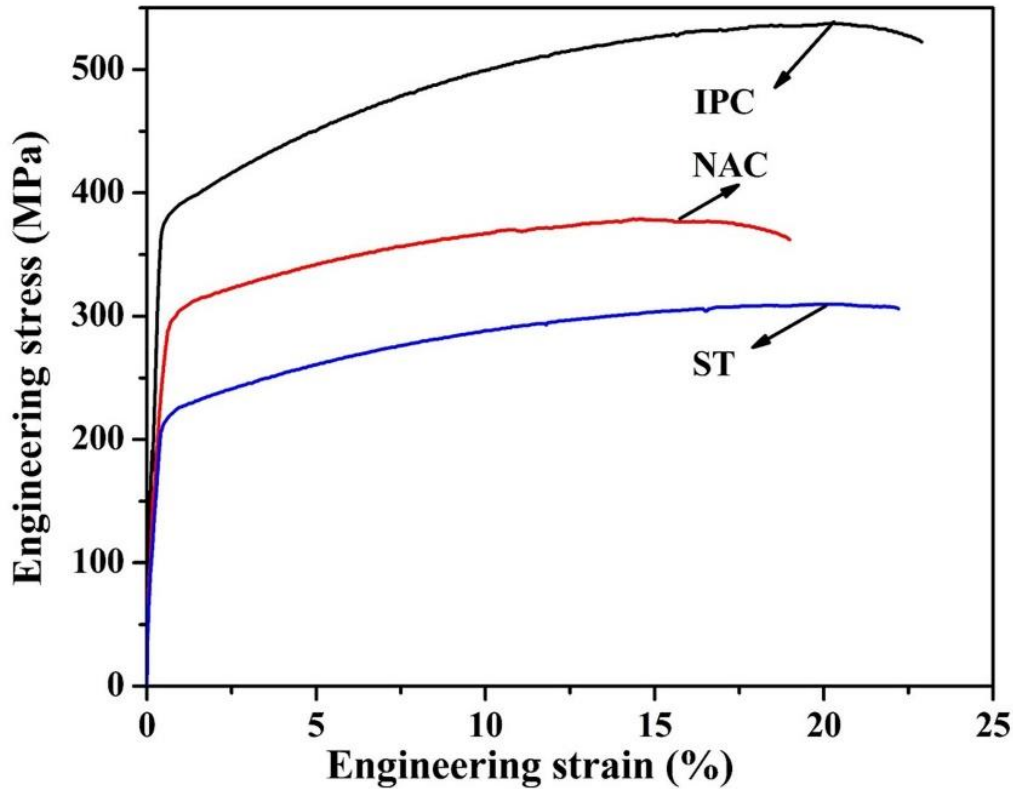


Fig. 4.35: Tensile curves of alloy processed at different cooling conditions.

Tensile fractured surfaces of the investigated samples were examined by SEM to correlate the mode of failure during tensile test with the resultant ductility of the corresponding specimen. Figure 4.36 shows the fractured surface morphology of the ST base metal and FSPed samples processed with and without in-process cryocooling effect. It is seen from Fig. 4.36a that the fractured surface of the ST sample exhibited well defined deep dimples over the entire surface with varying shapes and sizes, which is a typical characteristic of ductile dominated fracture. The FSP induced completely different fractured morphologies: both in the normal and IPC conditions FSPed samples after tensile failure exhibited finely distributed shallow dimples, which could be the characteristics of the recrystallized fine grains structure. The dimples in the fractured surface of the sample processed under the IPC condition are found to be finer due to the finer grain size and extra work hardening effect from the finer η' precipitates developed during the IPC FSP (Fig. 4.36c). The extra grain refinement as well as formation of finer η' precipitates is ascribed to the faster cooling rate employed in the IPC FSP technique. Thus, amount of uniform elongation for the sample FSPed under IPC condition is also increased. These findings are also in agreement with higher percent of the uniform elongation achieved in the FSPed (20%) sample under IPC environment as compared to that of the FSPed sample carried under NAC condition (<15%).

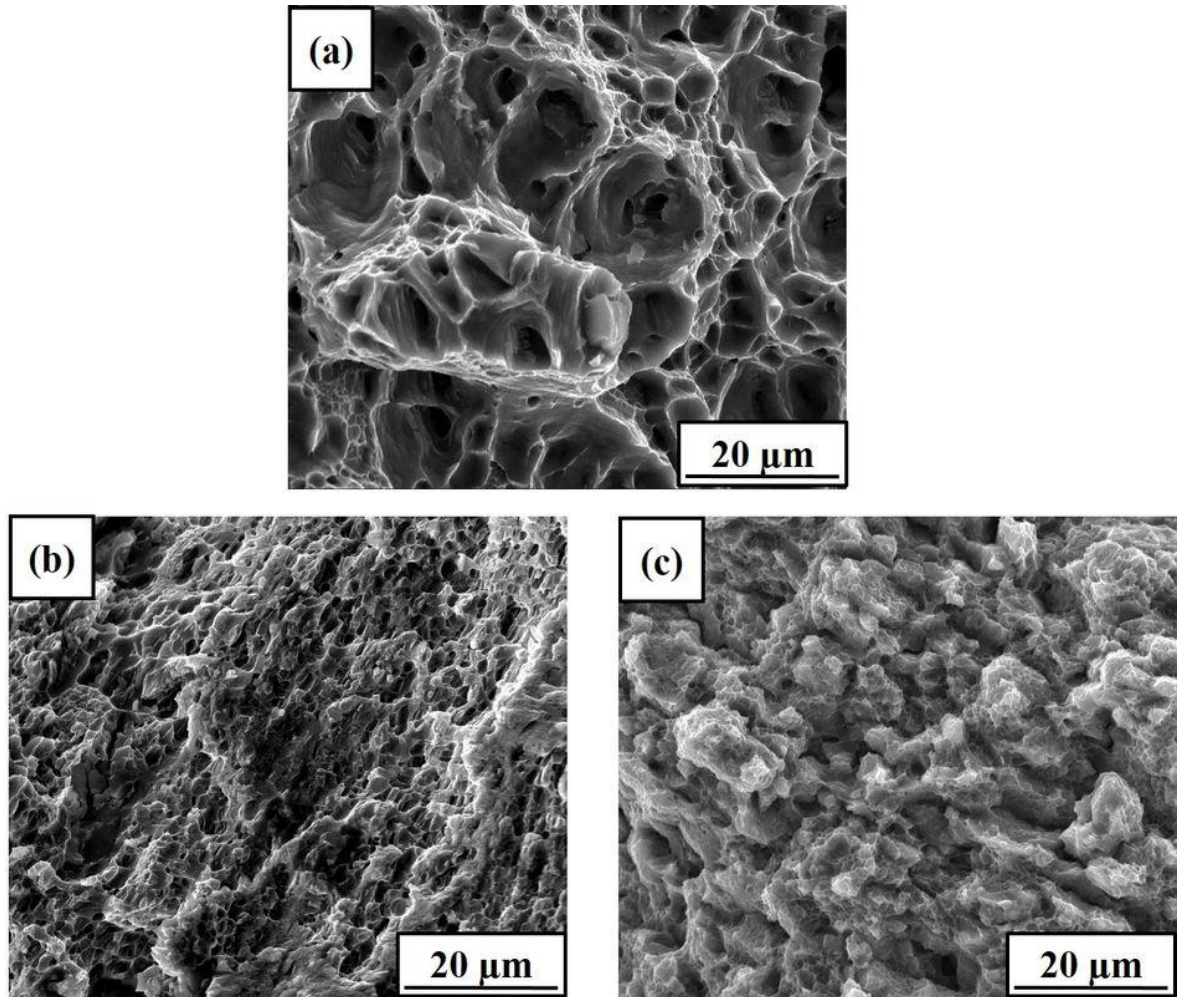


Fig. 4.36: SEM fractographs of (a) ST base metal, (b) FSPed sample with NAC and (c) FSPed sample with IPC.

4.3.3 Summary

In the current study, the solutionized Al7075 alloy plates were subjected to FSP under normal air cooling (NAC) and in-process cryocooling (IPC) conditions in order to investigate their influence on the microstructural features and mechanical properties (i.e. hardness and tensile properties). The FSP was carried out successfully to obtain defect free processed zones in both the conditions. Evolution of microstructure after the FSP and their effects on mechanical properties were analyzed and correlated with the major strengthening mechanisms, especially, grain boundary strengthening and precipitation hardening. The major findings of the present study could be summarized as follows:

- a) The FSP with IPC condition was found to be highly beneficial for achieving extra grain refinement ($2.4\ \mu\text{m}$) as compared to that of the FSP under NAC situation ($4.7\ \mu\text{m}$). The

effect of the IPC during FSP led to about 2 times more grain refinement in the nugget zone than that achieved in NAC FSP subjected to same rpm (720) and traversed speed (65 mm/min).

- b) Microstructural analysis through TEM and EBSD confirmed the formation of extremely fine matrix grains (2.4 μm) in which nanosize semi-coherent precipitates of η' phase (20-30 nm) are dispersed uniformly in IPC condition.
- c) Simultaneous improvement in the ductility as well as yield strength is observed for the sample processed with the IPC condition as compared that of the ST base metal (22%, 204 MPa); while for the sample processed with the NAC condition, the yield stress is found to increase, but in the cost of bit ductility. The yield strength (384 MPa) and ductility (22.8%) of the FSPed sample under the IPC situation are found to be much superior as compared to those (305 MPa, ~19%) for the FSPed sample under the NAC condition and ST base metal sample (22%, 204 MPa). This is ascribed to the formation of fine recrystallized matrix grains (2.4 μm) with high density of finely dispersed nanosize coherent/semi-coherent η' phase (20-30 nm) within the matrix.
- d) Fractography analysis of the tensile samples correlated well with the uniform elongation, microstructural features and strain hardening capability of the corresponding samples. For example, the smaller size dimples observed in the sample FSPed under the IPC condition could be attributed to the extra grain refinement and work hardening effect from the nanosize η' precipitates.

4.4 Cryo-FSP on Al7075-SiC nanocomposites and their analysis

In this section, in-process cryocooling FSP was conducted on the stir-cast Al7075-SiC nanocomposites samples. Initially, Al7075 alloy based nanocomposites reinforced with varying wt.% (2%, 3% and 5%) of nanosize SiC particles were produced through bottom pouring stir casting technique. The present study aims to develop high strength Al7075-SiC nanocomposites processed by integration of stir casting and cryo-FSP. Secondary processing through FSP under cryogenic condition could modify the distribution of SiC nanoparticles uniformly with the matrix, refine the matrix grain size, enhance the particle/matrix interface characteristics and eliminate the casting defects from the as-cast composites. These microstructural changes

drastically can improve the mechanical properties both strength (YS, hardness etc.) and ductility. To understand the fundamentals of the deformation characteristics and microstructural evolution, a systematic study on microstructural evolution has been performed by optical, scanning and transmission electron microscopy and the mechanical properties were evaluated by Vickers hardness measurements and tensile test.

4.4.1 Microstructural characterization

Figure 4.37 illustrates the SEM micrograph of the as-cast Al7075 alloy and their composites with varying wt.% of nanosize SiC particles (2%, 3% and 5%). The micrograph presented in Fig. 4.37a shows that Al7075 alloy without any reinforcement exhibits a coarse dendritic structure in comparison to the small dendritic grain structure segregated with SiC nanoparticles at interdendritic region observed in case of Al7075-SiC nanocomposites (Figs. 4.37b,c,d). These micrographs clearly show the heterogeneity in terms of both porosity and distribution of SiC particles. The agglomeration of SiC particles at the inter-dendritic regions in the stir cast AMCs can be accredited to the poor wettability of the reinforced particles (i.e. SiC) with the melt and the pushing effect (reinforcement particles either get rejected or pushed ahead) by the solidification front which lead to intergranular distribution of reinforcement. In addition, agglomeration and clustering of the nanosize SiC particles were found to be increased with increasing fractions of reinforcement, as shown in Figs. 4.37b,c,d. Moreover, the microstructure of the nanocomposites (Fig. 4.37) show that the dendritic grain size reduces with increasing the wt.% of nanosize SiC particles. The average grain size was estimated to be 245, 135, 120 and 116 μm , respectively, for the as-cast Al7075 alloy (AC), Al7075-2wt.% SiC nanocomposite (NC2), Al7075-3wt.% SiC nanocomposite (NC3), Al7075-5wt.% SiC nanocomposite (NC5) samples. This can be ascribed to the effect of SiC particles on grain growth. The reinforced nanoparticles not only hinder the coarsening of matrix grains by pinning, but also provide preferential nucleation sites for heterogeneous nucleation and consequently finer grain structure is developed. Other researchers (Ezatpour et al., 2016; Hoziefa et al., 2016) also reported similar type of observation in their works.

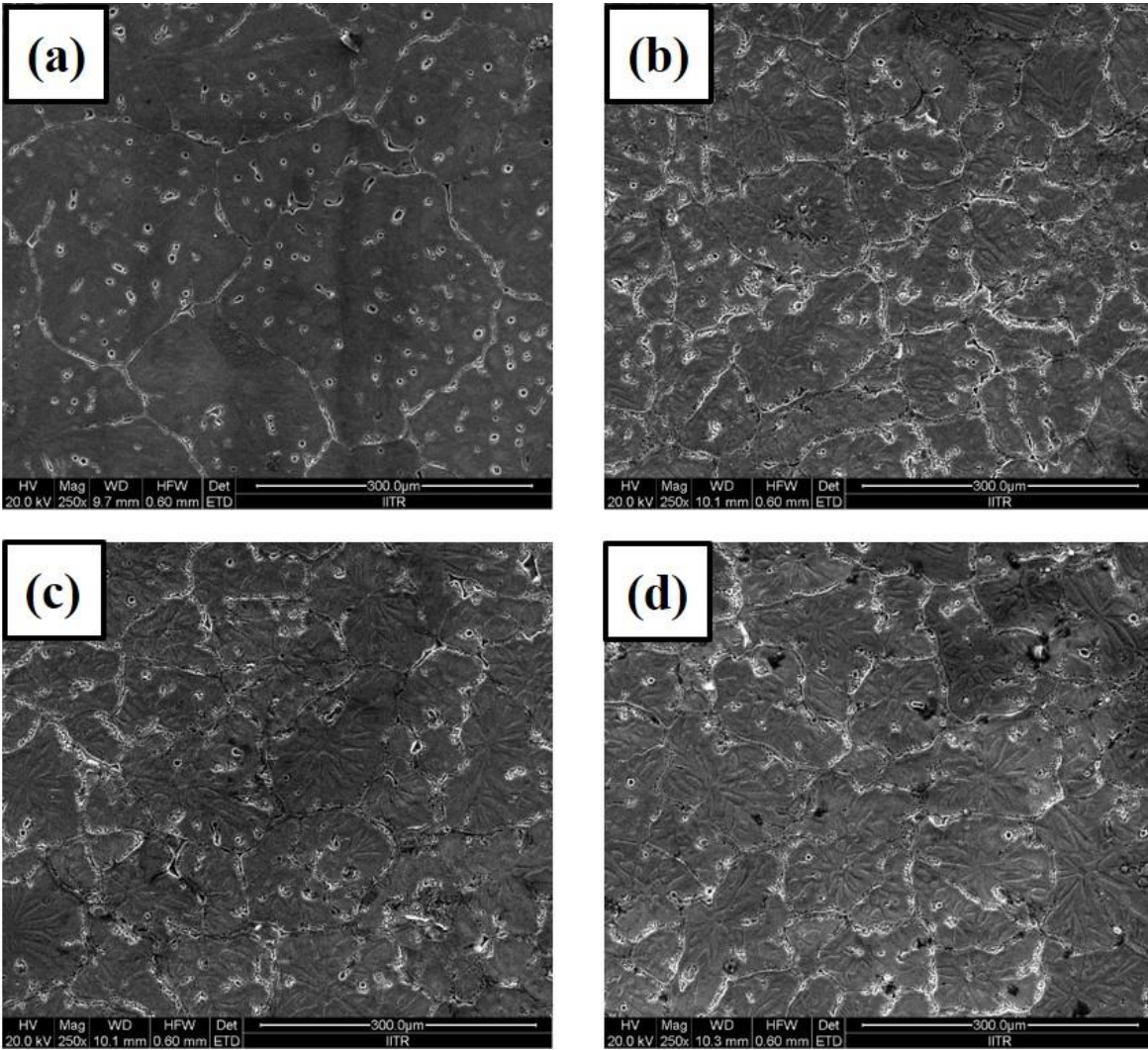


Fig. 4.37: Optical microstructures in as-cast condition of (a) Al7075 alloy, (b) Al7075-2wt.% SiC nanocomposite, (c) Al7075-3wt.% SiC nanocomposite and (d) Al7075-5wt.% SiC nanocomposite.

In order to modify the cast dendritic structure and improve the distribution of SiC nanoparticles, the as-cast Al7075 alloy and its composites were subjected to cryo-FSP. During FSP, material in the FSP zone is subjected to severe plastic deformation and high thermal exposure, which introduced complex material mixing thereby improving microstructural evolution with fine grained matrix with uniform distribution of reinforced particles. The grains in the NZ are so fine that they are not visible clearly in optical microscope (as also seen in section 4.3), especially in case of the cryo-FSP. In order to quantify the grain size and to observe the microstructural details, EBSD analysis was made on the cryo-FSP samples. Figure 4.38 shows the image quality (IQ) map of the FSPed Al7075 alloy and Al7075-SiC nanocomposites samples reinforced with different wt.% of nanosize SiC particles.

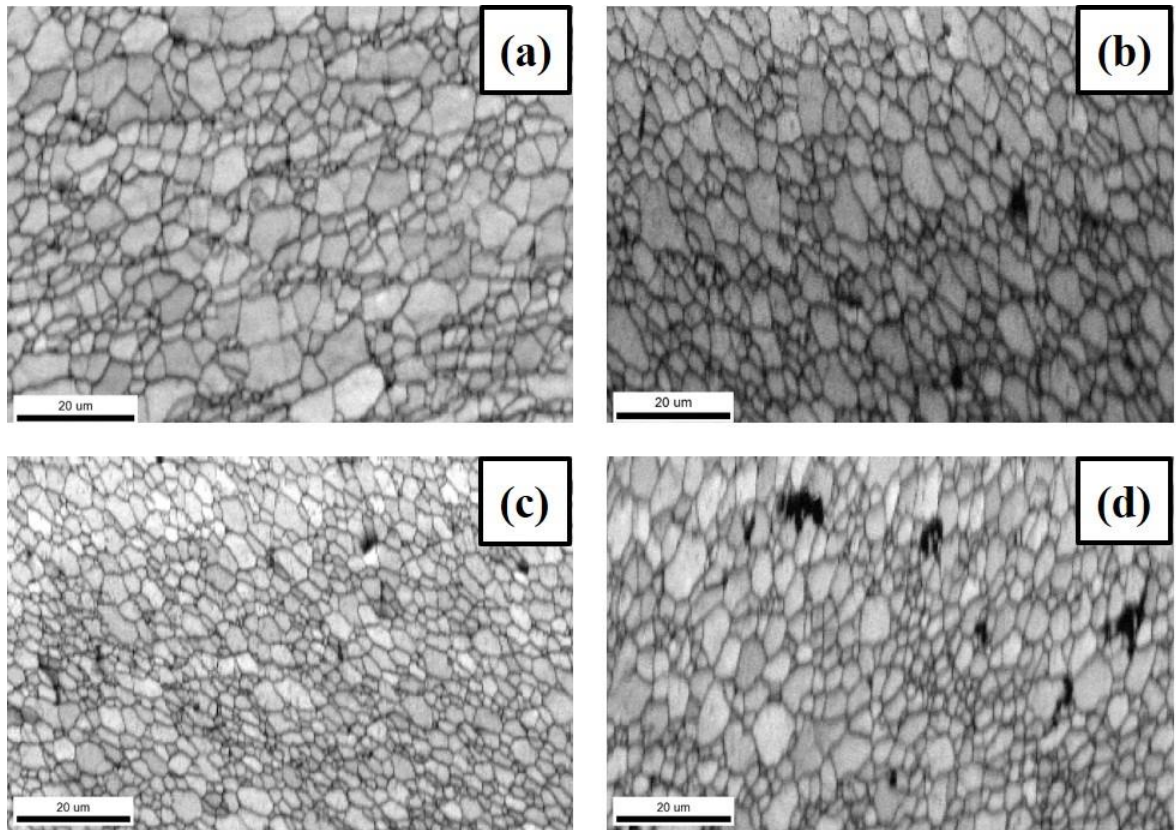


Fig. 4.38: Image quality map of the cryo-FSPed samples (a) Al7075 alloy, (b) Al7075-2wt.% SiC nanocomposite, (c) Al7075-3wt.% SiC nanocomposite and (d) Al7075-5wt.% SiC nanocomposite.

After the cryo-FSP, considerable amount of grain refinement and redistribution of the SiC particles are observed for all the microstructures as compared to that of the as-cast state of same. The cryo-FSP has also resulted in the closure of the micro-porosity and developed a homogenized microstructure. However, some small agglomeration of SiC nanoparticles could still be observed in case of the 5 wt.% SiC reinforced nanocomposite sample even after the cryo-FSP. The initial distribution of the reinforcement greatly affects the grain size and distribution of reinforcement. It is evident from Fig. 4.37d that the as-cast NC5 sample contains higher amount of clustering and agglomeration of the SiC particles. As a result, this sample even after the FSP at cryogenic condition showed inhomogeneous distribution of grains with some agglomerated SiC particles. This indicates that the single pass cryo-FSP is not effective enough to distribute the higher amount SiC reinforcement. Average grain sizes of the corresponding specimens were estimated from the grain size distribution profile of the EBSD micrographs. Grain size distribution maps as a function of number fraction for the FSPed Al7075 alloy and its composites are shown in Fig. 4.39. The average grain size after cryo-FSP was found to be ~ 3.5 , ~ 3.1 , ~ 2.1 , and ~ 2.8 μm

respectively, for the cryo-FSPed samples of AC, NC2, NC3 and NC5. Much wider grain size distribution is clearly observed from all the maps (Figs. 4.39a, b & d) except cryo-FSPed NC3 (Figs. 4.39c) sample. Wide grain size distribution is strongly related to the temperature of deformation during FSP, amount of SiC reinforcement and its redistribution. It is normally reported that the microstructure becomes more uniform as deformation temperature increases (Humphreys et al., 2004). However, in case of cryo-FSP, nugget zone experiences lower peak deformation temperature for a very short period of time with higher cooling rate as compared the room temperature FSP.

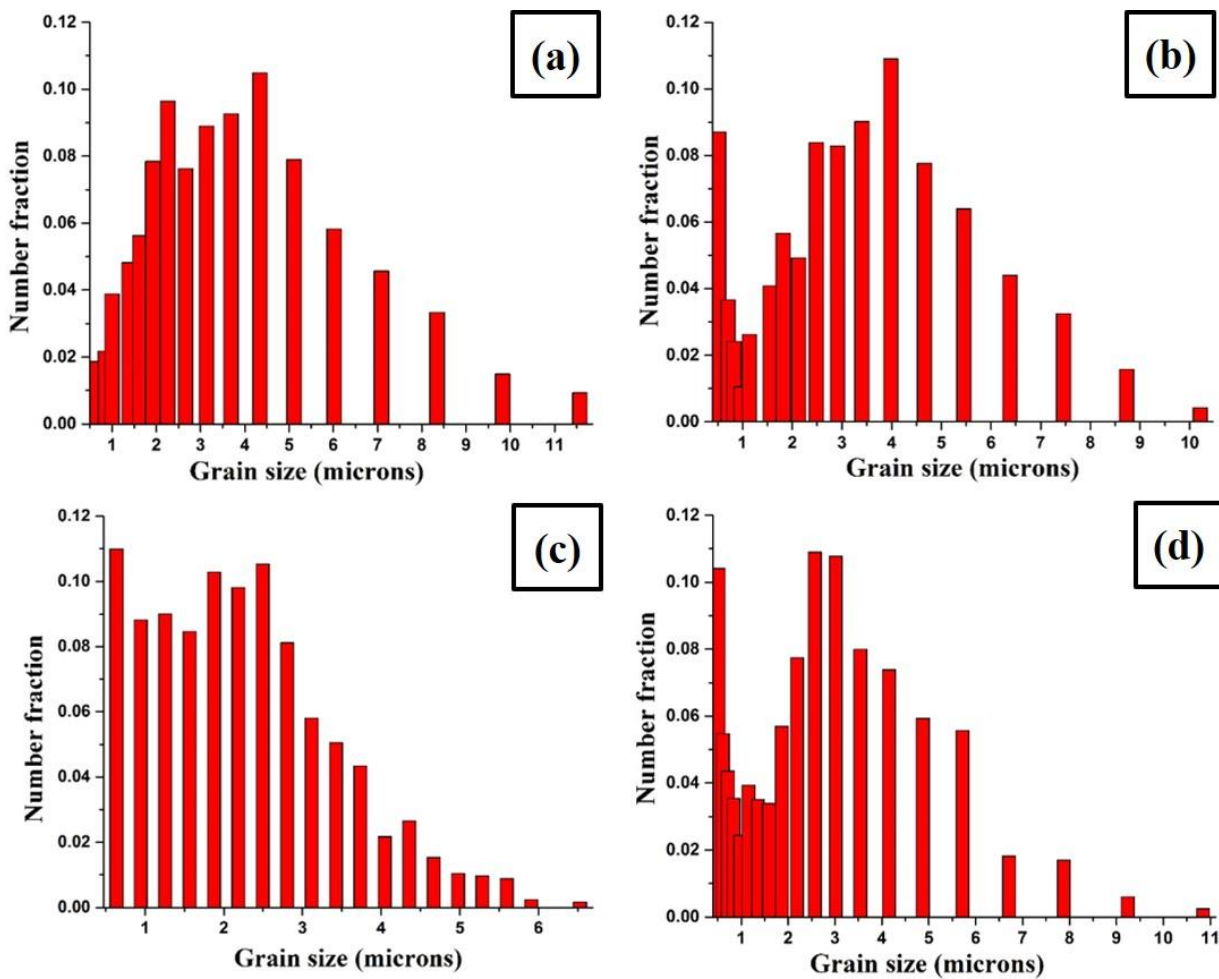


Fig. 4.39: Grain size distribution as a function of number fraction for (a) Al7075 alloy, (b) Al7075-2wt.% SiC nanocomposite, (c) Al7075-3wt.% SiC nanocomposite and (d) Al7075-5wt.% SiC nanocomposite.

Moreover, in case of the Al7075-3wt.% SiC nanocomposite, the grain size is more or less uniform and the major fraction of grains lies < 2 microns size. This could be due to the fact that the 3wt.% SiC particles could be the optimum level of reinforcement in Al7075 alloy, which can be

distributed uniformly within the matrix through cryo-FSP and hinders the grain growth by Zener pinning. The uniform distribution of nanosize SiC particles intensified grain boundary pinning and act as preferred sites for recrystallization mechanism, which is known as particle stimulated nucleation (PSN) (McNalley et al., 2008). Humphreys et al. (2004) also reported DRX through PSN in Al alloys containing second-phase particles.

Figures 4.40a-c show the EBSD maps (IQ+IPF) along with distribution of misorientation angles of the grain boundaries as a function of number fraction for the cryo-FSPed NC3 sample. The various color contrasts in the IPF map represent the different orientations of the grains and is interpreted by colors as shown in the inset unit triangle in the figure (Fig. 4.40b). Fig. 4.40c shows distribution of misorientation angles of the grain boundaries. The analysis shows that the random misorientation angles of the grain boundaries observed is the typical sign of thermo-mechanical processing with high strain levels as occur in the cryo-FSP (Huang et al., 2000). Further, microstructural study of A7075-3wt.% SiC composite by STEM could provide better understanding of the fine grained microstructure and distribution of second phase particles (i.e. nanosize SiC_p and precipitates). The representative STEM micrograph of the Al7075-3wt.% SiC nanocomposite sample after cryo-FSP is shown in Fig. 4.40d. The average grain size could be estimated to be ~2 micron as revealed by the STEM micrograph. It is to be noted that the EBSD grain size distribution is corroborating well with that obtained by TEM study. Fig. 4.40d also reveals the presence of two types of second phase particles, i.e. nanosize reinforcement particle (SiC) and strengthening precipitate phase (i.e. MgZn₂ and/or Mg₃Zn₃Al₂) throughout the fine-grained matrix. The second phase particles can be differentiated by their morphologies. The second phase particles with rounded shape, dark and clear contrast are identified as SiC; whereas, strengthening precipitate phase (i.e., MgZn₂ and/or Mg₃Zn₃Al₂) appears to homogeneously distributed mainly within the grains. From TEM micrograph, we can see that most of the SiC particles are present at the grain boundaries, which is a clear indication of their role in the final grain structure obtained in case of the 3wt.% nanocomposite sample. Particles at the grain boundaries could effectively pin them and decrease the grain growth. Overall, microstructural analysis through TEM and EBSD confirmed the formation of extremely fine matrix grains in which nanosize SiC particles and precipitates of η' phase are dispersed uniformly in the nanocomposite samples.

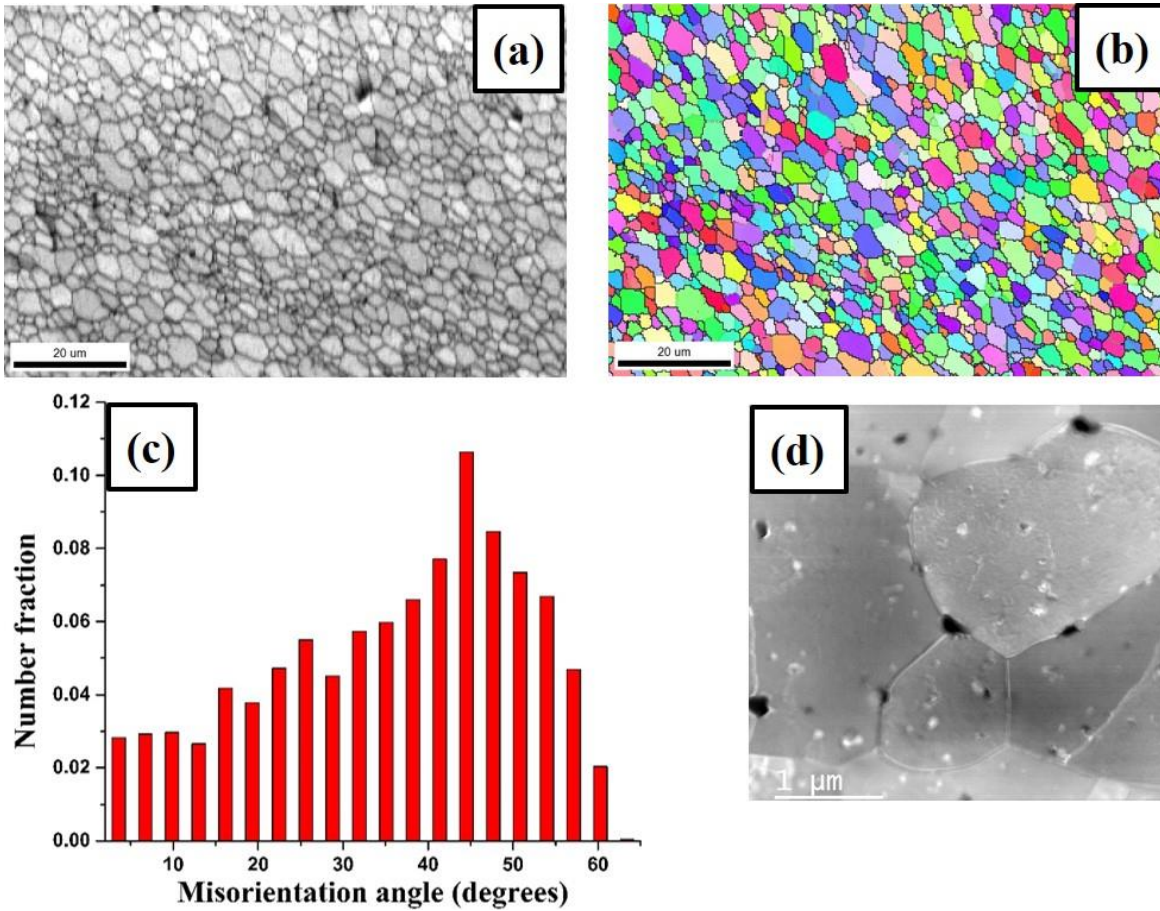


Fig. 4.40: (a,b,c) EBSD maps (IQ+IPF) and misorientation angle as a function of number fraction for Al7075-3wt.% SiC nanocomposite (d) STEM image of Al7075-3wt.% SiC nanocomposite.

4.4.2 Mechanical properties

The mechanical properties such as hardness and tensile strength of the cast Al 7075 alloy and its nanocomposite samples containing 2-5wt.% nanosize SiC particles were evaluated after FSP at cryogenic condition (Fig. 4.41). Variation in the Vickers hardness of the samples, before and after the cryo-FSP, is shown in Fig. 4.41. The results of the Vickers hardness values are also summarized in Table 4.4 for the convenience.

Table 4.4: Vickers hardness value of different investigated samples.

Condition	As-cast	Cryo-FSP
Al7075 alloy	69± 1.80	106 ±1.51
Al7075-2wt.% SiC	88±2.67	139±1.83
Al7075-3wt.% SiC	98.5±2.80	162±2.10
Al7075-5wt.% SiC	102±3.50	141±2.52

Each hardness value is an average of six (6) readings and the error bar shown in Fig. 4.41 indicates its standard deviation. It can be noticed (Fig. 4.41) that the hardness of the nanocomposites samples at any level of SiC content is higher than that of the base material in the as-cast condition. The average hardness of the as-cast Al7075 alloy, NC2, NC3 and NC5 samples are found to be 69, 88, 98.5 and 102 HV, respectively. The hardness of the nanocomposites increases with increasing the weight fraction of reinforcement in the Al7075 alloy. The observed improvement in the hardness levels with increasing SiC content is ascribed to the higher inherent hardness of the SiC particles (as per the rule of mixture) and grain size refinement produced because of the presence of nanoparticles during solidification (Fig. 4.37). In the as-cast state, a large scattering in the hardness value is observed due to the existence of inhomogeneity in the cast microstructures (porosity, micro-void, dendritic structure and clustering & agglomeration of SiC particles). FSP uses extreme plastic deformation and frictional force to mix the composite material and could refine the microstructure thereby eliminating/reducing these defects. Hence, the hardness in the nugget zone of the FSPed samples is observed to be quite uniform as shown in Fig. 4.41. As indicated in Fig. 4.41, a remarkable enhancement in the hardness value is obtained for all the examined specimens after the cryo-FSP in comparison to those observed in its as-cast condition. However, it appears that the rate of increase in hardness value is relatively high up to 3 wt.% of SiC reinforcement and thereafter, an insignificant improvement is observed. It should be noted that the NC5 sample contained significant agglomeration and clustering of the SiC particles (Fig. 4.37d) after the cryo-FSP, and single pass cryo-FSP may not be sufficient to redistribute the SiC particles uniformly. This may lead to formation of chunky SiC particles and bands of agglomerated particles within the matrix (Fig. 4.38d). Consequently, this could potentially be the reason to have lower hardness than those occurred in NC3 composite sample after the cryo-FSP. Peak hardness of 162 HV is observed in case of the NC3 sample after the cryo-FSP. Such improvement in the hardness values is mainly attributed to the: (i) redistribution of the harder phase SiC particles uniformly in the Al matrix, (ii) suppression of coarsening of the strengthening precipitate phase (i.e., $MgZn_2$ and/or $Mg_3Zn_3Al_2$) due to higher cooling rate and (iii) remarkable microstructural refinement because of restricted grain growth due to lower peak temperature and pinning effect of the particles on the grain boundaries. These results are consistent with the trends reported by other investigators (Alidokht et al., 2011, 2012).

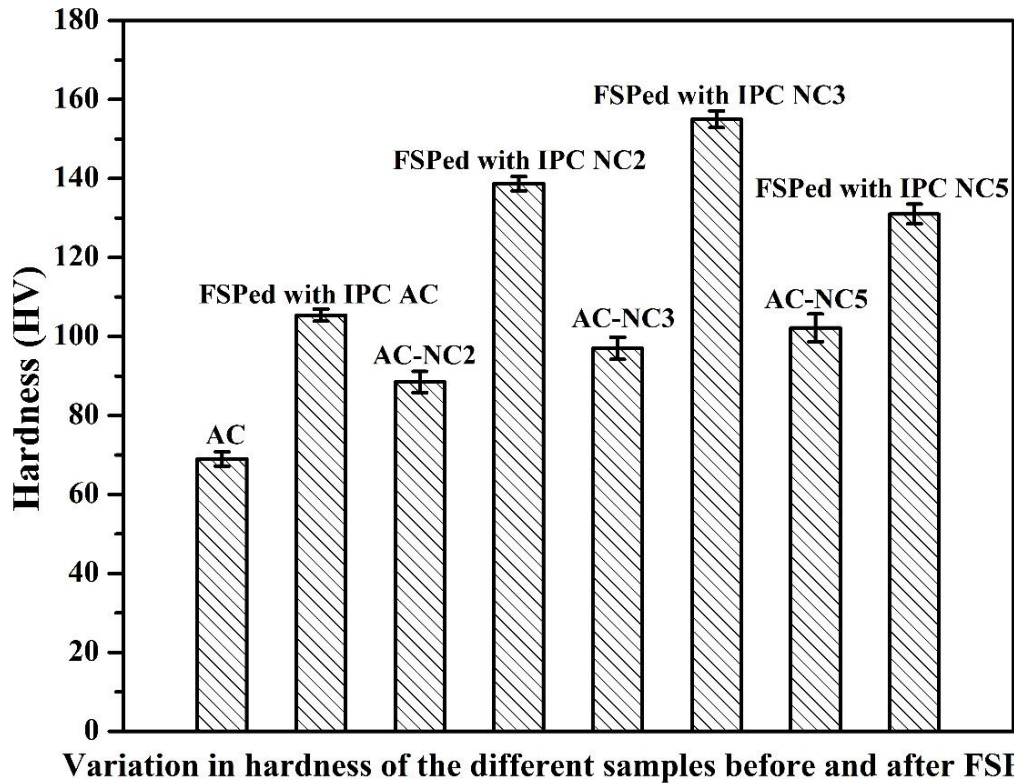


Fig. 4.41: Variation in hardness of the different samples before and after cryo-FSP.

The engineering stress-strain curves of the cryo-FSPed Al7075 alloy and its nanocomposite samples are shown in Fig. 4.42. The variation in the tensile properties (YS/UTS and % elongation) as a consequence of the stirring and cooling effects are represented by engineering stress-strain curves. However, it was difficult to realize the actual tensile properties of the as-cast materials due to dendritic structure, segregation of SiC particles at interdendritic region, heterogeneity in terms of both porosity and agglomeration of SiC particles. It is widely accepted that the existence of such type of defects restricts the plastic deformation capability of the material resulting in premature failure (Hoziefa et al., 2016; Shen et al., 2016). During FSP, because of the frictional heating and stirring action the material starts to flow (severe deformation) and thoroughly mixed thereby eliminating/reducing these defects and develops a homogeneous microstructure with uniform distribution of SiC particles. Thus, the improved microstructure after the FSP results in enhanced mechanical properties. The unreinforced alloy sample after FSP led to noticeable enhancement in both strength and ductility (UTS-437 MPa, YS-282 MPa, EI-21.5%). It could be noticed that (Fig. 42) after cryo-FSP, the YS and UTS of the nanocomposite samples are higher than that of the Al7075 sample. However, the %elongation of the alloy sample is bit higher as compared to that of the nanocomposite samples. As expected,

addition of nanoparticles has remarkably enhanced the strength of Al7075-SiC nanocomposites in expense of the ductility. A gradual improvement in the YS and UTS could be observed (Fig. 42) with increasing the SiC weight fraction up to 3wt.%. For example, the UTS of the cryo-FSPed NC2 and NC3 samples, respectively, are found to be 490 MPa and 552 MPa. In contradiction to the trend, cryo-FSPed NC5 sample showed lower tensile strength as well as ductility (UTS-484 MPa, EI-12%) than that of the cryo-FSPed NC3 sample. The obvious difference in the strength and ductility of the cryo-FSPed NC5 sample is closely related to the tendency of particle dispersion after cryo-FSP; the SiC nanoparticles were more clustered and agglomerated as discussed in earlier microstructural discussion. It is generally accepted that small agglomerates of reinforcement lead to high stress concentrations and tend to crack early during tensile deformation. On the other hand, uniform redistribution of the reinforcement phase could deflect and hinder further propagation of cracks. Such behaviour reduces the possibility of material cracking under low level of stress/load, which enhances the mechanical performance of the composites with uniform homogeneous microstructure.

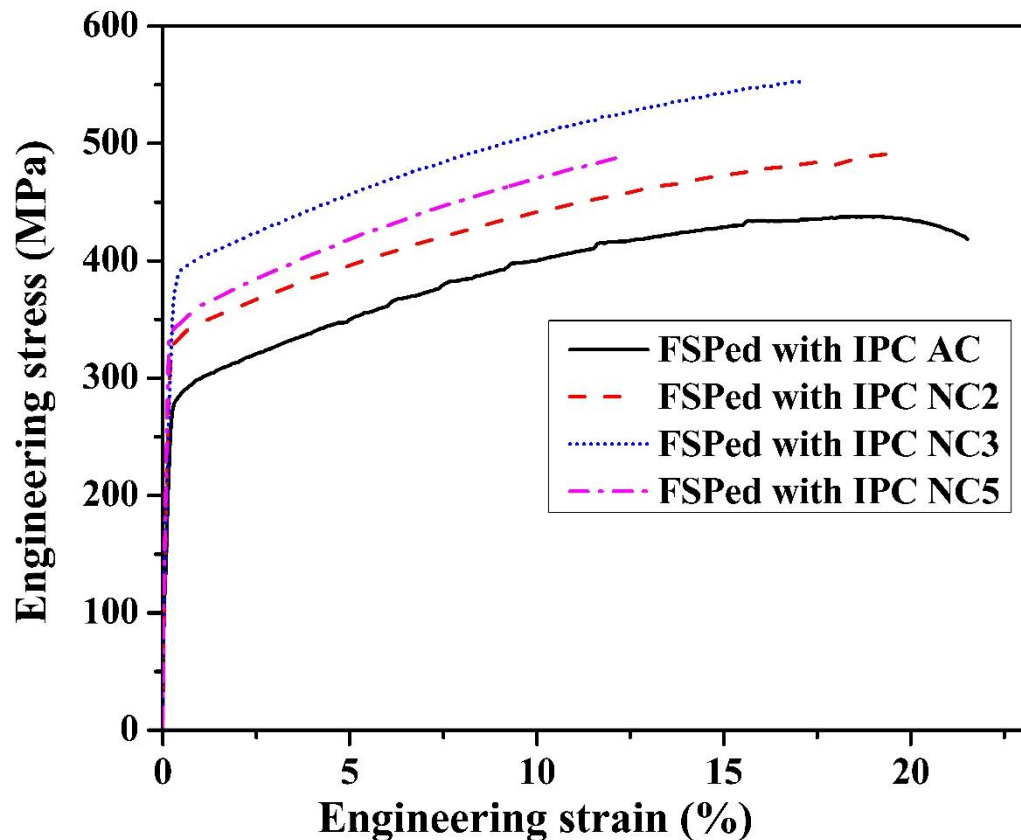


Fig. 4.42: Tensile curves of samples FSPed at in-process cryocooling condition.

Among all the cryo-FSPed samples, the 3wt.% reinforced Al7075-SiC nanocomposite exhibits the superior tensile properties in terms of YS (391 MPa), UTS (552 MPa) and %elongation (17%). The strength of materials after FSP under cryogenic condition depends on the following factors: (i) The homogenous SiC nanoparticle redistribution gives rise to better Orowan strengthening. As uniform distribution of the nanosized particles reduce the interparticle spacing, a strong positive influence on the Orowan strengthening is obtained ($\tau=Gb/l$). (ii) The development of a fine grained microstructure during cryo-FSP further contributes to the strength enhancement as per Hall–Petch relationship (Dieter, 1986). (iii) Moreover, it should be noted that the formation of fine η' precipitates (70-100 nm) also contributes to the precipitation strengthening after cryo-FSP. Hence, the improvement of strength can be accredited to the grain size effect as well as the role of ultrafine precipitates formation and uniform distribution of SiC nanoparticles. Elimination of the casting defects also plays an important role in improving the properties. Overall, the mechanical properties of the processed samples are well-corroborated with the microstructural characteristics (Fig. 4.38).

4.4.3 Summary

In this section, effect of in-process cryocooling during FSP of the cast Al7075-SiC nanocomposites (2%, 3% and 5%) has been investigated. FSP at cryogenic temperature was conducted successfully on Al7075-SiC nanocomposites (2%, 3% and 5%). Following conclusions can be drawn as the major outcome of the present study.

- Microstructural analysis through TEM and EBSD confirmed the formation of fine matrix grains in which nanosize SiC particles and precipitates of η' phase are dispersed uniformly. Better microstructural modification was achieved for the Al7075-3wt.% SiC nanocomposite (e.g. grain size 1-3 μm & η' phase size 70-100 nm).
- After the cryo-FSP, tensile strength was found to be superior for the Al7075-3wt.% SiC nanocomposite (UTS-552 MPa with 17% elongation) than other compositions (490 MPa for Al7075-2wt.% SiC and 488 MPa for Al7075-5wt.% SiC).
- The cryo-FSP modified the distribution of SiC nanoparticles, refined the matrix grain size, enhanced the particle/matrix interface characteristics and eliminated the casting

defects from the as cast composites. These microstructural changes drastically improve the mechanical properties both strength (UTS/YS/hardness) and ductility.

4.5 Comparison of properties of Al7075 and its composites FSPed in NAC and IPC conditions

Finally, in this section, a comparative study has been made to illustrate the variation in the mechanical properties (i.e. hardness, tensile strength & ductility), wear resistance and corrosion behavior of the Al7075 alloy and Al7075-SiC nanocomposites samples FSPed under normal air cooling (NAC) and in-process cryocooling (IPC) conditions.

- a) It can be noted from sections 4.1, 4.2, 4.3 and 4.4 (discussed earlier) that different properties of the Al7075 alloy and its composites FSPed under IPC condition are found to be much superior in comparison to that of the FSPed samples under NAC condition.
- b) The IPC during FSP of Al7075 alloy led to 65 and 72% improvement in the Vickers hardness and tensile strength, respectively, in comparison to the mechanical properties of the solutionized base metal (as shown in Fig. 4.43). This is attributed to the better grain size refinement and development of semi-coherent η' phase in the IPC FSPed sample.

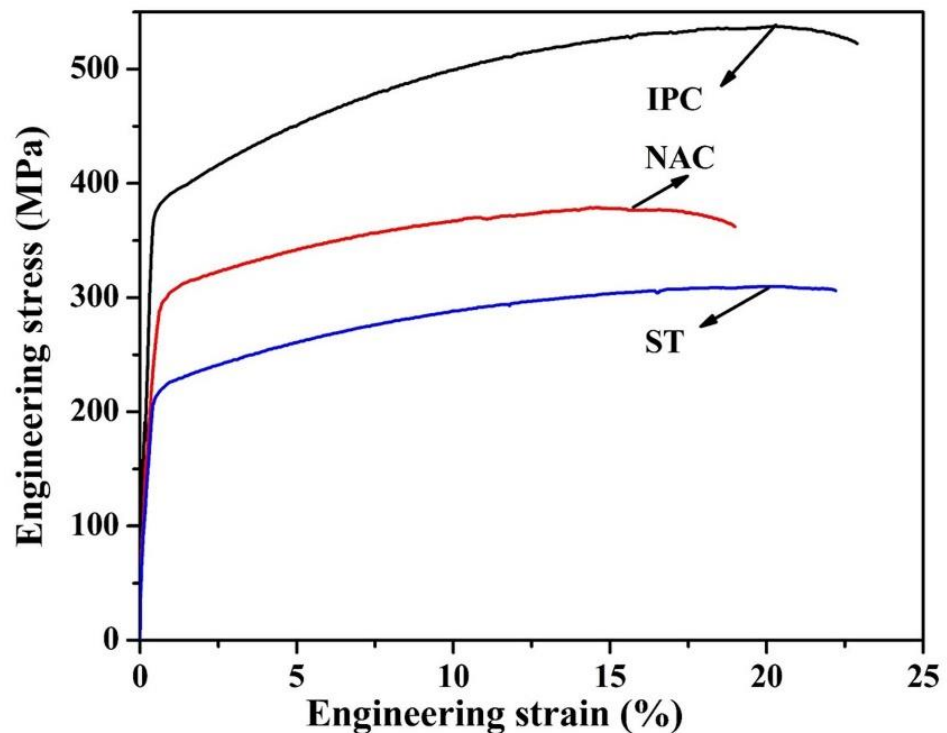


Fig. 4.43: Tensile curves of Al7075 alloy FSPed at different cooling conditions (Repeated from Fig. 4.35).

- c) The variation in the tensile properties of different samples as a consequence of change in the reinforcement wt.% and cooling effects are represented by engineering stress-strain curves in Fig. 4.44. It can be noted that the FSPed Al7075-SiC nanocomposite samples processed under IPC condition showed better mechanical properties (tensile strength with significant ductility) as compared to those for the FSPed nanocomposite samples under NAC condition and Al7075 cast sample FSPed under IPC condition (Fig. 4.44). Moreover, improvement in the mechanical properties is found to be maximum for the Al7075-3wt.% SiC nanocomposite sample FSPed under IPC condition (TS=552 MPa, and %El.=17 %) as compared to any other samples studied (Al7075 alloy/composites) in any condition.
- d) It can also be observed that the Al7075, Al7075-2wt.% SiC and Al7075-3wt.% SiC samples FSPed under IPC condition showed extra work hardening effect as compared to that of the other samples. In IPC condition, the positive influence of the controlled temperature and effective cooling rate has led to the formation of fine semi-coherent η' precipitates along with the formation of finer matrix grains. Hence, extra enhancement in the work hardening capacity could be related to the accumulation of additional dislocations by these finely dispersed η' precipitates within the finer grains.

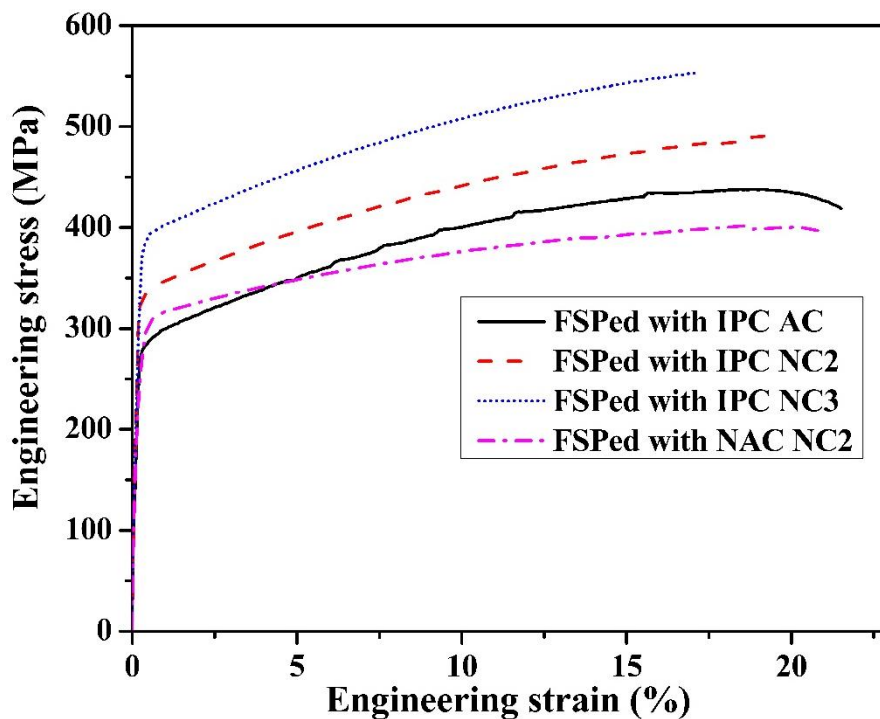


Fig. 4.44: Variation of engineering stress-strain curves of the FSPed Al7075 alloy and its nanocomposite samples as a function of different processing environments.

e) It can be noted from Fig. 4.45 that the average hardness value of the FSPed nanocomposite samples in both the conditions, NAC and IPC, is higher than that of the unreinforced alloy processed under IPC condition. This is due to the higher inherent hardness of the SiC particles (as per the rule of mixture), uniform dispersion of nanosize SiC particles after the FSP and extra grain size refinement because of grain boundary pinning by these particulates.

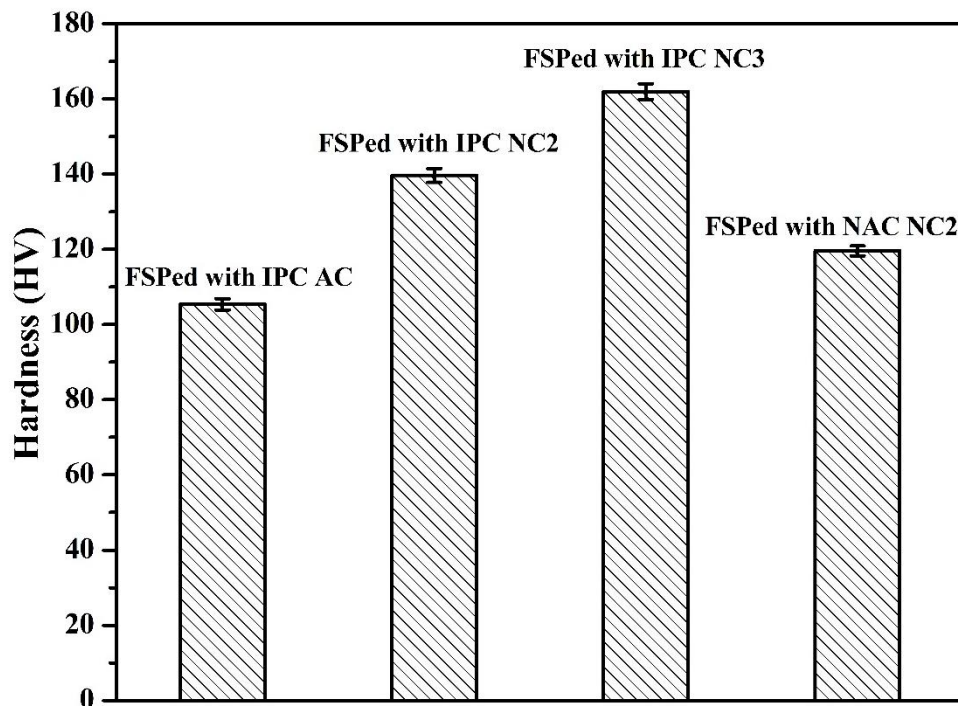


Fig. 4.45: Variation in hardness of the different samples after FSP with NAC and IPC condition.

f) Among all the specimens studied for the wear test, the Al7075-3wt.% SiC nanocomposite sample FSPed under IPC condition showed superior wear resistance (Fig. 4.46). The superior tribological behavior has been described in the light of better dispersion of the hard nanosize SiC particles within the finer matrix grains and evolution of semi-coherent of η' precipitates after FSP under IPC state. Uniform dispersion of the SiC particles reduces the real contact area between the sample and the counter body, thereby improving the dry sliding wear properties.

g) Overall, the FSPed Al7075-3wt.% SiC nanocomposite sample with IPC condition showed superior mechanical and wear resistance properties. This is ascribed to the maximum grain size reduction because of restricted grain growth (lower peak temperature

during cryo-FSP), distribution of SiC nanoparticles uniformly within the finer Al matrix grains, pinning effect of the particles on the grain boundaries, increase in the particle-matrix interface chemistry, suppression of coarsening of the strengthening η' phase due to higher cooling rate and elimination of casting defects (porosity, agglomeration etc.) after the cryo-FSP.

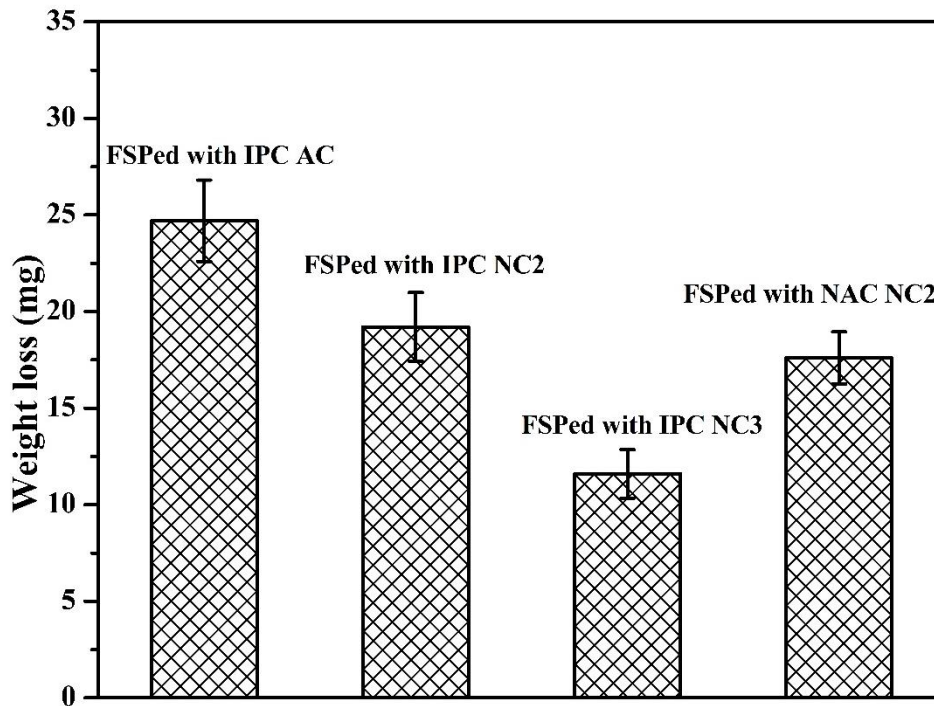


Fig. 4.46: Variation in weight loss of composites in the as-cast state and after the FSP.

- h) Corrosion resistance are found to be almost similar for the FSPed NC3 sample with IPC state and FSPed NC2 sample with NAC condition (Fig. 4.47), but it is much superior as compared to that of the other samples studied (Al7075 alloy/composites). The enhancement of the corrosion resistance after the FSP is attributed to the decrease in the heterogeneity on the surface and uniform dispersion of the reinforced particles. All such beneficial effects were found to be superior for the nanoparticles reinforced composites. It is presumed that the nanosize particles could cover more surface area of the exposed metallic surface to the corrosive solution and improved particle/matrix interface characteristics.

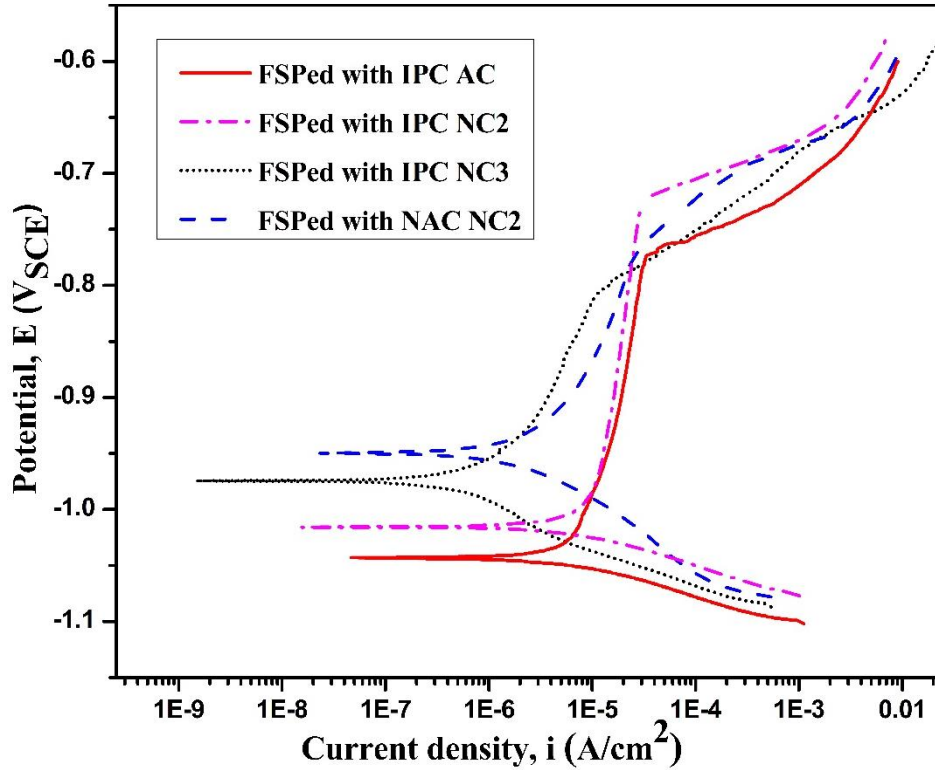


Fig. 4.47: Variation of potentiodynamic polarization curves of FSPed Al7075 alloy and its composites as a function of different processing environments.

- i) Though, FSP with IPC conditions, Al7075-SiC nanocomposites just could overcome the strength of the Al7075 alloy in T651, the stir casting followed by IPC FSP is economical, and able to produce nanocomposite structure easily in much simpler way. Moreover, the ductility of the FSPed nanocomposites was higher than the age-hardened alloy. Hence, the present method is industrially more viable than the production of age-hardenable alloy through casting followed by forging/rolling, solutionizing and age hardening.
- j) The nugget zone in the IPC FSP showed a great potential to achieve high strength with good ductility through development of fine grained Al7075-SiC nanocomposites. It is to be noted that the mechanical properties of the friction stir weld-joint is inferior compared to that of the base metal/alloy. As FSP is a derivative of friction stir welding (FSW) method, the FSW with controlled IPC could be highly useful to improve the mechanical properties of weld-joint of the components manufactured by FSW.
- k) Finally, it should be noted that the Al7075-SiC nanocomposites FSPed under IPC conditions showed the improvement of mechanical properties due to the evolution of fine η' phase in the range of 70-100nm besides the uniform distribution of SiC nanoparticles

and formation of fine matrix grains. However, the size as well as characteristic of the η' phase is not similar to that of the Al7075 alloy in T651 condition (i.e. size of the η' phase in T651 Al7075 alloy was in the range of 10-30nm in the present study). Hence, mechanical properties could be further enhanced, if the evolution of the η' precipitates is possible to control to produce them in the size range of 10-30nm making more coherent/semi-coherent with matrix by standardizing the IPC FSP parameters (e.g. enhancing the cooling rate during cryo-FSP). This would effectively arrest the dislocation movement to obtain high strength. Therefore, this tactic could combine the precipitation strengthening, grain size strengthening and particle strengthening mechanisms to achieve maximum strength in the age-hardenable Al7075 alloy and its composites. This could result in superior mechanical and wear properties compared to commercial 7075 alloy.

5.1 Conclusions

This section deals with the major outcomes and conclusions of the present study as follows:

- (a) Effective optimization of the FSP parameters has a pronounced effect on temperature generation during processing of the material, hence affects the grain size refinement, mechanical properties and corrosion behavior of the processed material. Results demonstrated that average grain size of the base Al7075-T651 alloy decreased with an increase in the traverse speed of the FSP due to decrease in the heat input with traverse speed. As a result, the yield strength, hardness and wear resistance of the FSPed samples increased gradually with an increase in the traverse speed. However, partial dissolution and/or overaging of precipitates during FSP caused softening and reduced mechanical properties of the FSPed samples relative to the base Al7075-T651 alloy.
- (b) After the FSP, the average grain size of the stir-cast Al7075-2wt.% SiC micro- and nanocomposites was found to be $\sim 9 \mu\text{m}$ and $\sim 4 \mu\text{m}$, respectively. The FSP led to modify the cast microstructure into uniformly distributed SiC particles within the matrix of refined grain structure with reduced casting defects. Thus, the vast improvement of the mechanical properties of the FSPed nanocomposite (tensile strength $\sim 190\%$, elongation 854% and wear resistance ~ 5 times simultaneously as compared to that of the as-cast counterpart) are mainly due to the microstructural modification arisen after the FSP. The major strengthening mechanisms involved in such composite structures were analyzed to be the grain boundary strengthening (i.e. Hall-Petch strengthening), Orowan strengthening through nanosize particle reinforcement and precipitation hardening (η' phase).
- (c) The corrosion potentials of the as-cast micro- and nanocomposites (both 2wt.% SiC reinforcement) were found to shift towards noble direction after the FSP. Enhancement of corrosion resistance after the FSP is attributed to the decrease in the heterogeneity on the surface and uniform dispersion of the reinforced particles. All such beneficial effects were found to be superior for the nanoparticles reinforced composite due to the nanosize

particles could cover more surface area of the exposed metallic surface to the corrosive solution and improved particle/matrix interface characteristics.

- (d) It was found that partial dissolution and/or overaging of η' precipitates during room temperature FSP caused softening. Hence, in-process cryocooling (IPC) strategy was successfully developed in order to control the precipitate kinetics besides the grain size refinement during FSP of Al7075 alloy and its composites. The effect of IPC during FSP led to about 2 times more grain size refinement in the nugget zone than that achieved in normal air cooling (NAC) FSPed samples. EBSD and TEM investigation confirmed the formation of fine grain (2.4 μm) with nanosize precipitates of η' phase (20-30 nm) in the IPC FSPed sample as compared to 4.7 μm average grain size after FSP at NAC state. This is due to the effective way of heat rejection from the processing zone (i.e. nugget zone) by circulating liquid mixture at cryogenic temperature in the IPC condition, which controls the thermal boundaries of the material during FSP. The yield strength (384 MPa) and ductility (22.8%) of the FSPed Al7075 sample under IPC situation are found to be much superior as compared to those for the FSPed sample under NAC condition (305 MPa, ~19%) and solution treated Al7075 sample (204 MPa, 22%).
- (e) Finally, it was found that the FSP with IPC approach offered a great potential in the development of fine grained Al7075-SiC nanocomposites with much improved mechanical properties through microstructural modification. In the last part of the study, stir-cast Al7075-SiC nanocomposite samples with varying weight percentage of nanosize SiC particles (2, 3 and 5%) were successfully processed by FSP under IPC condition. The superior results were obtained for the Al7075-3wt.% SiC nanocomposite sample (grain size: 1-3 μm ; η' phase: 70-100 nm) as compared to other composite samples. This has been confirmed through microstructural analysis using TEM and EBSD. After the cryo-FSP, tensile strength was found to be 490 MPa for Al7075-2wt.% SiC nanocomposite, 552 MPa for the Al7075-3wt.% SiC nanocomposite and 484 MPa for Al7075-5wt.% SiC nanocomposite samples. Secondary processing through cryo-FSP modified the distribution of SiC nanoparticles, refined the matrix grain size, controlled the formation of η' phase, enhanced the particle/matrix interface characteristics and eliminated the casting defects from the as-cast composites. These microstructural changes significantly improved the mechanical properties (i.e. yield strength, ductility and hardness).

Results obtained from the series of experiments in the present study demonstrated the significance of matrix material, reinforcement and secondary processing (FSP) to develop high strength fine grained Al7075-SiC nanocomposites. A change in the process parameters led to considerable difference in the evolution of microstructural features thereby final mechanical properties of the processed material. The FSP with IPC setup can be suggested in order to control the precipitate kinetics besides the grain size refinement during FSP of Al7075 alloy and its composites.

5.2 Future scope of the study

In the present study, effect of normal and in-process cryocooling during FSP on the microstructural evolution and mechanical properties of the Al7075 alloy and its composites was investigated. Following works relevant to the FSP of Al alloys could be studied in future.

- (a) Different computational models could be used to predict the optimum process parameter for the FSP. This could help in estimating the amount of heat generation during processing and required flow rates of coolant during in-process cooling for the optimum performance of FSP.
- (b) Multi-pass FSP could be studied to obtain bulk-size samples of the nanocomposites that enables to investigate fracture toughness, fatigue etc. These studies could reveal the understanding of fundamental deformation mechanisms operating before failure, which would be helpful to assess the practical applicability of the composites. Moreover, superplastic formation of the AMCs processed by multi-pass cryo-FSP could be studied and compared with the normal FSP condition.
- (c) In the present study, corrosion resistance was investigated using only Tafel test. Further analysis of the corrosion resistance could be carried out by electrochemical impedance spectroscopy. Moreover, in-depth wear study could be carried out with different counter-body and loads for the FSPed samples.

References

- [1] Agarwala, V. and Dixit, D., 1981. Fabrication of aluminium base composite by foundry technique. *Transactions of the Japan Institute of Metals*, 22(8), pp.521-526.
- [2] Al-Aqeeli, N., Abdullahi, K., Hakeem, A.S., Suryanarayana, C., Laoui, T. and Nouari, S., 2013. Synthesis, characterisation and mechanical properties of SiC reinforced Al based nanocomposites processed by MA and SPS. *Powder Metallurgy*, 56(2), pp.149-157.
- [3] Alidokht, S.A., Abdollah-Zadeh, A., Soleymani, S. and Assadi, H., 2011. Microstructure and tribological performance of an aluminium alloy based hybrid composite produced by friction stir processing. *Materials & Design*, 32(5), pp.2727-2733.
- [4] Alidokht, S.A., Abdollah-zadeh, A., Soleymani, S., Saeid, T. and Assadi, H., 2012. Evaluation of microstructure and wear behavior of friction stir processed cast aluminum alloy. *Materials Characterization*, 63, pp.90-97.
- [5] Amirizad, M., Kokabi, A.H., Gharacheh, M.A., Sarrafi, R., Shalchi, B. and Azizieh, M., 2006. Evaluation of microstructure and mechanical properties in friction stir welded A356+15% SiCp cast composite. *Materials Letters*, 60(4), pp.565-568.
- [6] Arab, M.S., El Mahallawy, N., Shehata, F. and Agwa, M.A., 2014. Refining SiCp in reinforced Al-SiC composites using equal-channel angular pressing. *Materials & Design*, 64, pp.280-286.
- [7] Arbogast, W.J. and Hartley, P.J., 1999. Friction stir weld technology development at Lockheed Martin Michoud Space System-an overview. *ASM International, Trends in Welding Research (USA)*, pp.541-546.
- [8] Ardakani, M.R.K., Khorsand, S., Amir Khanlou, S. and Nayyeri, M.J., 2014. Application of compocasting and cross accumulative roll bonding processes for manufacturing high strength, highly uniform and ultra-fine structured Al/SiCp nanocomposite. *Materials Science and Engineering: A*, 592, pp.121-127.
- [9] Asadi, P., Faraji, G. and Besharati, M.K., 2010. Producing of AZ91/SiC composite by friction stir processing (FSP). *The International Journal of Advanced Manufacturing Technology*, 51(1-4), pp.247-260.
- [10] Ashjari, M., Asl, A.M. and Rouhi, S., 2015. Experimental investigation on the effect of process environment on the mechanical properties of AA5083/Al₂O₃ nanocomposite fabricated via friction stir processing. *Materials Science and Engineering: A*, 645, pp.40-46.

- [11] Atrian, A., Majzoobi, G.H., Enayati, M.H. and Bakhtiari, H., 2014. Mechanical and microstructural characterization of Al7075/SiC nanocomposites fabricated by dynamic compaction. *International Journal of Minerals, Metallurgy, and Materials*, 21(3), pp.295-303.
- [12] Ayer, R., Koo, J.Y., Steeds, J.W. and Park, B.K., 1985. Microanalytical study of the heterogeneous phases in commercial Al-Zn-Mg-Cu alloys. *Metallurgical Transactions A*, 16(11), pp.1925-1936.
- [13] Azimzadegan, T. and Serajzadeh, S., 2010. An investigation into microstructures and mechanical properties of AA7075-T6 during friction stir welding at relatively high rotational speeds. *Journal of materials engineering and performance*, 19(9), pp.1256-1263.
- [14] Bachmaier, A., Kerber, M., Setman, D. and Pippan, R., 2012. The formation of supersaturated solid solutions in Fe-Cu alloys deformed by high-pressure torsion. *Acta Materialia*, 60(3), pp.860-871.
- [15] Balasubramanian, V., 2008. Relationship between base metal properties and friction stir welding process parameters. *Materials Science and Engineering: A*, 480(1-2), pp.397-403.
- [16] Barmouz, M., Givi, M.K.B. and Seyfi, J., 2011. On the role of processing parameters in producing Cu/SiC metal matrix composites via friction stir processing: Investigating microstructure, microhardness, wear and tensile behavior. *Materials characterization*, 62(1), pp.108-117.
- [17] Barnwal, V.K., Chakrabarty, S., Tewari, A., Narasimhan, K. and Mishra, S.K., 2018. Forming behavior and microstructural evolution during single point incremental forming process of AA-6061 aluminum alloy sheet. *The International Journal of Advanced Manufacturing Technology*, 95(1-4), pp.921-935.
- [18] Basariya, M.R., Srivastava, V.C. and Mukhopadhyay, N.K., 2014. Microstructural characteristics and mechanical properties of carbon nanotube reinforced aluminum alloy composites produced by ball milling. *Materials & Design*, 64, pp.542-549.
- [19] Bauri, R., 2014. Optimization of process parameters for friction stir processing (FSP) of Al-TiC in situ composite. *Bulletin of Materials Science*, 37(3), pp.571-578.
- [20] Bauri, R., Yadav, D. and Suhas, G., 2011. Effect of friction stir processing (FSP) on microstructure and properties of Al-TiC in situ composite. *Materials Science and Engineering: A*, 528(13-14), pp.4732-4739.
- [21] Besharati-Givi, M.K. and Asadi, P., 2014. *Advances in friction stir welding and processing*. Elsevier.

- [22] Bhushan, R.K., Kumar, S. and Das, S., 2013. Fabrication and characterization of 7075 Al alloy reinforced with SiC particulates. *The International Journal of Advanced Manufacturing Technology*, 65(5-8), pp.611-624.
- [23] Boostani, A.F., Tahamtan, S., Jiang, Z.Y., Wei, D., Yazdani, S., Khosroshahi, R.A., Mousavian, R.T., Xu, J., Zhang, X. and Gong, D., 2015. Enhanced tensile properties of aluminium matrix composites reinforced with graphene encapsulated SiC nanoparticles. *Composites Part A: Applied Science and Manufacturing*, 68, pp.155-163.
- [24] Brammer, T., Ray, P.K., Misra, S., Ye, Y.Y., Akinc, M. and Kramer, M.J., 2010. Computational and experimental design of novel high temperature alloys. In *Advances in Science and Technology*, 72, pp.31-39.
- [25] Buchibabu, V., Reddy, G.M., Kulkarni, D. and De, A., 2016. Friction stir welding of a thick Al-Zn-Mg alloy plate. *Journal of Materials Engineering and Performance*, 25(3), pp.1163-1171.
- [26] Callister, W.D. and Rethwisch, D.G., 2007. *Materials science and engineering: an introduction* (Vol. 7, pp. 665-715). New York: John Wiley & Sons.
- [27] Cao, Y., Li, H., Liang, Z. and Wang, D., 2017. Effect of water cooling on the microstructure and mechanical properties of 6N01 aluminum alloy P-MIG-welded joints. *Journal of Materials Engineering and Performance*, 26(8), pp.3929-3938.
- [28] Cavaliere, P., 2005. Mechanical properties of friction stir processed 2618/Al₂O₃/20p metal matrix composite. *Composites part A: applied science and manufacturing*, 36(12), pp.1657-1665.
- [29] Cavanaugh, M.K., Li, J.C., Birbilis, N. and Buchheit, R.G., 2014. Electrochemical characterization of intermetallic phases common to aluminum alloys as a function of solution temperature. *Journal of the Electrochemical Society*, 161(12), pp.C535-C543.
- [30] Chakrabarty, S., Mishra, S.K. and Pant, P., 2014. Crystallographic orientation and boundary effects on misorientation development in austenitic stainless steel. *Materials Science and Engineering: A*, 617, pp.228-234.
- [31] Chang, C.I., Du, X.H. and Huang, J.C., 2007. Achieving ultrafine grain size in Mg-Al-Zn alloy by friction stir processing. *Scripta Materialia*, 57(3), pp.209-212.
- [32] Chang, C.I., Lee, C.J. and Huang, J.C., 2004. Relationship between grain size and Zener-Holloman parameter during friction stir processing in AZ31 Mg alloys. *Scripta Materialia*, 51(6), pp.509-514.
- [33] Charit, I. and Mishra, R.S., 2005. Low temperature superplasticity in a friction stir processed ultrafine grained Al-Zn-Mg-Sc alloy. *Acta Materialia*, 53(15), pp.4211-4223.

- [34] Chen, Y., Ding, H., Li, J.Z., Zhao, J., Fu, M.J. and Li, X.H., 2015. Effect of welding heat input and post-welded heat treatment on hardness of stir zone for friction stir welded 2024-T3 aluminum alloy. *Transactions of Nonferrous Metals Society of China*, 25(8), pp.2524-2532.
- [35] Chen, Y.C., Feng, J.C. and Liu, H.J., 2009. Precipitate evolution in friction stir welding of 2219-T6 aluminum alloys. *Materials characterization*, 60(6), pp.476-481.
- [36] Chen, Z., Li, J., Borbely, A., Ji, G., Zhong, S.Y., Wu, Y., Wang, M.L. and Wang, H.W., 2015. The effects of nanosized particles on microstructural evolution of an in-situ TiB₂/6063Al composite produced by friction stir processing. *Materials & Design*, 88, pp.999-1007.
- [37] Chen, Z., Mo, Y. and Nie, Z., 2013. Effect of Zn content on the microstructure and properties of super-high strength Al-Zn-Mg-Cu alloys. *Metallurgical and Materials Transactions A*, 44(8), pp.3910-3920.
- [38] Das, P., Jayaganthan, R. and Singh, I.V., 2011. Tensile and impact-toughness behaviour of cryorolled Al 7075 alloy. *Materials & Design*, 32(3), pp.1298-1305.
- [39] Dasgupta, R., 2010. Sliding wear resistance of Al-alloy particulate composites: An assessment on its efficacy. *Tribology International*, 43(5-6), pp.951-958.
- [40] Dasharath, S.M., Ghosh, S. and Mula, S., 2017. Effect of SFE on tensile and fatigue behavior of ultrafine grained Cu-Zn and Cu-Al alloys developed by cryo-rolling/forging. *Materials Science and Engineering: A*, 693, pp.73-83.
- [41] Deuis, R.L., Subramanian, C. and Yellup, J.M., 1996. Abrasive wear of aluminium composites-a review. *Wear*, 201(1-2), pp.132-144.
- [42] Dey, A., Kayal, N., Molla, A.R. and Chakrabarti, O., 2014. Investigation of thermal oxidation of Al₂O₃-coated SiC powder. *Thermochimica acta*, 583, pp.25-31.
- [43] Dieter, G.E. and Bacon, D.J., 1986. *Mechanical metallurgy (Vol. 3)*. New York: McGraw-hill.
- [44] Dinaharan, I., Balakrishnan, M., Selvam, J.D.R. and Akinlabi, E.T., 2019. Microstructural characterization and tensile behavior of friction stir processed AA6061/Al₂Cu cast aluminum matrix composites. *Journal of Alloys and Compounds*, 781, pp.270-279.
- [45] El-Rayes, M.M. and El-Danaf, E.A., 2012. The influence of multi-pass friction stir processing on the microstructural and mechanical properties of aluminum alloy 6082. *Journal of Materials Processing Technology*, 212(5), pp.1157-1168.
- [46] Ezatpour, H.R., Parizi, M.T., Sajjadi, S.A., Ebrahimi, G.R. and Chaichi, A., 2016. Microstructure, mechanical analysis and optimal selection of 7075 aluminum alloy based composite reinforced with alumina nanoparticles. *Materials Chemistry and Physics*, 178, pp.119-127.

- [47] Feng, X., Liu, H. and Babu, S.S., 2011. Effect of grain size refinement and precipitation reactions on strengthening in friction stir processed Al-Cu alloys. *Scripta Materialia*, 65(12), pp.1057-1060.
- [48] Feng, X., Liu, H. and Lippold, J.C., 2013. Microstructure characterization of the stir zone of submerged friction stir processed aluminum alloy 2219. *Materials characterization*, 82, pp.97-102.
- [49] Fontana, M.G., 2005. *Corrosion engineering*. Tata McGraw-Hill Education.
- [50] Fratini, L., Buffa, G. and Shivpuri, R., 2009. In-process heat treatments to improve FS-welded butt joints. *The International Journal of Advanced Manufacturing Technology*, 43(7-8), pp.664-670.
- [51] Fuloria, D., Goel, S., Jayaganthan, R., Srivastava, D., Dey, G.K. and Saibaba, N., 2015. Mechanical properties and microstructural evolution of ultrafine grained zircaloy-4 processed through multiaxial forging at cryogenic temperature. *Transactions of Nonferrous Metals Society of China*, 25(7), pp.2221-2229.
- [52] Garcia, M., Martinez, H.V. and Ortiz, A., 2010. Compoforming of Al-Si metal matrix composites reinforced with beta-SiC: An alternative technique. *Open Industrial & Manufacturing Engineering Journal*, 3, pp.1-6.
- [53] Gazawi, A.A., Gabbitas, B., Zhang, D., Kong, C. and Munroe, P., 2015. Microstructure and mechanical properties of ultrafine structured Al-4wt% Cu-(2.5-10) vol.% SiC nanocomposites produced by powder consolidation using powder compact extrusion. *Journal of Research in Nanotechnology*, 2015, pp.1-5.
- [54] Gibson, B.T., Lammlein, D.H., Prater, T.J., Longhurst, W.R., Cox, C.D., Ballun, M.C., Dharmaraj, K.J., Cook, G.E. and Strauss, A.M., 2014. Friction stir welding: Process, automation, and control. *Journal of Manufacturing Processes*, 16(1), pp.56-73.
- [55] Giribaskar, S., Prasad, R. and Ramkumar, J., 2008. TEM studies on recovery and recrystallisation in equal channel angular extrusion processed Al-3%Mg alloy. *Transactions of the Indian Institute of Metals*, 61(2-3), pp.173-176.
- [56] Golezani, A.S., Barenji, R.V., Heidarzadeh, A. and Pouraliakbar, H., 2015. Elucidating of tool rotational speed in friction stir welding of 7020-T6 aluminum alloy. *The International Journal of Advanced Manufacturing Technology*, 81(5-8), pp.1155-1164.
- [57] Gourdet, S. and Montheillet, F., 2003. A model of continuous dynamic recrystallization. *Acta Materialia*, 51(9), pp.2685-2699.
- [58] Harichandran, R. and Selvakumar, N., 2016. Effect of nano/micro B₄C particles on the mechanical properties of aluminium metal matrix composites fabricated by ultrasonic cavitation-assisted solidification process. *Archives of Civil and Mechanical Engineering*, 16(1), pp.147-158.

- [59] Harnby, N., Edwards, M.F., Nienow, A.W., 1997. *Mixing in the process industries*. Butterworth-Heinemann.
- [60] Hashim, J., Looney, L. and Hashmi, M.S.J., 1999. Metal matrix composites: production by the stir casting method. *Journal of materials processing technology*, 92, pp.1-7.
- [61] Hashim, J., Looney, L. and Hashmi, M.S.J., 2001. The enhancement of wettability of SiC particles in cast aluminium matrix composites. *Journal of Materials Processing Technology*, 119(1-3), pp.329-335.
- [62] Hassan, K.A.A., Prangnell, P.B., Norman, A.F., Price, D.A. and Williams, S.W., 2003. Effect of welding parameters on nugget zone microstructure and properties in high strength aluminium alloy friction stir welds. *Science and Technology of Welding and joining*, 8(4), pp.257-268.
- [63] Hembrom, S., Roy, B.N., Khobragade, N. and Roy, D., 2016. Studies on amorphous alloy dispersed aluminum matrix composite prepared by high pressure torsion. *Journal of Materials Science Research*, 5(1), pp.89-96.
- [64] Hofmann, D.C. and Vecchio, K.S., 2005. Submerged friction stir processing (SFSP): An improved method for creating ultra-fine-grained bulk materials. *Materials Science and Engineering: A*, 402(1-2), pp.234-241.
- [65] Hong, S.J., Kim, H.M., Huh, D., Suryanarayana, C. and Chun, B.S., 2003. Effect of clustering on the mechanical properties of SiC particulate-reinforced aluminum alloy 2024 metal matrix composites. *Materials Science and Engineering: A*, 347(1-2), pp.198-204.
- [66] Hoziefa, W., Toschi, S., Ahmed, M.M.Z., Morri, A., Mahdy, A.A., Seleman, M.E.S., El-Mahallawi, I., Ceschini, L. and Atlam, A., 2016. Influence of friction stir processing on the microstructure and mechanical properties of a compocast AA2024-Al₂O₃ nanocomposite. *Materials & Design*, 106, pp.273-284.
- [67] Huang, J.C., Hsiao, I.C., Wang, T.D., Lou, B.Y., 2000. EBSD study on grain boundary characteristics in fine-grained Al alloys. *Scr. Mater.* 43, 213–220.
- [68] Humphreys, F.J. and Hatherly, M., 2012. *Recrystallization and related annealing phenomena*. Elsevier.
- [69] Huq, M.Z. and Celis, J.P., 1997. Reproducibility of friction and wear results in ball-on-disc unidirectional sliding tests of TiN-alumina pairings. *Wear*, 212(2), pp.151-159.
- [70] Ibrahim, I.A., Mohamed, F.A. and Lavernia, E.J., 1991. Particulate reinforced metal matrix composites-a review. *Journal of materials science*, 26(5), pp.1137-1156.
- [71] Imam, M., Ueji, R. and Fujii, H., 2016. Effect of online rapid cooling on microstructure and mechanical properties of friction stir welded medium carbon steel. *Journal of Materials Processing Technology*, 230, pp.62-71.

- [72] Inturi, R.B. and Szklarska-Smialowska, Z., 1992. Localized corrosion of nanocrystalline 304 type stainless steel films. *Corrosion*, 48(5), pp.398-403.
- [73] Jamalain, H.M., Ramezani, H., Ghobadi, H., Ansari, M., Yari, S. and Givi, M.K.B., 2016. Processing-structure-property correlation in nano-SiC-reinforced friction stir welded aluminum joints. *Journal of Manufacturing Processes*, 21, pp.180-189.
- [74] Jana, S., Mishra, R.S., Baumann, J.B. and Grant, G., 2010. Effect of friction stir processing on fatigue behavior of an investment cast Al-7Si-0.6Mg alloy. *Acta Materialia*, 58(3), pp.989-1003.
- [75] Jariyaboon, M., Davenport, A.J., Ambat, R., Connolly, B.J., Williams, S.W. and Price, D.A., 2010. Effect of cryogenic cooling on corrosion of friction stir welded AA7010-T7651. *Anti-Corrosion Methods and Materials*, 57(2), pp.83-89.
- [76] Jata, K. and Semiatin, S., 2000a. Continuous dynamic recrystallization during friction stir welding of high strength aluminum alloys (No. AFRL-ML-WP-TP-2003-441). Air Force Research Lab Wright-Patterson AFB OH Materials and Manufacturing Directorate.
- [77] Jata, K.V., Sankaran, K.K. and Ruschau, J.J., 2000b. Friction stir welding effects on microstructure and fatigue of aluminum alloy 7050-T7451. *Metallurgical and materials transactions A*, 31(9), pp.2181-2192.
- [78] Jia, D.C., 2000. Influence of SiC particulate size on the microstructural evolution and mechanical properties of Al-6Ti-6Nb matrix composites. *Materials Science and Engineering: A*, 289(1-2), pp.83-90.
- [79] Jin-Feng, L., Zhuo-wei, P., Chao-xing, L., Zhi-Qiang, J., Wen-Jing, C. and Zi-Qiao, Z., 2008. Mechanical properties, corrosion behaviors and microstructures of 7075 aluminium alloy with various aging treatments. *Transactions of Nonferrous Metals Society of China*, 18(4), pp.755-762.
- [80] Johannes, L.B. and Mishra, R.S., 2007. Multiple passes of friction stir processing for the creation of superplastic 7075 aluminum. *Materials Science and Engineering: A*, 464(1-2), pp.255-260.
- [81] Joshi, A., Kumar, N., Yogesha, K.K., Jayaganthan, R. and Nath, S.K., 2016. Mechanical properties and microstructural evolution in Al 2014 alloy processed through multidirectional cryoforging. *Journal of Materials Engineering and Performance*, 25(7), pp.3031-3045.
- [82] Kalaiselvan, K., Dinaharan, I. and Murugan, N., 2014. Characterization of friction stir welded boron carbide particulate reinforced AA6061 aluminum alloy stir cast composite. *Materials & Design*, 55, pp.176-182.

- [83] Kang, Y.C. and Chan, S.L.I., 2004. Tensile properties of nanometric Al₂O₃ particulate-reinforced aluminum matrix composites. *Materials chemistry and physics*, 85(2-3), pp.438-443.
- [84] Karbalaee Akbari, M., Rajabi, S., Shirvanimoghaddam, K. and Baharvandi, H.R., 2015. Wear and friction behavior of nanosized TiB₂ and TiO₂ particle-reinforced casting A356 aluminum nanocomposites: A comparative study focusing on particle capture in matrix. *Journal of Composite Materials*, 49(29), pp.3665-3681.
- [85] Khodabakhshi, F., Gerlich, A.P., Simchi, A. and Kokabi, A.H., 2015. Cryogenic friction stir processing of ultrafine-grained Al-Mg-TiO₂ nanocomposites. *Materials Science and Engineering: A*, 620, pp.471-482.
- [86] Kim, S.H., Erb, U., Aust, K.T. and Palumbo, G., 2001. Grain boundary character distribution and intergranular corrosion behavior in high purity aluminum. *Scripta Materialia*, 5(44), pp.835-839.
- [87] Kim, Y.G., Fujii, H., Tsumura, T., Komazaki, T. and Nakata, K., 2006. Three defect types in friction stir welding of aluminum die casting alloy. *Materials Science and Engineering: A*, 415(1-2), pp.250-254.
- [88] Koch, C.C., Langdon, T.G. and Lavernia, E.J., 2017. Bulk nanostructured materials. *Metallurgical and Materials Transactions A*, 48(11), pp.5181-5199.
- [89] Koch, C.C., Youssef, K.M., Scattergood, R.O. and Murty, K.L., 2005. Breakthroughs in optimization of mechanical properties of nanostructured metals and alloys. *Advanced Engineering Materials*, 7(9), pp.787-794.
- [90] Kok, M., 2005. Production and mechanical properties of Al₂O₃ particle-reinforced 2024 aluminium alloy composites. *Journal of Materials Processing Technology*, 161(3), pp.381-387.
- [91] Krämer, L., Kormout, K., Setman, D., Champion, Y. and Pippan, R., 2015. Production of bulk metallic glasses by severe plastic deformation. *Metals*, 5(2), pp.720-729.
- [92] Krishna, N.N., Sivaprasad, K. and Susila, P., 2014. Strengthening contributions in ultra-high strength cryorolled Al-4%Cu-3%TiB₂ in situ composite. *Transactions of Nonferrous Metals Society of China*, 24(3), pp.641-647.
- [93] Kumar, A., Godasu, A.K., Pal, K. and Mula, S., 2018. Effects of in-process cryocooling on metallurgical and mechanical properties of friction stir processed Al7075 alloy. *Materials Characterization*, 144, pp.440-447.
- [94] Kumar, A., Kumar, S. and Mukhopadhyay, N.K., 2018. Introduction to magnesium alloy processing technology and development of low-cost stir casting process for magnesium alloy and its composites. *Journal of Magnesium and Alloys*, 6(3), pp.245-254.

- [95] Kumar, A., Pal, K. and Mula, S., 2017. Simultaneous improvement of mechanical strength, ductility and corrosion resistance of stir cast Al7075-2% SiC micro-and nanocomposites by friction stir processing. *Journal of Manufacturing Processes*, 30, pp.1-13.
- [96] Kumar, A., Sharma, S.K., Pal, K. and Mula, S., 2017. Effect of process parameters on microstructural evolution, mechanical properties and corrosion behavior of friction stir processed Al 7075 Alloy. *Journal of Materials Engineering and Performance*, 26(3), pp.1122-1134.
- [97] Kumar, K., Kailas, S.V. and Srivatsan, T.S., 2011. The role of tool design in influencing the mechanism for the formation of friction stir welds in aluminum alloy 7020. *Materials and Manufacturing Processes*, 26(7), pp.915-921.
- [98] Kumar, N., Rao, P.N., Jayaganthan, R. and Brokmeier, H.G., 2015. Effect of cryorolling and annealing on recovery, recrystallisation, grain growth and their influence on mechanical and corrosion behaviour of 6082 Al alloy. *Materials Chemistry and Physics*, 165, pp.177-187.
- [99] Kurtyka, P., Rylko, N., Tokarski, T., Wójcicka, A. and Pietras, A., 2015. Cast aluminium matrix composites modified with using FSP process-Changing of the structure and mechanical properties. *Composite structures*, 133, pp.959-967.
- [100] Kwon, Y.J., Shigematsu, I. and Saito, N., 2003. Mechanical properties of fine-grained aluminum alloy produced by friction stir process. *Scripta Materialia*, 49(8), pp.785-789.
- [101] Lee, H.S., Yeo, J.S., Hong, S.H., Yoon, D.J. and Na, K.H., 2001. The fabrication process and mechanical properties of SiCp/Al-Si metal matrix composites for automobile air-conditioner compressor pistons. *Journal of Materials Processing Technology*, 113(1-3), pp.202-208.
- [102] Li, X., Yang, Y. and Cheng, X., 2004. Ultrasonic-assisted fabrication of metal matrix nanocomposites. *Journal of Materials Science*, 39(9), pp.3211-3212.
- [103] Li, X., Yang, Y. and Weiss, D., 2008. Theoretical and experimental study on ultrasonic dispersion of nanoparticles for strengthening cast aluminum alloy A356. *Metallurgical Science and Technology*, 26(2).
- [104] Li, X.P., Liu, C.Y., Ma, M.Z. and Liu, R.P., 2016. Microstructures and mechanical properties of AA6061-SiC composites prepared through spark plasma sintering and hot rolling. *Materials Science and Engineering: A*, 650, pp.139-144.
- [105] Liu, H.J., Zhang, H.J. and Yu, L., 2011. Effect of welding speed on microstructures and mechanical properties of underwater friction stir welded 2219 aluminum alloy. *Materials & Design*, 32(3), pp.1548-1553.

- [106] Liu, J., Suryanarayana, C., Ghosh, D., Subhash, G. and An, L., 2013. Synthesis of Mg-Al₂O₃ nanocomposites by mechanical alloying. *Journal of Alloys and Compounds*, 563, pp.165-170.
- [107] Liu, S.D., Chen, B., Li, C.B., Dai, Y., Deng, Y.L. and Zhang, X.M., 2015. Mechanism of low exfoliation corrosion resistance due to slow quenching in high strength aluminium alloy. *Corrosion Science*, 91, pp.203-212.
- [108] Lloyd, D.J., 1989. The solidification microstructure of particulate reinforced aluminium/SiC composites. *Composites Science and Technology*, 35(2), pp.159-179.
- [109] Lokesh, G.N., Ramachandra, M., Mahendra K.V., 2014. Effect of hot rolling on Al-4.5%Cu alloy reinforced fly ash metal matrix composite. *International Journal of Composite Materials*, 4(1), pp.21-29.
- [110] Ma, K., Wen, H., Hu, T., Topping, T.D., Isheim, D., Seidman, D.N., Lavernia, E.J. and Schoenung, J.M., 2014. Mechanical behavior and strengthening mechanisms in ultrafine grain precipitation-strengthened aluminum alloy. *Acta Materialia*, 62, pp.141-155.
- [111] Ma, S.M., Zhang, P., Ji, G., Chen, Z., Sun, G.A., Zhong, S.Y., Ji, V. and Wang, H.W., 2014. Microstructure and mechanical properties of friction stir processed Al-Mg-Si alloys dispersion-strengthened by nanosized TiB₂ particles. *Journal of Alloys and Compounds*, 616, pp.128-136.
- [112] Ma, Z.Y., Li, Y.L., Liang, Y., Zheng, F., Bi, J. and Tjong, S.C., 1996. Nanometric Si₃N₄ particulate-reinforced aluminum composite. *Materials Science and Engineering: A*, 219(1-2), pp.229-231.
- [113] Ma, Z.Y., Mishra, R.S. and Mahoney, M.W., 2002. Superplastic deformation behaviour of friction stir processed 7075Al alloy. *Acta Materialia*, 50(17), pp.4419-4430.
- [114] Ma, Z.Y., Pilchak, A.L., Juhas, M.C. and Williams, J.C., 2008. Microstructural refinement and property enhancement of cast light alloys via friction stir processing. *Scripta Materialia*, 58(5), pp.361-366.
- [115] Ma, Z.Y., Sharma, S.R. and Mishra, R.S., 2006. Effect of friction stir processing on the microstructure of cast A356 aluminum. *Materials Science and Engineering: A*, 433(1-2), pp.269-278.
- [116] Mahendra, K.V. and Radhakrishna, K., 2007. Fabrication of Al-4.5%Cu alloy with fly ash metal matrix composites and its characterization. *Materials Science-Poland*, 25(1), pp.57-68.
- [117] Mahmoud, E.R., Takahashi, M., Shibayanagi, T. and Ikeuchi, K., 2010. Wear characteristics of surface-hybrid-MMCs layer fabricated on aluminum plate by friction stir processing. *Wear*, 268(9-10), pp.1111-1121.

- [118] Mahmoud, T.S., El-Kady, E.S.Y. and Al-Shihiri, A.S.M., 2012. Corrosion behaviour of Al/SiC and Al/ Al₂O₃ nanocomposites. *Materials Research*, 15(6), pp.903-910.
- [119] Mahoney, M.W., Rhodes, C.G., Flintoff, J.G., Bingel, W.H. and Spurling, R.A., 1998. Properties of friction stir welded 7075 T651 aluminum. *Metallurgical and materials transactions A*, 29(7), pp.1955-1964.
- [120] Mallik, B., Sikdar, K., Roy, D., 2017. Synthesis and characterization of aluminium base in situ metal matrix composites by spark plasma sintering. *Journal of Materials Science Research*, 7(1), pp.14-19.
- [121] Mandal, P.K., Anant, R., Kumar, R. and Muthaiah, V.R., 2017. Effect of scandium on ageing kinetics in cast Al-Zn-Mg alloys. *Materials Science and Engineering: A*, 696, pp.257-266.
- [122] Manna, R., Mukhopadhyay, N.K. and Sastry, G.V.S., 2008. Effect of equal channel angular pressing on microstructure and mechanical properties of commercial purity aluminum. *Metallurgical and materials transactions A*, 39(7), pp.1525-1534.
- [123] Mazaheri, Y., Karimzadeh, F. and Enayati, M.H., 2013. Tribological behavior of A356/ Al₂O₃ surface nanocomposite prepared by friction stir processing. *Metallurgical and Materials Transactions A*, 45(4), pp.2250-2259.
- [124] Mazahery, A., Abdizadeh, H. and Baharvandi, H.R., 2009. Development of high-performance A356/nano-Al₂O₃ composites. *Materials Science and Engineering: A*, 518(1-2), pp.61-64.
- [125] McNelley, T.R., Swaminathan, S. and Su, J.Q., 2008. Recrystallization mechanisms during friction stir welding/processing of aluminum alloys. *Scripta Materialia*, 58(5), pp.349-354.
- [126] McQueen, H.J., Evangelista, E. and Kassner, M.E., 1991. The classification and determination of restoration mechanisms in the hot working of Al alloys. *Zeitschrift fur Metallkunde*, 82(5), pp.336-345.
- [127] Miao, W.F. and Laughlin, D.E., 2000. Effects of Cu content and preaging on precipitation characteristics in aluminum alloy 6022. *Metallurgical and Materials Transactions A*, 31(2), pp.361-371.
- [128] Mishra, R.S. and Komarasamy, M., 2016. Friction stir welding of high strength 7XXX aluminum alloys. Butterworth-Heinemann.
- [129] Mishra, R.S. and Ma, Z.Y., 2005. Friction stir welding and processing. *Materials science and engineering: R: reports*, 50(1-2), pp.1-78.
- [130] Mishra, R.S. and Mahoney, M.W., 2001. Friction stir processing: a new grain refinement technique to achieve high strain rate superplasticity in commercial alloys. In *Materials Science Forum*, 357, pp.507-514.

- [131] Mishra, R.S. and Mahoney, M.W., 2007. Friction stir welding and processing, ASM International. Material Park, Ohio, The Materials Information Society.
- [132] Mishra, R.S., Mahoney, M.W., McFadden, S.X., Mara, N.A. and Mukherjee, A.K., 1999. High strain rate superplasticity in a friction stir processed 7075 Al alloy. *Scripta Materialia*, 42(2), pp.163-168.
- [133] Mishra, S.K., Tiwari, S.M., Carter, J.T. and Tewari, A., 2014. Texture evolution during annealing of AZ31 Mg alloy rolled sheet and its effect on ductility. *Materials Science and Engineering: A*, 599, pp.1-8.
- [134] Mohseni, E., Zalnezhad, E., Sarhan, A.A. and Bushroa, A.R., 2014. Review Article: A study on surface modification of Al7075-T6 alloy against fretting fatigue phenomenon. *Advances in Materials Science and Engineering*, 2014, pp.1-17
- [135] Mondal, D.P. and Das, S., 2006. High stress abrasive wear behaviour of aluminium hard particle composites: Effect of experimental parameters, particle size and volume fraction. *Tribology international*, 39(6), pp.470-478.
- [136] Morishige, T., Hirata, T., Tsujikawa, M. and Higashi, K., 2010. Comprehensive analysis of minimum grain size in pure aluminum using friction stir processing. *Materials Letters*, 64(17), pp.1905-1908.
- [137] Mosleh-Shirazi, S., Akhlaghi, F. and Li, D.Y., 2016. Effect of SiC content on dry sliding wear, corrosion and corrosive wear of Al/SiC nanocomposites. *Transactions of Nonferrous Metals Society of China*, 26(7), pp.1801-1808.
- [138] Mosleh-Shirazi, S., Hua, G., Akhlaghi, F., Yan, X. and Li, D., 2015. Interfacial valence electron localization and the corrosion resistance of Al-SiC nanocomposite. *Scientific reports*, 5, 18154.
- [139] Mousavian, R.T., Khosroshahi, R.A., Yazdani, S., Brabazon, D. and Boostani, A.F., 2016. Fabrication of aluminum matrix composites reinforced with nano-to micrometer-sized SiC particles. *Materials & Design*, 89, pp.58-70.
- [140] Mukhopadhyay, N.K., Uhlenwinkel, V. and Srivastava, V.C., 2015. Synthesis and characterization of bulk Al-Cu-Fe based quasicrystals and composites by spray forming. *Journal of Materials Engineering and Performance*, 24(6), pp.2172-2178.
- [141] Mula, S., Pabi, S.K., Koch, C.C., Padhi, P. and Ghosh, S., 2012. Workability and mechanical properties of ultrasonically cast Al-Al₂O₃ nanocomposites. *Materials Science and Engineering: A*, 558, pp.485-491.
- [142] Mula, S., Padhi, P., Panigrahi, S.C., Pabi, S.K. and Ghosh, S., 2009. On structure and mechanical properties of ultrasonically cast Al-2% Al₂O₃ nanocomposite. *Materials Research Bulletin*, 44(5), pp.1154-1160.
- [143] Mula, S., Setman, D., Youssef, K., Scattergood, R.O. and Koch, C.C., 2015. Structural evolution of Cu (1-X) YX alloys prepared by mechanical alloying: Their thermal

- stability and mechanical properties. *Journal of Alloys and Compounds*, 627, pp.108-116.
- [144] Naher, S., Brabazon, D. and Looney, L., 2003. Simulation of the stir casting process. *Journal of Materials Processing Technology*, 143, pp.567-571.
- [145] Nia, A.A., Omidvar, H. and Nourbakhsh, S.H., 2014. Effects of an overlapping multi-pass friction stir process and rapid cooling on the mechanical properties and microstructure of AZ31 magnesium alloy. *Materials & Design*, 58, pp.298-304.
- [146] Nunes, P.C.R. and Ramanathan, L.V., 1995. Corrosion behavior of alumina-aluminum and silicon carbide-aluminum metal-matrix composites. *Corrosion*, 51(8), pp.610-617.
- [147] Onat, A., Akbulut, H. and Yilmaz, F., 2007. Production and characterisation of silicon carbide particulate reinforced aluminium-copper alloy matrix composites by direct squeeze casting method. *Journal of Alloys and Compounds*, 436(1-2), pp.375-382.
- [148] Orozco-Caballero, A., Hidalgo-Manrique, P., Cepeda-Jiménez, C.M., Rey, P., Verdera, D., Ruano, O.A. and Carreño, F., 2016. Strategy for severe friction stir processing to obtain acute grain refinement of an Al-Zn-Mg-Cu alloy in three initial precipitation states. *Materials Characterization*, 112, pp.197-205.
- [149] Ouyang, G., Ray, P.K., Kramer, M.J. and Akinc, M., 2016. High-temperature oxidation of ZrB₂-SiC-AlN composites at 1600° C. *Journal of the American Ceramic Society*, 99(3), pp.808-813.
- [150] Ozben, T., Kilickap, E. and Cakır, O., 2008. Investigation of mechanical and machinability properties of SiC particle reinforced Al-MMC. *Journal of materials processing technology*, 198(1-3), pp.220-225.
- [151] Padhi, P., Panigrahi, S.C. and Ghosh, S., 2008. A new method for preparation of metal matrix nanocomposites. In *AIP Conference Proceedings*, 1063(1), pp.371-375.
- [152] Panigrahi, S.K. and Jayaganthan, R., 2011a. Development of ultrafine grained high strength age hardenable Al 7075 alloy by cryorolling. *Materials & Design*, 32(6), pp.3150-3160.
- [153] Panigrahi, S.K. and Jayaganthan, R., 2011b. Effect of ageing on microstructure and mechanical properties of bulk, cryorolled, and room temperature rolled Al 7075 alloy. *Journal of Alloys and Compounds*, 509(40), pp.9609-9616.
- [154] Pargunde, D., Tampuskar, D. and Kulkarni, S.S., 2013. Review Article: Fabrication of metal matrix composite by stir casting method. *International Journal of Advanced Engineering Research and Studies*, II/ IV, 2013, pp.49-51.
- [155] Park, J.K. and Ardell, A.J., 1983. Microstructures of the commercial 7075 Al alloy in the T651 and T7 tempers. *Metallurgical Transactions A*, 14(10), pp.1957-1965.

- [156] Prabu, S.B., Karunamoorthy, L., Kathiresan, S. and Mohan, B., 2006. Influence of stirring speed and stirring time on distribution of particles in cast metal matrix composite. *Journal of Materials Processing Technology*, 171(2), pp.268-273.
- [157] Prangnell, P.B. and Heason, C.P., 2005. Grain structure formation during friction stir welding observed by the 'stop action technique'. *Acta Materialia*, 53(11), pp.3179-3192.
- [158] Proton, V., Alexis, J., Andrieu, E., Delfosse, J., Lafont, M.C. and Blanc, C., 2013. Characterisation and understanding of the corrosion behaviour of the nugget in a 2050 aluminium alloy friction stir welding joint. *Corrosion Science*, 73, pp.130-142.
- [159] Raghavan, R.S., Tiwari, S.M., Mishra, S.K. and Carsley, J.E., 2014. Recovery quantification and onset of recrystallization in aluminium alloys. *Philosophical Magazine Letters*, 94(12), pp.755-763.
- [160] Raghavan, V., 2015. *Physical metallurgy: principles and practice*. PHI Learning Pvt. Ltd.
- [161] Rahsepar, M. and Jarahimoghadam, H., 2016. The influence of multipass friction stir processing on the corrosion behavior and mechanical properties of zircon-reinforced Al metal matrix composites. *Materials Science and Engineering: A*, 671, pp.214-220.
- [162] Rajan, H.M., Dinaharan, I., Ramabalan, S. and Akinlabi, E.T., 2016. Influence of friction stir processing on microstructure and properties of AA7075/TiB₂ in situ composite. *Journal of Alloys and Compounds*, 657, pp.250-260.
- [163] Rajulapati, K.V., Scattergood, R.O., Murty, K.L., Horita, Z., Langdon, T.G. and Koch, C.C., 2008. Mechanical properties of bulk nanocrystalline aluminum-tungsten alloys. *Metallurgical and Materials Transactions A*, 39(10), pp.2528-2534.
- [164] Ramu, G. and Bauri, R., 2009. Effect of equal channel angular pressing (ECAP) on microstructure and properties of Al-SiCp composites. *Materials & Design*, 30(9), pp.3554-3559.
- [165] Ray, B.C., Mula, S., Bera, T. and Ray, P.K., 2006. Prior thermal spikes and thermal shocks on mechanical behavior of glass fiber-epoxy composites. *Journal of reinforced plastics and composites*, 25(2), pp.197-213.
- [166] Ray, P.K., Brammer, T., Ye, Y.Y., Akinc, M. and Kramer, M.J., 2010. A multi-stage hierarchical approach to alloy design. *JOM*, 62(10), pp.25-29.
- [167] Reddy, P.J., Kailas, S.V. and Srivatsan, T.S., 2011. Effect of tool angle on friction stir welding of aluminum alloy 5052: Role of sheet thickness. In *Advanced Materials Research*, 410, pp.196-205.
- [168] Rejil, C.M., Dinaharan, I., Vijay, S.J. and Murugan, N., 2012. Microstructure and sliding wear behavior of AA6360/(TiC+B₄C) hybrid surface composite layer

- synthesized by friction stir processing on aluminum substrate. *Materials Science and Engineering: A*, 552, pp.336-344.
- [169] Rhodes, C.G., Mahoney, M.W., Bingel, W.H. and Calabrese, M., 2003. Fine-grain evolution in friction stir processed 7050 aluminum. *Scripta Materialia*, 48(10), pp.1451-1455.
- [170] Rhodes, C.G., Mahoney, M.W., Bingel, W.H., Spurling, R.A. and Bampton, C.C., 1997. Effects of friction stir welding on microstructure of 7075 aluminum. *Scripta Materialia*, 36(1).
- [171] Robson, J.D. and Campbell, L., 2010. Model for grain evolution during friction stir welding of aluminium alloys. *Science and Technology of Welding and Joining*, 15(2), pp.171-176.
- [172] Rometsch, P.A., Zhang, Y. and Knight, S., 2014. Heat treatment of 7xxx series aluminium alloys-Some recent developments. *Transactions of Nonferrous Metals Society of China*, 24(7), pp.2003-2017.
- [173] Rouzbehani, R., Kokabi, A.H., Sabet, H., Paidar, M. and Ojo, O.O., 2018. Metallurgical and mechanical properties of underwater friction stir welds of Al7075 aluminum alloy. *Journal of Materials Processing Technology*, 262, pp.239-256.
- [174] Roy, D., Kumari, S., Mitra, R. and Manna, I., 2007. Microstructure and mechanical properties of mechanically alloyed and spark plasma sintered amorphous-nanocrystalline $Al_{65}Cu_{20}Ti_{15}$ intermetallic matrix composite reinforced with TiO_2 nanoparticles. *Intermetallics*, 15(12), pp.1595-1605.
- [175] Roy, D., Mitra, R., Ojo, O.A., Singh, S.S., Kolesnikov, D., Lojkowski, W., Scattergood, R.O., Koch, C.C. and Manna, I., 2012. Evaluation of mechanical properties of partially amorphous and nanocrystalline $Al_{50}Ti_{40}Si_{10}$ composites prepared by mechanical alloying and hot isostatic pressing. *Materials Science and Engineering: A*, 555, pp.21-27.
- [176] Sahraeinejad, S., Izadi, H., Haghshenas, M. and Gerlich, A.P., 2015. Fabrication of metal matrix composites by friction stir processing with different particles and processing parameters. *Materials Science and Engineering: A*, 626, pp.505-513.
- [177] Sajjadi, S.A., Parizi, M.T., Ezatpour, H.R. and Sedghi, A., 2012. Fabrication of A356 composite reinforced with micro and nano Al_2O_3 particles by a developed compocasting method and study of its properties. *Journal of Alloys and Compounds*, 511(1), pp.226-231.
- [178] Sakai, T., Belyakov, A., Kaibyshev, R., Miura, H. and Jonas, J.J., 2014. Dynamic and post-dynamic recrystallization under hot, cold and severe plastic deformation conditions. *Progress in materials science*, 60, pp.130-207.

- [179] Sakurada, D., Katoh, K. and Tokisue, H., 2002. Underwater friction welding of 6061 aluminum alloy. *Journal-Japan Institute of Light Metals*, 52(1), pp.2-6.
- [180] Samuel, A.M., Liu, H. and Samuel, F.H., 1993. On the castability of Al-Si/SiC particle-reinforced metal-matrix composites: Factors affecting fluidity and soundness. *Composites science and technology*, 49(1), pp.1-12.
- [181] Sato, Y.S., Kokawa, H., Enomoto, M. and Jogan, S., 1999. Microstructural evolution of 6063 aluminum during friction stir welding. *Metallurgical and Materials Transactions A*, 30(9), pp.2429-2437.
- [182] Sato, Y.S., Park, S.H.C. and Kokawa, H., 2001. Microstructural factors governing hardness in friction stir welds of solid-solution-hardened Al alloys. *Metallurgical and Materials Transactions A*, 32(12), pp.3033-3042.
- [183] Scattergood, R.O., Koch, C.C., Murty, K.L. and Brenner, D., 2008. Strengthening mechanisms in nanocrystalline alloys. *Materials Science and Engineering: A*, 493(1-2), pp.3-11.
- [184] Sert, A. and Celik, O.N., 2014. Wear behavior of SiC-reinforced surface composite A17075-T651 aluminum alloy produced using friction stir processing. *Indian Journal of Engineering and Materials Sciences*, 21, pp.35-43.
- [185] Shaeri, M.H., Shaeri, M., Ebrahimi, M., Salehi, M.T. and Seyyedein, S.H., 2016. Effect of ECAP temperature on microstructure and mechanical properties of Al-Zn-Mg-Cu alloy. *Progress in Natural Science: Materials International*, 26(2), pp.182-191.
- [186] Sharma, C., Dwivedi, D.K. and Kumar, P., 2012a. Influence of in-process cooling on tensile behaviour of friction stir welded joints of AA7039. *Materials Science and Engineering: A*, 556, pp.479-487.
- [187] Sharma, C., Dwivedi, D.K. and Kumar, P., 2012b. Friction stir welding of Al-Zn-Mg alloy AA7039. *Light Metals TMS 2012*, pp.503-507.
- [188] Sharma, P., Chauhan, G. and Sharma, N., 2013. Production of AMC by stir casting-an overview. *International Journal of Contemporary Practices*, 2(1), pp.23-46.
- [189] Sharma, V., 2015. Fabrication and tribology of friction stir processed Al alloy surface composites. Ph.D. Dissertation, Indian Institute of Technology Roorkee, India.
- [190] Shen, M.J., Ying, T., Chen, F.Y. and Hou, J.M., 2016. Effect of micro-and nano-SiC particulate reinforcements in magnesium-based metal matrix composites. *Journal of Materials Engineering and Performance*, 25(6), pp.2222-2229.
- [191] Shinde, S.S., Kulkarni, S.G, Kulkarni, S.S., 2015. Manufacturing of aluminium matrix composite using stir casting method. *International Journal of Innovations in Engineering Research and Technology*, 2(5), pp.1-6.

- [192] Singh, A.K., Ghosh, S. and Mula, S., 2016. Simultaneous improvement of strength, ductility and corrosion resistance of Al2024 alloy processed by cryoforging followed by ageing. *Materials Science and Engineering: A*, 651, pp.774-785.
- [193] Singla, M., Dwivedi, D.D., Singh, L. and Chawla, V., 2009. Development of aluminium based silicon carbide particulate metal matrix composite. *Journal of Minerals and Materials Characterization and Engineering*, 8(06), p.455.
- [194] Skibo, M.D. and Schuster, D.M., Dural Aluminum Composites Corp, 1988. Process for preparation of composite materials containing nonmetallic particles in a metallic matrix, and composite materials made thereby. U.S. Patent 4,786,467.
- [195] Srivastava, N. and Chaudhari, G.P., 2016. Strengthening in Al alloy nano composites fabricated by ultrasound assisted solidification technique. *Materials Science and Engineering: A*, 651, pp.241-247.
- [196] Starke Jr, E.A. and Staley, J.T., 1996. Application of modern aluminum alloys to aircraft. *Progress in aerospace sciences*, 32(2-3), pp.131-172.
- [197] Stoichev, N., Pramanick, A.K., Yaneva, S., Giurov, S., Lazarova, M., Setman, D. and Stefanov, G., 2010, September. Influence of Zr on structure development in rapidly solidified Al-Si alloys. In *Proc. 9th Workshop Nanoscience and Nanotechnology (Varna, Bulgaria) 2009*, pp.138-140.
- [198] Su, J.Q., Nelson, T.W. and Sterling, C.J., 2005a. Microstructure evolution during FSW/FSP of high strength aluminum alloys. *Materials Science and Engineering: A*, 405(1-2), pp.277-286.
- [199] Su, J.Q., Nelson, T.W. and Sterling, C.J., 2005b. Friction stir processing of large-area bulk UFG aluminum alloys. *Scripta Materialia*, 52(2), pp.135-140.
- [200] Su, J.Q., Nelson, T.W., Mishra, R. and Mahoney, M., 2003. Microstructural investigation of friction stir welded 7050-T651 aluminium. *Acta Materialia*, 51(3), pp.713-729.
- [201] Su, Y.H.F., Chen, Y.C. and Tsao, C.Y.A., 2004. Workability of spray-formed 7075 Al alloy reinforced with SiCp at elevated temperatures. *Materials Science and Engineering: A*, 364(1-2), pp.296-304.
- [202] Sujan, D. Oo, Z., Rahman, M.E., Maleque, M.A. and Tan, C.K., 2012. Physio-mechanical properties of aluminium metal matrix composites reinforced with Al₂O₃ and SiC. *International Journal of Engineering and Applied Sciences*, 6, pp.288-291.
- [203] Sun, Y.F. and Fujii, H., 2011. The effect of SiC particles on the microstructure and mechanical properties of friction stir welded pure copper joints. *Materials Science and Engineering: A*, 528(16-17), pp.5470-5475.

- [204] Surappa, M.K., 1997. Microstructure evolution during solidification of DRMMCs (Discontinuously reinforced metal matrix composites): State of art. *Journal of Materials Processing Technology*, 63(1-3), pp.325-333.
- [205] Suryanarayana, C. and Al-Aqeeli, N., 2013. Mechanically alloyed nanocomposites. *Progress in Materials Science*, 58(4), pp.383-502.
- [206] Suryanarayana, C. and Koch, C.C., 2000. Nanocrystalline materials-Current research and future directions. *Hyperfine Interactions*, 130(1-4), pp.5-44.
- [207] Taha, M.A., 2001. Industrialization of cast aluminum matrix composites (AMCCs). *Materials and manufacturing Processes*, 16(5), pp.619-641.
- [208] Thangarasu, A., Murugan, N., Dinaharan, I. and Vijay, S.J., 2014. Influence of traverse speed on microstructure and mechanical properties of AA6082-TiC surface composite fabricated by friction stir processing. *Procedia Materials Science*, 5, pp.2115-2121.
- [209] Upadhyay, P. and Reynolds, A.P., 2010. Effects of thermal boundary conditions in friction stir welded AA7050-T7 sheets. *Materials Science and Engineering: A*, 527(6), pp.1537-1543.
- [210] Vijayavel, P., Balasubramanian, V. and Sundaram, S., 2014. Effect of shoulder diameter to pin diameter (D/d) ratio on tensile strength and ductility of friction stir processed LM25AA-5% SiCp metal matrix composites. *Materials & Design*, 57, pp.1-9.
- [211] Vishwanatha, H.M., Eravelly, J., Kumar, C.S. and Ghosh, S., 2016. Microstructure and mechanical properties of aluminum-alumina bulk nanocomposite produced by a novel two-step ultrasonic casting technique. *Metallurgical and Materials Transactions A*, 47(11), pp.5630-5640.
- [212] Vishwanatha, H.M., Eravelly, J., Kumar, C.S. and Ghosh, S., 2017. Dispersion of ceramic nano-particles in the Al-Cu alloy matrix using two-step ultrasonic casting and resultant strengthening. *Materials Science and Engineering: A*, 708, pp.222-229.
- [213] Woo, W., Balogh, L., Ungár, T., Choo, H. and Feng, Z., 2008. Grain structure and dislocation density measurements in a friction stir welded aluminum alloy using X-ray peak profile analysis. *Materials Science and Engineering: A*, 498(1-2), pp.308-313.
- [214] Xu, N., Ueji, R. and Fujii, H., 2014. Enhanced mechanical properties of 70/30 brass joint by rapid cooling friction stir welding. *Materials Science and Engineering: A*, 610, pp.132-138.
- [215] Xu, W.F., Liu, J.H., Chen, D.L., Luan, G.H. and Yao, J.S., 2012. Improvements of strength and ductility in aluminum alloy joints via rapid cooling during friction stir welding. *Materials Science and Engineering: A*, 548, pp.89-98.

- [216] Xue, P., Xiao, B.L., Zhang, Q. and Ma, Z.Y., 2011. Achieving friction stir welded pure copper joints with nearly equal strength to the parent metal via additional rapid cooling. *Scripta Materialia*, 64(11), pp.1051-1054.
- [217] Yadav, D. and Bauri, R., 2015. Friction stir processing of Al-TiB₂ in situ composite: effect on particle distribution, microstructure and properties. *Journal of Materials Engineering and Performance*, 24(3), pp.1116-1124.
- [218] Yang, R., Zhang, Z., Zhao, Y., Chen, G., Guo, Y., Liu, M. and Zhang, J., 2015. Effect of multi-pass friction stir processing on microstructure and mechanical properties of Al₃Ti/A356 composites. *Materials Characterization*, 106, pp.62-69.
- [219] Yong, Y., Lan, J. and Li, X., 2004. Study on bulk aluminum matrix nano-composite fabricated by ultrasonic dispersion of nano-sized SiC particles in molten aluminum alloy. *Materials Science and Engineering: A*, 380(1-2), pp.378-383.
- [220] Yazdipour, A. and Dehghani, K., 2009. Modeling the microstructural evolution and effect of cooling rate on the nanograins formed during the friction stir processing of Al5083. *Materials Science and Engineering: A*, 527(1-2), pp.192-197.
- [221] Youssef, K.M., Scattergood, R.O., Murty, K.L. and Koch, C.C., 2006. Nanocrystalline Al-Mg alloy with ultrahigh strength and good ductility. *Scripta Materialia*, 54(2), pp.251-256.
- [222] Zabihi, M., Toroghinejad, M.R. and Shafyei, A., 2013. Application of powder metallurgy and hot rolling processes for manufacturing aluminum/alumina composite strips. *Materials Science and Engineering: A*, 560, pp.567-574.
- [223] Zakaria, H.M., 2014. Microstructural and corrosion behavior of Al/SiC metal matrix composites. *Ain Shams Engineering Journal*, 5(3), pp.831-838.
- [224] Zhang, F., Su, X., Chen, Z. and Nie, Z., 2015. Effect of welding parameters on microstructure and mechanical properties of friction stir welded joints of a super high strength Al-Zn-Mg-Cu aluminum alloy. *Materials & Design*, 67, pp.483-491.
- [225] Zhang, L.J., Qiu, F., Wang, J.G. and Jiang, Q.C., 2015. High strength and good ductility at elevated temperature of nano-SiCp/Al2014 composites fabricated by semi-solid stir casting combined with hot extrusion. *Materials Science and Engineering: A*, 626, pp.338-341.
- [226] Zhao, Y.H., Liao, X.Z., Jin, Z., Valiev, R.Z. and Zhu, Y.T., 2004. Microstructures and mechanical properties of ultrafine grained 7075 Al alloy processed by ECAP and their evolutions during annealing. *Acta Materialia*, 52(15), pp.4589-4599.
- [227] Zhou, D., Qiu, F. and Jiang, Q., 2015. The nano-sized TiC particle reinforced Al-Cu matrix composite with superior tensile ductility. *Materials Science and Engineering: A*, 622, pp.189-193.

- [228] Zhou, L., Wang, T., Zhou, W.L., Li, Z.Y., Huang, Y.X. and Feng, J.C., 2016. Microstructural characteristics and mechanical properties of 7050-T7451 aluminum alloy friction stir welded joints. *Journal of Materials Engineering and Performance*, 25(6), pp.2542-2550.

List of publications

Journals:

- [1] **Atul Kumar**, A. Kumar, K. Pal, S. Mula, “Effects of in-process cryocooling on metallurgical and mechanical properties of friction stir processed Al7075 alloy”, **Materials Characterization**, April 2018, Vol. 144, pp. 440-447. (Journal Impact Factor: **3.22**).
- [2] **Atul Kumar**, K. Pal, S. Mula, “Simultaneous improvement of mechanical strength, ductility and corrosion resistance of stir cast Al7075-2% SiC micro- and nanocomposites by friction stir processing”, **Journal of Manufacturing Processes**, December 2017, Vol. 30, pp. 1-13. (Impact Factor: **3.46**).
- [3] **Atul Kumar**, S.K. Sharma, K. Pal, S. Mula, “Effect of process parameters on microstructural evolution, mechanical properties and corrosion behavior of friction stir processed Al 7075 alloy”, **Journal of Materials Engineering and Performance**, March 2017, Vol. 26 (3), pp. 1122–1134. (Impact Factor: **1.46**).
- [4] **Atul Kumar**, K. Pal, S. Mula, “Effects of in-process cryocooling on microstructural evolution and mechanical properties of friction stir processed Al7075-SiC cast nanocomposites”, (Communicated).

Conferences:

- [1] **Atul kumar**, Kaushik Pal, Suhrit Mula. “Characterization of microstructural evolution and mechanical properties of cryorolled Al7075-SiC nanocomposites”. International Conference on Nanotechnology: Ideas, Innovations and Initiatives (ICN:3I-2017), Organized by Centre of Nanotechnology and Department of Mechanical & Industrial Engineering, Indian Institute of Technology Roorkee, India on 6th-8th Dec, 2017.
- [2] **Atul kumar**, Ashwin Kumar, Kaushik Pal, Suhrit Mula. “Effects of active-cooling on metallurgical and mechanical properties during friction stir processing of Al 7075 alloy”. International Conference on Advanced Materials and Processes: Challenges and Opportunities (AMPCO-2017), Organized by Department of Metallurgical and Materials Engineering, Indian Institute of Technology Roorkee, India on 30th Nov-2nd Dec,2017.
- [3] **Atul kumar**, Kaushik Pal, Suhrit Mula. “Development of ultrafine-grained Al7075-SiC nanocomposite by stir casting followed by cryorolling”. NMD ATM 2017, BITS, Pilani-K K Birla Goa Campus, 55th National Metallurgist day & 71st Annual technical meeting, 11-14 November 2017.
- [4] **Atul kumar**, Kaushik Pal, Suhrit Mula. “Effect of process parameters on microstructure and mechanical properties of friction stir processed Al 7075 alloy”. NMD ATM 2015, Le Meridian, Coimbatore, 53rd National Metallurgist day & 69th Annual technical meeting, 13-16 Nov, 2015.
- [5] **Atul kumar**, attained National conference on physical simulation of thermo-mechanical processing of materials and 7th Gleeble User Workshop (**GUWI'18**) held from 12-13 October 2018, IIT Roorkee, Uttarakhand, India.